

THE EFFECT OF MICRITE CONTENT AND MACROPOROSITY ON
THE TRANSPORT AND ELASTIC PROPERTIES OF CARBONATES

A DISSERTATION
SUBMITTED TO THE DEPARTMENT OF GEOPHYSICS
AND THE COMMITTEE ON GRADUATE STUDIES
OF STANFORD UNIVERSITY
IN PARTIAL FULFILLMENT OF THE REQUIREMENTS
FOR THE DEGREE
OF DOCTOR OF PHILOSOPHY

Ammar El Hussein
August 2016

ABSTRACT

Carbonate rocks are major sedimentary rocks playing an important role both as water and hydrocarbon reservoirs. Thus, understanding the functional relationships between remotely probed, geophysical parameters and sedimentology-related properties is essential for better characterization of reservoir resources.

Carbonates, however, are well known for their complex dual-particle size and dual-porosity microstructures, which create significant scatter in fundamental rock physics relationships such as the porosity-permeability and porosity-velocity relationship. The main factor controlling carbonate heterogeneity is the complex post-depositional diagenesis, which superimposes on the original microstructures inherited from the depositional environment. The micrite and macroporosity content in carbonate rocks are sedimentology-related parameters that vary because of both the energy of the depositional environment and the extent of leaching/washing that the rock experiences upon diagenesis. Thus, the primary focus of this thesis is to investigate how sedimentology-related parameters such as micrite content and macroporosity affect the variability of transport

(porosity and permeability) and elastic (P- and S-wave velocities) properties. By understanding the interplay between these factors, the final objective of this research is to better inform modeling by providing quantifiable, textural parameters, which can improve the interpretation of transport and elastic properties of carbonate reservoirs. Previous attempts to investigate the role of these sedimentology-related parameters remained mainly qualitative and not systematic. As a consequence, results in the literature still appear inconclusive. Overall, this has led to poor agreement in the geophysics literature about the effect of micrite and macroporosity on the transport and elastic properties of carbonates.

In this dissertation, we conduct a comprehensive study starting with controlled analogs serving as a proof of concept for the analysis and then extending the investigation to natural carbonates. The novelty lays on the fact that we prepare analog samples in the laboratory using natural calcite grains and micrite with the goal of studying the role of the content of micrite. In addition, we introduce controlled volumes of acetone-soluble solid matter (camphor) into the microstructures at the expense of the micrite aggregates. Once dissolved, the mold functions as macropores. We perform a series of experimental measurements to obtain porosity, permeability, and acoustic velocities under both bench-top conditions and as a function of confining pressure. We then investigate the correlation between the measured properties and the sedimentology-related parameters, and then attempt to quantitatively model the observed trends. Finally, we extend the investigation to carbonate reservoir rocks in order to test the hypothesis and methodology developed from the work on analog samples. Toward this goal, we study 15 samples from Tengiz Field, an isolated carbonate platform, where the sedimentology-related parameters are estimated based on image analysis of micro-CT scans and thin sections of the samples.

The results obtained from the analogs and natural samples showed consistent trends regarding the effect of micrite content and macroporosity on the transport and elastic properties. With regard to the effect of micrite content and macroporosity on the transport properties, samples with higher micrite content and lower macroporosity exhibit lower permeability at any given porosity. Results show that the fraction of macropores in the samples is strongly correlated with the measured permeability since such pores do contribute more significantly to fluid flow compared to micropores. We used the varying micrite-to-grains ratio and its effect on the porosity-permeability relationship to inform the

Kozeny-Carman relation suitable for a pack of spheres. Our analysis showed that micrite affects the porosity-permeability relationship of carbonates by reducing the effective particle size and increasing the percolation porosity. Additionally, the coefficient of determination (R^2) between porosity and permeability was found to increase significantly when incorporating the micrite content and macroporosity into the analysis. This study shows that knowledge of both micrite content and macroporosity is of paramount importance to interpret and model porosity-permeability relationships in carbonates.

Our results regarding the effect of micrite content on elastic properties show that the sensitivity of acoustic velocity to pressure decreases as the micrite content increases. This suggests a stiffer pore structure in micrite rich samples compared to that in grain-supported samples. Such conclusion is supported by a) observations from SEM images showing rounder pores in micrite-supported samples compared to grain-supported samples characterized by microcracks at grain contacts, and b) smaller change in length (i.e., strain) measured under pressure for the micrite-rich samples, compared to grain-supported samples. Unlike micrite content, the fraction of macroporosity shows no strong correlation with acoustic velocities, at a given porosity, or with the sensitivity of velocity to pressure. This is contrary to what is frequently reported in literature suggesting that the fraction of macroporosity correlates with an increasing velocity at a given porosity. In our case, the effect of subrounded macropores (stiff pores) is in general compensated by a decrease in the content of micrite (stiff component) and thus, the overall acoustic velocity remains uncorrelated with the fraction of macropores.

ACKNOWLEDGEMENTS

I would like to take a moment to share with my respected reader my gratitude toward those who made this journey not just possible but also enjoyable. For me, my PhD journey and research have much deeper meaning than just the science and experimental procedures behind them. They are the sum of all the joyful and difficult moments I have gone through, they are the support, dedication and sacrifice of my loved ones. I see my work as a mean to show gratitude to all those who taught me, trained me, supported me and to all my beloved ones. In this section, I share with my respected reader part of my life in showing gratitude to those who made this work possible, those who contributed significantly to making me the person I am.

I would like to start by expressing my deep gratitude to my advisor: Tiziana Vanorio for advising, and supporting me during the 5 years I spent here in Stanford. Through our discussion and interactions, Tiziana taught me the value of thinking out of the box and being persistent while solving problems. It was such a great experience and honor to be part of her group. I am also thankful for Gary Mavko for bringing me to Stanford in the first place and for all of his inspiring discussions. I would also like to thank Tapan Mukerji and Jack Dvorkin for being on my defense committee and for all of their feedback and

comments throughout my years in Stanford. I want also to thank Jonathan Payne for being the committee chair for my oral defense. Additionally, I would like to thank all of my colleagues from the rock physics laboratory (SRPL) and rock physics and borehole geophysics project (SRB) especially Yuki, Adam Allan, Humberto, Dario, Priyanka and Nishank. It was a pleasure to work with and learn from all of you. I am also very thankful to Tony for his assistance in lab-related issues that included (but not limited) repairing equipment, and maintaining the lab in a good shape. Special thanks to all the staff in the Geophysics Department: Tara, Nancy, Fuad, Jared, Claudia, Vanessa and Michelle for their effort in handling all the administrative work and being always there for help.

I am indebted to Abu Dhabi National Oil Company (ADNOC) for sponsoring my study and for all the support the scholarship department has provided to me during my PhD journey. I am also grateful to Luca Duranti, Ted Playton, Tengizchevroil and Chevron for providing the samples studied in this work, as well as for their comments that improved the work. I would also like to thank all of the faculty and staff in the Petroleum Institute (in Abu Dhabi, UAE) for making my undergraduate experience very fruitful and enjoyable. This has definitely encouraged me to apply for further studies. Very special thanks go to Sandra Vega who encouraged me (during my undergraduate studies) to pursue my graduate studies and apply to Stanford. Sandra has also advised me during my undergraduate research which was such an awesome experience.

Outside the academic environment, I enjoyed being part of the Muslim community of Stanford University that I considered to be my big second family at Stanford. Through the Muslim community, I have made lifelong friends with whom I share unforgettable memories. Many thanks go to Waqas, Galym, Fahim, Kenneth, Mohammad, Ramy, Abdullah, Salahaddin, Leith, Adnan, Firas and many others. Several pages would be needed to mention the name of every single one from this awesome community, but I can only hope that this sentence covers it: thank you all. I was also honored by serving as member in the leadership of the Muslim community where I worked with amazing people including Zeshan, Kate, Tariq, Farah, Sevde, Osama and Mariam. I am also very thankful to all the friends of my wife especially Kate who is, without doubt, the best friend for my wife. Kate has been actually a friend for the whole family including my little son who found joy in playing with her every single time she visits us. I would also like to thank my

great neighbors: Motaz and Noha, Khalid and Maha for all the support and friendly company.

During my 5 years in Stanford, I also found a great company of the small Egyptian community at Stanford: Amr Abdelrazik who is the master of the grill in all of our gathering, Ahmed Essisi who gives me all the reasons to talk about politics every single time we meet, Sherif Halawa, Mamdouh Nasr, Mahmoud Sawaby, Mohammed Sabry, Hussein Adel, and Omar Alnaggar for all the great support and time they provided to my family and my-self. Among all the friends I made at Stanford, I am particularly grateful to Amr Essawi, my best friend and one of the greatest blessings I had during my PhD journey. I consider Amr as my older brother whose compassionate, sincerity, and support has impacted me from the first day I met him. I really enjoyed his company during my stay here, where we share together plenty of unforgettable moments and adventures. I am sure I will miss him the most when it is time to leave. Outside Stanford, I was part of a larger Egyptian community of the Silicon Valley. Such family-friendly support was very needed for me and my family....Thank you all. Special thanks go to Mohamed and Ahmed Elzeftawi, Ahmed Arafa, Ahmed Alsum, Hatem Bedair, Magdy Abdelrahman, Ahmed Ragab, Mohamed Abdel Halim, Khaile Alashmouny and their families for all the great times we spent together.

Last but not least, I would like to acknowledge my loved ones. None of what I have done could have been possible without the support of my parents. They loved me, and cared about me more than they do for themselves. They did not save any time, effort or money to support, teach and encourage me through every single step in my life. I believe I came to realize more the significance of what they have done for me after I had to live away from them, and after I became a father. Despite all the distances between us, I could still feel their unconditional love and support. I owe them everything and feel very proud and thankful to have such great parents. Although they never were waiting for anything in return, they gave me all the reasons to work hard, to make them proud of me, and to put a smile on their face. I would never be able to give them back even a tiny portion of what they have done for me, no matter what I do or will do. I ask Allah (God) to reward them for everything they have done for me, to shower them with His blessing and mercy, and I pray that I become the person they wanted me to be. I would like also to acknowledge all

of my siblings: Sumaya, Mohammed, Hamza and Mariam for all the support and the great times we have spent together. I always find happiness in spending time with them all whenever I visit Egypt. It filled my heart with joy to see my sister and brother starting their families with their loving spouses. I also spend a nice time during the vacation with my niece Hana and nephew Mosab, especially that my son loves them so much.

Finally, I would like to express my deep appreciation and special thanks to my dearest friend, my soul mate, my love, my sweetheart and lovely wife: Sarah. I am sure that there are no words that can really thank Sarah enough for all of her patience, dedication, love, and for being always there for me. I could not really dream of a better support for me during my PhD journey, other than Sarah, the coolness of my eyes. She indeed has the most beautiful loving heart, I have ever seen. A warm smile or hug from her at the end of the day, was really able to meltdown the ice of any hardship I was going through during the day. The way she tolerates and heals my frustration sometimes with a smile is just amazing. We share together unforgettable memories, going through both joyful and difficult moments. Besides being an awesome wife, Sarah is a very good mother too. It fills my heart with happiness to see our baby, Ayoub, growing and getting more handsome, where the best part is that he looks like his mam. I need also to acknowledge him for behaving “in general” and putting a smile in our face because of the funny way he speaks and acts sometimes. I will not also forget to thank my father and mother in law for raising such a great person, with whom I realize every day the amount of the care and effort her parents took so that Sarah is the person she is now. The love of my little family gave me really every reason to wake up every morning and work hard. For all of what Sarah has done for me, I really hope that Allah helps me to be able to make her the happiest person on earth. From my heart and soul, I would like to dedicate this thesis to you, honey.

Throughout my entire life, especially my PhD journey, I have been showered by the blessings of Allah. All praise is due to Him for blessing me with my family and with all the amazing people surrounding me. He is the one who guided me through everything, and with His blessing and mercy I have succeeded to finish my PhD. I ask Allah to guide me and grant me success through the next chapter of my life, and to give me the ability to praise Him for all of His bounties. I also pray that He helps me to use what He bestowed upon me to serve Him, His creation and leave a positive impact on this world.

TABLE OF CONTENTS

ABSTRACT	v
ACKNOWLEDGEMENTS	viii
TABLE OF CONTENTS	xii
LIST OF FIGURES	xv
LIST OF TABLES	xix
CHAPTER 1: INTRODUCTION	1
1.1 Carbonate Complexity and Motivations.....	1
1.2 Approach to the Problem.....	7
1.3 Objectives and Research Questions.....	8
1.4 Thesis Outline.....	9
CHAPTER 2: METHODOLOGY AND EXPERIMENTAL PROCEDURES	13
2.1 Introduction.....	13
2.2 Materials.....	14
2.3 Sample Preparation.....	16
2.3.1 Samples with Varying Micrite-to-Grain Ratio (Set MCR).....	16
2.3.2 Samples with Newly Created Macroporosity (Set MACRO).....	17
2.4 Rock Physics Experiments and Measurements.....	19
2.4.1 High Resolution Imaging Using Scanning Electron Microscopy (SEM).....	19
2.4.2 Helium Porosimetry.....	20

2.4.3 Klinkenberg-Corrected Permeability	21
2.4.4 Acoustic Velocities	22
2.4.5 Injection of CO ₂ -rich Water	22
CHAPTER 3: THE EFFECT OF MICRITE CONTENT AND MACROPOROSITY ON THE TRANSPORT PROPERTIES OF CARBONATE ANALOGS.....	25
3.1 Introduction.....	26
3.2 Methodology.....	29
3.3 Experimental Results.....	29
3.3.1 Sample Characterization and Microstructure.....	29
3.3.2 Micrite-Porosity Relationship in Set MCR Samples	32
3.3.3 The Porosity-Permeability Relationship	32
3.4 Discussion	35
3.4.1 Microstructure of the analogs	35
3.4.2 Micrite-Porosity Relationship in Set MCR Samples	37
3.4.2.1 Micro-Geometrical Interpretation	37
3.4.2.2 Modeling Micrite-Porosity Relationship	38
3.4.2.2.a Ideal Packing of Spheres.....	39
3.4.2.2.b Non-ideal Packing of Spheres.....	41
3.4.2.2.c Non-Ideal Packing of Non-Spherical Particles.....	45
3.4.2.2.d Modified Model to Estimate Porosity for Binary Mixtures of Non-Spherical Particles.....	47
3.4.2.2.e Validation of the Proposed Approach.....	51
3.4.2.2.f Limitations and Final Remarks.....	54
3.4.3 Porosity-Permeability Relationship in Analog Samples.....	57
3.4.3.1 The Effect of Micrite Content on the Porosity-Permeability Relationship.....	57
3.4.3.2 The Effect of Varying both Micrite Content and Macroporosity on Permeability.....	62
3.5 Conclusions.....	65
CHAPTER 4: THE EFFECT OF MICRITE CONTENT AND MACROPOROSITY ON THE ELASTIC PROPERTIES OF CARBONATE ANALOGS.....	68
4.1 Introduction.....	69
4.2 Methodology.....	73
4.3 Results and Discussion.....	73
4.3.1 Micrite Effect on Dry Acoustic Velocities and Their Sensitivity to Pressure...	73
4.3.2 Modeling the Changes in Pore Shape as a Function of Micrite Content.....	79
4.3.3 Modeling the Relationship between Micrite Content and Acoustic Velocities...	81

4.3.4 Effect of Macroporosity on Acoustic Velocities.....	86
4.3.5 Effect of Micrite on Fluid-Frame Interaction.....	88
4.4 Conclusions.....	91
CHAPTER 5: THE EFFECT OF MICRITE CONTENT AND MACROPOROSITY ON THE TRANSPORT AND ELASTIC PROPERTIES OF CARBONATE RESERVOIR ROCKS	93
5.1 Introduction.....	94
5.2 Study Area and Sample Selection.....	95
5.3 Methodology.....	98
5.3.1 Sample Characterization.....	98
5.3.2 Velocity Sensitivity to Pressure.....	98
5.3.3 Estimation of Microstructural parameters.....	98
5.3.3.1 Estimation of Microstructural parameters from CT scans.....	100
5.3.3.2 Estimation of Microstructural parameters from SEM Images.....	102
5.4 Results.....	106
5.5 Discussion.....	115
5.5.1 Parameter Estimation based on Image Analysis.....	115
5.5.1.1 Uncertainty Associated with Parameter Estimation.....	115
5.5.1.2 Limitations in Characterizing Microporosity Indirectly.....	120
5.5.2 Porosity-Permeability Relationships.....	124
5.5.3 Effect of Micrite Content and Macroporosity on Elastic Properties.....	129
5.5.4 Limitations and Possible Future Work.....	135
5.6 Conclusions.....	137
CHAPTER 6: FINAL REMARKS	140
REFERENCES	149
APPENDICES	157
Appendix A: Composition and Transport Properties of Analog Samples.....	157
Appendix B: Ideal Packing Model for Grains-Micrite Mixtures.....	158
Appendix C: Summary of Non-ideal Packing Model for Binary Mixtures of Spheres.....	159
Appendix D: Determination of Equivalent Packing Diameter.....	161
Appendix E: Relating Equivalent Packing Diameter to size and shape.....	164
Appendix F: Defining Sphericity in terms of Specific Surface Area	165
Appendix G: Defining the Specific Surface Area for Different Uniform Shaped Particles.....	166
Appendix H: Transport and Elastic Properties of Analog Samples.....	168
Appendix I: Summary of DEM Theory.....	169
Appendix J: Properties of Tengiz Samples.....	170
Appendix K: Modeling the Effect of Micrite on Permeability	172

LIST OF FIGURES

1.1	SEM image of a carbonate sample highlighting the microporous micrite.....	4
1.2	Schematic showing the different carbonate textures, after Dunham's (1962) classification.....	5
1.3	Schematic facies profile for carbonates.....	5
1.4	Classification of micrite microstructures and morphology, after Deville de Periere et al. 2011.	6
2.1	SEM images of skeletal grains highlighting their microstructure.....	15
2.2	SEM image of the microporous micrite aggregate showing the microstructure.....	15
2.3	Split steel cube with a cylindrical cavity used in cold pressing.....	16
2.4	SEM images for a grain supported sample before (a) and after (b) removing camphor.....	18
2.5	A schematic of the SEM set up; figure modified after Allan (2015).....	20
3.1	SEM images of several samples from set MCR.....	30
3.2	Some microfeatures in the created analogs including cement and micrite.....	31
3.3	SEM images of macropores created in grain-supported and micrite-supported samples.....	31
3.4	Plot of porosity as function of micrite content.....	32
3.5	Plot of permeability as function of porosity for set MCR and MACRO samples.....	33
3.6	Plot of permeability as function of porosity, data is color coded by micrite content.....	34
3.7	Permeability as function of porosity, highlighting changes as macropores were introduced...	35
3.8	Comparison between microstructure created in our analog samples and that of natural samples.....	36
3.9	Plot of permeability as function of micrite content.....	38
3.10	Porosity as function of clay content for the dry un-compacted sand-clay mixtures from Marion data set.....	40

3.11	Porosity as function of micrite fraction for the grain-micrite mixtures from set MCR samples.....	40
3.12	Porosity as function of small spheres fraction in binary mixture of spheres from McGeary data.....	42
3.13	Demonstration of the loosening effect in packing of spheres.....	42
3.14	Demonstration of the wall effect in packing of spheres.....	43
3.15	Modeling results for porosity as function of small spheres fraction (McGeary data set).....	45
3.16	Demonstration of the equivalent packing diameter concept.....	46
3.17	Summary of the proposed approach to estimate the porosity of binary mixtures.....	49
3.18	Modeling results for the porosity as function of micrite content.....	51
3.19	Validation of the proposed approach to estimate porosity of binary mixtures, using several published data.....	53
3.20	Un-compacted and compacted packing porosity for binary mixtures of crushed granite (Kwan data set).....	55
3.21	Porosity of sand-clay mixtures as a function of clay fraction (Knoll data set) with prediction of model.....	57
3.22	Percolation porosity and geometric factor as a function of micrite content for set MCR samples	61
3.23	Permeability as a function of porosity for all analog samples along with modeling results using Kozeny-Carman relations.....	62
3.24	Permeability (linear scale) as a function of porosity for samples with increasing content of introduced macropores.....	63
3.25	Permeability as function of both micrite content and induced macroporosity	64
4.1	P- and S-wave bench-top velocities as a function of micrite content for set MCR samples.....	74
4.2	Plot of P-wave velocity and S-wave velocity of set MCR samples, normalized by velocity at 1 MPa, as a function of confining pressure.....	75
4.3	Plot of bulk and shear modulus of set MCR samples, normalized by modulus at 1 MPa, as a function of confining pressure.....	75
4.4	Normalized percentage change in length as a function of micrite content measured at different pressures.....	76
4.5	SEM images of pure micrite and pure grain samples highlighting the rounder pores in the micrite.....	79
4.6	Schematic showing the conceptual model used to estimate the average aspect ratio using DEM model.....	80
4.7	Plot of the estimated aspect ratio using the DEM model as a function of micrite content of the analog samples from set MCR.....	81
4.8	Schematic showing the conceptual model describing the inclusion and host material when using DEM to predict elastic moduli of set MCR samples.....	83

4.9	Demonstration of the modeling results for velocity-micrite, and velocity-porosity relationships	85
4.10	P-wave and S-wave bench-top velocity as a function of porosity for set MACRO samples.....	87
4.11	SEM image of a grain-supported sample from set MACRO showing the presence of micro-cracks beside the introduced macropores.....	88
4.12	Percentage change in bulk modulus and shear modulus due to injection of CO ₂ -rich water as a function of confining pressure.....	90
5.1	Location of the Caspian region and Tengiz field.....	97
5.2	Schematic geologic model of Tengiz representing an isolated carbonate platform.....	97
5.3	2D slice image extracted from the micro-CT scan of a selected sample from Tengiz field.....	99
5.4	Demonstration of the segmentation scheme utilized to estimate parameters from CT scans.....	101
5.5	Thin section imaged under optical microscope and SEM.....	104
5.6	Demonstration of the segmentation of SEM image.....	105
5.7	Demonstration of the segmentation of SEM images of micrite aggregates.....	106
5.8	SEM images of some Tengiz samples with varying texture.....	107
5.9	Plot of permeability as function of porosity for the selected Tengiz samples.....	108
5.10	Plot of permeability as function of porosity for the selected Tengiz samples, color coded by micrite content.....	109
5.11	Plot of permeability as function of porosity for the selected Tengiz samples, color coded by micrite content, while the size of data point is proportional to macroporosity.....	110
5.12	Plot of P- and S-wave benchtop velocities as function of porosity; data is color coded by micrite content.....	111
5.13	Plot of P-wave velocity and S-wave velocity, both normalized by velocity at 1 MPa, as a function of confining pressure; data is color coded by micrite content.....	112
5.14	Plot of maximum normalized P-wave velocity (V_p measured at 30 MPa divided by V_p measured at 1 MPa) as function of several properties and microstructural parameters including: micrite content, porosity, permeability, and macroporosity.....	113
5.15	Plot of maximum normalized S-wave velocity (V_s measured at 30 MPa divided by V_s measured at 1 Mpa) as function of several properties and microstructural parameters including: micrite content, porosity, permeability, and macroporosity.....	114
5.16	Normalized percentage change in length as a function of micrite content measured at different pressures.....	115
5.17	Plot of micrite content estimated from SEM versus that obtained from CT scans.....	118
5.18	RMSE as function of micrite content estimated from SEM.....	118
5.19	Plot of the macroporosity estimated from SEM versus that obtained from CT scans.....	119
5.20	RMSE as function of macroporosity estimated from SEM.....	119
5.21	Plot of the microporosity within micrite aggregate estimated directly from SEM, versus the microporosity within micrite estimated indirectly.....	121

5.22	SEM image for Tg5 sample highlighting the presence of micro-cracks.....	123
5.23	Pictures for one-inch core plug samples showing the presence of large vugs.....	123
5.24	Plots of permeability as function of porosity, as function of both micrite content and porosity, and as function of both porosity and macroporosity (3D plots).....	127
5.25	Plot of macroporosity versus micrite content estimated from the selected Tengiz samples.....	128
5.26	SEM images demonstrating: the presence of macropores within the grains due to dissolution in sample Tg5, and the reduction of macroporosity in sample Tg12 due to cementation.....	128
5.27	Plot of logarithm of measured permeability versus the predicted permeability.....	129
5.28	Plots of P-wave velocity as function of porosity, as function of both micrite content and porosity, and as function of both porosity and macroporosity (3D plots)	132
5.29	Plots of S-wave velocity as function of porosity, as function of both micrite content and porosity, and as function of both porosity and macroporosity (3D plots)	133
5.30	SEM images for grain supported samples Tg12 and Tg5 highlighting the presence of crack-like pores between and within the grains.....	134
5.31	Plot of maximum normalized P-wave and S-wave velocity (velocity measured at 30 MPa divided by that measured at 1 MPa) as function of macro-to-microporosity ratio.....	137
6.1	Thin section imaged under the optical microscope showing abundant micritized oolites (spherical particles).....	143
6.2	Schematic showing cubic packing of non-micritized grains (a) and completely micritized grains	144
6.3	SEM images of four different OMV samples characterized by varying content of fractures.....	145
6.4	Permeability as a function of porosity for all Tengiz samples beside OMV samples.....	146
6.5	P- and S-wave velocity as a function of porosity for the four samples characterized by fractures.....	147
D.1	Porosity of binary mixtures of spherical particle and spheres of different diameters, at constant fractional solid volume (data from Yu and Standish, 1993).....	162
D.2	Porosity of binary mixtures of cylinder (length, L= 12 mm, diameter, D=6 mm) and spheres of different diameters, at constant fraction of spheres of 0.5 (data from Yu and Standish, 1993).....	163
E.1	Dependence of d_v/d_p on sphericity ψ ; Figure modified after Zou and Yu, 1996.....	165
K.1	Permeability as function of porosity for all selected Tengiz samples, showing the modeling results using Konzev-Carman relations.....	174
K.2	Percolation porosity and geometric factor as function of micrite content for Tengiz samples.....	174

LIST OF TABLES

3.1	Specific surface area for micrite and skeletal grains	50
5.1	Relations for predicting V_p as function of several microstructural parameters for Tengiz samples.....	132
5.2	Relations for predicting V_s as function of several microstructural parameters for Tengiz samples.....	133
A.1	The volume percentages of the four components in the created analogs including: solid micrite, solid grains, primary porosity (predominantly microporosity) and newly created macropores.....	157
H.1	Summary of transport and elastic properties of set MCR samples	160
H.2	Summary of transport and elastic properties of set MACRO samples.....	168
J.1	Summary of the measured transport and elastic properties of the selected Tengiz samples; as well as the microstructural parameters estimated using both micro-CT scans and SEM images	170
J.2	Acoustic velocities as function of confining pressure for 10 selected samples from Tengiz field.....	171

Chapter 1

INTRODUCTION

1.1 Carbonate Complexity and Motivations

Carbonate rocks play a major role as hydrocarbon and water reservoirs (Chilingar et al., 1967) as well as a primary source for industrial applications of cement making (Grasby and Betcher, 2002; Hawkins et al., 2003). Understanding the properties of carbonates is thus relevant to many different specialized fields, such as geotechnical engineering, hydrology, and characterization of reservoir resources. Despite the widespread role, the characterization of carbonate rocks still presents several challenges and a number of open questions. As with siliciclastics, the energy of the depositional environment plays a large role in determining the grain size distribution, and in turn, controlling the ratio between the fraction of grains and that of the microcrystalline calcite (i.e., micrite) as well as primary porosity. Unlike siliciclastics, however, the multiple diagenetic processes that superimpose

upon each other over time controls the presence of secondary macroporosity. Diagenetic processes provide the rock with a significant variability in rock fabric, pore size, and shape, all of which superimpose on the original microstructure inherited from the depositional environment (Dunham, 1962; Folk, 1962; Lucia, 1999). Such heterogeneity creates significant scatter in fundamental rock physics relationships such as porosity-permeability (e.g., Lucia, 1995, Petty, 1988; Weger et al., 2009; Teh et al., 2011) and the velocity-porosity relationship (e.g., Anselmetti and Eberli, 1993; Assefa et al., 2003; Eberli et al., 2003; Baechle et al., 2005; Weger et al., 2009; Wang et al., 2015).

Thus, the scientific question underlying this thesis is, broadly, how sedimentology-related parameters such as micrite-to-grain ratio and macro-to-microporosity ratio affect the variability of transport (porosity and permeability) and elastic (P- and S-wave velocities) properties. By understanding the interplay between these factors, the final objective of this research is to better inform modeling and, in turn, improve the interpretation of transport and elastic properties of carbonate reservoirs.

A large body of literature examined the factors contributing to the microstructural complexity of carbonates and their control on transport and elastic properties. The main factors considered in literature include rock texture/fabric (i.e., from grainstones to mudstones), and pore structure (i.e., pore type and size). Some studies have reported qualitative trends in the relationships between porosity and permeability on the one hand (e.g., Lucia, 1995, Petty, 1988; Brigaud et al., 2010; Teh et al., 2011), and between porosity and velocity on the other (e.g., Anselmetti and Eberli, 1993; Assefa et al., 2003; Brigaud et al., 2010; Regnet et al., 2015) for different carbonate rock textures which were classified based on petrographic analysis of thin sections. Nevertheless, the analysis of the bulk texture of the rock seems not to be sufficient as a noticeable scatter in the data is still observed for a given rock texture (Lucia, 1995; Assefa et al., 2003; Brigaud et al., 2010, Teh et al., 2011; Regnet et al., 2015). Other studies have investigated the effect of pore structures on the transport (e.g., Weger et al., 2009; Dou et al., 2011; Verwer et al., 2011; Ling et al., 2014) and elastic (Anselmetti and Eberli, 1993; Eberli et al., 2003; Assefa et al., 2003; Weger et al., 2009) properties of carbonates. The general approach was to classify samples based on the dominant pore type, including macromoldic porosity, interparticle porosity, and microporosity, and then to relate the pore type back to the transport and elastic

properties of the samples. The analysis, however, remained mainly qualitative and not conclusive due to the presence of significant variability in the transport and elastic properties of samples characterized by the same dominant pore type (Anselmetti and Eberli, 1993; Eberli et al., 2003; Ling et al., 2014).

The findings from the literature briefly highlighted in this introduction suggest the need for a characterization that could describe both the rock texture and the pore structure by quantifiable parameters. These, in turn, could be used to inform the modeling of the transport and elastic properties in carbonates.

One of the sedimentology-related parameters which relate to the depositional environment determining the carbonate texture is the fractional amount of micrite (Folk, 1962; Tucker and Wright, 1990). This microcrystalline calcite is a product of diagenesis which leads to recrystallization of pre-existing calcite and aragonite mud (Lambert et al., 2006). Aggregates of micrite particles (shown in Figure 1.1) consist of clay-size particles (1- 4 μm) whose proportion in carbonates is the basis of their Dunham classification (Figure 1.2), which places them into categories ranging from grainstone (micrite < 10 %) to mudstone (> 90% micrite) (Dunham, 1962). Micrite forms in low-energy settings, including the basin of the shelf margin and the inner ramp (lagoon setting), as shown in Figure 1.3. A mixture of grains (skeletal and non-skeletal) and micrite can be found in the mid-ramp setting, as well as along the ramp slope (Figure 1.3). Leighton and Pendexter (1962) suggested that the determination of the micrite-to-coarse-grain ratio in carbonates has value for their textural classification. Variations in the micrite-to-coarse-grain ratio also control particle-size distribution and, in turn, pore size distribution (Arya and Paris, 1981; Nimmo et al., 2007). Consequently, micrite content has a major influence on the transport properties of carbonates. The fine micritic particles are largely responsible for the microporosity in carbonates (Cantrell and Hagerty, 1999; Vanorio and Mavko, 2011), which leads to extremely low rock permeabilities upon compaction (Lucia, 1999; Mallon et al., 2005). Despite this documented effect of micrite content on the transport properties of carbonates, a quantitative relationship describing such effect does not exist. With regard to the effect of micrite on elastic properties of carbonate, there is contradiction in the conclusions reached by different researchers. When modeling the acoustic velocities, Fournier et al. (2011) treated the microporous micritized materials in well-cemented

carbonates as the “less stiff component.” Conversely, micrite aggregates were modeled as the “stiffer component” compared to grain aggregates as suggested by Vanorio and Mavko, 2011. The latter study also showed that low micrite content, which may result from natural leaching, increases porosity and reduces rock bulk and shear modulus. In their study, however, the content of the micrite phase was indirectly estimated from the analysis of CT scan images. This approach in quantifying the micrite content has inherent uncertainty introduced by the limited resolution and representation of the CT-scanned rock volumes compared to those of the core plugs used for the measurements. This raises the question of how the error/uncertainty associated with estimating micrite content from CT scans affects the results and conclusions of the study.

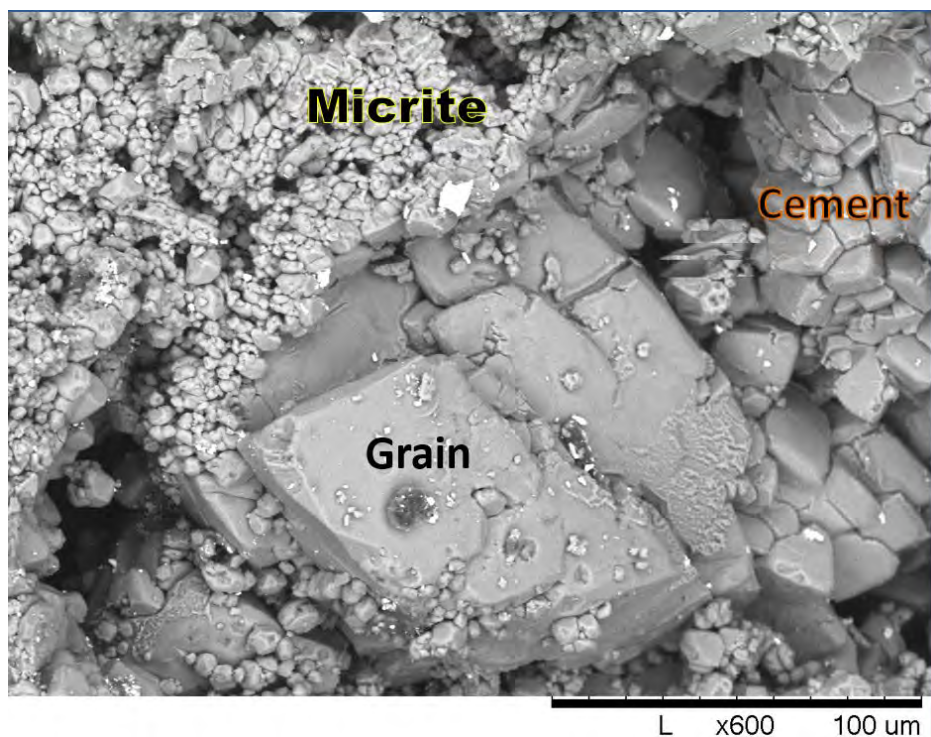


Figure 1.1: Scanning electron microscopy (SEM) image of a carbonate sample (courtesy of Tiziana Vanorio). The image shows three different solid phases in carbonates including: microporous micrite, bulky cement, and grain. The cement phase tends to have relatively coarser particle size and less microporosity compared to micrite.




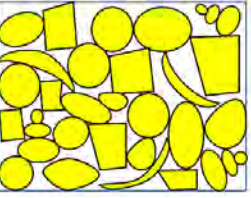
Grains are dispersed in mud		Grains are touching	
Mud-supported		Grain-supported	
>90% mud			<10% mud
Mudstone	Wackstone	Packstone	Grainstone
			

Figure 1.2: Schematic showing the different carbonate textures, simplified after Dunham's (1962) classification.

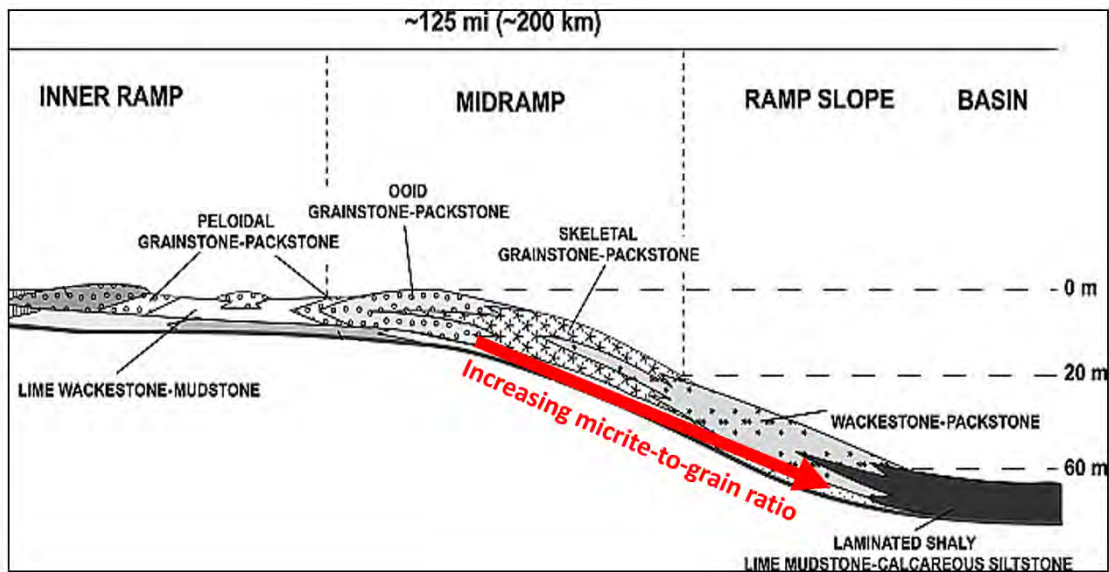


Figure 1.3: Schematic facies profile for the Mississippian carbonates (Figure modified after Wynn and Read, 2006) as an example of the shelf margin environment showing the variations in the textures from the basin up to the inner ramp. The red arrow highlights the increase in micrite content from the mid-ramp to basin.

It is important to mention that micrite can vary in terms of its size and morphology as classified by Deville de Periere et al., 2011 (Figure 1.4). Some studies provided ranges for the transport and elastic properties associated with micrite morphologies and established a link between those morphologies and transport and elastic properties (Deville de Periere et al., 2011; Regnet et al., 2015). Coarser and anhedral compact/fused micrite particles tend to result in lower porosities and higher acoustic velocities in carbonates compared to finer

and more rounded micrite, as suggested by Regnet et al. (2015). However, their results are only applicable for tight microporous and micrite rich carbonates where the microporosity within micrite aggregates predominantly makes up the total rock porosity. That is, the correlations between micrite morphology and rock properties may not be valid for dual porosity carbonates. Moreover, the micrite-to-grain ratio (micrite content) of the microporous samples was not incorporated in the analysis of the rock properties from those studies.




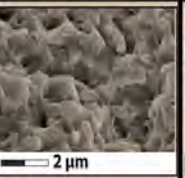
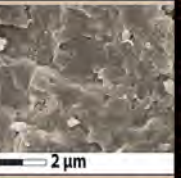
	Micro-rhombic	Rounded	Sub-rounded	Anhedral compact	Fused
SEM images					
Crystal shape	Euhedral/Rhombic	Anhedral/Roundness	Subhedral	Subhedral/Anhedral	Anhedral
Contacts	Punctic/Partially coalescent			Fully coalescent but distinct	Mostly indistinct

Figure 1.4: Classification of micrite microtextures simplified and modified after Deville de Periere et al. 2011. The classification is based mainly on the crystal morphology and type of contact between crystals.

While the micrite-to-grain ratio can be used as a quantifiable parameter to describe rock texture, the macro-to-micro-porosity ratio is a sedimentology-related parameter that can be used to describe the relative pore sizes in the dual-porosity system frequently observed in carbonates. This ratio defines the proportion of porosity that contributes more significantly to the fluid flow in carbonates (Tiab and Donaldson, 1996; Lucia, 1999). The fraction of macroporosity might also be indirectly related to the micrite content since secondary macropores can be formed at the expense of micrite, which is prone to diagenetic processes due to its high surface area (Vanorio and Mavko, 2011). Processes affecting micrite, such as leaching and dissolution, are very common in nature (i.e., metadiagenesis), changing the original pore network (Tucker and Bathurst, 1990; Tucker and Wright, 1990; Vanorio and Mavko, 2011). Ultimately, such processes affect both porosity and permeability. Despite the importance of these processes to rock properties, the interplay among diagenetic processes and transport rock properties is rarely discussed in the context of the rock physics of carbonates. Only recently, the literature has included studies of the microstructural

evolution of pore networks in carbonates and the resultant effect on transport properties (Vanorio et al., 2015). However, a systematic study investigating the evolution of porosity and permeability due to controlled variations in both micrite content and macroporosity has never been carried out in carbonates. Additionally, the effect of the macro-to-microporosity ratio on the elastic properties is not well understood yet. While Eberli et al. (2003) and Weger et al. (2009) suggested that macroporosity makes the rock stiffer by increasing its velocity, Brigaud et al. (2010) reported velocities being higher in microporous mudstones/wackestones with respect to macroporous grainstones characterized by the same porosity. On the other hand, Vanorio and Mavko (2011) pointed out that pore size carries no information whatsoever about pore shape — i.e., microporosity does not necessarily imply elastic compliance or *vice versa*.

1.2 Approach to the Problem

This thesis aims to fill the gaps mentioned above and investigate the role of micrite-to-grain and macro-to-microporosity ratios in controlling the elastic and transport properties of carbonates. Investigations have been done so far on natural carbonate rocks, as such, they contain all the complexity that carbonates may exhibit in terms of pore shape and size, texture, and micrite content. Such complexity contributes to the observed scatter in the transport and elastic properties and it has prevented the development of quantitative relationships. One approach that can be used to address the limitations of the existing work mentioned earlier is to work with experimental analogs defined by controlled parameters whose effect on the transport and elastic properties can be investigated one at a time. Previous studies based on analog samples have shown high potential for addressing some of the basic questions raised for understanding the rock physics of granular media in general (e.g., Winkler, 1983; Berge et al., 1995; Argo IV et al., 2011) and siliciclastic rocks in particular (e.g., Marion et al., 1992; Vanorio et al., 2003). This approach is increasingly necessary for carbonates, where the heterogeneity hinders our understanding of the fundamental relations between elastic and transport properties. The majority of the studies, carried out using carbonate analogs, have focused on processes that affect carbonate sediments such as lithification, pressure solution, and cementation processes (e.g., Badiozamani et al., 1977; Bhattacharyya and Friedman, 1979; Ismail et al., 2002; Zhang

and Spiers, 2005). None of these studies, however, aimed to investigate the role of specific sedimentology-related parameters characterizing the microstructure of carbonates on transport and elastic properties.

In this research study, we followed an approach that is comprehensive of analog and natural-rock samples. The workflow consists of several main tasks. First, we prepared analog samples using natural calcite grains and micrite to control the (1) texture (i.e., micrite-to-grain ratio) and (2) pore size (i.e., macro-to-microporosity ratio). Second, we performed a series of experimental measurements to obtain porosity, permeability, acoustic velocities, and scanning electronic microscopy (SEM) images. We also measured velocity under increasing confining pressure before and after exposing the samples to a reactive fluid. Third, we investigated the correlation between the measured properties and the sedimentology-related parameters, and then attempted to quantitatively model any observed trends. Finally, we extended the investigation to natural carbonate samples in order to analyze the data based on what was learned from the analog samples. The analysis in natural carbonates consists of a combination of (1) multi-scale imaging which includes SEM images and CT scans to estimate sedimentology-related parameters, and (2) experimental measurements of porosity, permeability, and velocities as function of pressure. This comprehensive study, starting with controlled analogs to serve as a baseline for the analysis and then extending the investigation to natural carbonates, is the first of its kind in carbonates.

1.3 Objectives and Research Questions

Throughout this thesis, we attempt to improve the understanding of the effect of micrite content and macroporosity on the transport and elastic properties of carbonates by addressing the following questions:

1. How does micrite content affect the transport properties of carbonate analogs exhibiting variable micrite content in the absence of macroporosity (Chapter 3)?
2. How does the introduction of macropores which replace volumes of micrite aggregates affect the porosity-permeability relationship, and how can the knowledge about micrite-to-grain ratio and macro-to-microporosity ratio inform

the modeling of the porosity-permeability relationship in dual porosity carbonates (Chapter 3)?

3. What is the effect of micrite content and macroporosity on the acoustic velocity, the sensitivity of velocity to pressure, and the changes in velocity resulting from dissolution upon saturation with a reactive fluid (Chapter 4)?
4. What approach can be followed on natural reservoir samples to estimate sedimentology-related parameters including the micrite-to-grain ratio and the macro-to-microporosity ratio, and what tools can be used to quantify the uncertainty associated with the estimations (Chapter 5)?
5. Will the trends observed in the analog samples hold true for natural carbonates, and how can the estimation of the sedimentology-related parameters inform modeling of transport and elastic properties (Chapter 5)?

1.4 Thesis Outline

Chapter 2 describes the approach and materials used to make the analog samples. The general approach in preparing the analogs includes mixing coarse skeletal grains and micrite powder in different proportions. We then use a cold-compression technique to consolidate the mixture under pressure. Two different sets of samples were prepared: (1) samples with varying micrite content (in the absence of introduced macropores), and (2) samples with newly created macropores introduced at the expense of micrite. In this chapter, we also describe the methodologies followed to characterize the samples including: (1) high resolution SEM imaging; (2) bench-top porosity, permeability, and acoustic velocities; (3) acoustic velocities as a function of pressure (dry); and (4) acoustic velocities after the injection of reactive fluid.

Chapter 3 presents the measured transport properties of the created analogs. We particularly discuss in detail two important relationships including the micrite-porosity and porosity-permeability relationships. With regard to the micrite-porosity relationship, it exhibits a characteristic v-shaped trend, which is typical of dual-particle-size mixtures.

This micrite-porosity relationship is modeled utilizing a modified packing model for binary mixtures. We utilize existing equations available in the literature for estimating porosity in binary mixtures of spheres, with equation modifications such that they can be used to estimate porosity in binary mixtures of non-spherical particles. We show that the modified model can be applied successfully to predict the porosities of the analog samples characterized by variable micrite content. With regard to the porosity-permeability relationship, we show that permeability decreases as the micrite content increases at a given porosity. When macropores are introduced at the expense of micrite aggregates, permeability increases exponentially with porosity. The rate of increase in permeability decreases, however, as the micrite content of the original microstructure increases. Finally, we show examples of incorporating the content of micrite and macropores as inputs to inform the modeling of the porosity-permeability relationship using both empirical relations and existing theoretical models. Our analysis in this chapter shows that knowledge of both micrite content and macroporosity is of paramount importance to interpret and model the porosity-permeability relationships in carbonates. This outcome is used in interpreting and modeling the porosity-permeability relations of natural carbonates (Chapter 5).

In Chapter 4, we focus on the effect of micrite content and macroporosity on the elastic properties of the analogs. We start by describing the velocity-porosity relationship which shows that micrite rich samples have higher acoustic velocity despite their higher porosity compared to grain supported samples. Observing that the sensitivity of velocity to pressure decreases as the micrite content increases, we hypothesize a stiffer pore structure in the micrite-richer fabrics. Such hypothesis was supported by observations from SEM images. The outcome of this study shows that microporosity does not necessarily have a softening effect as concluded by other studies. Our results indicate that the elastic properties of the samples are not correlated with the dominant pore size, thus the pore size carries no information about elastic compliance. Moreover, the results from the injection experiment show that the content of micrite seems to affect the change in elastic moduli upon dissolution. Micrite rich samples experience a drop in elastic moduli after fluid injection with respect to the moduli measured under dry conditions. This is interpreted as likely due to dissolution which weakens the rock frame. This effect seems to overcome stiffening that

results from dispersion mechanisms under high-frequency conditions. With regard to the modeling of the elastic properties, we show an approach to model the benchtop micrite-velocity and porosity-velocity relationships using the properties of the end-members alone (pure micrite and pure grain samples). The approach utilizes the equations used in Chapter 3 to model the micrite-porosity relations, along with the differential effective medium (DEM) model, as well as Ruess and Voigt averages.

In Chapter 5, we extended our previous study on carbonate analogs to natural carbonate samples from the Tengiz Field in order to test the hypothesis and methodology developed in the earlier chapters. Specifically, we investigated how sedimentology-related parameters (such as micrite content and macroporosity) can be quantified and then utilized to better interpret and model the rock properties of natural carbonates. We studied 15 samples that have varying texture and pore structure from Tengiz Field, an isolated carbonate platform. Based on the image analysis of SEM images and CT scans, we present an approach to quantify sedimentology-related parameters and the associated uncertainty. The results indicated that similar to the analogs, carbonate reservoir rocks show the same trends regarding the effect of micrite and macroporosity on the porosity-permeability relationship as well as sensitivity of acoustic velocities to pressure. We also show how the estimated parameters can be used to improve the interpretation and inform the modeling of the transport and elastic properties. For example, the coefficient of determination (R^2) between porosity and permeability was found to increase from 0.75 to 0.98 when incorporating the micrite content and macroporosity into the analysis.

Chapter 6 provides a summary of the general conclusions as well as some final remarks on the results of this dissertation, their applicability and limitation, as well as possible future problems and questions concerning the rock physics of carbonates.

Chapter 2

METHODOLOGY AND EXPERIMENTAL PROCEDURES

2.1 Introduction

As identified in the previous chapter, the overall complexity of carbonate microstructures suggests the importance of working with controlled analogs of carbonate. The majority of the studies carried out using carbonate analogs, have focused on processes that affect carbonate sediments such as lithification, pressure solution, and cementation processes (e.g., Badiozamani et al., 1977; Bhattacharyya and Friedman, 1979; Ismail et al., 2002; Zhang and Spiers, 2005). Only a few studies have measured the porosity and permeability of carbonate analogs created by using hot-pressed dry calcite powder (Bernabe et al., 1982; Zhang et al., 1994). None of these studies, however, aimed to investigate the role of specific sedimentology-related parameters characterizing the microstructure of carbonates on transport and elastic properties.

The genetic relationship between depositional processes and rock properties provides a

potentially powerful tool for interpreting the effect of depositional environments on log data. In our study, we thus aim to address how dual particle size (i.e., varying micrite-to-grain ratio) and dual porosity (i.e., varying macro-to-microporosity ratio) affect transport and elastic properties of carbonates. Therefore, we prepared carbonate analogs that have well quantified parameters including samples where micrite-to-grain ratio is the only parameter changing as well as samples with newly created macroporosity introduced at the expense of micrite. We then measured the transport and elastic properties of the samples and investigated the correlation between the measured properties and the sedimentology-related parameters, as will be discussed in Chapters 3 and 4. In this chapter, we describe both the materials and approach used to make the analog samples. We also describe the methodologies followed to examine the microstructure of the samples and measure their transport and elastic properties.

2.2 Materials

The solid constituents of the analog samples consist of natural, coarse, and very fine natural calcite particles. The solid fractions are mixed in different proportions that allow the resultant mixtures to cover a variety of textures ranging from mud-supported to grain-supported (Dunham, 1962). Coarse grains are composed of sand-size carbonate beach sediments (i.e., skeletal grains) as shown in Figure 2.1, which were sieved to obtain grain diameters ranging between 250 and 500 μm . The skeletal grains are skeletal parts of organisms and they form in a relatively high energy environment (Tucker and Wright, 1990). They consist of irregular and complex shaped particles, which are characterized by intraparticle micropores (Figure 2.1). The micrite particles have an average particle diameter of 4 μm and were provided by Huber Engineering Materials. Figure 2.2 shows the microstructure of the micrite aggregate which exhibits subhedral (subrounded) morphology following the classification (Figure 1.4) adopted from Deville de Periere et al. (2011). This subhedral micrite is the most common type of microcrystalline micrite found in carbonates as reported by several studies (Deville de Periere et al. 2011; Volery et al., 2011; Regnet et al., 2015).

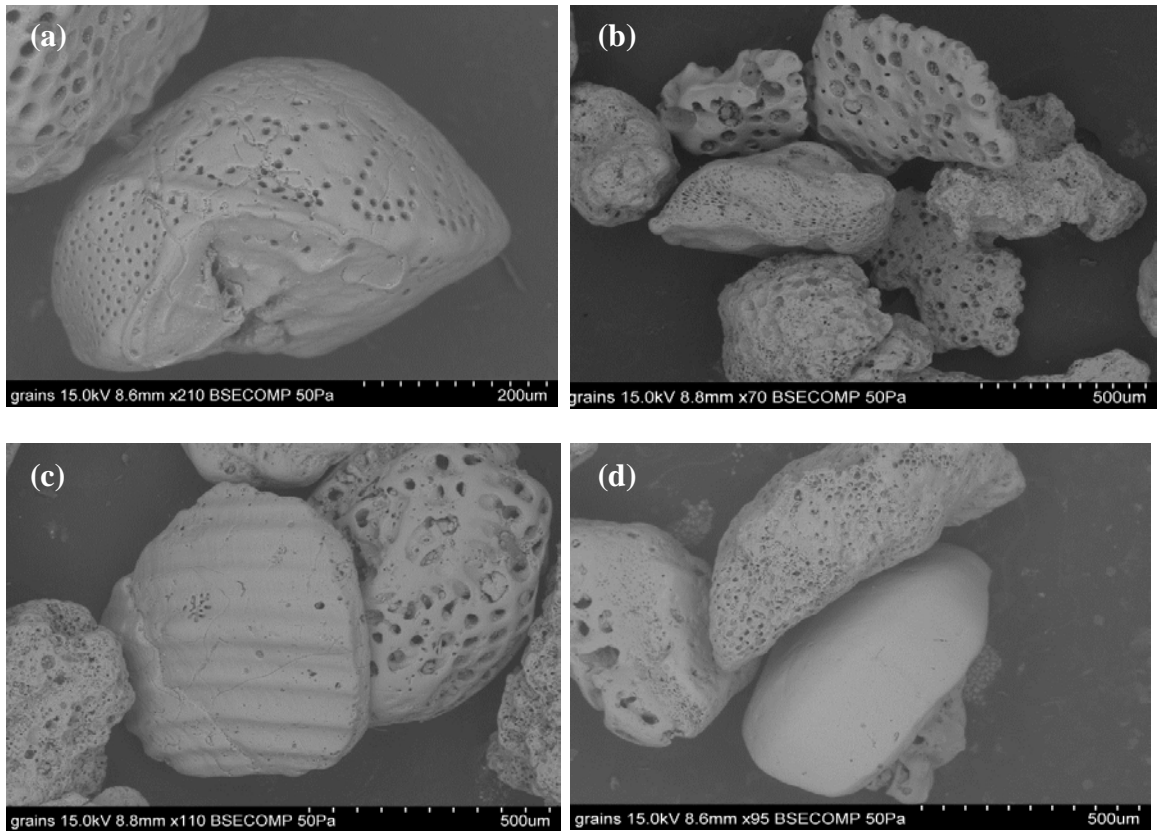


Figure 2.1: Scanning electron microscopy (SEM) images of skeletal grains highlighting their microstructure. Intraparticle pores are mainly spherical and they have different sizes. Particles vary in shape from sub-rounded (a), to irregular and platy (b, c, and d).

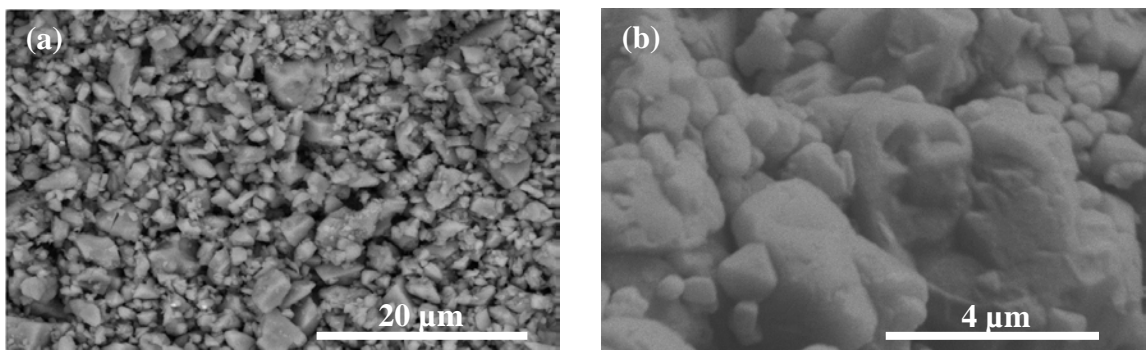


Figure 2.2: SEM image of the microporous micrite aggregate showing the microstructure of micrite aggregates (a). The morphology of this microcrystalline micrite is subrounded/ subhedral (b).

2.3 Sample Preparation

The sediments described above were cold-pressed at room temperature to form a cohesive sample. We used a cold pressing procedure described by Vanorio et al. (2003), consisting of a split steel cube with a cylindrical cavity (Figure 2.3). Pistons on both sides of the cavity were used to apply uniaxial stress on the sediment mixtures placed in the cavity. The split steel cube allows the sample to be recovered easily without stressing it. We prepared two sets of samples: (1) set “MCR” consists of samples with varying micrite content, and (2) set “MACRO” consists of samples with macropores introduced within the sample at the expense of micrite.

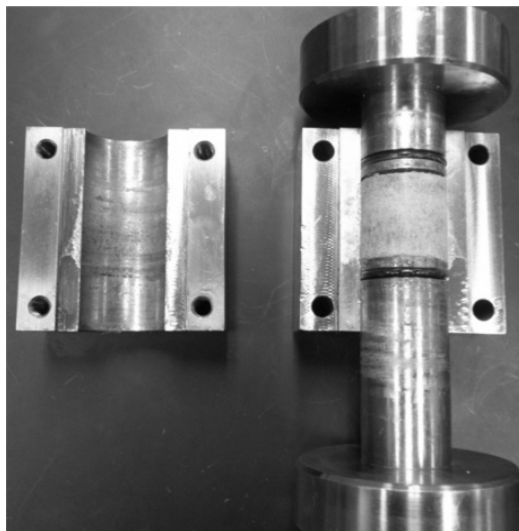


Figure 2.3: Split steel cube with a cylindrical cavity used in cold pressing, after removing one part of the of the split cube to recover the sample. Note the sample formed in between the two pistons (sample is one inch in diameter).

2.3.1 Samples with Varying Micrite-to-Grain Ratio (Set MCR)

For the first set of samples, skeletal grains and micrite were mixed with Portland cement to achieve consolidation without applying very high pressure, in order to avoid drastic reduction in the permeability of samples. Portland cement consists mainly of silicate minerals, where the major components include tricalcium silicate and dicalcium silicate (Boumiz et al., 1997). As water is added, the cement reacts with it and starts to harden. We added water to the cement to obtain a slurry, which we then mixed with the sediments to coat the particles prior to cold pressing them. We tested several parameters, such as cement percentage, water-to-cement ratio, and amount of pressure. In particular, the water-to-

cement ratio is an important parameter when using Portland cement. We tested different water-to-cement ratios looking for a good trade-off between obtaining a slurry characterized by low viscosity, which facilitated mixing, and cement hardening. The optimum ratio that we found was 1.8 by weight, which we used consistently for all samples.

Sediment mixtures were then cold-pressed, at 2 MPa for one day to obtain consolidated samples. Upon recovery, samples were oven-dried before any measurements were taken. We made eight samples by varying micrite content, while maintaining constant the cement percentage at 3% of the solid volume. Though energy considerations of the depositional environment (Folk, 1962) impose a decrease of the cement, which forms preferentially in a high energy environment as micrite increases, we fixed the amount of cement to investigate the effect of the micrite content alone on transport and elastic properties. In addition, we created three more samples with 0%, 30%, and 100% micrite content, following the same approach used for set MCR while exposing the sample to higher pressure of 5 MPa. The rationale behind this choice was to have samples with lower porosity and permeability values, which could extend the trend of the measured porosity-permeability data to lower porosity ranges.

Samples from set MCR, are the main ones used throughout this thesis and are used to investigate the effect of micrite content on the transport (Chapter 3) and elastic (Chapter 4) properties. The experiments/measurements performed on this set of samples include: (1) high resolution SEM imaging; (2) bench-top porosity, permeability, and acoustic velocities; (3) acoustic velocities as function of pressure (dry); and, (4) acoustic velocities after injection of reactive fluid. Details on the approach followed to carry out each experiment are shown in Section 2.4.

2.3.2 Samples with Newly Created Macroporosity (Set MACRO)

Unlike the previous set of samples, which includes analogs with only varying micrite-to-grain ratio, the second set includes an additional component (i.e., macropores) which forms in nature due to post depositional diagenesis. Through this set of samples, we aim to investigate the effect of macropores, as induced by micrite leaching and dissolution, on the transport and elastic properties. Therefore, samples were prepared by replacing controlled amounts of the micrite fraction with sub-rounded camphor particles (0.25 to 0.5 mm in

diameter) and including them with the sediments prior to cold pressing the mixture. Macropores were introduced in both the micrite-supported and grain-supported samples. Once the sample consolidated, we placed it in acetone, which allowed us to easily dissolve the camphor component while leaving the calcite component unaffected (Pingitore et al., 1993) thus populating the final sample structure with macropores. Figure 2.4 shows SEM images for a sample before and after removing the camphor particles. Camphor particles were added in increments of 5% of the solid volume while the micrite solid volume was reduced by the same percentage. We measured the porosity and grain density of the sample after dissolving the camphor to ensure it dissolved completely.

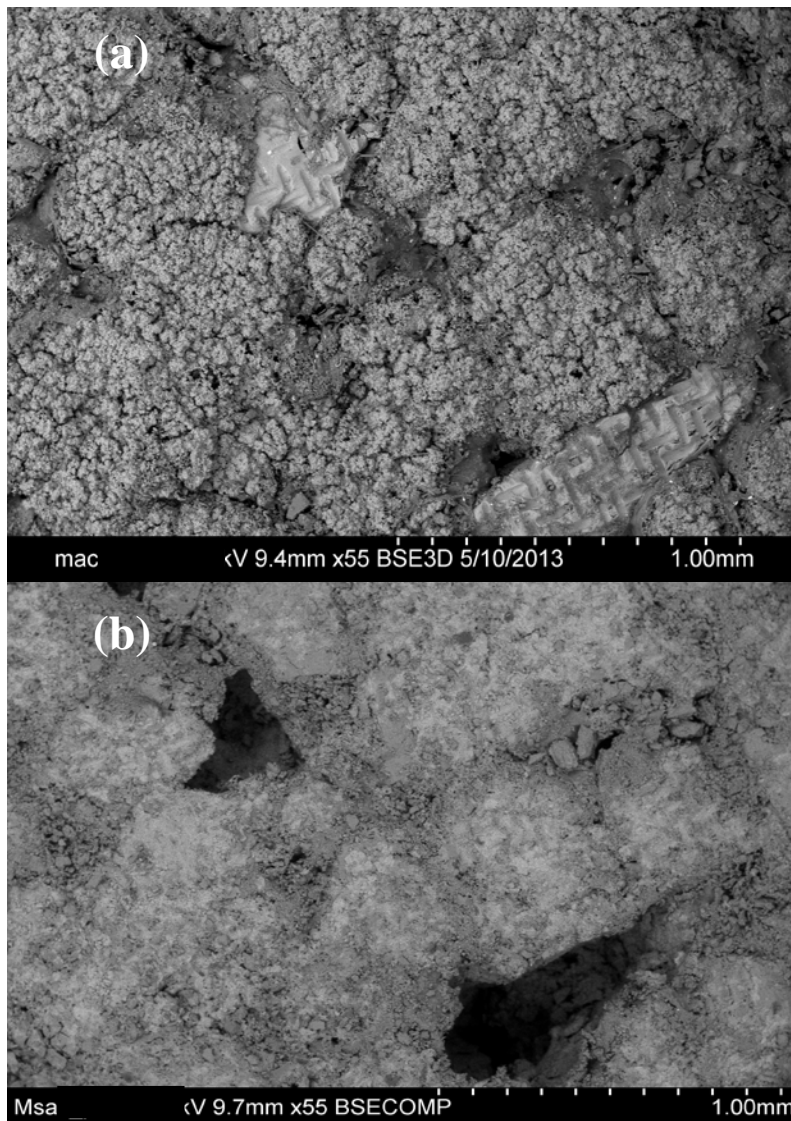


Figure 2.4: SEM images for a grain supported sample before (a) and after (b) removing camphor to form macropores.

2.4 Rock Physics Experiments and Measurements

2.4.1 High Resolution Imaging Using Scanning Electron Microscopy (SEM)

SEM was used to obtain high-resolution images for the microstructure of the samples. SEM can provide information about the topology and composition of a surface (Egerton, 2005). This imaging technique uses a beam of electrons generated by heating a metallic filament, which is commonly made of Tungsten. The beam is directed toward the sample by an anode, and then is focused by a magnetic lens as shown in the schematic in Figure 2.5. The focused beam is then mapped over the field of view by scanning coils before the electrons interact with sample. Two detectors will then record electrons that are elastically backscattered from the sample surface or those ejected from atomic orbits (i.e, secondary electrons) as demonstrated in Figure 2.5. The SEM images in this thesis were all collected at the Cell Science Imaging Facility (CSIF) in the Stanford Medical School. Images were acquired using the Hitachi S-3400N variable pressure (VP-SEM) system under the backscattered electron mode and a 50 Pa vacuum. A beam voltage of 15 kV was used when acquiring SEM images for all samples.

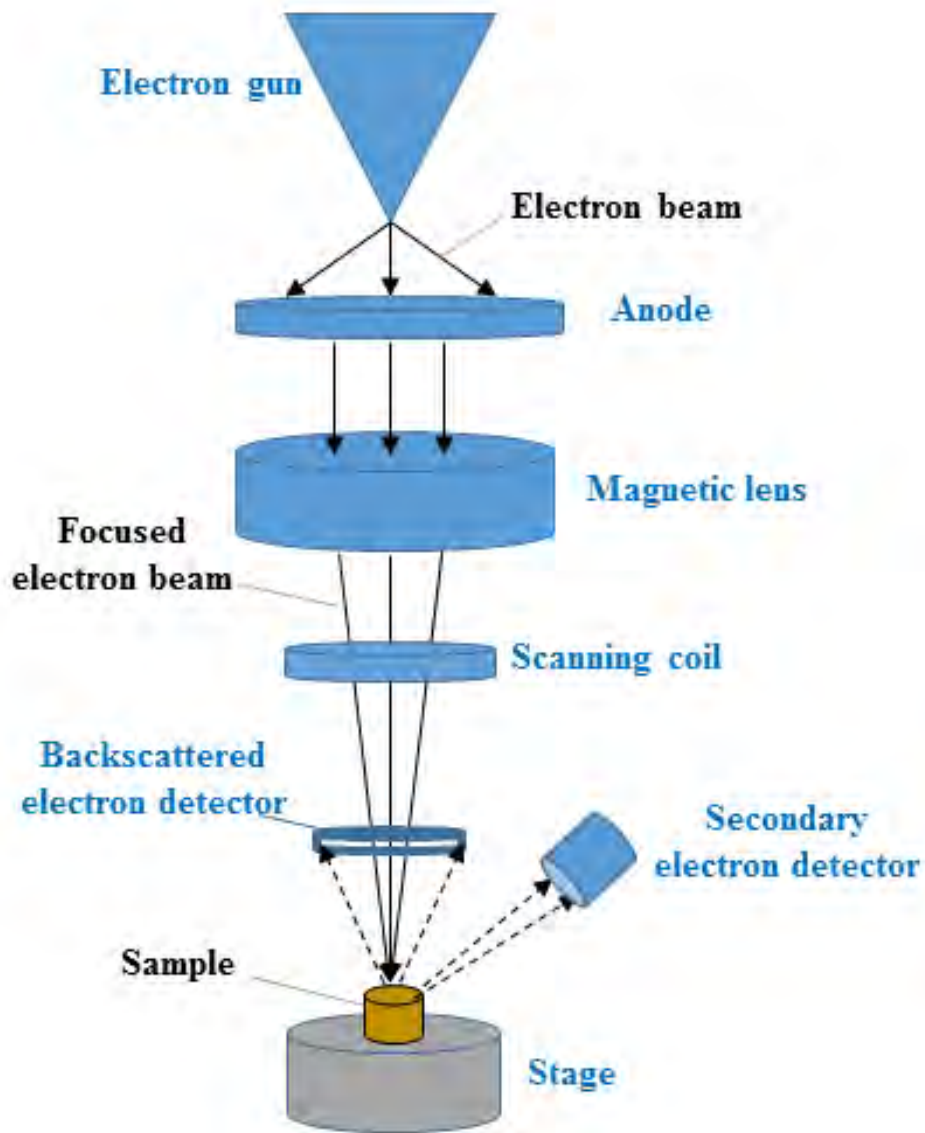


Figure 2.5: A schematic of the SEM set up; figure modified after Allan (2015).

2.4.2 Helium Porosimetry

The effective porosity and grain density were measured using a helium porosimeter which uses the principles of gas expansion as described by Boyle's law (equation 2.1):

$$P_1 V_1 = P_2 V_2 \quad (2.1)$$

Boyle's law relates the initial pressure (P_1) and volume (V_1) of the gas to the expanded pressure and volume (P_2 and V_2 , respectively). Assuming an ideal gas, the product of pressure and volume is constant for a gaseous system at a given temperature. The idea

behind using Boyle's law to determine porosity is that changes in pressure can be used to obtain changes in volume of the expanded gas within a certain space before and after placing the sample. The pressure drop upon expansion can be related to the solid volume of the sample. The porosity and grain density of the sample were then calculated from the solid volume given the mass and bulk volume of the sample. The mass of the samples was measured after the samples were oven-dried prior to the helium porosimetry experiment. The length and diameter of the samples were measured 10 times using a caliper, and the average values were then used to calculate the average bulk volume of the samples assuming a right cylindrical shape. Errors associated with non-flat surface or chipped samples were quantified using the standard deviation, and they were then propagated throughout the calculation of porosity. In this thesis, the overall uncertainty associated with the reported porosity was found to be 1% on average.

It is worth mentioning that helium gas is used in this method since it has very small molecules that can enter very tiny pores. Moreover, helium is a noble gas that will not react with the rock frame ensuring no chemical alteration of the rock samples.

2.4.3 Klinkenberg-Corrected Permeability

In order to measure the permeability of the samples, we used a Nitrogen permeameter which utilizes a constant head method (i.e., steady-state method). A constant head drop (i.e., pressure gradient) is applied across the sample while measuring the volumetric flow rate. Permeability (k) is then calculated using Darcy's relation:

$$k = \frac{q \mu L}{A (P_1 - P_2)} \quad (2.2)$$

where q is volumetric flow rate, A is cross sectional area of the sample, L is sample length, μ is Nitrogen viscosity, and $P_1 - P_2$ is pressure drop between the inlet and outlet across the sample. This relation assumes laminar flow and hence, permeability is determined from the slope of the relation between q/A and $(P_1 - P_2)/L$ when it is linear. All measurements were done under room temperature, and the experimental error was 2%.

The measured permeability to gas is however relatively larger than the permeability to liquids due to the slippage effect where gases exhibit some finite velocity at the solid-gas interface. This phenomenon is known as the Klinkenberg effect, and it can be corrected for

using Klinkenberg's factor, c , a constant for a particular gas in a particular porous medium (Klinkenberg, 1941). Given gas permeability, k_g , measured using a mean pressure, P_m , where $P_m = (P_1 + P_2)/2$, the equivalent liquid permeability (i.e., absolute permeability), k_L , can be obtained using the relation:

$$k_g = k_L + c \left(\frac{1}{P_m} \right) \quad (2.3)$$

In practice, we simply measure the gas permeability for several mean pressure values and fit the data of k_g versus $(1/P_m)$ with a straight line. The absolute permeability, k_L , is then equal to the y-intercept of this line.

2.4.4 Acoustic Velocities

P- and S-wave velocities were measured under both benchtop (room temperature and pressure) conditions, and as function of increasing confining pressure. The benchtop acoustic setup consisted of a digital oscilloscope (Tektronix TDS 1012B), a pulse generator (Panametrics 5052 PR), and two pairs of transducers (Panametrics V103 for 1 MHz P-waves and V154 for 0.7 MHz S-waves). The arrival times and sample lengths were used to obtain the P- and S-wave velocities with associated errors of 1% and 2%, respectively. Regarding the measurements of acoustic velocities as a function of pressure, the experimental setup consists of a digital oscilloscope (Tektronix TDS 340A) and a pulse generator (AVTECH AVR-7B-B). The samples were jacketed with a Tygon tubing to isolate them from the confining pressure medium, which was hydraulic oil. P- and S-wave velocities were measured using a pulse transmission technique as the confining pressure was increased. Samples were lodged between two steel endplates mounting a stack of two piezoelectric-crystals that generated P- and S-waves. A high viscosity-bonding medium (molasses) was used to bond the endplates to the sample. We used three potentiometers to measure changes in length (i.e., strain) of the samples as a function of pressure. All strain is assumed to arise from pore compactions while the mineral frame is assumed incompressible.

2.4.5 Injection of CO₂-rich Water

In order to investigate the effect of fluid-frame interaction on acoustic properties of the samples with varying micrite content, P-wave and S-wave velocities were measured as a function of confining pressure after injecting CO₂-rich water and then drying the samples. The injection experiment was carried out on samples from set MCR only. We injected carbonated water (pH ~2.8) into the samples under a confining pressure of 10 MPa and at room temperature, while the pore pressure was kept at approximately 5 MPa. The total volume injected in each sample was equivalent to 13 times the sample pore volume. The samples were then dried in place by injecting helium gas at 8 MPa using a gas booster until no more fluids could be collected from the output and then by flowing the gas at 0.5 MPa for three hours. After drying, we re-measured P-wave and S-wave velocities as a function of confining pressure. Porosity enhancement due to dissolution was estimated using the method described in Vanorio et al. (2011) by monitoring the Ca²⁺ concentration of the output fluid using titration:

$$\Delta\phi_c(t_i) = \frac{\sum_1^n \Delta m_n}{V_{bulk} \rho_g} = \frac{V_{inj}(t_i) \sum_1^n C_n M_{min}}{V_{bulk} \rho_g} \quad (2.4)$$

In this equation, $\Delta\phi_c(t_i)$ represents the change in porosity calculated from the measured concentration of the dissolved cations over the period $[t_{i-1}, t_i]$. V_{bulk} is the bulk volume of the sample, $V_{inj}(t_i)$ is the volume of the injected fluid over that period, and ρ_g is particle density. Δm_n is the change in mass due to the n th dissolved mineral over the same period, and it is calculated by knowing the mean concentration of the dissolved cations C_n , the molecular weight of the dissolved mineral M_{min} , and the volume of injected fluid $V_{inj}(t_i)$.

On the other hand, length changes were used to compute the loss in porosity by compaction assuming that the pore contraction was the sole source of strain. The loss in porosity due to only mechanical compaction under pressure at time t_i is given by:

$$\Delta\phi_{pi} = \frac{(V_{bulk} - \Delta V_{pi}) - V_{solid}}{(V_{bulk} - \Delta V_{pi})} \quad (2.5)$$

where V_{solid} is the volume of the solid particles, and ΔV_{pi} is the change in sample bulk volume measured during the experiment.

Chapter 3

THE EFFECT OF MICRITE CONTENT AND MACROPOROSITY ON THE TRANSPORT PROPERTIES OF CARBONATE ANALOGS

Abstract

In this chapter, we investigate the effect of micrite content and macroporosity on the transport properties of dual-particle-size and dual-porosity carbonates using analog samples created in the laboratory, as described in Chapter 2. Specifically, we use analog samples where the micrite-to-grain ratio is the only parameter changing (set MCR) as well as the samples characterized by the presence of macropores introduced into the analog structures at the expense of the micrite aggregates (set MACRO). The focus here is on two main functional relationships: the micrite-porosity and the porosity-permeability relationships. With regard to the micrite-porosity relationship, it exhibits a characteristic v-shaped trend, which is typical of dual-particle-size mixtures. Adding micrite to analog samples exhibiting grain-supported microstructure reduces the porosity. By increasing the

content of micrite up to 20-30%, the sample becomes micrite-supported, at which point adding more micrite increases the porosity. This micrite-porosity relationship is modeled using a modified packing model for binary mixtures. We used existing equations available in the literature for estimating porosity in binary mixtures of spheres, and modified the equations so that they can be used to estimate porosity in binary mixtures of non-spherical particles. We show that the modified model can be applied successfully to predict the porosities of the analog samples characterized by variable micrite content. Using published data for the porosity of binary mixtures of non-spherical particles, we also validate the modified model whose predictions show good agreement with the measured porosity.

With regard to the porosity-permeability relationship, samples with high micrite content were found to have lower permeability at any given porosity. When macropores are introduced at the expense of micrite aggregates, permeability increases exponentially with porosity. The rate of increase in permeability decreases, however, as the micrite content of the original rock frame increases. Additionally, at any given micrite content, the permeability increases as the percentage of macropores increases since such pores do contribute more significantly to fluid flow as compared to micropores. We then used the varying micrite-to-coarse-grains ratio and its effect on the porosity-permeability relationship obtained experimentally to inform the Kozeny-Carman relation for a pack of spheres. Our analysis showed that micrite affects the porosity-permeability relationship of carbonates by reducing the effective particle size and increasing the percolation porosity. Moreover, incorporating the content of micrite and macropores into the analysis of the porosity-permeability relationship increased the coefficient of determination (R^2) from 0.24 to 0.78. This study shows that knowledge of both micrite content and macroporosity is of paramount importance to interpret and model porosity-permeability relationships in carbonates.

3.1 Introduction

Carbonates are frequently known for having a complex dual-particle size and dual-porosity microstructure (Tiab and Donaldson, 1996; Lucia, 1999), which creates a significant scatter in fundamental rock physic relationships such as the porosity-permeability relationship (Lucia, 1995; 1999; Ehrenberg et al., 2006). As pointed out in

the first chapter, the micrite-to-grain ratio and the macro-to-microporosity ratio are two important sedimentology-related parameters whose quantification can be of significant importance for characterizing rock texture and pore structure as well as for informing modeling of transport properties. Leighton and Pendexter (1962) suggested that the determination of the micrite-to-grain ratio in carbonates has value for their textural classification. Variations in the micrite-to-coarse grain ratio also control particle-size distribution which in turn affect pore size distribution (Arya and Paris, 1981; Nimmo et al., 2007). Micrite content thus has a major influence on the transport properties of carbonates. The fine micrite particles are largely responsible for the microporosity in carbonates (Cantrell and Hagerty, 1999; Vanorio and Mavko, 2011), which leads to extremely low rock permeabilities upon compaction (Lucia, 1999; Mallon et al., 2005). Despite this documented effect of micrite content on the transport properties of carbonates, a quantitative relationship describing such effect does not exist. Due to the similarity between micrite and clay in terms of their particle size, the effect of micrite on transport properties of carbonates can be seen as an analog of the clay effect in siliciclastics. The effect of clay content on the transport properties of siliciclastics has been investigated and quantified using controlled sand-clay mixtures (Marion 1990; Yin 1992). The authors reported a relationship between clay content and porosity that followed a v-shaped trend, which was modeled by Marion et al. (1992), using a packing model for binary mixtures of spheres. Despite the potential of using controlled mixtures to establish quantitative relationships between micrite content and transport properties, the use of such approach has never been carried out.

In addition to the content of micrite, macropores commonly formed during post-depositional diagenesis, also known as secondary porosity (Tucker and Bathurst, 1990), represent a major contributor to the porosity and permeability of carbonates (Lucia, 1995; Tiab and Donaldson, 1996).). Ling et al. (2014) qualitatively classified the porosity-permeability data based on the dominant pore type and concluded that macro interparticle pores are the most important contributor to flow (in the absence of fractures), which also agrees with the results reported by Lucia (1999). Following a more quantitative approach, Weger et al. (2009) used parameters derived from thin sections including the perimeter over area (PoA) and dominant pore size to describe the pore network complexity and pore

size, respectively. The authors investigated the effects of those parameters on the porosity-permeability relationship of carbonates. They observed that for a given porosity, high permeability samples tend to have large (i.e., macro) and simple (i.e., lower PoA) pores. Incorporating the derived parameters into Kozeny's (1927) equation to estimate permeability resulted in a coefficient of determination (R^2) of 0.415 (Weger et al., 2009). One limitation reported by the authors is that the pore structure analysis based on thin sections does not capture pore geometries below 30 μm and thus, parameters characterizing such geometries could not be obtained. Additionally, this approach in quantifying the pore structure parameters has inherent uncertainty due to heterogeneity, which is introduced by the limited representation of thin sections compared to the core plugs used for the porosity and permeability measurements.

The macroporosity might also be indirectly related to the micrite content since secondary macropores can be formed at the expense of micrite, which is prone to diagenetic processes due to its high surface area (Vanorio and Mavko, 2011). Processes affecting micrite, such as leaching and dissolution, are very common in nature (i.e., metadiagenesis), changing the original pore network (Tucker and Bathurst, 1990; Tucker and Wright, 1990; Vanorio and Mavko, 2011). Ultimately, such processes affect both porosity and permeability. Despite the importance of these processes to rock properties, the interplay among diagenetic processes and transport rock properties is rarely discussed in the context of the rock physics of carbonates. The literature has only recently included studies of the microstructural evolution of pore networks in carbonates and the resultant effect on transport properties (Vanorio et al., 2015). However, a systematic study investigating the evolution of porosity and permeability due to controlled variations in both micrite content and macroporosity has never been carried out in carbonates.

The literature presented here suggests the need for a methodological approach, which could quantify sedimentology-related parameters including micrite content and macroporosity. Thus, to overcome the limitations mentioned above, we used analog samples characterized by well-quantified dual-particle size and dual-porosity systems (as shown previously in Chapter 2) and investigated the effect of micrite content and macroporosity on transport properties. In this chapter, we first examine the microstructure of the analog samples from set MCR and set MACRO. We then report the transport

properties of the samples addressing two major relationships including: micrite-porosity and porosity-permeability relationships. Specifically, the main objectives of this chapter are to investigate: (1) how micrite content affects the porosity and permeability of carbonates exhibiting variable micrite-to-grain ratios in the absence of introduced macroporosity, (2) how the introduction of macropores which replace volumes of micrite aggregates affects the porosity-permeability relationship, and (3) how the knowledge about the content of micrite and macropores can inform the modeling of the porosity-permeability relationship.

3.2 Methodology

In order to characterize the properties of the samples, Klinkenberg-corrected nitrogen permeability, Helium porosity, and SEM images were obtained as explained in Chapter 2. We then analyzed the porosity and permeability data obtained from set MCR and set MACRO samples, investigating the correlation between sedimentology-related parameters, including micrite content and macroporosity, and the measured transport properties.

3.3 Experimental Results

3.3.1 Sample Characterization and Microstructure

Table A.1 (Appendix A) reports the main composition and transport properties of the created analogs in this study. The analogs are composed of four main components (all reported as bulk volume percentage ignoring the cement percentage) including: solid micrite, solid grains, primary interparticle porosity, and newly created macroporosity. The newly created macropores volume fraction is obtained by dividing the volume of camphor added by the total pore volume obtained from the porosimeter. The rest of the measured porosity is then considered to be primary porosity (predominantly microporosity). The last column in Table A.1 corresponds to the parameter “micrite-to-grain indicator” which refers to the percentage of micrite solid volume out of the total solid (micrite+grains) volume. Figure 3.1 shows the SEM images of several samples from set MCR. The samples span a wide range of texture and microstructure, from grain-supported (Figures 3.1a and 3.1b) to

micrite-supported (Figures 3.1c, 3.1d, and 3.1e), ending with a pure mud texture (i.e., 100% micrite) as shown in Figure 3.1f. Figure 3.2 highlights some pore-scale features, including the cement between grains (Figure 3.2a), and micrite partially filling pores (Figure 3.2b). Figure 3.3 shows the SEM images for some samples from set MACRO highlighting the presence of the newly created macroporosity.

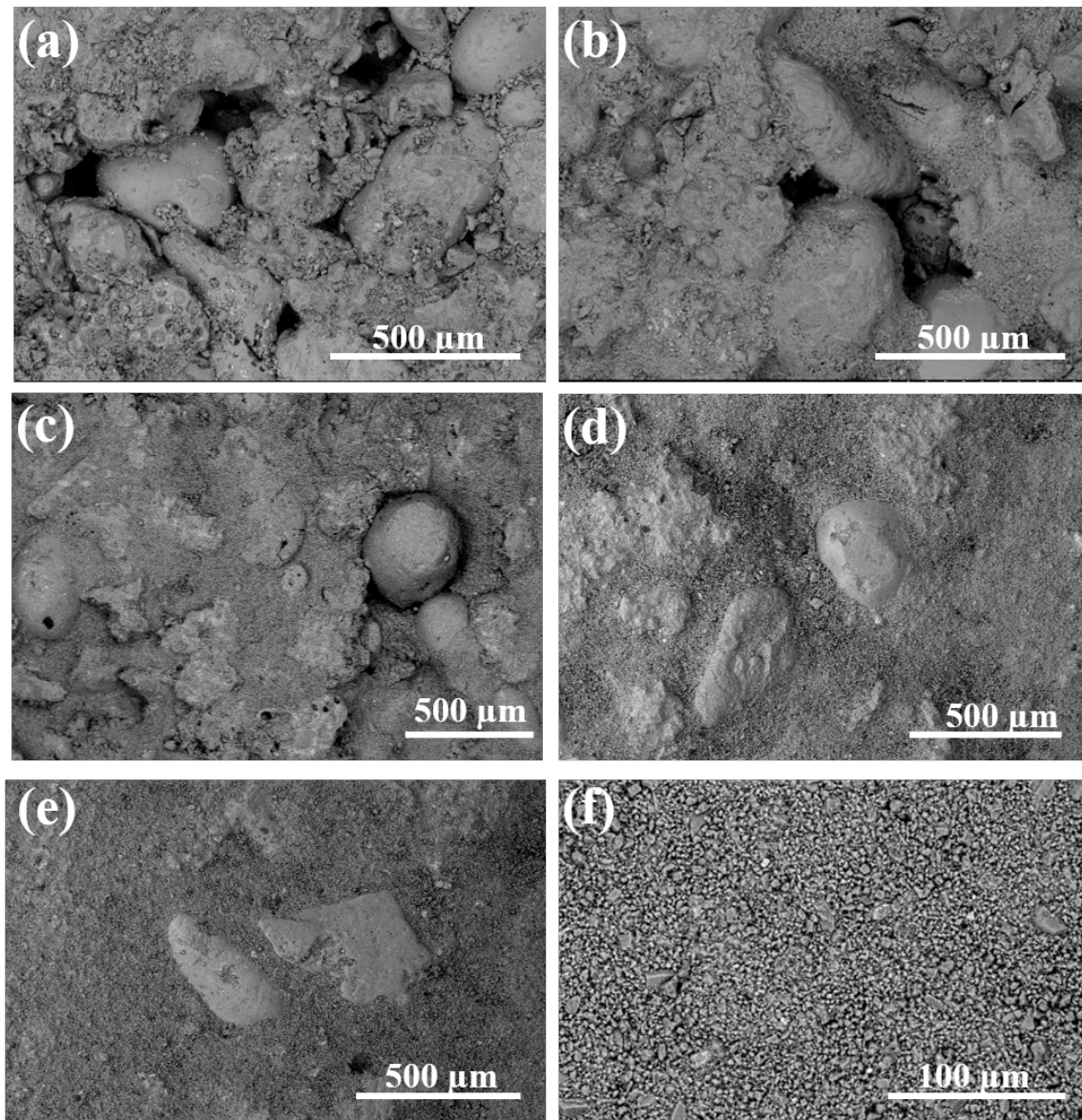


Figure 3.1: SEM images of several samples from set MCR, where the micrite-to-grain indicators are: (a) 0% , (b) 20%, (c) 40%, (d) 60%, (e) 80%, and (f) 100%.

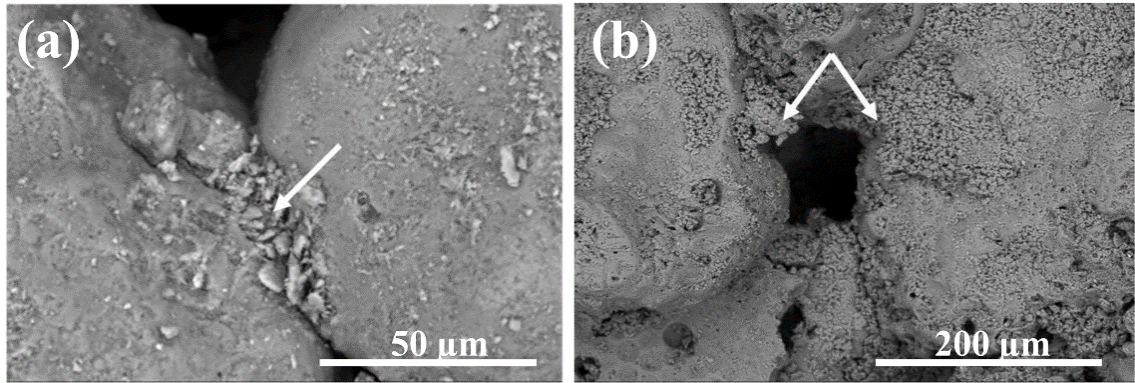


Figure 3.2: Some microfeatures in the created analogs: (a) SEM of 100% grain sample showing the cement (highlighted by a white arrow) between grains, (b) 20% micrite sample showing micrite partially filling pores between grains.

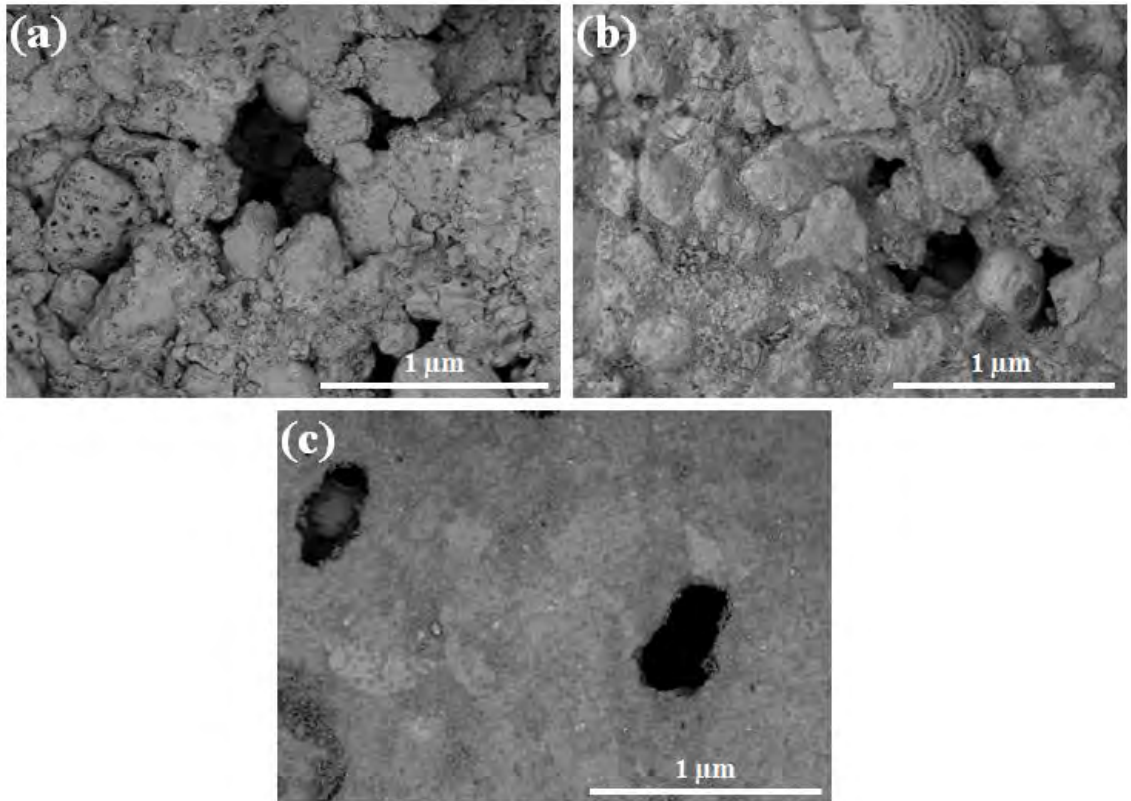


Figure 3.3: SEM images of macropores created in grain-supported samples (a and b) as well as in a micrite-rich sample (c) from set MACRO. The micrite-to-grain indicators for the three samples are 0%, 11%, and 78%, respectively.

3.3.2 Micrite-Porosity Relationship in Set MCR Samples

Figure 3.4 shows how porosity varies with increasing micrite content for set MCR samples, highlighting a v-shaped trend. Adding up to 20-30% micrite to the mixture at first reduces the porosity which then starts to increase as more micrite is added.

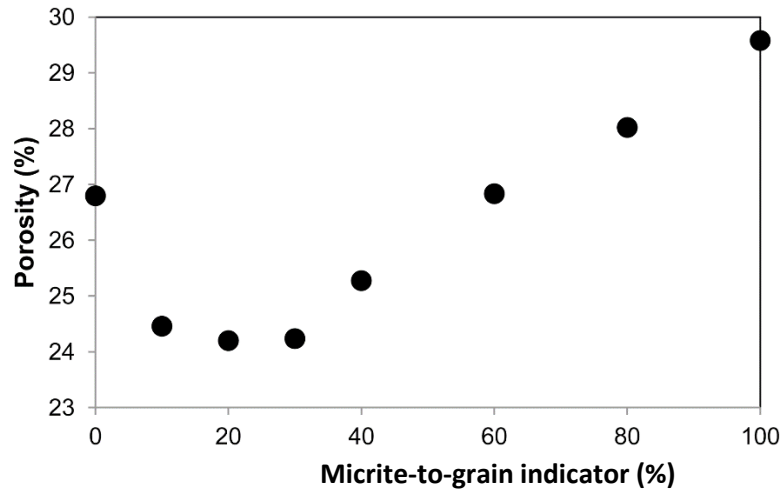


Figure 3.4: Plot of porosity as function of micrite content (micrite-to-grain indicator) for set MCR samples, created using a pressure of 2 MPa.

3.3.3 The Porosity-Permeability Relationship

Figure 3.5 shows a porosity-permeability cross plot for the analog samples from set MCR and MACRO along with a dataset referring to natural carbonate samples (Scotellaro et al., 2008; Vanorio et al., 2008). As with natural carbonates, the relationship exhibits a noticeable scatter (Figure 3.5) with no prominent trend across the data. This observation suggests two interesting points: 1) porosity alone does not fully control permeability in the samples, and 2) additional sedimentology-related parameters need to be extracted to explore relevant trends. Figure 3.6 shows the same porosity-permeability cross plot as in Figure 3.5, except that data points are now color coded by micrite content. The yellow-to-brown circles refer to the analog samples of set MCR, showing permeability to drastically decrease (although porosity does not decrease significantly) as micrite content increases by up to 30%. The addition of micrite beyond this value did not significantly affect permeability, which thus leveled out while porosity increased (Figure 3.6). The yellow-to-

brown squares in Figure 3.6 show the porosity and permeability data of the samples from set MACRO; where the size of the squares indicates increasing amounts of macroporosity. The dashed curves in Figure 3.6 connect the porosity-permeability data points for samples with similar micrite content (i.e., less than 5% variations in micrite content for samples connected by the same curve). The results in Figure 3.6 show that for any given porosity, samples with higher micrite content have lower permeability. Figure 3.7 highlights the change in permeability with porosity as macropores populate the sample structure, at the expense of micrite. The tail of the arrows refers to samples from set MCR (i.e., original microstructure in the absence of introduced macropores). The rest of the samples along each arrow are characterized by an increasing amount of macropores and decreasing amount of micrite, compared to the original microstructure. It can be noted that the rate of increase in permeability decreases as the micrite content of the original microstructure increases.

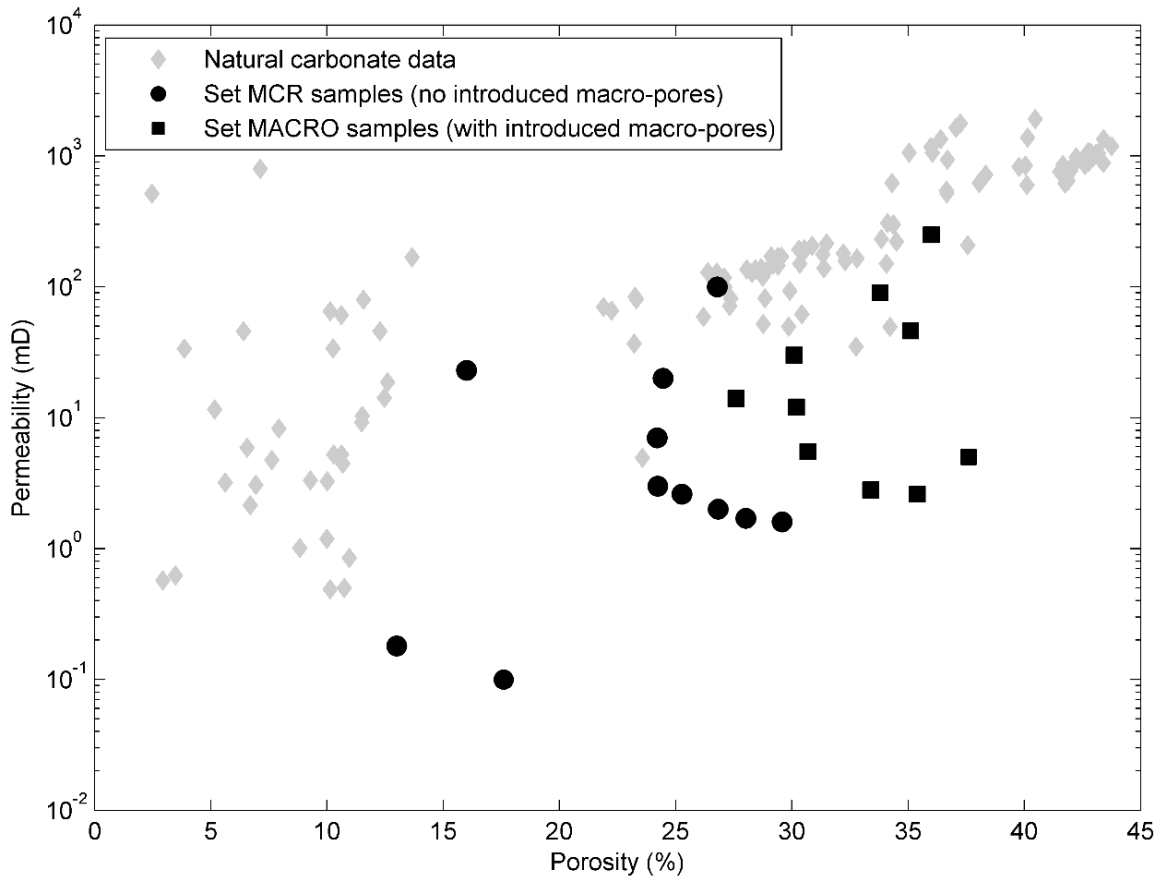


Figure 3.5: Plot of permeability as function of porosity for set MCR (circles) and MACRO (squares) samples.

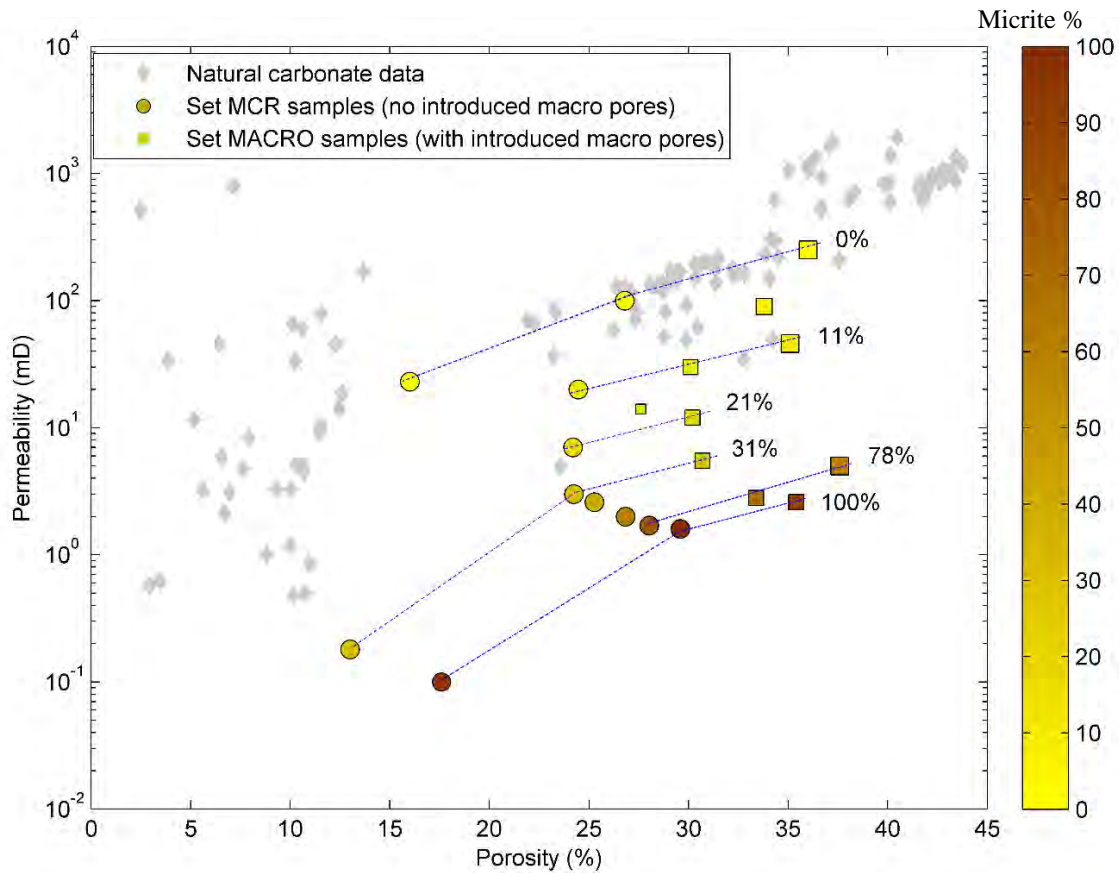


Figure 3.6: Plot of permeability as a function of porosity for analog samples from set MCR (circles) and set MACRO samples (squares). The plot has the same data as in Figure 3.5 but is color-coded by micrite content (micrite-to-grain indicator) while the size of the squares is proportional to the percentage of the macroporosity in set MACRO samples. The solid dashed lines highlight the porosity-permeability relationships for samples with similar average micrite content (shown by the percentage beside each curve). The three circles with 13-18% porosity (leftmost circles) refer to the three additional samples from set MCR made using the higher pressure of 5 MPa (compared with 2 MPa pressure for the rest of the MCR samples).

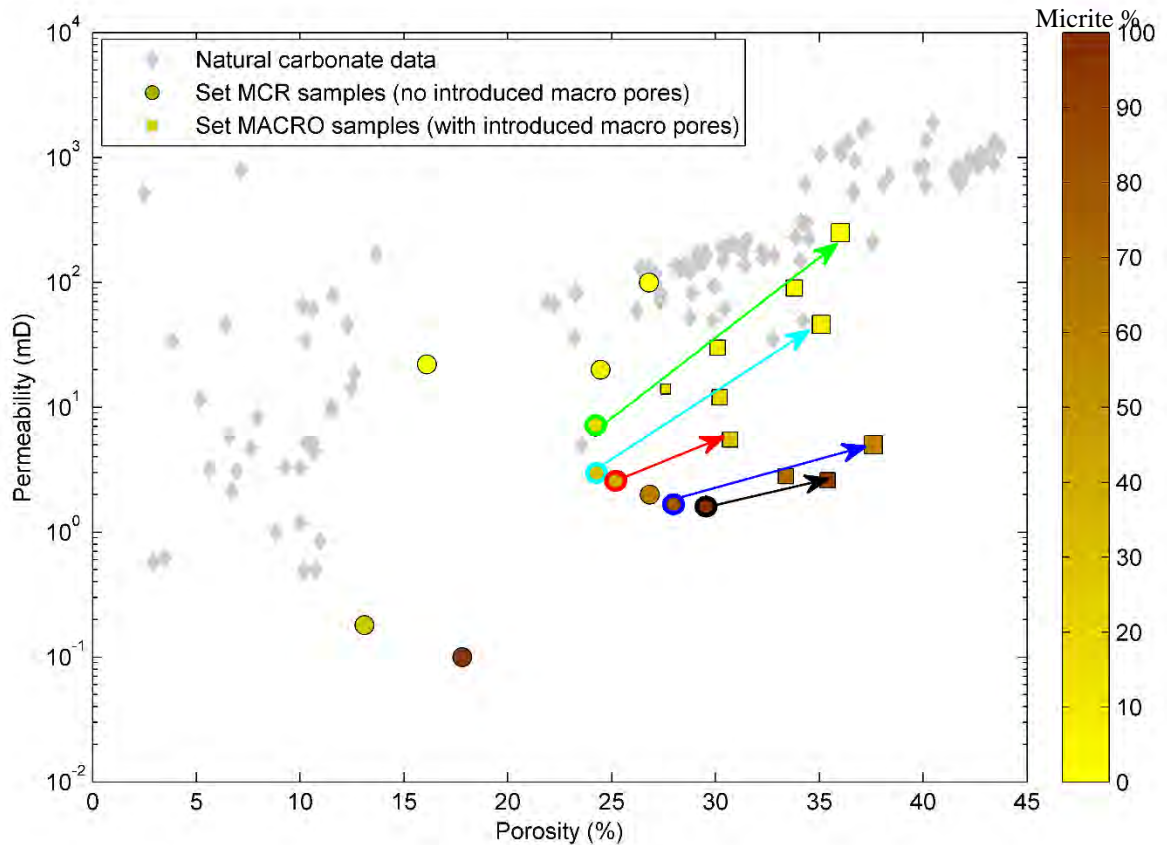


Figure 3.7: Permeability as a function of porosity (same data as in Figure 3.6). The green, cyan, red, blue, and black arrows refer to changes in permeability with porosity as macropores are introduced at the expense of micrite, to the 20%, 30%, 40%, 80%, and 100% micrite content samples, respectively. The green, cyan, red, blue, and black circles (at the tail of the arrows) refer to original microstructures characterized by no induced macro-pores (samples from set MCR). Each sample along the arrow is characterized by lower micrite content but higher macroporosity compared to the preceding sample.

3.4 Discussion

3.4.1 Microstructure of the analogs

The comparison between the SEM images of the natural and laboratory-created carbonate microstructures (Figure 3.8), characterized by similar micrite content, shows that the resemblance is fairly good, mimicking fairly well the variability of natural carbonates. We are not claiming here that our analogs are identical to natural carbonates in all aspects

but we show the comparison to demonstrate that our approach in reproducing carbonate microstructures was quite successful, lending confidence to the validity of the results.

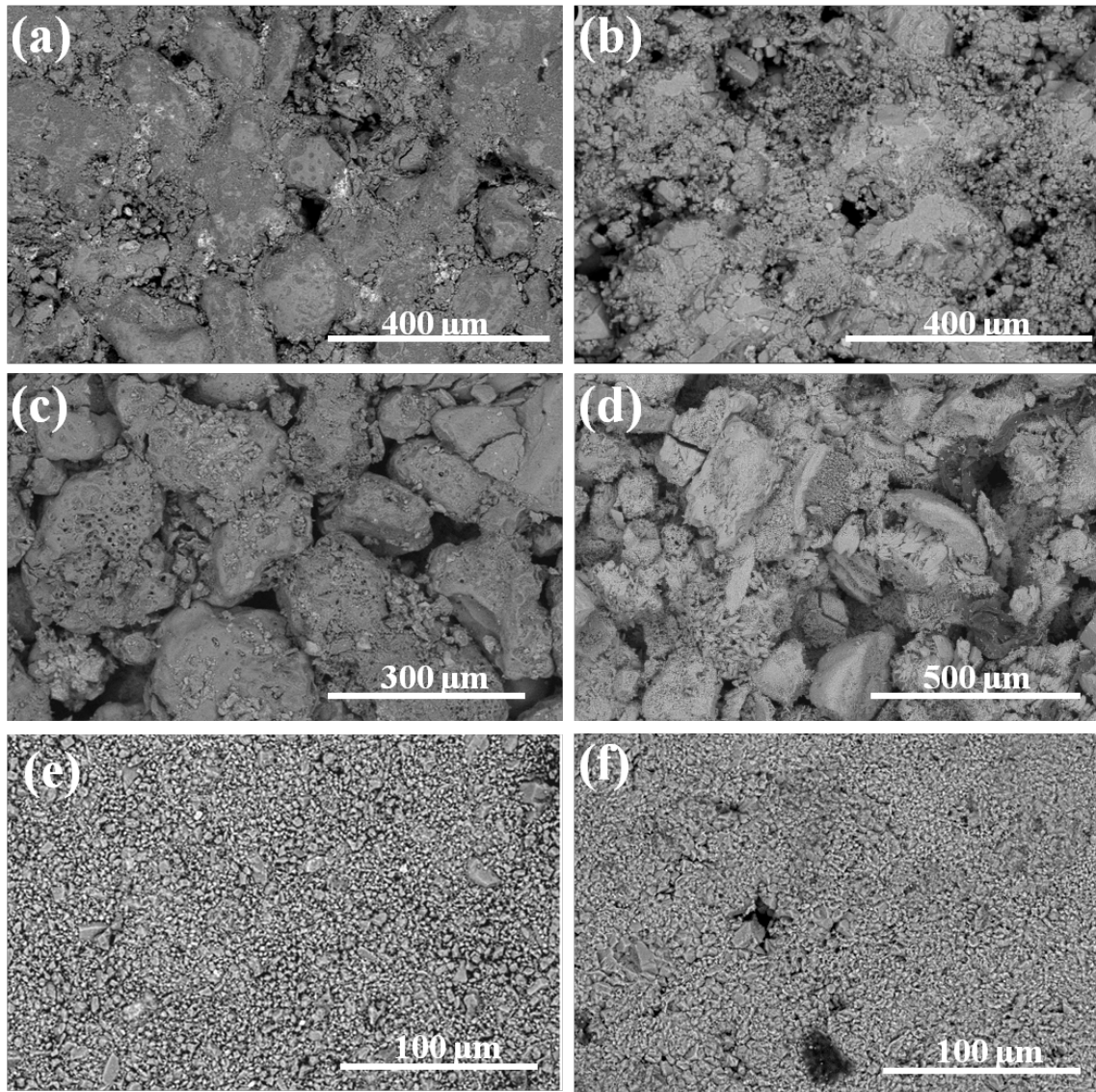


Figure 3.8: Comparison between microstructure created in our analog samples (to the left) and that of natural samples (Vanorio and Mavko, 2011) (to the right); panels (a) and (b) are grain-supported rocks, (c) and (d) are 100% grains, and (e) and (f) are 100% micrite.

3.4.2 Micrite-Porosity Relationship in Set MCR Samples

3.4.2.1 Micro-Geometrical Interpretation

The relationship between micrite content and porosity followed a v-shaped trend (Figure 3.4), which is similar to that observed by Marion (1990) and Yin (1992) in sand-clay mixtures. This trend has also been observed in well log data from stratigraphic sequences composed of non-laminar clay-sand mixtures (Dvorkin et al., 2002; Florez and Mavko, 2003). We can explain this behavior by considering a micro-geometrical model describing the change in the microstructural arrangement of the grain/micrite fabric within the sample as micrite is gradually added to the mixture. The microstructure of the carbonate analogs covers a wide range of fabrics, ranging from grain-dominated fabrics where grains are the load-bearing component and micrite is the dispersed phase, to fabrics where micrite is the load-bearing phase. As micrite is initially added to the mixture (i.e., grain-supported regime), micrite particles tend to fill the pore space available between the coarser grains, gradually reducing it as more micrite is added, until all pores are filled. This microstructural arrangement leads permeability to significantly decrease (Figure 3.9) as a result of micrite blocking the pore throats. Nevertheless, as the volume of micrite increases, the mixture becomes micrite-supported and porosity begins to increase because of the replacement of solid grains by the microporous micrite aggregates. In the micrite-supported regime, microporosity dominates the arrangement, thus making up the total porosity. Microporosity does not however contribute to permeability, and hence further change in permeability is minimal (Figure 3.9). Based on the data from Figure 3.4, the transition from the grain-supported to the micrite-supported regime occurs at micrite content ranging between 20% and 30%. This volume percentage of micrite represents a critical point along the trend and it is consistent with the porosity exhibited by the sample composed of 100% grains (26.7%). That is, this critical volume corresponds to the amount of micrite needed to completely fill the pore space available between the coarser grains. Such an observation agrees with the definition of the critical volume fraction of clay, i.e., the lowest porosity point along the trends of the sand-clay mixtures, which is equivalent to the porosity of 100% sand samples (Thomas and Stieber, 1975; Marion et al., 1992).

It is worth noting that both the micrite-porosity relationship and micrite-permeability (Figures 3.4 and 3.9) for set MCR are in general consistent with those observed for sand-clay mixtures (Marrion 1990; Yin, 1992). The main reason behind the similarity in the observed trends is that both sand-clay mixtures (Marrion 1990; Yin, 1992) and set MCR samples from this study are composed of coarse and fine particles in the absence of secondary macroporosity, which instead is characteristic of carbonate rocks. Vanorio and Mavko (2011) reported a trend of porosity as a function of micrite content that is different than that reported by Marion (1990) and this study. The trend was from natural carbonate samples inherently populated with macropores, which formed secondary porosity. The presence of this additional type of porosity can create different patterns in the evolution of porosity and permeability in carbonates. This will be discussed in Section 3.4.3.

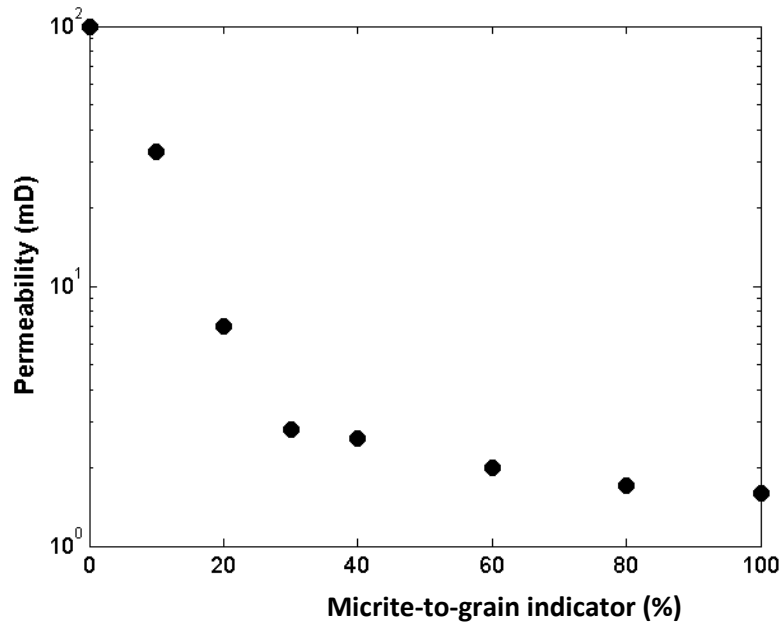


Figure 3.9: Plot of permeability as function of micrite content (micrite-to-grain indicator) for set MCR samples.

3.4.2.2 Modeling Micrite-Porosity Relationship

The purpose of this section is to model the data shown in Figure 3.4 by predicting the porosity of the grain-micrite mixtures using the properties of the end members only (pure grains and pure micrite). Since both skeletal grains and micrite were sieved to have narrow particle size range, as mentioned in Chapter 2, the grain-micrite mixtures can be considered as binary mixtures. There is extensive literature on the packing and porosity of binary

mixtures due to their importance in many fields including powder and concrete technology (e.g., Furnas 1928, Yu and Standish, 1988; Yu et al., 1993; De Larrard, 1999), filter designs (e.g., Mota et al., 2001, Mota et al., 2002), civil and materials engineering (e.g., Yu and Standish, 1991; Zou et al., 2005; Osuji and Inerhunwa, 2015), as well as earth sciences (e.g., Marion et al., 1992; Revil and Cathles, 1999, Kamann et al., 2007). We first start by reviewing literature on porosity prediction for binary mixtures of spheres and then extend the analysis to the case of grain-micrite mixtures.

3.4.2.2.a Ideal Packing of Spheres

Experiments on binary mixtures of spheres (McGeary 1961; Ridgway and Tarbuck, 1968) have shown that the packing (and porosity) of binary mixtures depends on diameter ratio of the particles. When the fine-to-coarse spheres diameter ratio (R) of the spheres is very small (typically less than 0.1), the packing of the binary mixture can be described as “ideal” (McGeary 1961). This implies that the very fine spheres do not disturb the original packing of coarse spheres and vice versa. That is, the porosity of the two pure end-members remains the same after mixing. The porosity of such an ideal packing system has been quantified by several studies (Furnas, 1928; Westman and Hugill, 1930) using a linear packing model. The porosity of the mixture in the case of ideal packing can be defined using the porosity of the pure end-members, where no other inputs are needed in the model. Marion et al. (1992) utilized this concept of ideal packing to describe the geometry of the sand-clay mixtures and model their porosities. Although the ideal packing model was successful in qualitatively describing the overall clay-porosity trends, it under-predicted the measured porosities (Marion et al., 1992) as shown in Figure 3.10. Since the fine-to-coarse particle diameter ratio between the coarse skeletal grains and micrite is very small ($\approx 4/375 = 0.01$), we first attempted to utilize the ideal packing model to predict the porosities for our grain-micrite mixtures. Following the set of equations used by Marion et al. (1992), we redefined the input parameters to describe the grain-micrite mixture, and the equations are shown in Appendix B. Figure 3.11 shows that the prediction of the ideal packing model significantly under-estimated the porosities of our mixtures. This suggests that the packing of particles in the grain-micrite mixtures deviates drastically from the ideal packing despite the very small diameter ratio between the coarse grains and fine micrite.

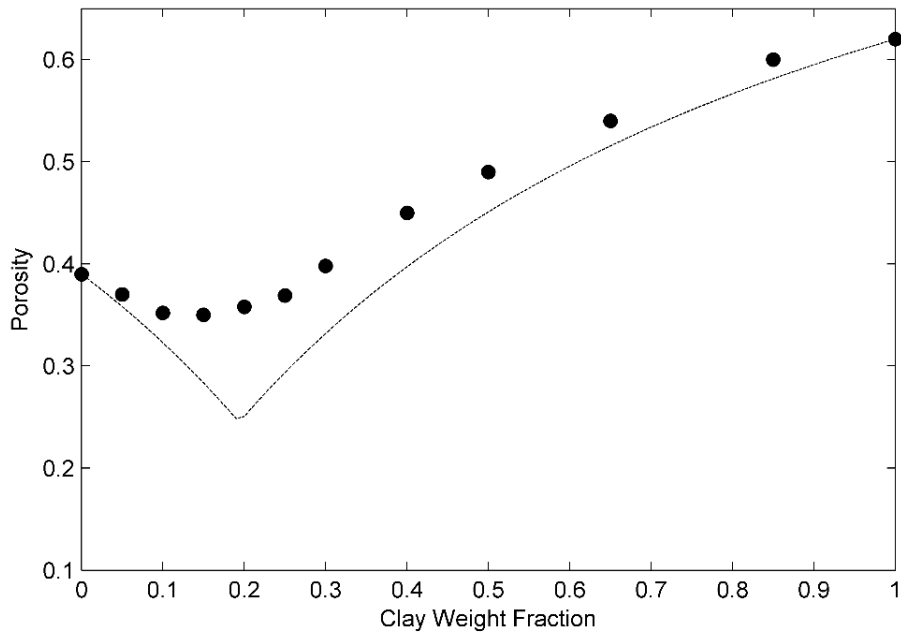


Figure 3.10: Porosity as function of clay content for the dry un-compacted sand-clay mixtures (Marion et al., 1992). The dashed curve corresponds to the ideal packing model prediction.

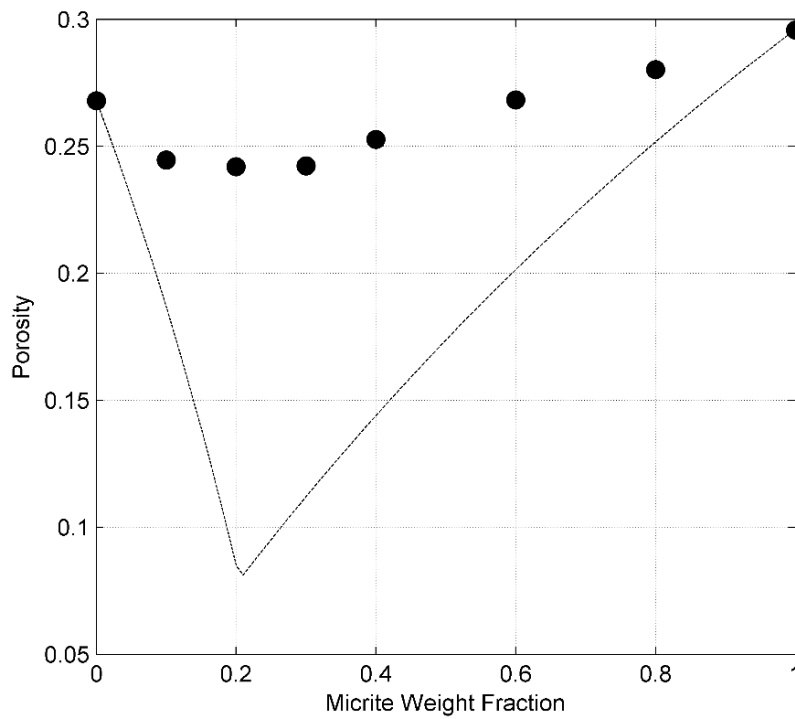


Figure 3.11: Porosity as function of micrite fraction for the grain-micrite mixtures from set MCR samples. The dashed curve corresponds to the ideal packing model prediction.

3.4.2.2.b Non-ideal Packing of Spheres

The deviation from ideal packing for spheres has been attributed to the increase of diameter ratio (typically > 0.1) between the fine and coarse spheres in a binary mixture (McGeary 1961; Ridgway and Tarbuck, 1968). Experiments have shown that the deviation from ideal packing increases as the diameter ratio increases (McGeary 1961; Ridgway and Tarbuck, 1968), where the maximum deviation occurs around the minimum porosity as shown in Figure 3.12. As the diameter ratio increases, the presence of fine spheres disturbs the original packing of the coarse spheres and vice versa (Cumberland and Crawford, 1987; Yu and Standish, 1991). Consequently, the porosity of the mixture will be larger than the values predicted by the ideal packing model (Figure 3.12). Two main mechanisms, or effects, were introduced to explain the increase in porosity associated with packing disturbance, namely: loosening effect and wall effect (Stovall et al., 1986; Yu and Standish, 1991; De Larrard, 1999). The loosening effect impacts the packing when the coarse particles are dominant (i.e., coarse-particles-supported regime), where fine particles loosen the packing of the coarse particles by occupying the space between them (Stovall et al., 1986; Yu and Standish, 1991) as demonstrated in Figure 3.13. The wall effect, on the other hand, occurs when the fine particles are dominant (i.e., fine-particles-supported regime), where the coarse particles disrupt the original packing of the fine particles, thus producing larger pores at the wall boundaries of the coarse particles (Stovall et al., 1986; Yu and Standish, 1991) as demonstrated in Figure 3.14.

The effect of these two mechanisms on porosity is accounted for using correction functions expressed in terms of the diameter ratio, R (Stovall et al., 1986; Yu and Standish, 1991). The correction functions are obtained by regression analysis of the porosity values measured for binary mixtures of spheres with varying diameter ratio (Stovall et al., 1986; Yu and Standish, 1991; Yu et al., 1996). The linear packing model is then modified to incorporate the two correction functions for both the loosening and wall effect. Of particular interest here is a modified linear packing model developed by Yu et al. (1996) since the authors extended the model to the case of non-spherical particles (discussed in the next section). A summary of the non-ideal linear packing model for spherical particles

with the incorporated correction functions is shown in Appendix C, while more details can be found in Yu et al. (1996).

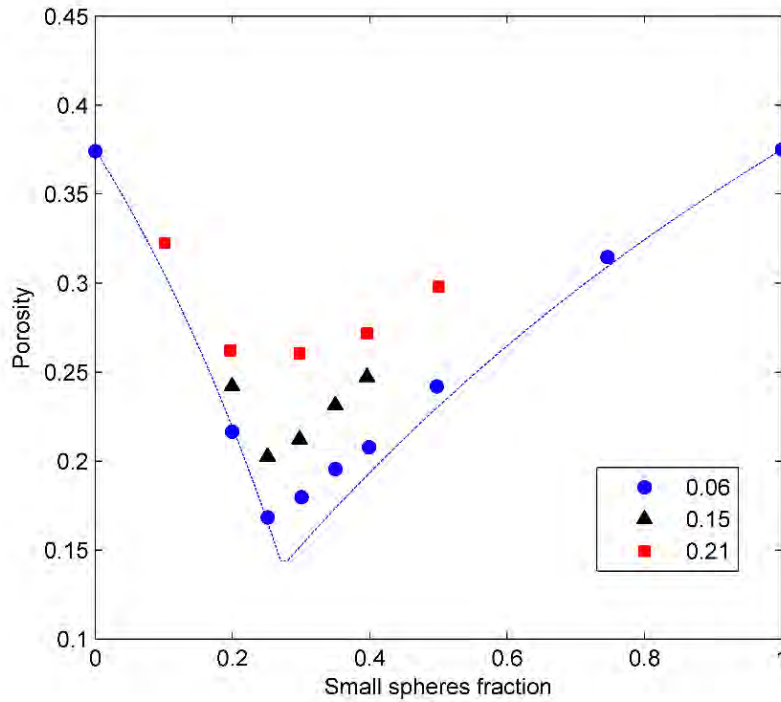


Figure 3.12: Porosity as function of small spheres fraction in binary mixture of spheres with different diameter ratios (shown in the legend). Data is from McGeary (1961). The porosity of the end members is the same for all three mixtures. The blue curve corresponds to the ideal packing model prediction; note the increase of deviation from the ideal packing prediction as the diameter ratio increases.

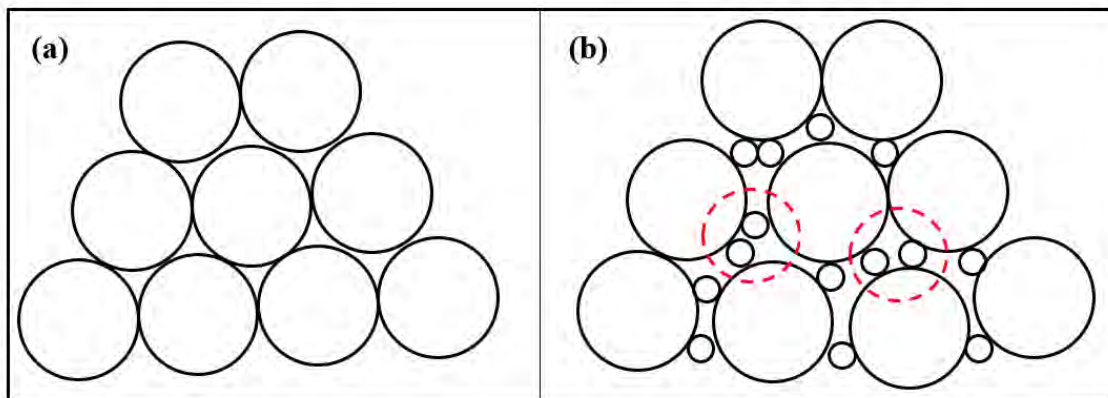


Figure 3.13: Demonstration of the loosening effect: (a) original packing of the coarse spheres, (b) disturbance and loosening of the coarse sphere packing due to the presence of small spheres in between (examples are highlighted by dashed red circles).

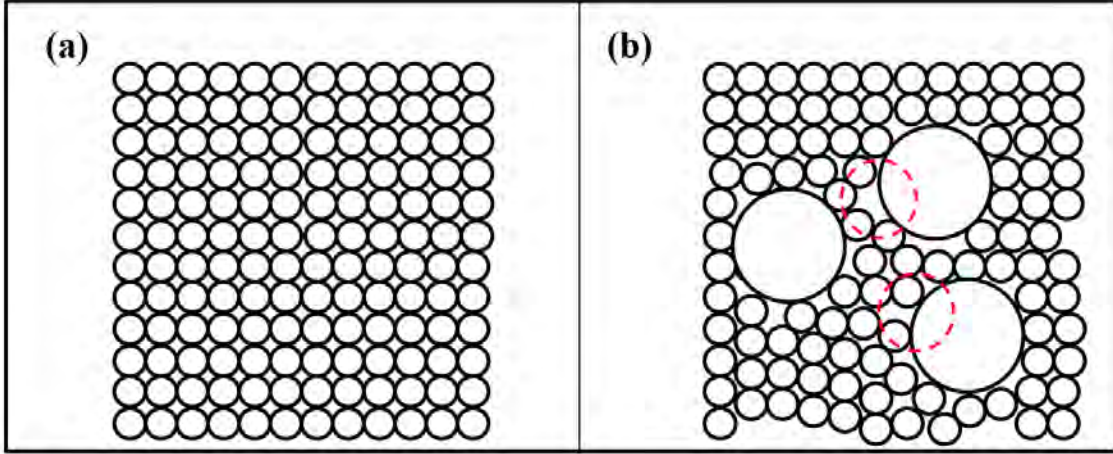


Figure 3.14: Demonstration of the wall effect: (a) original packing of the fine spheres, (b) disturbance of fine sphere packing and presence of larger pores at the wall of coarse spheres (examples are highlighted by dashed red circles).

The original formations of the non-ideal packing model (Yu et al., 1996) use various notations (such as specific volumes as shown in Appendix C) that are not generally used in geophysics. Therefore, we re-derived the equations so that the final set of equations is expressed in terms of porosity as follows:

- a) When the coarse spheres are dominant (coarse-spheres-supported regime), the loosening effect would dominate the packing. The porosity of this mixture (ϕ_a) can be calculated using:

$$\frac{1}{1 - \phi_a} = \left(\frac{f_f}{1 - \phi_f} + \frac{f_c}{1 - \phi_c} \right) - (1 - L(R)) \frac{f_f}{1 - \phi_f} \quad (3.1)$$

where f_f is the fraction of fine spheres, f_c is the fraction of coarse spheres ($f_c = 1 - f_f$), and ϕ_f and ϕ_c are the porosities of the pure fine and coarse spheres packing, respectively. The subscripts f and c will refer to fine and coarse particles, respectively, throughout this study. $L(R)$ is the correction function for the loosening effect and is a function of the ratio between the diameter of the fine spheres to the coarse ones ($R = d_f / d_c$). The correction function, $L(R)$, is given by (Yu et al., 1996):

$$L(R) = 1 - (1 - R)^{3.3} - 2.8 R (1 - R)^{2.7} \quad (3.2)$$

b) When the fine spheres are dominant (i.e., fine-spheres-supported regime with dispersed coarse spheres), the wall effect would be dominant. The porosity of such mixture (ϕ_b) and the correction function for the wall effect $W(R)$ can be calculated using the following equations:

$$\frac{1}{1 - \phi_b} = \left(\frac{f_f}{1 - \phi_f} + \frac{f_c}{1 - \phi_c} \right) - (1 - W(R)) \phi_c \frac{f_c}{1 - \phi_c} \quad (3.3)$$

$$W(R) = 1 - (1 - R)^{2.0} - 0.4 R (1 - R)^{3.7} \quad (3.4)$$

The fraction of fine spheres (f_f), at which the structural arrangement changes from a coarse-spheres-supported to a fine-spheres-supported regime, is not known *a priori*. However, such value of f_f can be estimated by finding f_f at which $\phi_a = \phi_b$, which corresponds to the lowest porosity point along the v-shaped trend. Alternatively, the porosity (ϕ) of the mixture at any given f_f can be determined in practice simply by (Yu et al., 1996):

$$\phi = \text{maximum} \{ \phi_a, \phi_b \} \quad (3.5)$$

Figure 3.15 shows a good match between the predictions of the non-ideal linear packing model (using equations 3.1 to 3.5) and the data shown earlier in Figure 3.12. It should be noted that when the diameter ratio is very small ($R \approx 0$), both $L(R)$ and $W(R)$ will be zero, and hence, equations 3.1 and 3.3 will reduce to the ideal packing condition.

reduce to the ideal packing condition.

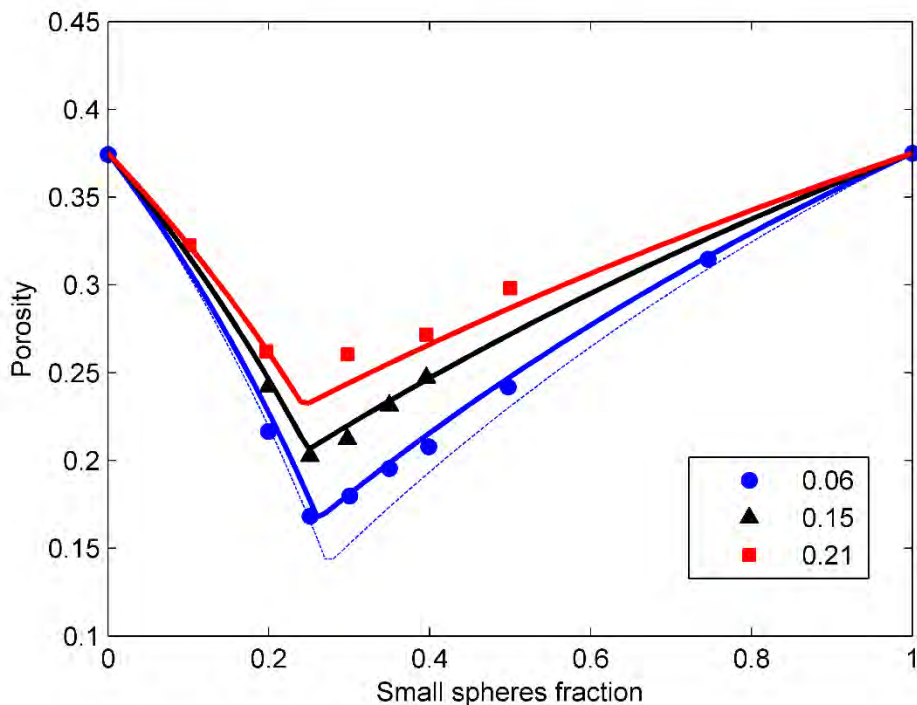


Figure 3.15: Porosity as function of small spheres fraction in binary mixture of spheres with different diameter ratios (shown in the legend). Same data as shown in Figure 3.12 from McGearry (1961). The solid bold blue, black, and red curves refer to prediction of the non-ideal packing model using equations 3.1 through 3.5.

3.4.2.2.c Non-Ideal Packing of Non-Spherical Particles

It is known that the particles involved in engineering and earth sciences are frequently non-spherical. Therefore, estimating the porosity of binary mixtures made out of non-spherical particles is of significant interest. In our case, we would like to model the porosity of the grain-micrite mixtures. A large body of literature indicated that the packing of non-spherical particles is dependent on both the size and shape of the particles (e.g., Brown et al., 1950; Yu and Standish, 1993; Podczec and Sharma, 1996). Several studies reported that packing behavior of non-spherical particles is similar to that of spherical particles, thus the theory of packing in spherical particles can be extended to the packing of non-spherical particles (German, 1989; Yu et al., 1993; Yu and Standish, 1993). Yu et al. (1996) hypothesized that the linear packing model used for porosity estimation in binary mixtures of spheres can be applied to mixtures of non-spherical particles given that the non-spherical packing system is represented by an equivalent system of spheres. The authors utilized the concept of “equivalent packing diameter” d_p (Yu et al., 1993; Zou and Yu, 1996) to

characterize the packing of non-spherical particles and define the equivalent system of spheres. The equivalent packing diameter d_p is defined as the diameter of a sphere having the same size-dependent packing behavior as the particle (Yu et al., 1993). This can be determined experimentally as explained in detail in Appendix D. The concept of d_p is simplified in the 2D example demonstrated in Figure 3.16. Once d_p of the fine and coarse non-spherical particles is determined, it can be used to re-define the diameter ratio R which becomes: $R = d_{pf} / d_{pc}$, where d_{pf} and d_{pc} are the equivalent packing diameter of the fine and coarse non-spherical particles, respectively. This ratio can then be used along with equations 3.1 through 3.5 to estimate the porosity of the binary mixture of non-spherical particles (Yu et al., 1996). That is, the non-ideal packing model for spheres (equations 3.1-3.5) can be used for non-spherical particles given that R is defined in terms of the equivalent packing diameter, d_p .

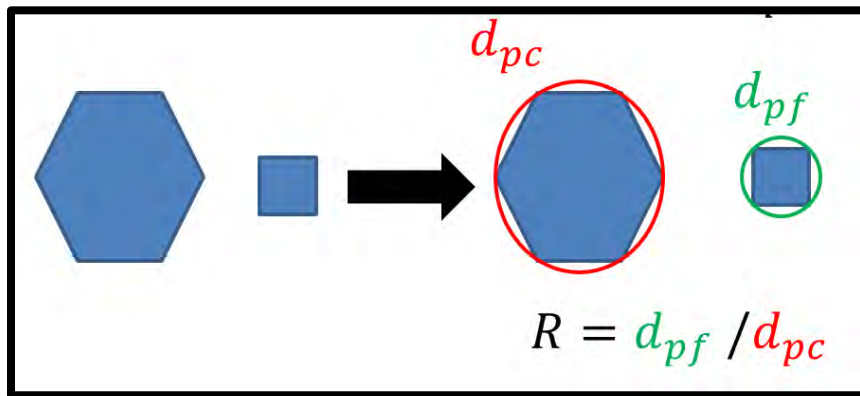


Figure 3.16: Demonstration of the equivalent packing diameter d_p concept. The binary mixture composed of coarse hexagonal particles and fine square particles (to the left). The d_p for both particles is highlighted by red and green circles (to the right). Defining R in terms of d_p and using equations 3.1-3.5 would allow the estimation of porosity for the binary packing of hexagonal and square particles.

Since measuring d_p requires extensive experimental procedures (see Appendix D), an empirical attempt was made to relate d_p to the shape and size analysis of non-spherical particles (Yu and Standish, 1993; Zou and Yu, 1996). The authors suggested classifying the packing behavior of non-spherical particles into size and shape dependent behavior which can be represented using two parameters, namely: equivalent volume diameter, d_v , and sphericity, ψ . The equivalent volume diameter, d_v , of a particle is the diameter of a sphere having the same volume as the particle, while sphericity ψ is defined as the ratio of

the surface area of a sphere having the same volume as the particle to the actual surface area of the particle (Yu and Standish, 1993). Both d_v and ψ can be calculated for uniform particles (such as cylinders and cubes) based on geometry. Zou and Yu (1996) extended this concept and empirically related the experimentally measured values of d_p to the calculated values of d_v and ψ for uniform non-spherical particles including cylinders, disks, and cubes (a summary of what was done to establish this relation is given in Appendix E). The expression of d_p as a function of the d_v and ψ for a non-spherical particle, is given by the following equation (Zou and Yu, 1996):

$$d_p = \frac{d_v}{\psi^{2.785} \exp[2.946(1 - \psi)]} \quad (3.6)$$

Yu et al. (1996) proposed using equation 3.6 to find d_p for both the coarse and fine non-spherical particles, obtain $R = d_{pf} / d_{pc}$, and finally use equations 3.1 through 3.5 to predict the porosity of the non-spherical binary mixture. Predictions following this approach showed good agreement with measured porosities for binary mixtures of cylinders (Yu et al., 1996)). However, utilizing equation 3.6 for non-uniform geological materials, such as skeletal grains and micrite, may encounter several issues and limitations. First, unlike the uniform non-spherical particles, obtaining d_v and ψ for geological materials that have complex or irregular shape may not be feasible based on geometry. Moreover, equation 3.6 was empirically derived based on data for particles with uniform shapes such as cylinders and cubes, and hence, its applicability might be questioned in geological materials. Last but not least, the sphericity of natural materials (such as sand or skeletal grains) might vary significantly from one particle to another despite their similar sizes as is the case for skeletal grains (Figure 2.1 in Chapter 2). Therefore, ψ can be seen as an effective average property (i.e., mean of a distribution for a single end-member). Those limitations suggest the need for an alternative approach to predict the porosity of binary mixtures composed of geological materials (i.e., irregular non-spherical particles).

3.4.2.2.d Modified Model to Estimate Porosity for Binary Mixtures of Non-Spherical Particles

It is evident that the equivalent diameter ratio R , is the key parameter to predict porosity of binary mixtures composed of non-spherical particles (Yu and Standish, 1993; Yu et al.,

1996). Since the use of d_v and ψ to obtain d_p (and then R) may not be possible in geological materials due to the limitations mentioned earlier, we propose here an alternative approach to estimate the ratio of the equivalent packing diameters. The purpose here is to find an expression for R that can capture the size- and shape-dependent packing behavior and can be utilized at the same time for geological materials. In order to achieve that, we start with the expression of R for spherical particles and we re-write that expression in a more general form. Assuming we have a binary mixture of two spheres (fine and coarse) and both are non-deformable and have equal density (which are the assumptions for the non-ideal packing model as shown in Appendix C), we then have:

$$R = \frac{d_{pf}}{d_{pc}} = \frac{d_f}{d_c} \quad (3.7)$$

Note that d_p for a sphere is equal to its diameter, as demonstrated in Appendix C. Since both fine and coarse spheres have the same particle density, we can then write:

$$R = \frac{d_{pf}}{d_{pc}} = \frac{d_f}{d_c} = \frac{r_f}{r_c} = \frac{\rho_f r_f}{\rho_c r_c} = \frac{3/(\rho_c r_c)}{3/(\rho_f r_f)} \quad (3.8)$$

where r_f and r_c are the radius of the fine and coarse spheres, respectively, and ρ_f and ρ_c are the corresponding particle densities of the spheres. For any sphere, the expression $3/(\rho r)$ corresponds to the specific surface area A (i.e., surface area per gram) as shown in the following:

$$\begin{aligned} \frac{3}{\rho r} &= \frac{4 \pi r^2}{\rho \frac{4}{3} \pi r^3} = \frac{(S_{one\ sphere})(N)}{\rho(\mathcal{V}_{one\ sphere})(N)} = \frac{(S_{one\ sphere})(N)}{1\ gram} \\ &= \text{surface area/gram} \end{aligned} \quad (3.9)$$

where ρ is particle density, S and \mathcal{V} are the surface area and volume of one sphere, and N is the number of spheres in one gram. Therefore, writing equation 3.8 in terms of specific surface area of the fine (A_f) and coarse (A_c) spheres leads to:

$$R = \frac{A_c}{A_f} \quad (3.10)$$

That is, the diameter ratio R for spheres is equivalent to the ratio between the specific surface areas of the coarse and fine spheres. The advantage of this expression (equation 3.10) is that specific surface area is a quantity that can be measured for geological

materials. Moreover, specific surface area is dependent on both the size and shape of the particles which are the two major controls on the packing behavior of non-spherical particles (Yu and Standish, 1993). Additionally, we show in Appendix F that it is possible to fully define both d_v and ψ in terms of the surface area and specific surface area of a particle. That is, the use of specific surface area can capture information about both d_v and ψ . Equation 3.10 can be seen as a general form that can be used for both spherical and non-spherical particles to estimate the equivalent packing diameter ratio R . Therefore, equation 3.10 might be used to estimate R , instead of using d_p , d_v , and ψ , and then equations 3.1-3.5 can be used to predict the porosity of the binary mixtures of non-spherical particles. A summary of our proposed approach is shown in Figure 3.17. In order to apply this approach for the grain-micrite mixtures from this study, we needed to measure the specific surface area of skeletal grains and micrite.

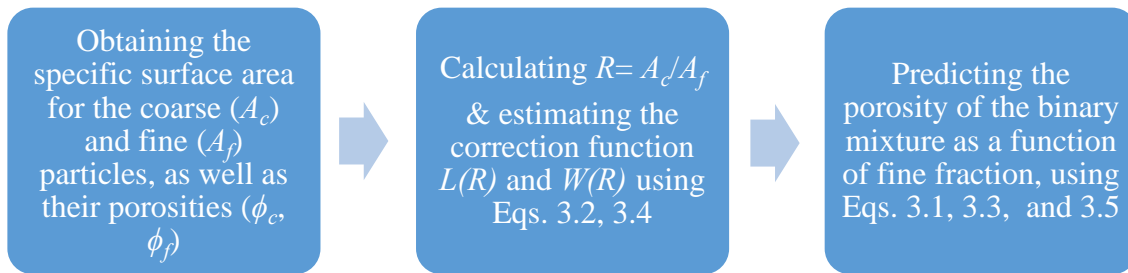


Figure 3.17: Summary of the proposed approach to estimate the porosity of binary mixtures. Note that the specific surface area can be calculated for uniform shaped particles while it has to be measured for geological materials.

We measured the specific surface area for both micrite and skeletal grains using the standard Brunauer-Emmett-Teller (BET) method (Brunauer et al., 1938). This was part of the second project research focusing on the Nuclear Magnetic Resonance (NMR) of carbonate sediments (El Husseiny and Knight, 2016). The measurements were collected with the Accelerated Surface Area and Porosimetry System (ASAP 2020, Micromeritics Instrument Corp.) using nitrogen gas as the adsorbate. The specific surface area for the micrite and skeletal grains is reported in Table 3.1. The BET surface area measurements indicate that the skeletal grains have a specific surface area that is almost 60% that of micrite ($A_{grains}/A_{micrite} = 0.57$), much higher than what would be expected based on their particle sizes ($d_{micrite}/d_{grains}=0.01$). This suggests that micrite particles have smoother and

more regular particle shape compared to the grains. Examining the SEM images of skeletal grains and micrite (Figures 2.1 and 2.2 in Chapter 2), we can observe the irregular shape of the grains as well as the presence of intra-particle micro-pores. This can contribute to increasing the surface area of the grains. The relatively high specific surface area of skeletal grains was also observed by Walter and Morse (1984) and Vincent et al. (2011).

Using the measured specific surface area, we obtained $R= 0.57$, and we then used equations 3.1-3.5 to predict the porosity of the grain-micrite mixtures where micrite is the fine particle (subscript f) and skeletal grains is the coarse component (subscript c). The only input parameters needed are the specific surface area and the porosity of both pure skeletal grains and pure micrite samples. The output of the model is the porosity of the mixture as a function of micrite fraction. Figure 3.18 shows that the proposed approach was successful in predicting the porosity of the grain-micrite mixture fairly well, using the properties of the end-members alone. The use of the specific surface area ratio as an input in the model resulted in a significant improvement compared to the use of size ratio (Figure 3.18).

Table 3.1: Specific surface area for micrite and skeletal grains

Micrite	Skeletal grains
$1.567 \pm 0.005 \text{ m}^2/\text{g}$	$0.896 \pm 0.003 \text{ m}^2/\text{g}$

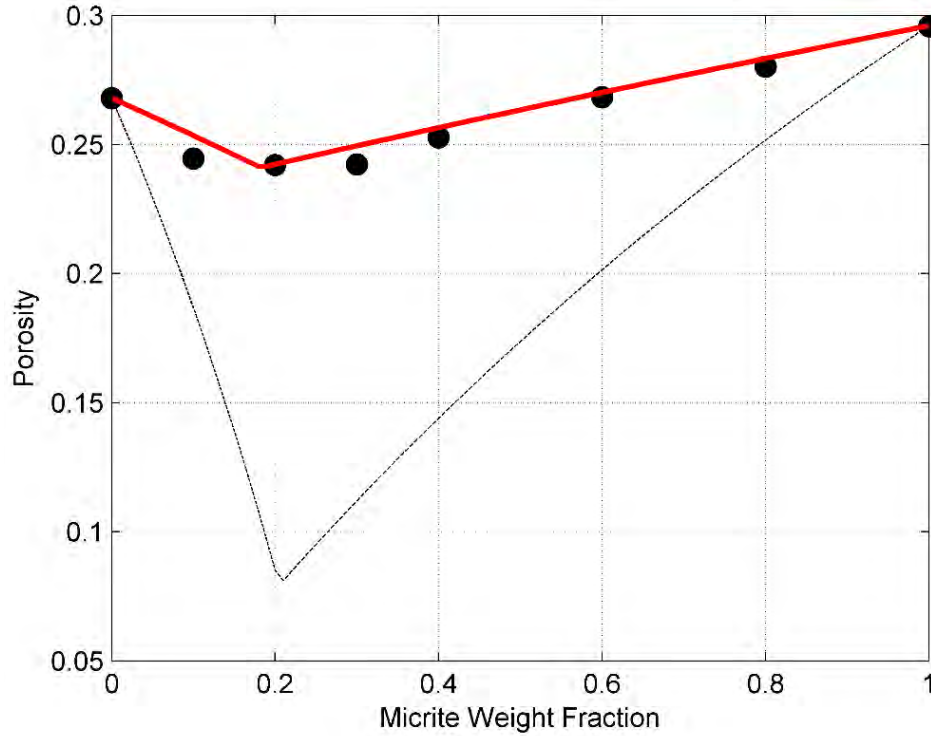


Figure 3.18: Porosity as function of micrite fraction for the grain-micrite mixtures from set MCR samples. The dashed black curve corresponds to the model prediction when using size ratio (0.01) to obtain R while the red solid curve corresponds to the prediction when using specific surface area ratio (0.57) to obtain R .

3.4.2.2.e Validation of the Proposed Approach

Although this approach was successful in predicting the porosity of the grain-micrite mixture, it is important to validate the approach using other published data. Specific surface area is not, however, frequently measured or reported in studies of binary mixtures composed of geological materials (e.g., Phillips, 2005; Kwan et al., 2015; Zhang et al., 2010; Yilmaz, 2009). On the other hand, specific surface area of uniform non-spherical particles (e.g., cylinders, cubes, etc.) can be calculated. Therefore, we validated our approach using published data of binary mixtures prepared using uniform non-spherical particles as shown in Figure 3.19. Appendix G shows the calculation of the specific surface area for the different uniform particles used in the validation of the proposed approach. Our proposed approach shows a good agreement with published data and with predictions obtained using the approach proposed by Yu et al., 1996 (using d_p , d_v , and ψ as shown in equation 3.6). The only exception is for the mixture of small and very large cylinders

(Figure 3.19d). The approach proposed by Yu et al. (1996) fits the data better which is expected since those cylinders were part of the data set used to produce the empirical relation in equation 3.6. The large cylinders ($L/D = 15.5$) have highly anisotropic shape which is not frequently observed for granular geological materials such as sand and calcareous grains. It is evident from Figure 3.19d that the porosity of large cylinders increases drastically as the size (L/D) of the cylinder increases. On the other hand, the porosity of geological materials such as sand and granite, reported by several studies (e.g., Phillips, 2005; Kwan et al., 2015; Zhang et al., 2010; Yilmaz, 2009), does not show such increase in porosity with increasing particle size. This suggests that the packing behavior of large cylinders is very different from that of other granular geological materials. The use of the proposed approach in this study does not seem to describe well the packing of binary mixtures of cylinders characterized by very large L/D . In such cases, the use of equation 3.6 instead is recommended to obtain R and predict the porosity.

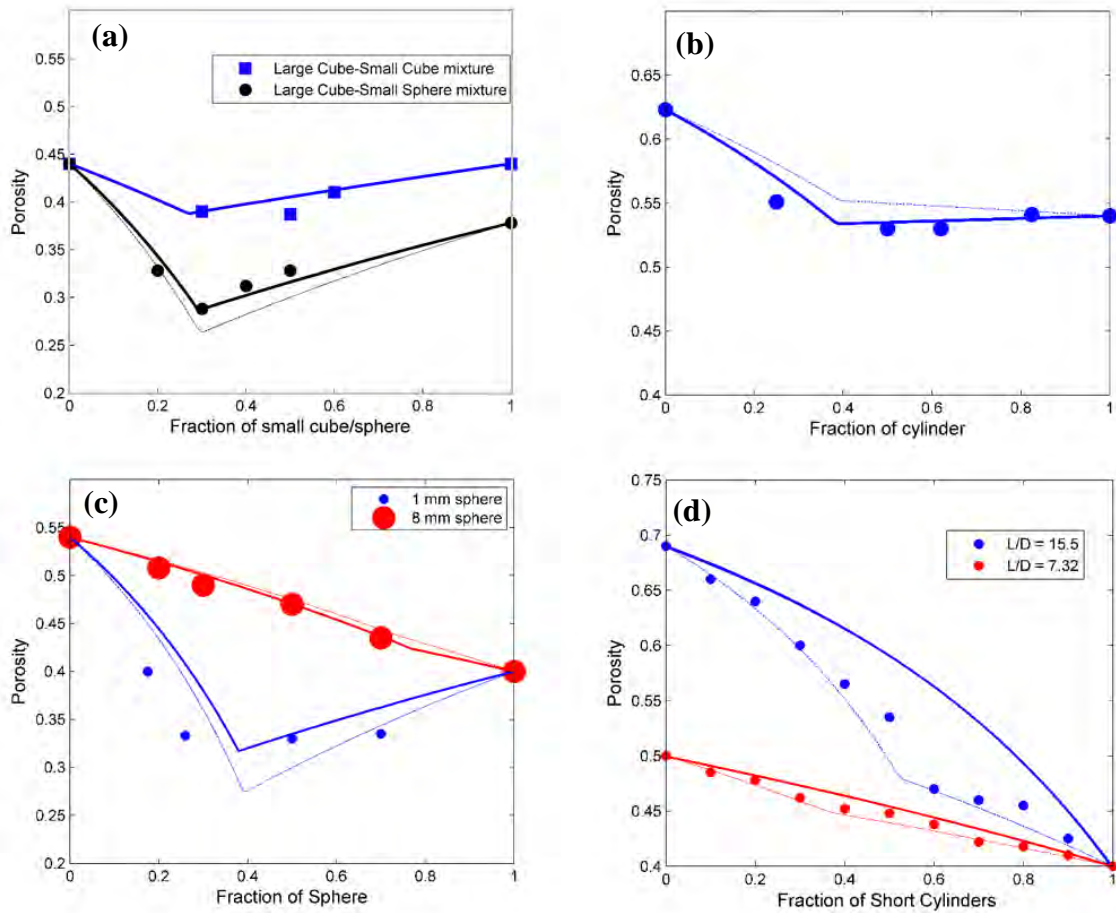


Figure 3.19: Validation of the proposed approach using several published data: the prediction of the proposed method is shown in bold solid curves while the prediction using the approach proposed by Yu et al., 1996 is shown in dashed curves. (a) Porosity of binary mixture of large cube (length=4 mm) and other shaped particles; data is from Iannella, 1985. (b) Porosity of binary mixture of disk (L=1.384 mm, D=19.374 mm) and cylinder (L=30 mm, D=4 mm), as function of cylinder fraction, data from Yu et al., 1992. (c) Porosity of mixtures of cylinders (L=30 mm, D=4 mm) and spheres of different diameters, data from Yu et al., 1992. (d) Porosity of binary mixture of short cylinders (L=3.91 mm, D=2.09 mm) and cylinders of different L values while D is kept the same, data from Milewski, 1973.

3.4.2.2.f Limitations and Final Remarks

It is important to note that the linear packing model for binary mixtures has some inherent limitations that apply to the proposed approach in this study as well. First, the model can be applied strictly to binary mixtures, where the two end members have uniform or narrow particle size distribution. For example, a mixture of poorly sorted coarse sand and clay is not considered a binary mixture. This is because the coarse particles are not well sorted and hence, they can have bi-modal particle size distribution instead of a narrow Gaussian distribution. A discussion on the porosity of mixtures composed of materials with a known particle size distribution can be found in Yu et al., 1996. Secondly, the model may not describe well the porosity in reservoir rocks affected by diagenesis since porosity could be altered by cementation or dissolution. Utilizing the approach shown here to porosity prediction in shallow sand-clay mixtures might be possible, however, given the following conditions: a) the sand is well sorted, and b) the sediments were not subjected to major diagenesis processes.

One important aspect of the linear packing model is that its formulation was based on pouring-of-particles (un-compacted) experiments. Although some studies (De Larrard, 1999; Kwan et al. 2015) suggested modification of the correction functions $L(R)$ and $W(R)$ to better predict the porosity of compacted binary mixtures, the proposed modifications were not significant. In order to test the applicability of the model to compacted binary mixtures, we used the measurements reported by Kwan et al. (2015) for binary mixtures of crushed granite rocks, sieved to have different sizes (Figure 3.20). The measurements were done under both un-compacted and compacted conditions. Compaction was applied using 30 compacting blows with a tamping rod where each blow was applied by releasing the tamping rod at a height of 50 mm above the surface of the aggregate (Kwan et al., 2015). The specific surface area was not reported for the samples, so we empirically fit the data for the un-compacted case using the linear packing model (equations 3.1-3.5) by finding a suitable value of R that would best match the measured porosity. For the compacted case, we found that the data can be fitted reasonably well using the same R and correction functions applied for un-compacted mixtures (Figure 3.20). In this case, the effect of compaction on the packing and porosity of the mixtures seems to be accounted for by the changes in the initial porosity of the end-members due to compaction. This suggests that

the linear packing model (and hence, the proposed approach) can be used to predict porosities of compacted binary mixtures as long as the porosities of the end-members are measured and used as inputs in the model. Consequently, applying the proposed approach to the compacted grain-micrite mixtures can be valid, and it also provided reasonable predictions as shown earlier in Figure 3.18.

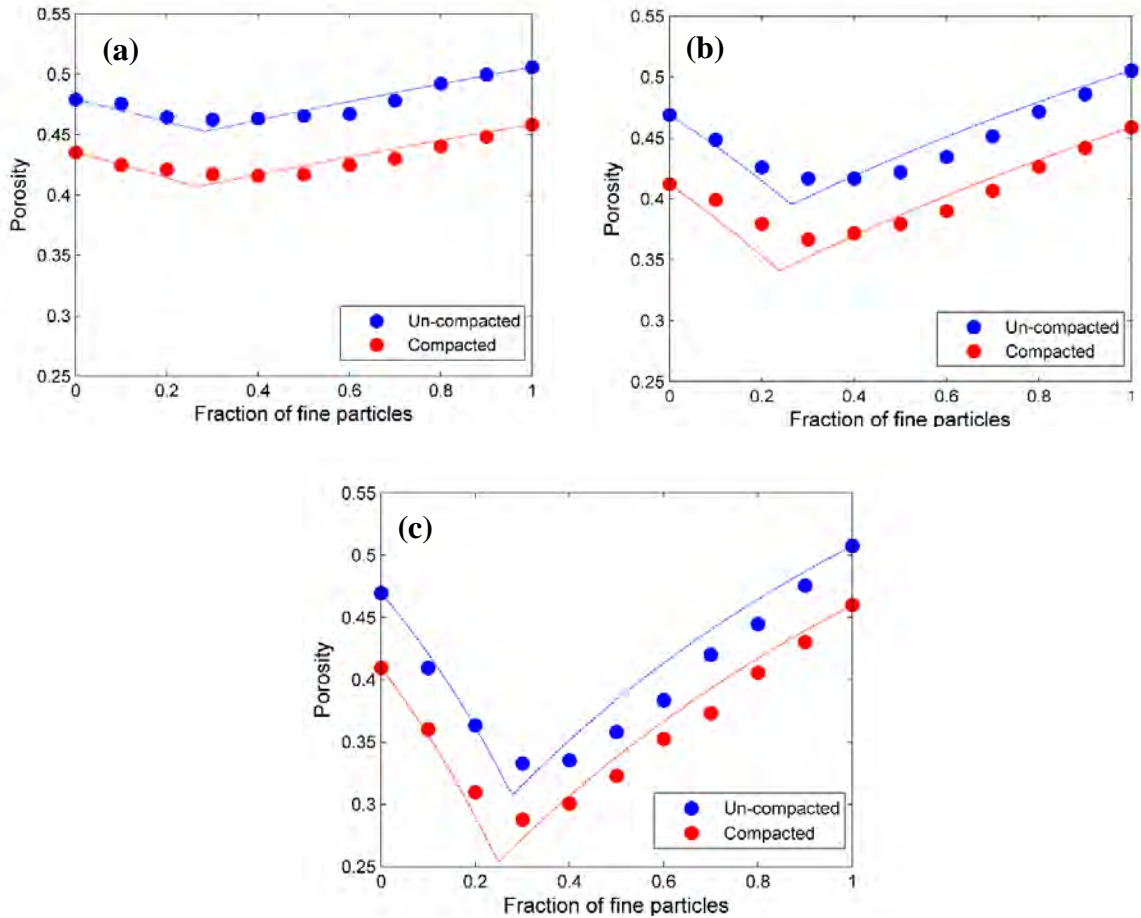


Figure 3.20: Un-compacted (in blue) and compacted (in red) packing porosity for binary mixtures of crushed granite as a function of fine particles fraction, data from Kwan et al., 2015: (a) binary mixture of 3.44 mm and 7.07 mm sized crushed granite, (b) binary mixture of 3.44 mm and 16.73 mm sized crushed granite, (c) binary mixture of 0.84 mm and 16.73 mm sized crushed granite. Curves correspond to the prediction of the linear packing model assuming the same R and correction functions for both the un-compacted and compacted cases.

It is finally important to mention that the linear packing model is more applicable for particles where gravity is the main force affecting the packing, a condition that works well

for coarse particles (Yu et al., 1997). In very fine materials (such as micrite or clay), however, the interparticle forces (i.e., van der Waal and electrostatic forces) becomes dominant compared to the force of gravity (Visser, 1989). Consequently, fine particles are cohesive and their packing behavior could be different from that of coarse particles (Yu et al., 1997; Santomaso et al., 2003). In such a case, the porosity of the fine particles would be larger than what is predicted by the linear packing model (Yu et al, 1997; Zou et al., 2011). However, when compaction is applied, the effect of interparticle forces can be reduced and the packing behavior of fine particles may be similar to that of coarse particles as pointed out by Zou et al. (2011). Therefore, the linear packing model might provide a reasonable estimation for the porosity of a binary mixture composed of compacted very-fine and coarse particles. The use of pressure (2 MPa) in preparing the samples seems to minimize the effect of interparticle forces in micrite, thus the packing model could predict the porosity of the grain-micrite mixtures fairly well. Moreover, the use of compaction in sand-clay mixtures prepared by Knoll (1996) resulted in binary mixtures whose porosity could be accurately predicted by the proposed approach as shown in Figure 3.21. On the other hand, un-compacted sand-clay mixtures prepared by Marion et al. (1992) had porosities that were higher than the model predictions (Figure 3.10) which suggests that interparticle force is dominating the packing of the un-compacted clay.

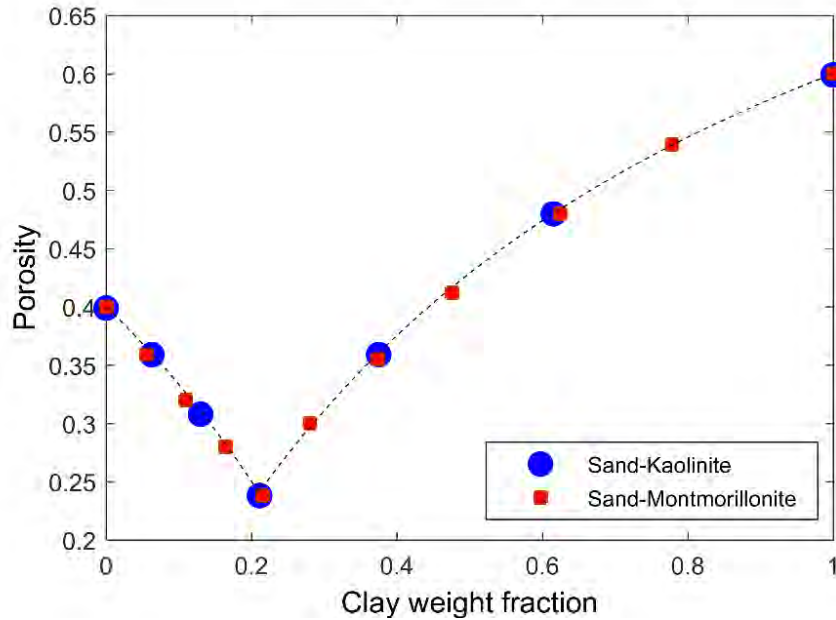


Figure 3.21: Porosity of sand-clay mixtures as a function of clay fraction, data is from Knoll, 1996. Samples were compacted using low confining pressure (exact pressure was not reported) that reduced the porosity of the pure clay from 0.8 to 0.6 (Knoll, 1996). The dashed curve corresponds to the linear packing model predictions (same curve for both mixtures) using the proposed approach in this study where the specific surface areas for sand, kaolinite, and Montmorillonite are 0.39, 25, and 65 m²/g, respectively, as reported by Knoll, 1996. The very low specific surface area ratio (A_{sand}/A_{clay}) suggests that the packing is close to ideal which is consistent with the measurements of porosity (unlike the un-compacted sand-clay mixtures shown in Figure 3.10).

3.4.3 Porosity-Permeability Relationship in Analog Samples

In this section, we discuss the porosity-permeability relationship of the analog samples. Figure 3.6 shows that the porosity-permeability data for the analog samples of both set MCR and set MACRO exhibit a significant scatter, implying that the volumetric fraction of the pore space, and hence the porosity, alone does not fully describe flow in carbonates. Nevertheless, knowledge of both micrite content and macropores helps to highlight trends in porosity-permeability data (Figures 3.6 and 3.7). Three trends can be observed including the porosity-permeability relationship for: (a) set MCR samples where micrite content is the only parameter varying (circles in Figure 3.6), (b) samples with similar micrite content but with varying macroporosity (dashed lines in Figure 3.6), and (c) set MACRO samples where both micrite content and macroporosity are changing (arrows in Figure 3.7).

3.4.3.1 The Effect of Micrite Content on the Porosity-Permeability Relationship

In the absence of introduced macropores (set MCR), permeability decreases drastically with the addition of micrite up to 30%, after which the addition of micrite does not significantly affect permeability (circles in Figure 3.6). The effect of micrite on the porosity-permeability can be explained by the microstructural arrangements that define the grain-supported and micrite-supported regimes as mentioned earlier in Section 3.4.2.1.

The data shown in Figure 3.6 suggest that the volume fraction of micrite is a major factor controlling the porosity-permeability relationships in the analog samples. Each dashed line in Figure 3.6 highlights the dependence of permeability on porosity for samples with similar micrite content (although their macroporosity is varying). At any given porosity, permeability decreases as the micrite content increases. Beard and Weyl (1973) observed similar trends for mixtures of coarse to fine unconsolidated sand where the permeability decreases as the median grain size decreases at a given porosity. In addition, Chilingarian and Walf (1975) reported similar patterns for the porosity-permeability relations of clean to shaley sandstones. In order to demonstrate how the micrite content might be used to inform existing models for the porosity-permeability relationship, we utilized the Kozeny-Carman equation (Carman, 1937) where permeability is expressed as a function of porosity, grain diameter (assuming spheres), and pore geometry (Dias et al., 2006; Mavko et al., 2009). Using this equation, we reproduce the porosity-permeability trends observed in Figure 3.6. The aim here is not to model the porosity-permeability data but rather to show an example of using micrite content as an input in the Kozeny-Carman equation. Moreover, we aim to investigate how the variation in micrite content affects the different physical parameters controlling permeability in the equation. A common approximation of the Kozeny-Carman equation, for a pack of spheres with particle diameter d , can be expressed as (Mota et al., 2001; Dias et al., 2006; Mavko et al., 2009):

$$k = \frac{\phi^3 d^2}{36 K_o (1 - \phi)^2 \tau^2} , \quad (3.11)$$

where k is permeability, ϕ is porosity, K_o is shape factor which depends on the shape of pores, and τ is the tortuosity defined as the length of the average flow-path divided by the sample length. The product $K_o \tau^2$ is frequently expressed as the geometric factor B (Mavko

et al., 2009) and it is also referred to as Kozeny's constant (Mota et al., 2001; Ozgumus et al., 2014). Physically, this factor accounts for the irregularities and complexities in the pore structure (Mavko et al., 2009; Ozgumus et al., 2014) and is largely affected by specific surface area (Li and Gu, 2005). Several observations and studies also suggested the introduction of the percolation porosity term, ϕ_c , below which the remaining porosity is disconnected and does not contribute to the flow (Mavko and Nur, 1997; Bentz et al., 1999; Mavko et al., 2009). The effect of percolation porosity can be incorporated into the Kozeny-Carman relationship shown in equation 3.11 by replacing ϕ by $(\phi - \phi_c)$. We also use $B = K_o \tau^2$ and hence, equation 3.11 becomes:

$$k = \frac{(\phi - \phi_c)^3 d^2}{36 B (1 - \phi - \phi_c)^2} , \quad (3.12)$$

For granular media with mixed grain sizes (poor sorting), Rumpf and Gupta (1971) and Dullien (1992) suggest that the effective grain diameter d to be used in equation 3.12, is given by:

$$\frac{1}{d} = \sum_i \frac{f_i}{d_i} , \quad (3.13)$$

where f_i is the volume fraction of the particle i with average diameter d_i . The average particle size is known for both micrite and grains as well as their solid volume fraction for samples along each dashed curve in Figure 3.7. Using equation 3.13, the corresponding average effective particle diameter can be calculated. The porosity-permeability relationship for samples with a certain micrite content can be represented by the Kozeny-Carman relation utilizing equation 3.12, for a given d (i.e., given micrite %) determined by equation 3.13. We then examined all possible values of B and ϕ_c in an effort to fit the data for samples with similar micrite content.

Figure 3.22 shows the possible ranges of the ϕ_c and B values used to reproduce the porosity-permeability relationships for samples characterized by similar micrite content as shown in Figure 3.23. The data in Figure 3.22 show that micrite-supported samples have larger percolation porosities, ϕ_c , but lower geometric factor, B , compared to grain-supported samples. The increase of percolation porosity with micrite content could be

hypothesized by the micrite likely reducing and blocking more pore throats, and adding more microporosity that does not contribute to the flow. Consequently, the amount of porosity that does not support the flow increases and hence, percolation porosity increases.

With regard to the geometric factor, Li and Gu (2005) report that it increases with the irregularity of the particle shape. The geometric factor values in micrite rich samples are similar to those obtained experimentally by Carman (1937) and Ergun (1952) for packed beds of spheres ($B= 4.8$ and 4.2 , respectively). Higher geometric factor values of 12.8 and 12.5 were obtained for more complex non-spherical materials including fibrous particles (Li and Gu, 2005) and Fontainebleau sandstone (Bourbie and Zinszner, 1985), respectively. The higher geometric factor exhibited by grain-supported samples suggests that grains have more irregular and complex particle shapes compared to micrite. Supporting this argument are the SEM images (Figures 2.1 and 2.2 in Chapter 2) showing that the grains have more irregular surfaces compared to the micrite particles. We also measured the surface area for both micrite and grains using the standard Brunauer-Emmett-Teller (BET) method (Brunauer et al., 1938) in order to quantify the complexity of the particles. The measurements were collected with the Accelerated Surface Area and Porosimetry System (ASAP 2020, Micromeritics Instrument Corp.) using nitrogen gas as the adsorbate. The surface area per gram for the grains was found to be $0.825 \text{ m}^2/\text{g}$ while for micrite it is equal $1.560 \text{ m}^2/\text{g}$. To quantitatively evaluate the sphericity of the grains, we calculated the ratio between the measured specific surface area per gram of grains and the theoretical surface area per gram of calcite spheres that have average diameter of $375 \text{ }\mu\text{m}$ (theoretical value= $3/\text{grain density} \times \text{particle radius}$). This ratio (measured/theoretical) was found to be 140 for the grains which indicates that they have very irregular and rough surfaces compared to that of spheres. On the other hand, the ratio is equal to 2.8 for micrite, considering calcite spheres of $4 \text{ }\mu\text{m}$ in diameter for the theoretical calculation. This suggests that micrite particles have more spherical and regular particle shape compared to the grains. The presence of irregular shaped-grains as well as micropores within the grains (Figure 2.1) can contribute to increasing the surface area of the grains and reducing their sphericity. Such low sphericity of the grains was then compensated by using very high B values to account for the reduction in permeability caused by having very irregular-shaped (high surface area) particles instead of spheres.

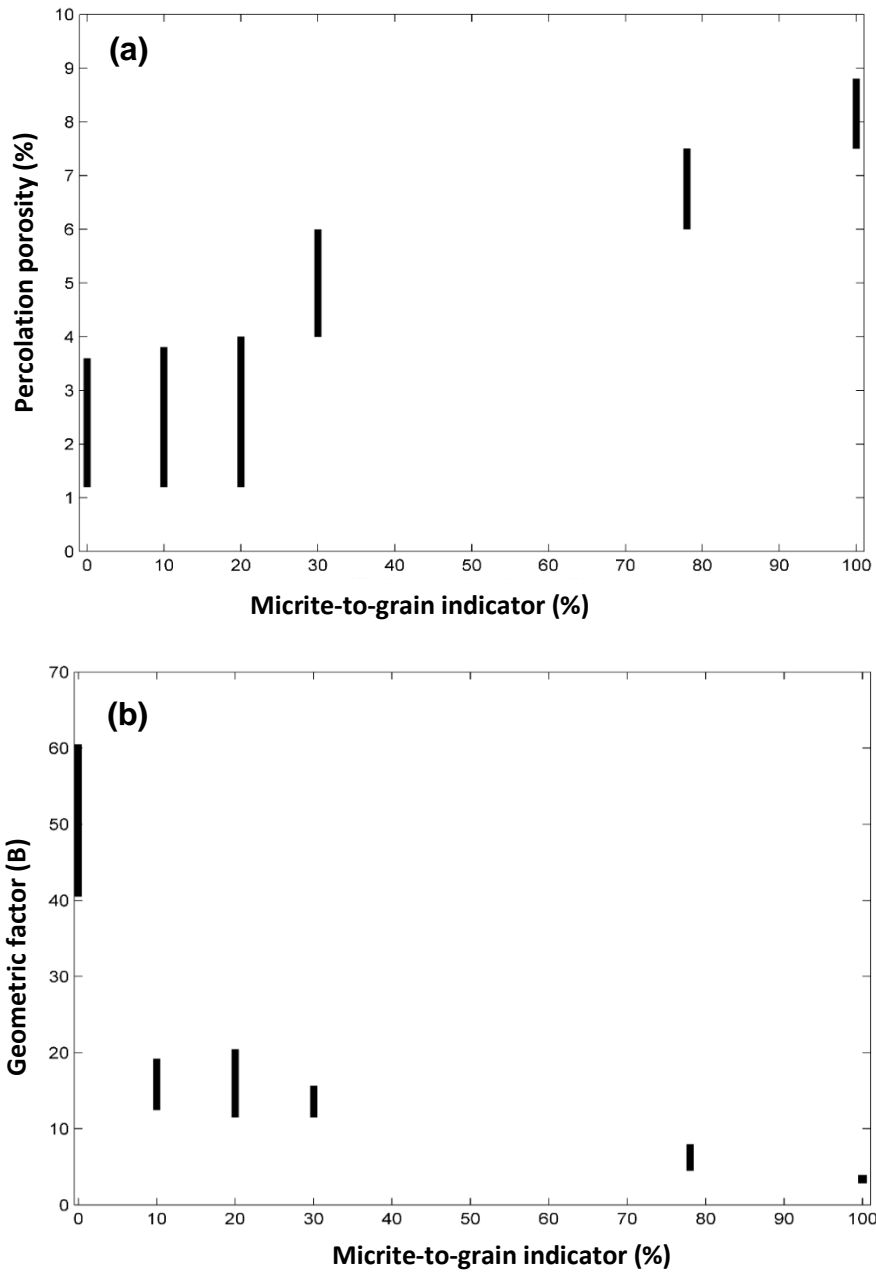


Figure 3.22: Percolation porosity (a) and geometric factor (b) as a function of micrite content. Each micrite percentage corresponds to one curve in Figure 3.23. The ranges of the percolation porosities and geometric factors cover all possible values that can fit data for samples with similar micrite content using equation 3.12.

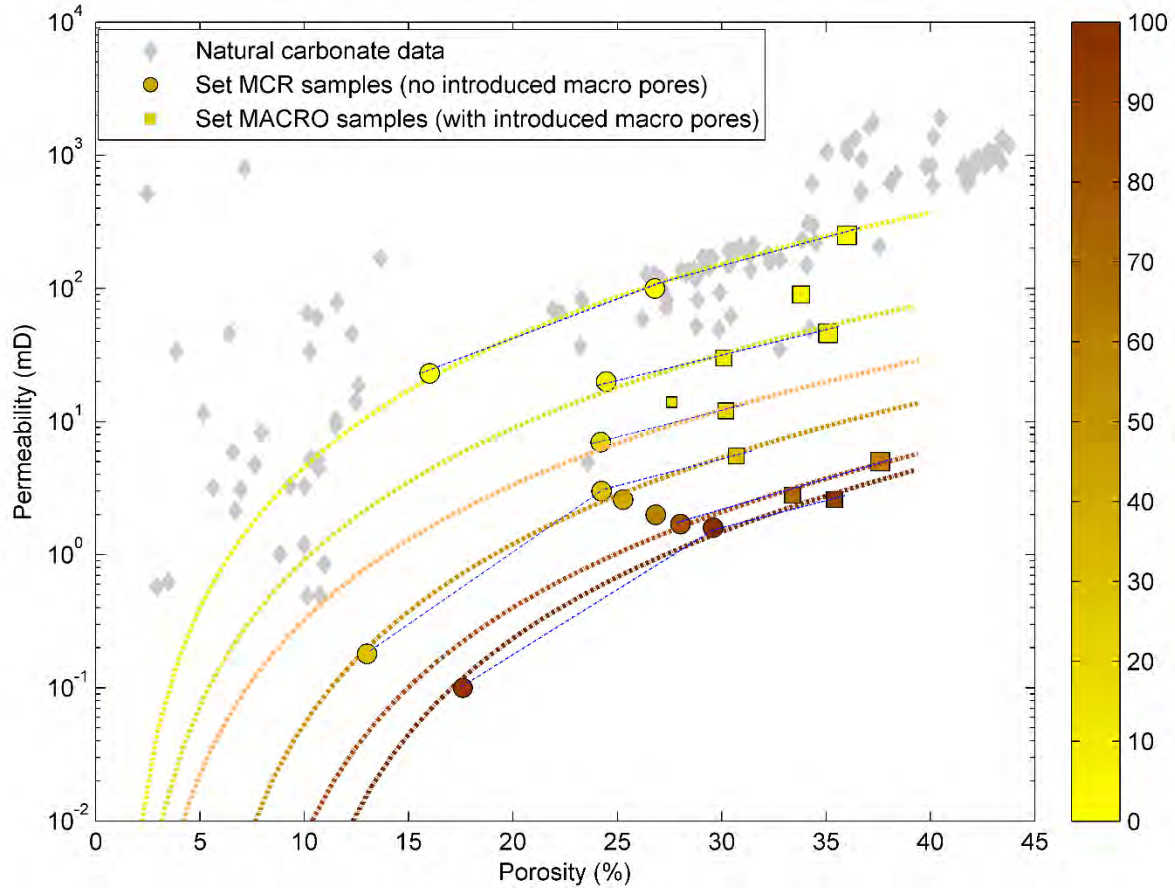


Figure 3.23: Permeability as a function of porosity for all analog samples along with blue dashed lines which connect data points for samples with similar micrite content. The superimposed dashed curves (yellow to brown color) correspond to the porosity-permeability relationship estimated using equation 3.12 by selecting one value of B and ϕ_c (from their ranges shown in Figure 3.22) for each curve.

3.4.3.2 The Effect of Varying both Micrite Content and Macroporosity on Permeability

Both permeability and porosity change drastically as macropores populate the sample structure at the expense of micrite (Figure 3.7). By examining the dependence of permeability on porosity when both micrite content and macroporosity vary, we notice that permeability increases exponentially with porosity (Figure 3.24). Data also show that the rate at which permeability increases with the addition of macropores decreases as the initial micrite content of the sample increases (Figures 3.7 and 3.24). That is, micrite-rich samples require a greater volume of macropores compared to grain-supported microstructures before being able to create the necessary increase in pore connectivity.

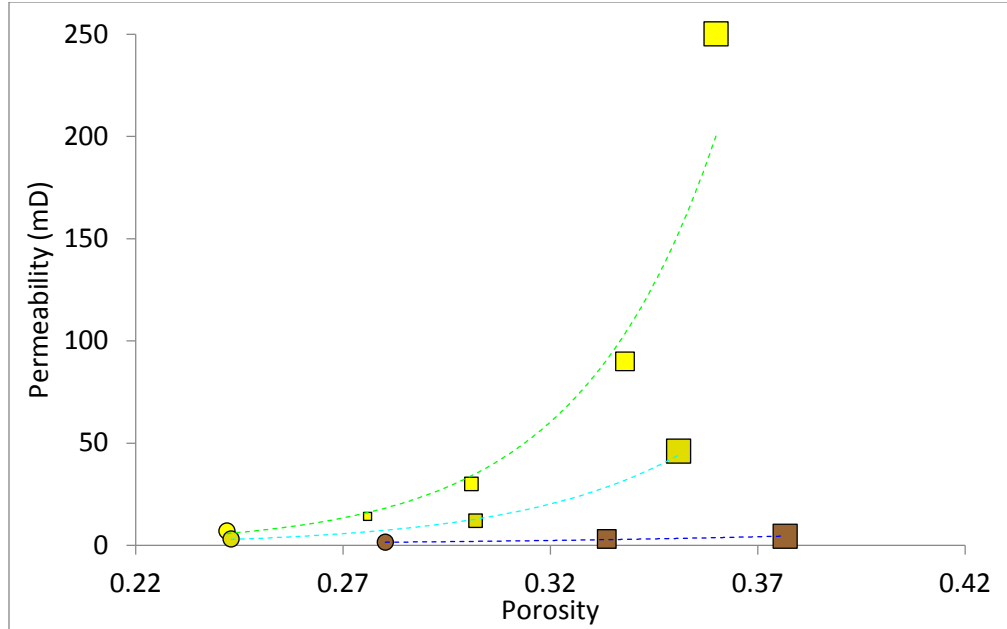


Figure 3.24: Permeability (linear scale) as a function of porosity for samples with increasing content of introduced macropores. The green, cyan, and blue dashed curves correspond to the exponential fitting of the data and they refer to the same trends highlighted by the same colors in Figure 3.7. The circle data points correspond to the micrite content of the original rocks (same as the ones highlighted by circles in Figure 3.7) before the addition of macropores.

The combined effect of varying the amount of micrite and induced macroporosity on permeability is demonstrated in Figure 3.25. The data in Figure 3.25 shows the permeability as a function of both micrite content and induced macroporosity. At a given micrite content, the permeability increases as the macroporosity increases, which can be hypothesized by the significant contribution of macropores to fluid flow due to their larger pore sizes compared to micropores (Lucia 1999, Vanorio and Mavko, 2011). On the other hand, permeability increases at a given macroporosity as the micrite content decreases (Figure 3.25). This is because the connectivity between the induced macropores is controlled by the size of the interparticle pore throats, which decreases as the micrite-to-grain ratio increases. The combined effect of increasing macroporosity while decreasing micrite content results in the highest permeability values (Figure 3.25). The equation relating permeability (k) in mD, to macroporosity (ϕ_{macro}) and micrite content ($f_{micrite}$) in percentages, is given by:

$$\log(k) = 3.617 - 0.105(f_{micrite}) + 0.1099 (\phi_{macro}) + 0.00066 (f_{micrite}^2) + 0.00056 (\phi)(f_{micrite}) \quad (3.14)$$

Using equation 3.14, the permeability can be estimated based on the content of micrite and macropores, where the coefficient of determination (R^2) is equal 0.78. On the other hand, the use of total porosity alone to predict permeability (i.e., best fit second degree polynomial) results in R^2 of 0.24 which is significantly lower than the R^2 obtained when using equation 3.14. This suggests that the knowledge about the content of micrite and macroporosity can be of significant importance for the modeling and interpretation of permeability in dual porosity carbonates.

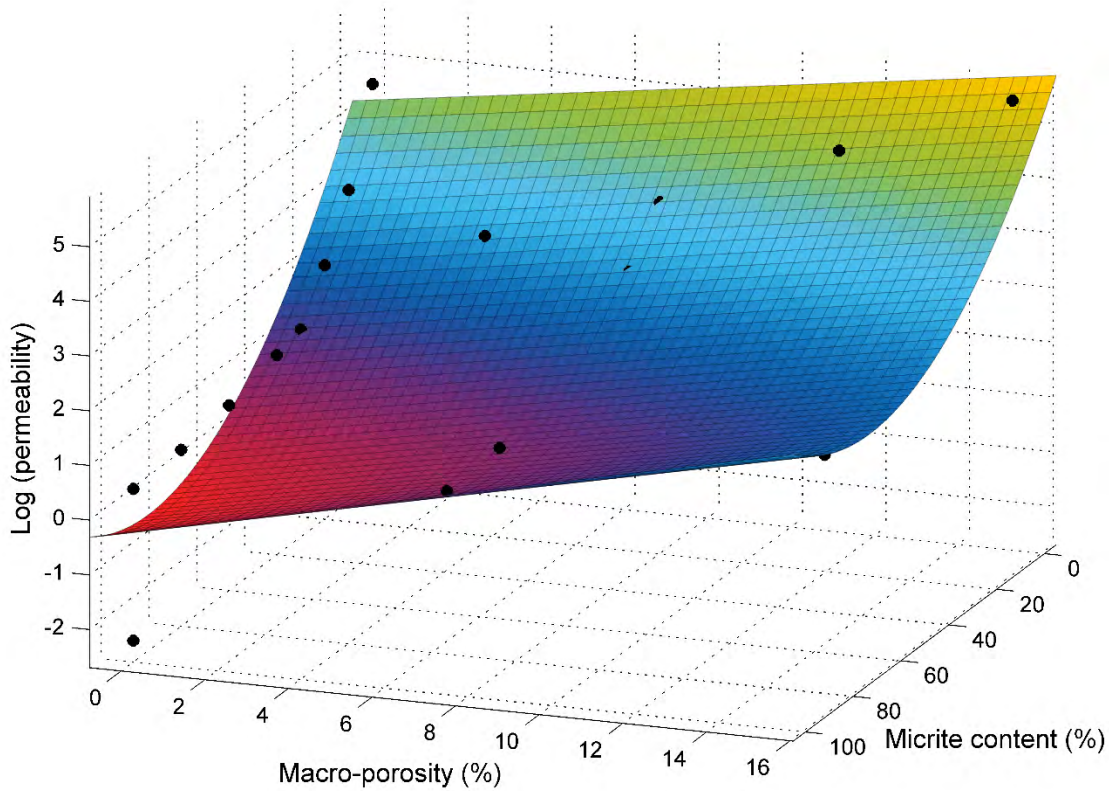


Figure 3.25: Permeability as function of both micrite content (micrite-to-grain indicator) and induced macroporosity. The surface corresponds to the best fit function (2x1 polynomial), as shown in equation 3.14, that relates the three variables. The coefficient of determination is equal to 0.78. The largest values of permeability (surface is colored in yellow) correspond to samples with largest macroporosity and smallest micrite content.

In natural carbonates, quantification of micrite content and macroporosity could be carried out using image analysis of thin section or CT scans. Estimating micrite content

can provide a quantitative approach for the classification of the different rock textures/types, while estimating macroporosity could be used to quantify the proportion of the pore system that contributes significantly to the fluid flow. In Chapter 5, we apply the workflow of this current study to natural carbonate rocks characterized by dual-particle-size and dual-porosity microstructures.

3.5 Conclusions

Carbonate rocks are commonly characterized by dual grain size and dual porosity, which lead to significant scatter in the porosity-permeability relationship. In this chapter, we investigated the effect of micrite content and macroporosity on the transport properties of analog samples characterized by variable content of micrite and macroporosity. Specifically, we used analog samples where micrite-to-grain ratio is the only parameter changing (set MCR) as well as samples characterized by macropores introduced into the structures at the expense of the micrite aggregates (set MACRO). We focused on two main functional relationships: the micrite-porosity and the porosity-permeability relationships.

The micrite-porosity relationship exhibited a characteristic v-shaped trend, which is typical of dual-particle-size mixtures. Adding micrite to analog samples exhibiting grain-supported microstructure reduced the porosity. By increasing the content of micrite up to 20-30%, the sample becomes micrite-supported, at which point adding more micrite increased the porosity. The v-shaped trend could be explained by a micro-geometrical model describing the change in the grain/micrite fabric as micrite was gradually added to the mixture. Specifically, we proposed an approach that successfully predicted the measured porosities of the grain-micrite mixture, utilizing a modified packing model for binary mixtures of spheres. Our analysis showed that knowledge about the specific surface area of the geological materials can be essential in understanding their packing behavior and predicting the porosity of their binary mixtures.

With regard to the porosity-permeability relationship, samples with high micrite content were found to have lower permeability at any given porosity. As macropores are introduced at the expense of micrite, permeability increased exponentially with porosity. The rate of permeability increase, however, was curbed by the initial micrite content of the samples, and decreased as the micrite content of the original microstructure increased. In

this study, we also showed an example of how micrite-to-coarse-grains ratio can be used as an input parameter to inform the modeling of the porosity-permeability relationship, using the Kozeny-Carman relation for a pack of spheres. Our analysis showed that as the content of micrite increases, it exerts a major influence on the porosity-permeability relation of carbonates by reducing the effective grain size while increasing the threshold of percolation porosity. One important finding is that the coefficient of determination (R^2) increased from 0.24 to 0.78 when permeability was empirically expressed as a function of both the micrite content and macroporosity, instead of the total porosity alone. We therefore concluded that estimating both micrite content and macroporosity could play a significant role in the interpretation and modeling of porosity-permeability relationships in dual-particle size, dual-porosity carbonates.

Chapter 4

THE EFFECT OF MICRITE CONTENT AND MACROPOROSITY ON THE ELASTIC PROPERTIES OF CARBONATE ANALOGS

Abstract

In this chapter we investigate the effect of micrite content and macroporosity on the elastic properties of carbonates using analog samples characterized by variable content of micrite and macroporosity. In particular, we examine: a) the effect of micrite content on the acoustic velocity and its sensitivity to pressure, b) the effect of introducing macroporosity at the expense of micrite on the acoustic velocity, and c) the effect of micrite content on the evolution of acoustic velocity upon interaction with a reactive fluid. Acoustic velocities are measured under bench-top conditions and as functions of confining pressure before and after the injection of a CO₂ aqueous solution.

The P- and S-wave velocity measured under bench-top conditions indicates that micrite aggregates make the frame of the samples stiffer. Acoustic velocities measured as a function of confining pressure show that the sensitivity of velocity to pressure decreases as the content of micrite increases. Thus, we hypothesize a stiffer pore structure in micrite-richer fabrics. This is supported by observations from SEM images, which show rounder pores in micrite-supported samples compared to grain-supported samples characterized by micro-cracks at grain contacts. Introducing macropores at the expense of micrite results in increasing the porosity and decreasing the acoustic velocity of the samples, due to the removal of a stiff component (i.e., micrite). Our results from the injection experiment suggest that the content of micrite affects the change in elastic moduli upon dissolution. Micrite-rich samples experience a larger drop in elastic moduli after fluid injection compared to grain-supported samples. This is interpreted as likely due to dissolution, which weakens the rock frame. This effect seems to overcome the elastic stiffening that results from dispersion mechanisms under high-frequency conditions used in the laboratory.

4.1 Introduction

The complexity of carbonates in terms of textures and pore structure creates significant scatter in fundamental rock physics relationships such as the velocity-porosity relationship (e.g., Eberli et al., 2003; Brigaud et al., 2010; Vanorio and Mavko, 2011). Consequently, the interpretation of elastic properties in carbonates presents several challenges and a number of open questions still persist.

Several studies in the literature have examined factors that contribute to the microstructural complexity of carbonates and their control on elastic properties. The main factors considered in literature include rock texture/fabric (i.e., from grainstones to mudstones), and pore structure (i.e., pore type and size). Some studies have reported qualitative trends in the relationships between porosity and velocity (e.g., Anselmetti and Eberli, 1993; Assefa et al., 2003; Brigaud et al., 2010; Regnet et al., 2015) for different carbonate rock textures, which were classified based on petrographic analysis of thin sections. Nevertheless, the qualitative analysis of the bulk texture of the rock seems not to be sufficient as a noticeable scatter in the data is still observed for a given rock texture (Lucia, 1995; Assefa et al., 2003; Brigaud et al., 2010, Teh et al., 2011; Regnet et al., 2015).

Other studies have investigated the effect of pore structures on the elastic properties of carbonates (Anselmetti and Eberli, 1993; Eberli et al., 2003; Assefa et al., 2003; Weger et al., 2009). The general approach was to classify samples based on the dominant pore type, including macromoldic porosity, intergranular porosity, and microporosity, and then to relate the pore type back to the elastic properties of the samples. Anselmetti and Eberli (1993) and Eberli et al. (2003) associated the scatter in the velocity data to pore type suggesting that intragranular pores (i.e., moldic and vuggy porosity) correlate with higher velocity values compared to intergranular pores. The analysis, however, remained mainly qualitative and inconclusive due to the presence of significant variability in the acoustic velocity of samples characterized by the same porosity and dominant pore type (Anselmetti and Eberli, 1993; Eberli et al., 2003; Ling et al., 2014). Following a more quantitative approach, Weger et al. (2009) used parameters derived from thin sections including the perimeter over area (PoA) and aspect ratio (α , the ratio between the smallest to largest dimensions of the pore) to describe the pore geometry. The authors investigated the correlations between those parameters and the acoustic velocity of carbonates. They observed that samples characterized by lower average pore PoA and higher α tend to have higher velocity at a given porosity. However, a scatter of a few km/s in the measured acoustic velocity could be observed for samples characterized by the same porosity and average PoA and α (Weger et al., 2009). This suggests that PoA and α are not appropriate/sufficient descriptors of pore space and that they may not fully explain the scatter in the velocity-porosity relationship. PoA and α are simplistic mathematical representations of the pore space rather than sedimentology-related rock descriptors, thus they cannot be related to the depositional environment and rock texture.

The literature review presented here suggests the need for quantifiable sedimentology-related parameters that can describe both the rock texture and the pore structure. These, in turn, can be used to inform the modeling of the elastic properties in carbonates. One of the parameters that relates to the depositional environment determining the carbonate texture is the fractional amount of micrite (Folk, 1962; Dunham, 1962; Tucker and Wright, 1990). Leighton and Pendexter (1962) suggested that the determination of the micrite-to-coarse-grain ratio in carbonates has value for their textural classification. The fraction of micrite also determines the microstructural arrangement of the rock, i.e., matrix-supported or

grain-supported (Lambert et al., 2006; Vanorio and Mavko, 2011). Besides microcracks, the fine micritic particles are largely responsible for the microporosity in carbonates (Cantrell and Hagerty, 1999; Vanorio and Mavko, 2011), which leads to extremely low rock permeabilities upon compaction (Lucia, 1999; Mallon et al., 2005). The documented effect of micrite on transport properties (Cantrell and Hagerty, 1999; Lucia, 1999; Mallon et al., 2005), rock texture (Dunham, 1962; Leighton and Pendexter, 1962), and microstructural arrangement of the rock (Lambert et al., 2006; Vanorio and Mavko, 2011) suggests a strong link between micrite content, the sedimentological processes controlling it, and the elastic properties of carbonates. Nevertheless, a systematic study documenting a quantitative cause-effect relationship between micrite content and elastic properties does not exist. Additionally, there is contradiction in the conclusions reached by different researchers with regard to modeling the effect of micrite aggregates on elastic properties of carbonate. When modeling the acoustic velocities, Fournier et al. (2011) treated the microporous micritized materials in well-cemented carbonates as the “less stiff component.” Conversely, micrite aggregates were modeled as the “stiffer component” compared to grain aggregates as suggested by Vanorio and Mavko (2011). The latter study also showed that low micrite content, which may result from natural leaching, increases porosity and reduces rock bulk and shear modulus.

While the micrite-to-grain ratio can be used as a quantifiable parameter to describe rock texture, the macro-to-microporosity ratio is a sedimentology-related parameter that can be used to describe the relative pore sizes in carbonates. Since variations in the micrite-to-coarse-grain ratio control particle-size distribution (i.e., sorting), this ratio also affects the pore size distribution (Arya and Paris, 1981; Nimmo et al., 2007), and hence, the macro-to-microporosity ratio. The fraction of macroporosity might also be indirectly related to the micrite content since secondary macropores can be formed at the expense of micrite, which is prone to diagenetic processes due to its high surface area (Vanorio and Mavko, 2011). Processes affecting micrite, such as leaching and dissolution, are very common in nature (i.e., metadiagenesis), changing the original pore network and microstructure (Tucker and Bathurst, 1990; Tucker and Wright, 1990; Vanorio and Mavko, 2011). There is disagreement in literature about the effect of the macro-to-microporosity ratio on the elastic properties of carbonates. While Eberli et al. (2003) and Weger et al. (2009) suggested that

the percentage of macropores, obtained from quantitative digital image analysis of thin sections, correlates with an increasing velocity, Brigaud et al. (2010) reported velocities being higher in microporous mudstones/wackestones with respect to macroporous grainstones characterized by the same porosity. On the other hand, Vanorio and Mavko (2011) pointed out that pore size carries no information about pore shape — i.e., microporosity does not necessarily imply elastic compliance or *vice versa*. It is also worth mentioning that the traditional approach used in literature to quantify the content of micrite, macro-, and microporosity is based on the image analysis of thin sections (e.g., Weger et al., 2009; Fournier et al. 2011) or CT scan images (Vanorio and Mavko, 2011). This also raises the question of how the error/uncertainty associated with estimating these parameters from thin sections or CT scans affects the results and conclusions of the studies mentioned earlier.

Lastly, the fine particle texture of micrite aggregates leads to microporous patches of microcrystalline matrix characterized by high-surface area, affecting the fluid-rock interaction. Some studies (Vanorio et al., 2008; Vega et al., 2010; Vialle and Vanorio, 2011; Vanorio et al., 2011) have indicated that the presence of fluid-rock chemical interactions is responsible for changing the elastic properties of the carbonate frame upon saturation. Such changes in elastic properties of the frame upon injections or fluid saturation violate some of the assumptions of fluid substitution models such as Gassmann's equations (Gassmann, 1951). In particular, the shear modulus has been reported to change with fluid saturation which contradicts Gassmann's prediction of constant shear modulus upon saturation, i.e., the effective shear modulus of a porous system depends on the shear modulus of the solid alone, being unaffected by the fluid (Baechle et al., 2005; Adam et al., 2006). The presence of micrite can control reactivity and dissolution-driven compaction of carbonates, which, in turn, can influence the evolution of acoustic velocities upon exposure to reactive fluids (Vanorio et al., 2011; Vanorio et al., 2015). Nevertheless, the role of micrite in controlling the fluid-rock interaction and the resultant changes in elastic properties has not been systematically investigated.

The work presented in this chapter has been motivated by the absence of a systematic study investigating the effect of quantifiable sedimentology-related parameters such as micrite content and macroporosity on the elastic properties of carbonates. Thus, in this

chapter we investigate the effect of these parameters on the elastic properties using analog samples with controlled microstructure (set MCR and MACRO samples). By using analog samples, we obtain samples characterized by well-quantified micrite content and macroporosity whose effect on elastic properties can be investigated one at a time. Our primary objective is to investigate: (1) the effect of micrite content on acoustic velocity and its sensitivity to pressure, (2) the effect of introducing macroporosity at the expense of micrite on the acoustic velocity, and (3) the effect of micrite on velocity changes due to interaction with reactive fluid.

4.2 Methodology

In order to investigate the effect of micrite content on the elastic properties, we used the analog samples from set MCR, characterized by varying micrite content as shown earlier in Chapter 2. The acoustic velocities were measured under bench-top conditions and as a function of confining pressure. The details of the approach used to obtain the different measurements were given in Chapter 2. We also measured the bench-top acoustic velocity for six samples from set MACRO characterized by variable content of macroporosity induced at the expense of micrite. This was done to examine how the removal of micrite by introducing macroporosity affects the acoustic velocity. In order to examine the effect of micrite on the fluid-rock interaction and the resulting changes in acoustic velocity, we measured the acoustic velocity as a function of confining pressure after injecting a CO₂ aqueous solution, and then drying the samples.

4.3 Results and Discussion

4.3.1 Micrite Effect on Dry Acoustic Velocities and Their Sensitivity to Pressure

Table H.1 (Appendix H) summarizes the elastic properties for the dry samples of set MCR. Figure 4.1 shows the bench-top measured acoustic velocities as a function of micrite content for this set of samples. Data show that both P- and S-wave velocities of the samples increase with increasing micrite content. Figure 4.2 reports the variation of P- and S-wave velocities, normalized by velocity measured at 1 MPa as functions of confining pressure. Data clearly show that the velocity in the samples with a larger proportion of coarse grains

appears to be much more sensitive to pressure than in the more micrite-rich samples. A similar trend was observed for the normalized bulk and shear moduli as a function of confining pressure (Figure 4.3). The change in length normalized by sample length (i.e., strain) is shown in Figure 4.4, which indicates that grain-supported samples experienced larger length changes compared to micrite-supported samples.

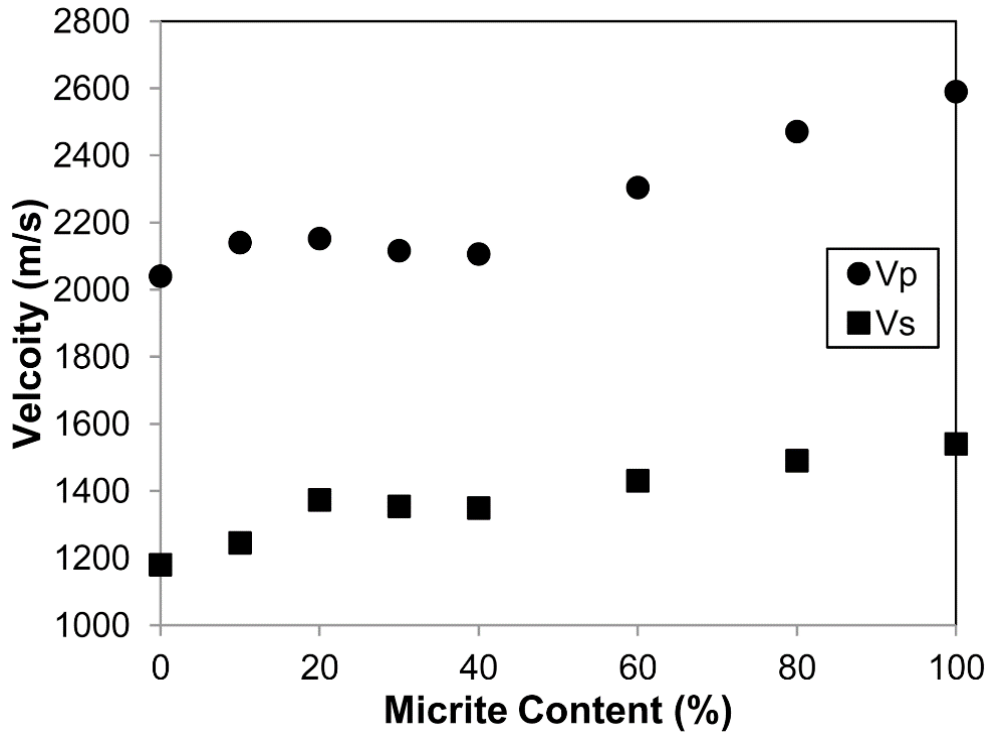


Figure 4.1: P- and S-wave bench-top velocities as a function of micrite content for set MCR samples. Measurements are done under dry conditions.

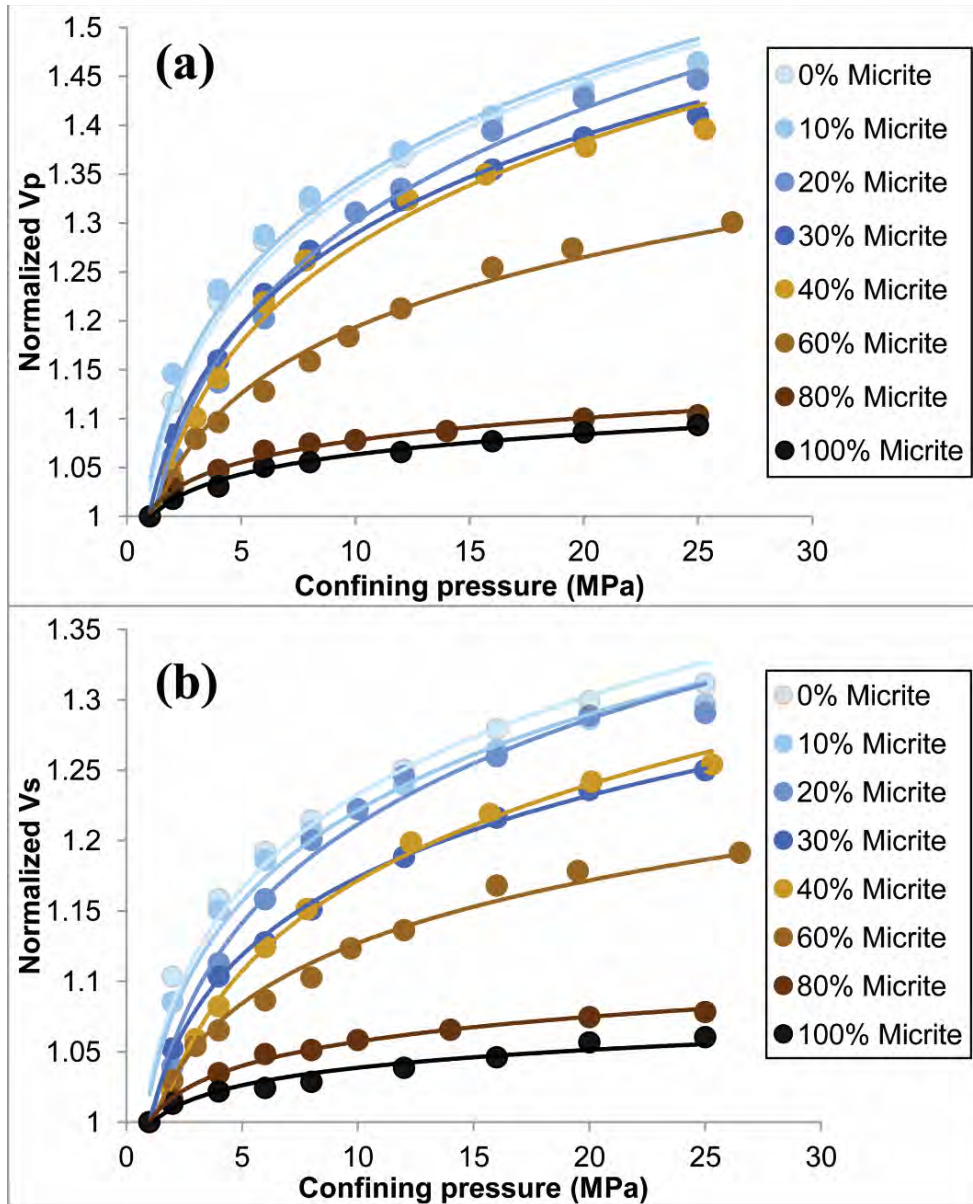


Figure 4.2: Plot of (a) P-wave velocity and (b) S-wave velocity of set MCR samples, both normalized by velocity at 1 MPa, as a function of confining pressure. Data are color coded by micrite content. The data points for each micrite content were fitted by a best-fit power function.

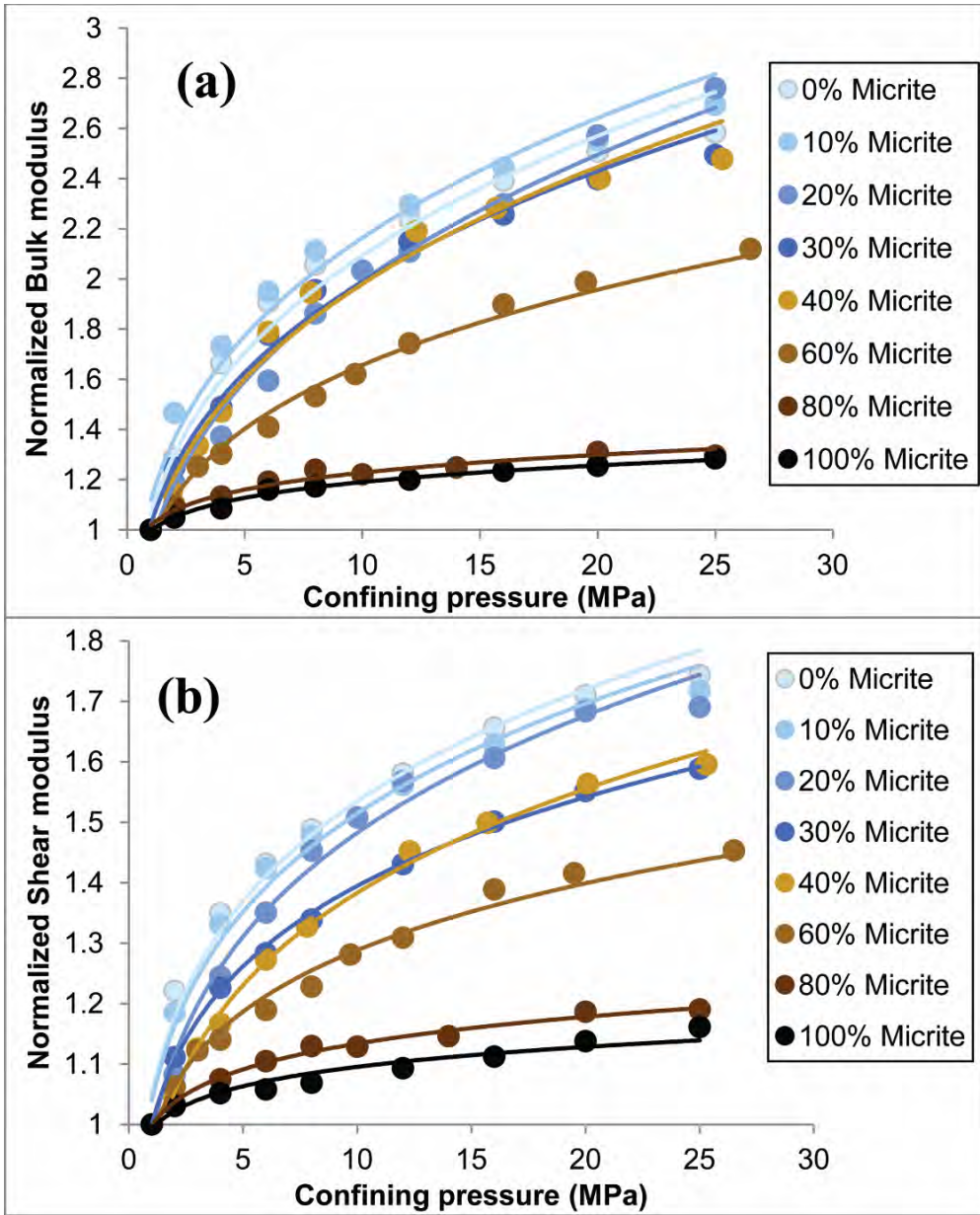


Figure 4.3: Plot of (a) bulk modulus and (b) shear modulus of set MCR samples, both normalized by modulus at 1 MPa, as a function of confining pressure. Data are color coded by micrite content. The data points for each micrite content were fitted by a best-fit power function.

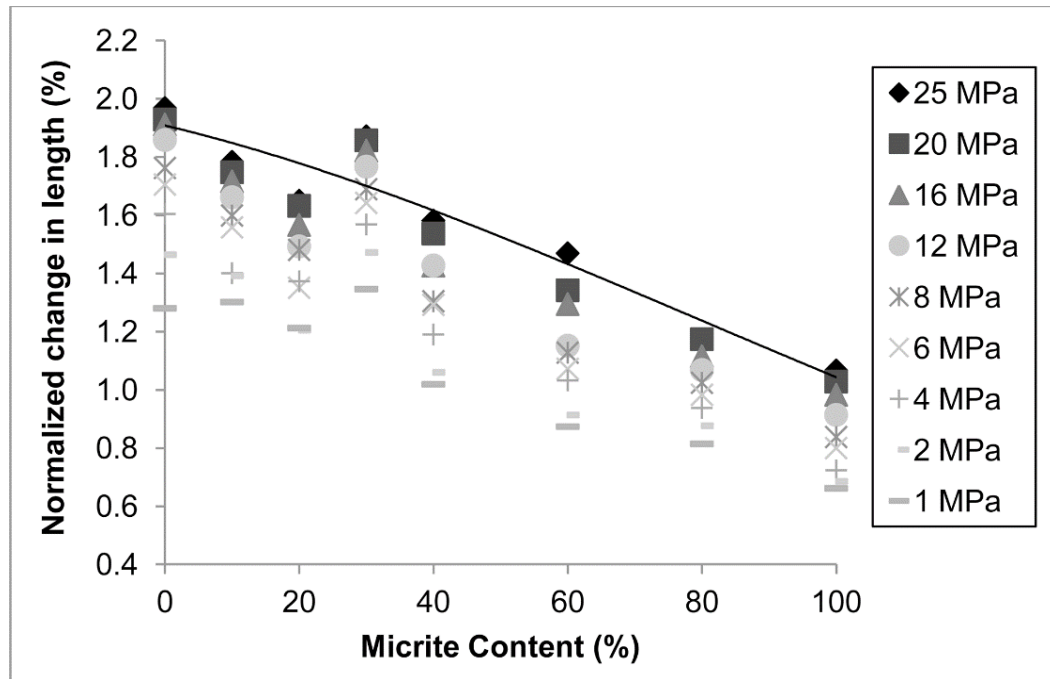


Figure 4.4: Normalized percentage change in length ($100 \times \text{change in length} / \text{sample length}$) as a function of micrite content measured at different pressures. The solid curve refers to the polynomial fit for the data at 25 MPa.

We notice from the measurements of bench-top velocities (Figure 4.1) that micrite-rich samples are stiffer than the grain-supported samples although micrite-rich samples have higher porosity (Table H.1). This suggests that porosity alone cannot explain the trends seen in Figure 4.1. Therefore, an additional factor is intervening to overcome the effect of porosity on velocity, making the samples characterized by high micrite content stiffer than others with lower micrite content. Since the sensitivity of velocity to pressure decreases as the micrite content increases (Figures 4.2 and 4.3), we hypothesize a stiffer pore structure in micrite-rich samples. The small variation in P- and S-wave velocities with confining pressure in the 100% micrite sample indicates that the sample is stiff, with very few compliant pores. Conversely, as the micrite content decreases, the sensitivity of velocity to pressure increases suggesting that grain-supported samples have more compliant pores that close with pressure, increasing the acoustic velocity. This hypothesis is supported by the strain that was experienced by the samples under increasing confining pressure, as the grain-supported samples suffered from larger decrease in length (Figure 4.4), i.e., larger closure of soft pores. Supporting the same argument, a close examination of the SEM images of the samples shows that the intercrystalline micropores within the micrite

aggregates (Figure 4.5a) are rounder, and hence stiffer, compared to the pores characterizing grain-richer microstructures (Figure 4.5b). The micro-crack-type pores at the coarse grain contacts contribute to a larger sensitivity of velocity to pressure in the grain-supported samples. Contrary to what is reported in the literature suggesting that micropores make the rock more compliant (Weger et al., 2009), microporosity in carbonates can make the rock either compliant (Figure 4.5b) or stiffer (Figure 4.5a) depending on the type of microporosity. The observations from Weger et al. (2009) are likely correct as they refer mainly to microcracks, but generalization to all types of microporosity should be avoided. This result highlights the importance of reporting both size and type of porosity (i.e., micro-cracks within grain aggregates versus micropores within micrite aggregates) when discussing the effect of pore structure on the elastic properties of carbonate rocks.

The irregularity and low sphericity of the coarse grains (as shown in Chapter 3) might explain the presence of more compliant pores in grain aggregates, compared to micrite aggregates. According to Santamrina et al. (2001) and Cho et al. (2006), the acoustic velocity decreases while its sensitivity to pressure increases as the sphericity and regularity of the particles decreases. Two coexisting effects were given as explanations for such a trend: (a) irregularity promotes looser packing and lower number of contact points between particles (i.e., lower coordination number) (Cho et al., 2006), and (b) contacts between irregular particles tend to be more deformable under confining pressure compared to more regular and spherical particles (Goddard 1990; Cho et al., 2006). In this case, the likelihood of forming micro-cracks between grain contacts increases as the micrite content decreases.

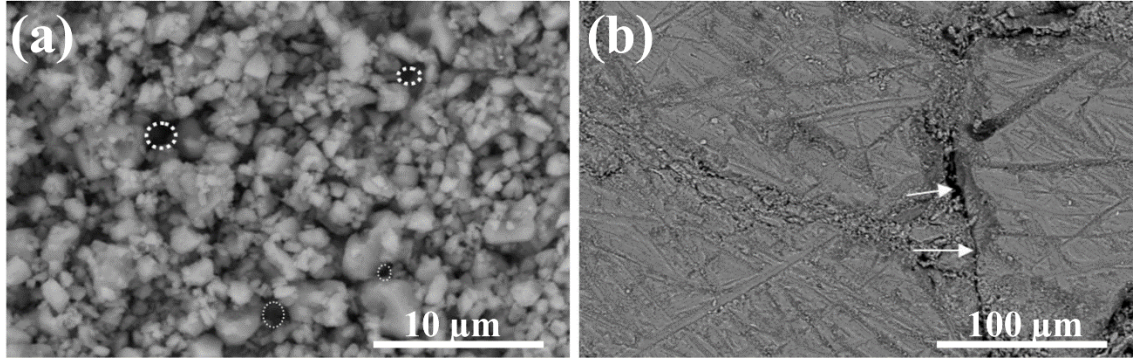


Figure 4.5: SEM images of (a) 100% micrite sample where the dashed circles show round to sub-rounded pores in the micrite aggregate, and (b) 0% micrite (100% grains) sample where the arrows highlight the crack-like pores between the grains.

4.3.2 Modeling the Changes in Pore Shape as a Function of Micrite Content

Since both micrite particles and grains have the same mineralogy, any variation in the acoustic velocity of the analog samples depends on the fraction of pores (i.e., porosity) and their shape. As pointed out earlier, the SEM images as well as the higher acoustic velocities and the lower sensitivity of velocity to pressure in the micrite-rich samples (despite their higher porosity) indicate that they have stiffer pore structure, compared to grain-supported samples. We used the differential effective medium (DEM) model to test the hypothesis that micrite aggregates make the rock stiffer due to their stiffer pore structure compared to aggregates of grains. In the DEM theory, the elastic moduli of two-phase composites are modeled by adding infinitesimal quantities of inclusions to a host phase (Norris, 1985). The DEM model solves a coupled system of equations as shown in Appendix I, where the elastic moduli are functions of the fraction of the inclusions and their aspect ratio, α , defined as the ratio between the smallest to largest dimensions of the inclusion. The relative changes in the aspect ratio of the pores can be used to describe variations in the pore shape (and hence stiffness) as micrite content changes: The higher the aspect ratio, the higher the stiffness of the pores. We utilized the DEM theory to estimate the average aspect ratios of the pores in the analog samples from set MCR and we then examined their variations with micrite content. Each sample could be represented by a two-phase composite where the host material is calcite mineral ($K_{calcite} = 71$ GPa and $G_{calcite} = 32$ GPa for the calcite bulk and shear moduli respectively), while pores are the inclusions as demonstrated in Figure 4.6. The measured P- and S-wave velocities and bulk density were used to calculate the

effective bulk (K) and shear (G) moduli of the composite for each sample. The fraction of the pore inclusions is equal to the measured porosity of the sample. We then used the DEM model to invert for the aspect ratio of the pores that would reproduce the measured effective K and G of the sample. Figure 4.7 shows the estimated average aspect ratio as a function of the micrite content for the analogs. Our analysis shows that the micrite-rich samples are characterized by higher aspect ratio (i.e., stiffer pores) compared to grain-supported samples (Figure 4.7). This is consistent with our hypothesis regarding the stiffer pore structure in micrite-rich samples as well as with the velocity sensitivity to pressure data (Figure 4.2).

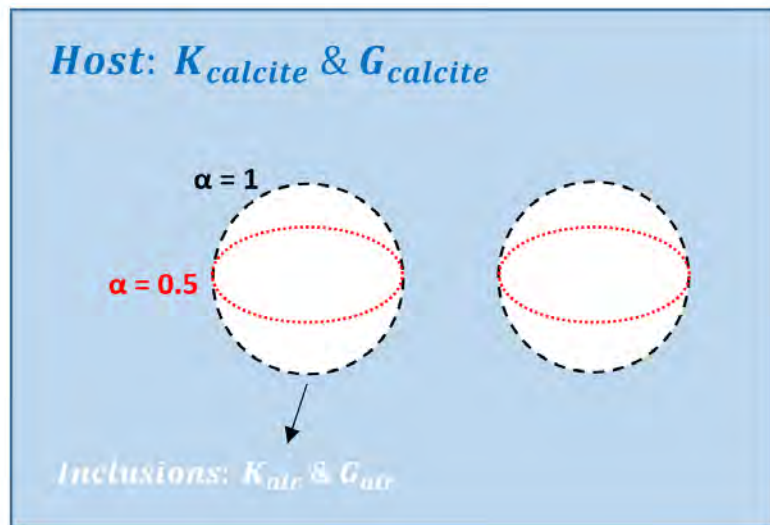


Figure 4.6: Schematic showing the conceptual model used to estimate the average aspect ratio, α , of the pores within samples. Since both micrite and grains have calcite mineralogy, the host (blue color) can be represented by calcite mineral while the inclusions are pores (white) whose fraction is known from the measured porosity of the sample. The DEM model is then used to invert for the suitable α which would reproduce the measured elastic properties of the sample. The dashed black and red ellipsoids refer to pores with different α values for demonstration.

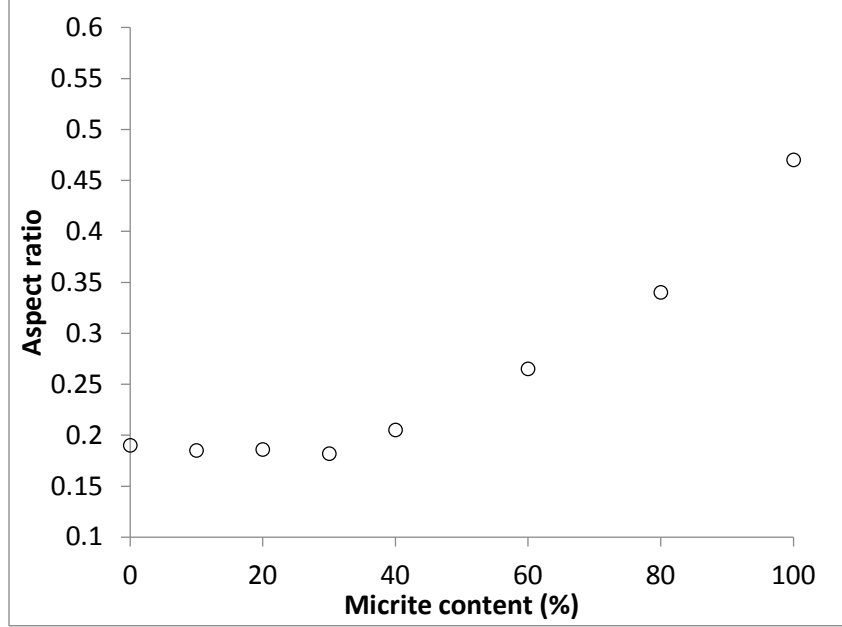


Figure 4.7: Plot of the estimated aspect ratio using the DEM model as a function of micrite content of the analog samples from set MCR. Samples characterized by higher micrite content have higher aspect ratio indicating stiffer pore structure compared to grain-supported samples.

4.3.3 Modeling the Relationship between Micrite Content and Acoustic Velocities

In this section, we attempt to model the relationship between micrite content and acoustic velocities shown in Figure 4.1. We utilized three different approaches (mixing rules) to model the acoustic velocities of the micrite-grain mixtures including: Reuss average, Voigt average, and DEM model. In each approach, the micrite-aggregates and grain-aggregates are treated as two distinct composites whose moduli are calculated based on the measured elastic properties of the pure micrite (stiffer component) and pure grain (less stiff component) samples. Based on the properties of these two end-members, we then attempt to reproduce the trends observed in Figure 4.1 for the analog samples characterized by varying micrite-to-grain- ratios. The Reuss average for the bulk (K) and shear modulus (G) of the analog samples can be calculated using the following equations (Reuss, 1929):

$$\frac{1}{K} = \frac{f_{micrite}}{K_{micrite}} + \frac{1 - f_{micrite}}{K_{grains}} \quad (4.1)$$

$$\frac{1}{G} = \frac{f_{micrite}}{G_{micrite}} + \frac{1 - f_{micrite}}{G_{grains}} \quad (4.2)$$

where $f_{micrite}$ is the fraction of micrite and $K_{micrite}$ and K_{grains} are the bulk modulus of the pure micrite and pure grains samples, respectively. The moduli of these two end-members were calculated based on the measured P- and S-wave velocities as well as the bulk density of the pure grains and micrite samples. The Ruess average provides a lower bound for the estimated moduli (Ruess, 1929; Mavko et al., 2009). On the other hand, the Voigt average is considered an upper bound where the moduli can be estimated using the relations (Mavko et al., 2009):

$$K = (f_{micrite}) K_{micrite} + (1 - f_{micrite})K_{grains} \quad (4.3)$$

$$G = (f_{micrite}) G_{micrite} + (1 - f_{micrite})G_{grains} \quad (4.4)$$

Figure 4.8 demonstrates the conceptual model utilized to calculate the elastic moduli using the DEM approach. The properties of the inclusion and host phase are determined based on the microstructural arrangement (grain-supported versus micrite-supported) of the samples. For grain-supported samples, micrite-aggregates were treated as spherical inclusions in grain-aggregate hosts (Figure 4.8a). In contrast, grain-aggregates were considered dispersed inclusions in micrite-aggregate hosts, when samples were characterized by micrite-supported textures (Figure 4.8b). The inclusions were assumed to have an aspect ratio of one ($\alpha=1$) for both cases while the bulk and shear moduli of the grain- and micrite-aggregates were obtained based on the measured properties of the end-members as mentioned earlier. The fraction of the inclusions is determined based on the micrite-to-grain ratio of the mixtures.

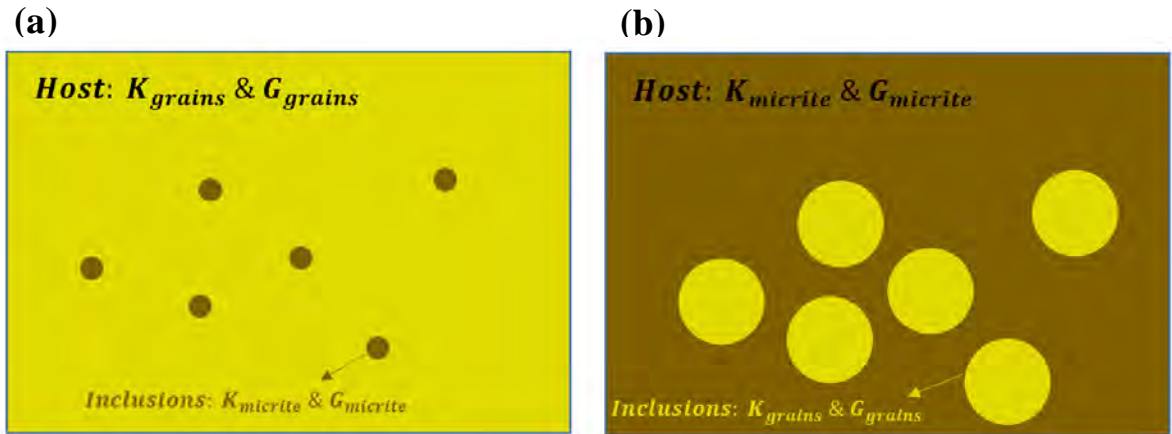


Figure 4.8: Schematic showing the conceptual model describing the inclusion and host material when using DEM to predict elastic moduli of the (a) grains-supported samples, and (b) micrite-supported samples. The host is represented by the background while the inclusions are shown in circles ($\alpha=1$). Yellow is used to refer to aggregates of grains, while brown corresponds to the micrite aggregates. The bulk and shear moduli of each aggregate are obtained based on the measured properties of the end-member samples. The fraction of inclusion changes as the micrite-to-grain ratio of the mixture changes.

The three different models (Reuss, Voigt, and DEM) shown here calculate the bulk and shear moduli for the analog mixtures, while the corresponding P- and S-wave velocities are calculated based on the following relations:

$$V_p = \sqrt{\frac{K + \left(\frac{4}{3}G\right)}{\rho}} \quad (4.5)$$

$$V_s = \sqrt{\frac{G}{\rho}} \quad (4.6)$$

The bulk density, ρ , in the previous relations is obtained using the following equation:

$$\rho = \phi \rho_{air} + (1 - \phi)\rho_{calcite} \quad (4.7)$$

where the density of air (ρ_{air}) and density of calcite ($\rho_{calcite}$) are equal to 1.2 and 2700 Kg/m³, respectively (Mavko et al., 2006). The porosity (ϕ) of the analog samples, corresponding to a certain micrite content, was obtained using the modified packing model for binary mixtures as shown in Chapter 3 (equations 3.1 to 3.5). The use of the modified packing model provides the porosity of the samples as a function of micrite content, which allowed the modeled acoustic velocities to be plotted as a function of both micrite content

and porosity. Based on the discussion shown here, the only required inputs to predict the acoustic velocities as a function of micrite content or porosity, include the measured porosity, bulk density, and acoustic velocity of the end-members. Figure 4.9 shows the modeling results for the velocity-micrite and velocity-porosity relationships. The data show that our modeling approach was successful in reproducing the overall trends observed in the velocity-micrite and velocity-porosity relationships. The DEM predictions show intermediate values between the upper (Voigt) and lower (Ruess) bounds, while the difference between the three models is not significant (Figure 4.9). The velocity-porosity relationship exhibits a two-segment trend where micrite-supported samples tend to have higher acoustic velocities at a given porosity.

From the modeling results shown in Figure 4.9, we also notice that the acoustic velocities in some samples are not within the upper and lower bounds (especially for samples characterized by 10-30% micrite). This is physically not possible assuming that the end members maintain their properties in the mixtures compared to end-members. However, the general under estimation of the models suggest that the elastic properties of the grains or micrite has increased in the mixture compared to the end member sample. One possible explanation is that the stiffness of the grain aggregates increased as micrite was added to the sample. This could be due to the effect of micrite in reducing the amount of micro-cracks between the within grains as mentioned earlier (Goddard 1990; Cho et al., 2006).

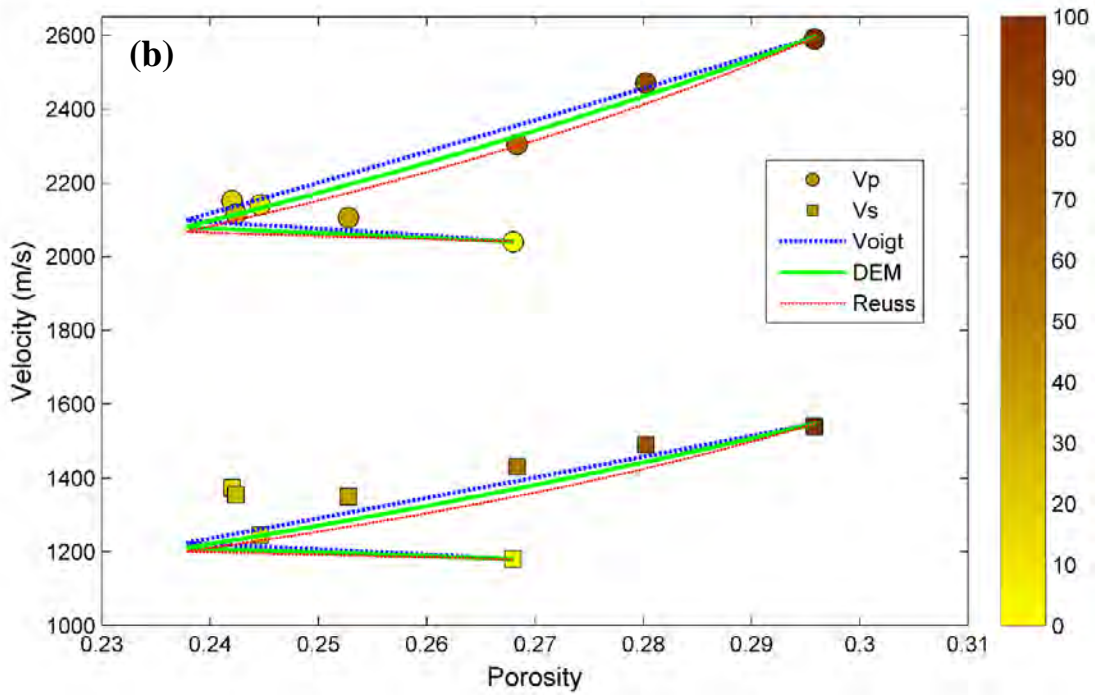
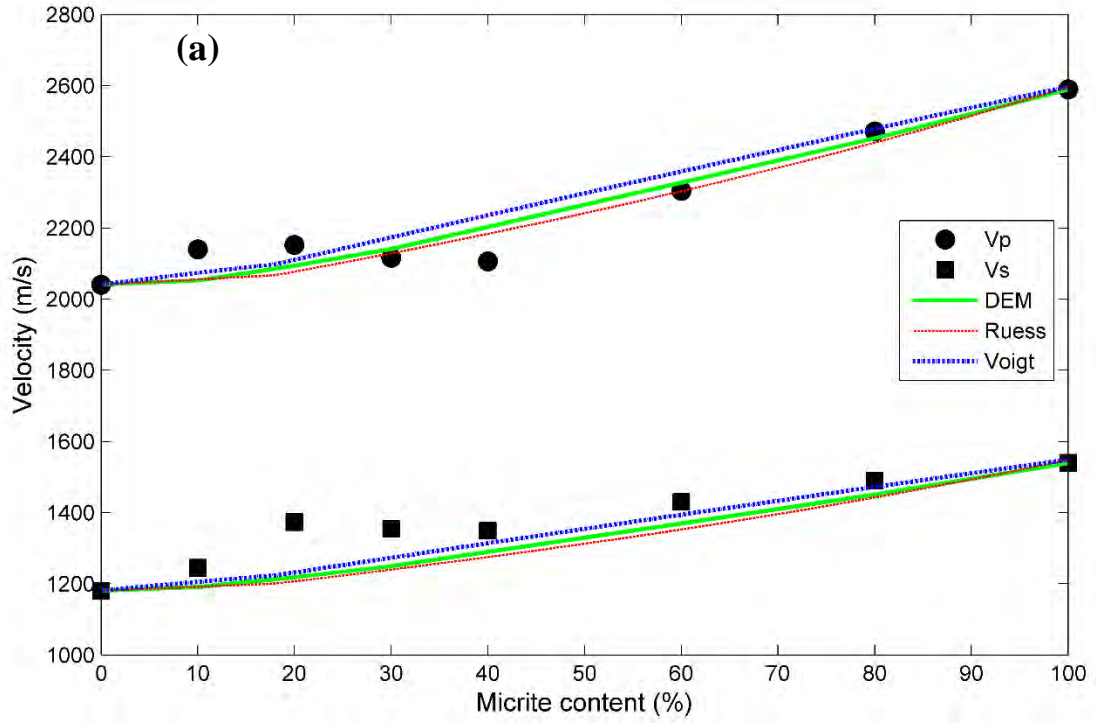


Figure 4.9: Demonstration of the modeling results for (a) velocity-micrite, and (b) velocity-porosity relationships. DEM predictions (green) plot between the Reuss (red) and Voigt (blue) bounds. Data points in the velocity-porosity relationship are color coded by micrite content. Note that micrite-supported samples, represented by the upper segment of the trend in (b), tend to have higher acoustic velocities, compared to grain supported samples, at a given porosity.

4.3.4 Effect of Macroporosity on Acoustic Velocities

The bench-top acoustic velocities measured on samples from set MACRO are reported in Table H.2 (Appendix H). Figure 4.10 shows the bench-top P- and S-wave velocities as a function of effective porosity (measured by helium porosimeter) for both set MCR and set MACRO samples. The data is color coded by micrite content while the size of the data points is proportional to the amount of macropores. The arrows highlight the change in acoustic velocity as the macropores were introduced at the expense of micrite. Data shows that adding macropores at the expense of micrite increases porosity and decreases acoustic velocity (Figure 4.10). The reduction in the acoustic velocity can be explained by the removal of micrite which is the stiff component in the samples as mentioned earlier. The results shown here are consistent with those reported by Vanorio and Mavko (2011).

Comparing the acoustic velocity of samples characterized by similar effective porosity, we observe that samples with higher macroporosity have lower acoustic velocity (Figure 4.10), despite the sub-rounded shape of the introduced macropores (as shown in Chapter 3). This is because those samples with higher fraction of macropores are also characterized by low micrite content (i.e., grain-supported samples). Microstructures characterized by a large amount of macropores but low micrite content can still have a considerable amount of micro-cracks (or low aspect ratio pores) especially at grain contact, as shown in Figure 4.11. This can lower the overall stiffness in the grain-supported samples compared to the micrite-supported samples, despite the higher content of sub-rounded macro-pores in the grain-supported samples. The results shown in Figure 4.10 indicate that the larger fraction of macropores may not necessarily correlate with higher acoustic velocity at a given porosity, contrary to what is suggested in the literature (e.g., Eberli et al., 2003; Weger et al., 2009). The positive correlation between macroporosity and acoustic velocity at a given porosity may hold true only if: a) macropores are rounded/sub-rounded, and b) other controlling factors such as fracture and micrite content are not changing.

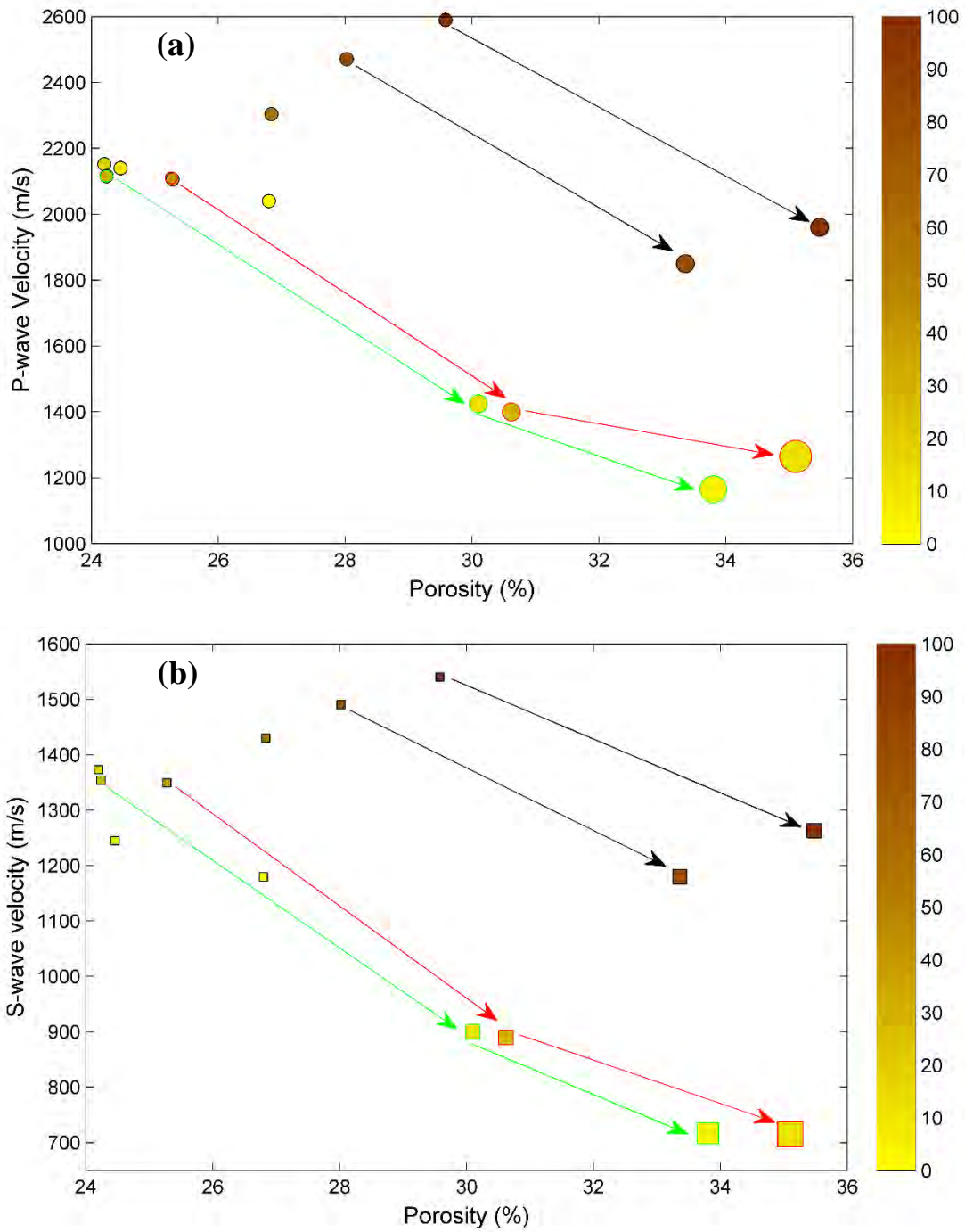


Figure 4.10: P-wave (a) and S-wave (b) bench-top velocity as a function of porosity for set MACRO samples (large symbols that have porosities larger than 30%), along with data for set MCR (smaller symbols at the upper left corner). Data points are color coded by micrite content while the size of the symbol is proportional to the content of macroporosity. The arrows highlight the change of acoustic velocity and porosity as macropores were added at the expense of micrite.

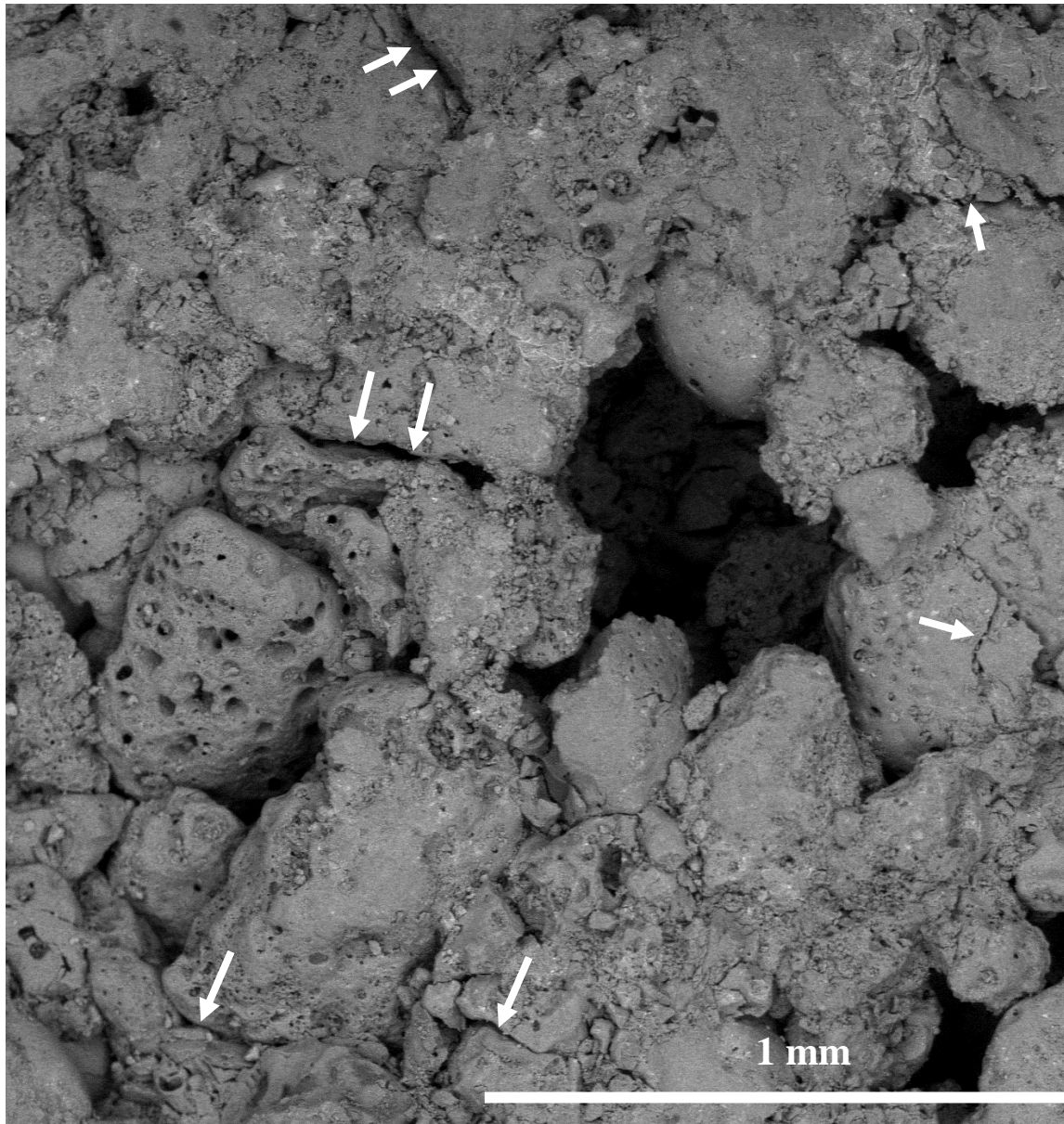


Figure 4.11: SEM image of a grain-supported sample from set MACRO showing the presence of introduced macropores (large sub-rounded pores). The white arrows highlight the presence of low aspect ratio pores and micro-cracks, especially between grains.

4.3.5 Effect of Micrite on Fluid-Frame Interaction

With regard to the effect of micrite on post injection elastic properties, Figure 4.12 shows the percentage change in bulk and shear moduli after injection. Figure 4.12 shows that (1) the change in bulk and shear moduli (ΔK and ΔG , respectively), with respect to the

moduli measured under dry conditions, goes from positive (stiffening) to negative (weakening) values with increasing micrite content; and (2) the greatest change in moduli occurs under low pressure conditions, where increasing the pressure minimizes the observed changes both for samples exhibiting weakening and for those experiencing stiffening. The trends observed in Figure 4.12 are also similar to those reported by Vanorio et al. (2007) in shaley-sandstones. It is important to note that after recovering the samples from the pressure vessel post-drying, we found them to have some residual water saturation (~8-17%). This is probably due to the low permeability of the samples, which made it impossible to dry them completely by injecting helium under pressure. Since samples were not completely dry after injection, moduli are affected by high frequency mechanisms such as squirt flow (Mavko and Jizba, 1991). We therefore hypothesize that the trends observed in Figure 4.12 depend on the balance between rock-fluid interactions and dispersion mechanisms. Under low-pressure conditions, the opening of the most compliant pores (i.e., low-aspect-ratio pores, as suggested by the sensitivity of elastic properties to pressure shown in Figures 4.2 and 4.3), is responsible for creating high-frequency effects (Mavko and Jizba, 1991). This leads to dispersion overcoming the effect of dissolution in grain-rich samples and thus, to positive values of ΔK and ΔG as shown in Figure 4.12. In contrast, micrite-rich samples have stiff pore structure as mentioned earlier and hence, the squirt dispersion is smaller. Moreover, opening pores under low-pressure conditions are responsible for creating a larger reactive surface area in micrite-rich samples. This favors dissolution and thus, a negative change in moduli. As the pressure increases, pores start to close diminishing the effect of both rock-fluid interactions and dispersion mechanisms. Since dissolution affects the elastic moduli in a way that is opposite compared to dispersion, Gassmann theory may either overestimate or fit high frequency, saturated velocities. That will depend on the balancing of dissolution against dispersion mechanisms and determine what Adam et al. (2006) defined as a paradox on Gassmann's theory applicability.

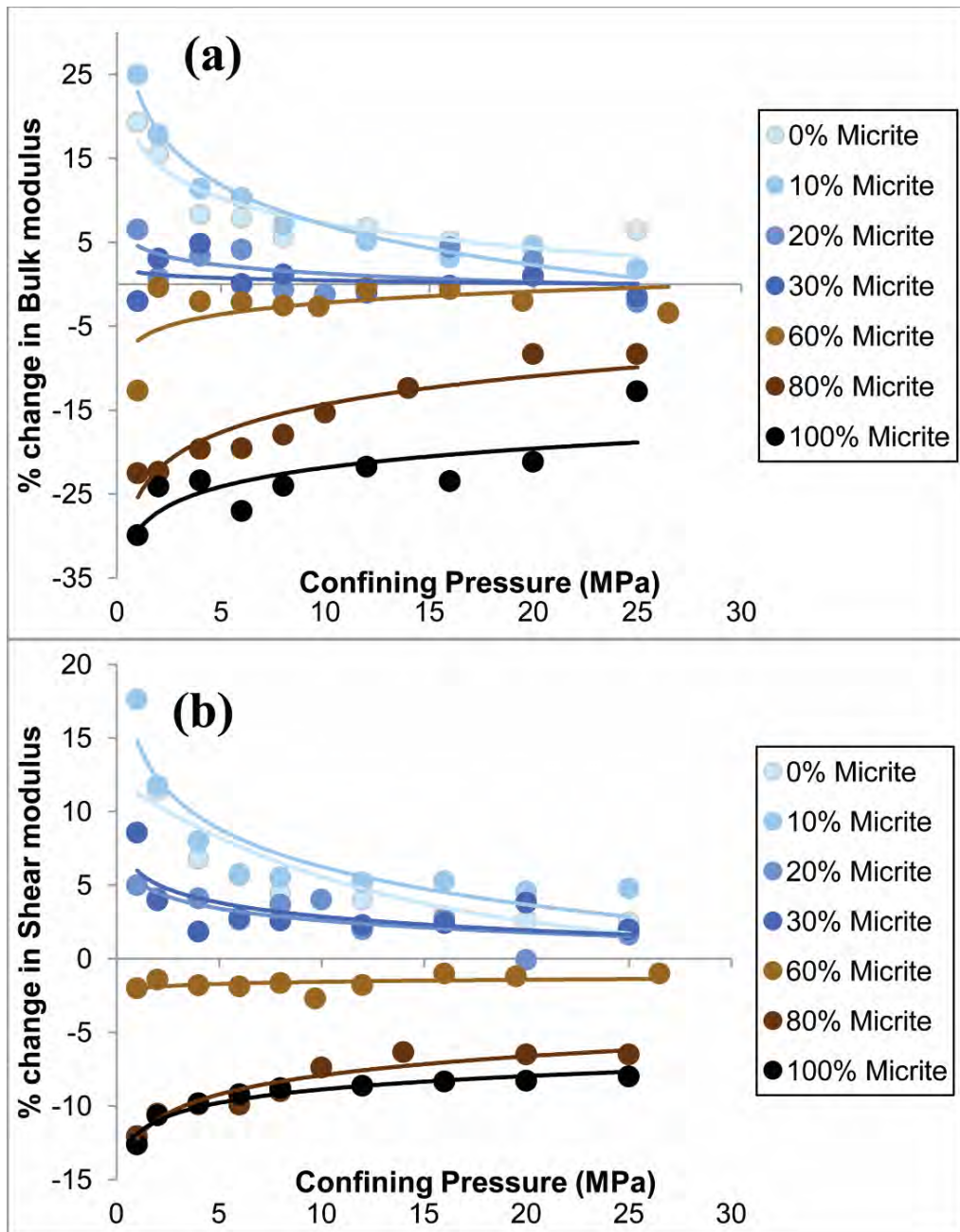


Figure 4.12: Percentage change in (a) bulk modulus, and (b) shear modulus due to injection of CO₂-rich water as a function of confining pressure. The percentage change was calculated as $100 * (\text{Modulus}_{\text{post}} - \text{Modulus}_{\text{pre}}) / \text{Modulus}_{\text{pre}}$. Data is color coded by the micrite content and fitted by best-fit logarithmic function as represented by the curves.

4.4 Conclusions

In this chapter, we investigated the effect of the fraction of micrite and macroporosity on the elastic properties of carbonates using analog samples. This study shows that the fractional amount of micrite in microstructures varying from grain-supported to micrite-supported, determines clear trends in the elastic properties, their sensitivity to pressure, and their response to the injection of a reactive fluid.

Our results indicated that increasing the content of micrite leads P- and S- wave velocities to increase, making the rock frame stiffer. Since the sensitivity of the elastic velocity to pressure decreases as the content of micrite increases, we hypothesize a stiffer pore structure in micrite-richer fabrics. Such hypothesis was supported by a) observations from SEM images showing the presence of rounder pores in micrite-supported samples, and b) smaller change in length (i.e., strain) measured under pressure for the micrite-rich samples, compared to grain-supported samples. When macropores were introduced at the expense of micrite, porosity increased and acoustic velocity decreased. This was explained by the effect of removing the stiff micrite aggregates from the microstructure.

Furthermore, the micrite content seems to affect the evolution of velocity upon interaction with reactive fluids. Post-injection velocities in micrite rich samples showed a decrease in magnitude as a result of dissolution that overwhelms high frequency effects (i.e., squirt flow). This study suggests that the content of micrite in carbonates can affect how the elastic properties change when carbonates are exposed to pressure changes and reactive fluids, both being of great importance to 4D studies.

Chapter 5

THE EFFECT OF MICRITE CONTENT AND MACRO-POROSITY ON THE TRANSPORT AND ELASTIC PROPERTIES OF CARBONATE RESERVOIR ROCKS

Abstract

In this chapter, we extend our previous study on carbonate analogs to natural carbonate samples from the Tengiz Field, in western Kazakhstan, in order to test the hypothesis and methodology developed from the earlier study. Specifically, we investigate how microstructural parameters (such as micrite content and macro-porosity) can be quantified and then utilized to better interpret and model the rock properties of natural carbonates. We studied 15 samples that have varying micrite content and pore structure from Tengiz Field, an isolated carbonate platform oil reservoir. We present an approach to estimate micrite content, micro-, and macro-porosity based on micro-CT scans and thin sections of the samples. In order to characterize the properties of the samples, Klinkenberg-corrected nitrogen permeability, Helium porosity, and SEM images were obtained. Additionally, P- and S-wave velocities were measured under benchtop condition and as a function of confining pressure. Similar to the analogs, carbonate reservoir rocks show the same trends

regarding the effect of micrite and macro-porosity on porosity-permeability relationship as well as sensitivity of acoustic velocities to pressure.

With regard to the effect of micrite content and macro-porosity on the transport properties, samples with higher micrite content and lower macro-porosity exhibit lower permeability at any given porosity. The porosity-permeability relationship for samples with similar micrite content could be modeled using the Kozeny-Carman relation for a pack of spheres. Our analysis shows that as the content of micrite increases, it exerts a major influence on the porosity-permeability relation of carbonates by reducing the effective grain size while increasing the threshold of percolation porosity. In addition, the fraction of macro-pores in the samples was also found to be strongly correlated with the measured permeability since such pores do contribute more significantly to fluid flow compared to micro-pores. This study suggests that estimates of both micrite content and macro-porosity are significantly important to the modeling of porosity-permeability relations in dual-grain size, dual-porosity carbonates. The coefficient of determination (R^2) between porosity and permeability was found to increase from 0.75 to 0.98 when incorporating the micrite content and macro-porosity into the analysis.

With regard to the effect of micrite content on elastic properties, our analysis shows that the sensitivity of acoustic velocity to pressure decreases as the micrite content increases. This suggests a stiffer pore structure in samples characterized by higher micrite content compared to grain-supported samples. Such conclusion is supported by a) observations from SEM images showing the presence of more micro-cracks in grain-supported samples, and b) smaller change in length (i.e., strain) measured under pressure for the micrite-supported samples, compared to grain-supported samples. Unlike micrite content, the macro-to-micro-porosity ratio shows no strong correlation with acoustic velocities.

5.1 Introduction

Our work on carbonate analogs, created in the laboratory by controlling and quantifying micrite content and macro-porosity, revealed distinctive trends in both porosity-permeability (Chapter 3) and acoustic velocity (Chapter 4) relationships. For the

sake of convenience, the main findings can be summarized as follows: a) the interpretation and modeling of apparently scattered porosity-permeability trends can be enhanced by incorporating the knowledge of micrite content and macro porosity, and b) the sensitivity of the acoustic velocity to pressure decreases as the micrite content increases. Since the previous conclusions were based on analog samples, we needed to evaluate their applicability to complex natural carbonates. Most importantly, unlike the analog samples, micrite and macro-porosity contents, which characterize such complex micro-structures are not known *a priori* in carbonate reservoir rocks. Thus, the objective of this study is to explore how to extend the work done on the analog samples to carbonate reservoir samples. Primarily, this chapter aims to answer the following questions: a) what approach can be adopted on natural samples to estimate key sedimentological parameters such as micrite content and macro-porosity, and b) will the functional relationships among the micro-structural parameters characterizing the analog samples hold true for natural carbonates? The outcome of this study provides a data-driven modeling scheme for the interpretation of the porosity- permeability and acoustic velocity data in carbonate rocks.

5.2 Study Area and Sample Selection

Core samples were provided by Tengizchevroil and come from the Tengiz field in western Kazakhstan (Figure 5.1). The Tengiz field is an isolated carbonate buildup (Figure 5.2) located in the southeastern Pricaspian Basin (Collins et al., 2006; Collins et al., 2013; Skalinski et al., 2015). The buildup consists of a succession of shallow-water, grain-dominated platform carbonates ranging in age from late Famennian to early Bashkirian (Weber et al., 2003; Collins et al., 2006; Collins et al., 2013). Serpukhovian progradation resulted in steeply-dipping depositional slopes that flanked the buildup, as shown in Figure 5.2. These carbonate slopes consisted of microbial boundstones in upper slope positions that graded downdip into middle slope breccias and grainstones (Weber et al., 2003; Collins et al., 2006). Interbedded grainstones, mudstones, and volcanics constituted the majority of lower slope to basinal settings. The rim and flank facies include: lower slope mudstone and volcanic ash, as well as upper slope skeletal packstone to grainstone. Reservoir quality in the shallow water platform and slope varies due to both the depositional environment and a subsequent complex diagenetic overprint consisting of multiple phases of fracturing,

cementation, and dissolution, and bitumen cementation (Collins, et al., 2006). Such variations in depositional environments and diagenesis processes resulted in the wide variability of pore types, rock textures, and hence, physical properties of Tengiz carbonates (Collins, et al., 2006; Skalinski et al., 2015). Consequently, the selection of samples from the Tengiz field offered an enormous opportunity to have samples characterized by varying proportions of microcrystalline calcite (micrite content) and pore structure (varying micro-to-macro-porosity ratio). We selected 15 samples from different wells and depths where the samples were examined under the microscope in order to ensure that sample selection covered different micrite content and pore structures. The selected samples were from the Bashkirian, Serpukhovian, and Visean formations (Figure 5.2). Although the samples belong predominantly to inner platform settings which are dominated by grain-rich fabrics, the complex variable diagenetic overprint resulted in variable content of micrite and macroporosity. That is, the main factor behind variations in the microstructure of the selected samples is variations in extent of diagenesis rather than in the depositional environment. Throughout this chapter, the term “micrite” refers to the microcrystalline calcite which can have multiple origins including: 1) patches of carbonate mud occupying the matrix within a grain-dominated fabric; 2) rock components that have been recrystallized into microcrystalline fabrics; 3) microcrystalline cements in grain-dominated fabrics or micritic ground-masses in microbial boundstones (Collins et al. 2013).

It is also important to mention that the following criteria were taken into consideration when selecting the samples: (1) samples should not be densely fractured, and (2) XRD and volume-of-bitumen data provided by Tengizchevroil were used to exclude samples with major solid composition other than calcite (such as bitumen and quartz). The reason for these two criteria is to study specifically the role of micrite content and macroporosity, thus eliminating as much as possible the contribution of fractures or varying mineralogy. The presence of dense fractures can particularly dominate the transport and elastic properties of the rocks, and hence such a factor should receive different treatment compared to textural parameters. The effect of fractures is not the focus of this study.

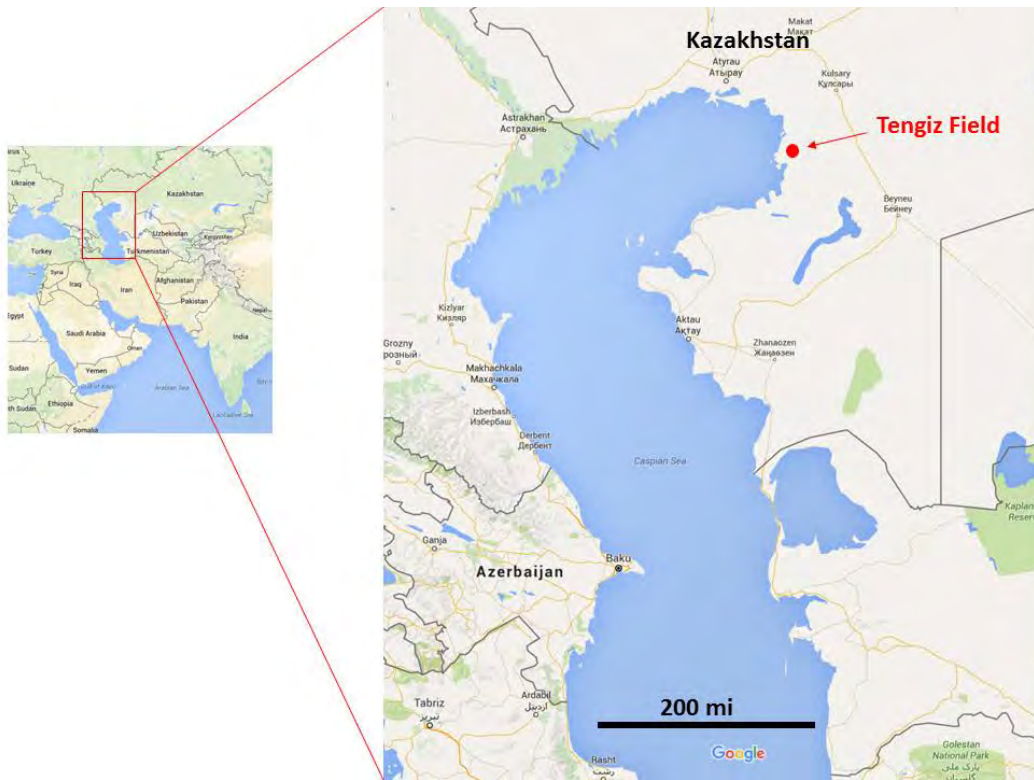
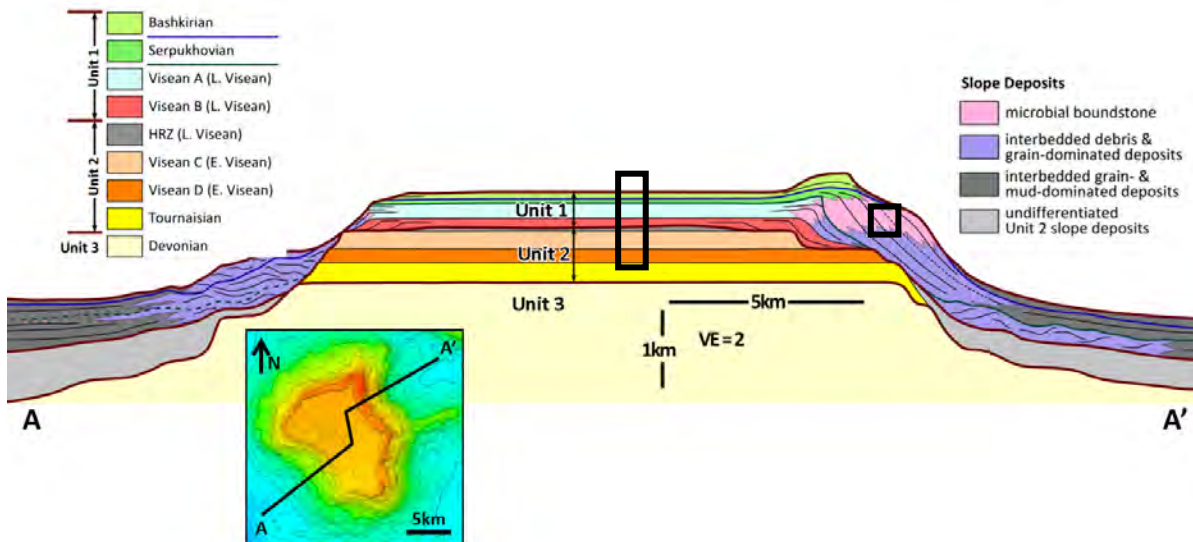


Figure 5.1: Location of the Caspian Sea region and Tengiz field

Figure 5.2: Schematic geologic cross section of the Tengiz isolated carbonate platform reservoir, modified after Skalinski et al. (2015). Black boxes schematically show



where the samples come from including the inner platform (middle of the structure) and the upper slope boundstone (only for two samples).

5.3 Methodology

5.3.1 Sample Characterization

In order to characterize the properties of the samples, Klinkenberg-corrected nitrogen permeability, Helium porosity, and SEM images were obtained. P- and S-wave velocities were measured under benchtop conditions. The benchtop acoustic setup consisted of a digital oscilloscope (Tektronix TDS 1012B), a pulse generator (Panametrics 5052 PR), and two pairs of transducers (Panametrics V103 for 1 MHz P-waves and V154 for 0.7 MHz S-waves). Porosity, permeability, and velocity measurements have uncertainties of 1%, 2%, and 1%, respectively.

5.3.2 Velocity Sensitivity to Pressure

We selected a subset of 10 samples with variable porosity, permeability, and rock texture, and then measured P- and S-wave velocity of the dry samples under increasing confining pressure. The experimental setup for the pressure tests consists of a digital oscilloscope (Tektronix TDS 340A) and a pulse generator (AVTECH AVR-7B-B). The samples were jacketed with a Tygon tubing to isolate them from the confining pressure medium. P- and S-wave velocities were measured using a pulse transmission technique as the confining pressure was increased up to 30 MPa. Samples were lodged between two steel endplates mounting a stack of two PZT-crystals that generated P- and S-waves. The principal frequency was about 1 MHz for P-waves and 700 MHz for S-waves. Molasses was used as a high viscosity-bonding medium to ensure acoustic coupling between the endplates and the sample. We used three potentiometers to measure changes in length of the samples as a function of stress, based on which the axial strain was calculated. Prior to the measurements, samples were pre-stressed by applying one loading cycle (up to 30 MPa) to make sure the measurements are not affected by micro-cracks induced during coring.

5.3.3 Estimation of Micro-structural Parameters

We characterized the micro-structure of the samples using three main parameters: micro-porous micrite (microcrystalline calcite crystals and associated micro-porosity), solid grains (non microcrystalline fabric), and macro-porosity. Mineral composition cannot be used as a discriminant between micrite and grains since they both have the same

mineralogy. However, the presence of micro-porosity within the micrite aggregates lowers their overall density compared to the solid calcite grains, thus making it possible to separate them based on the density contrast in micro-CT scans. Therefore, we used micro-CT scans and image-processing techniques to quantify the key parameters characterizing the micro-structure of the samples. The approach used here was originally proposed by Vanorio and Mavko, 2011. We built upon that approach by also taking advantage of the information from higher resolution SEM images as well as thin sections of the samples to (1) estimate parameters where micro-CT scans were not available, and (2) overcome some of the limitations in characterizing the micro-porosity arising from the use of CT-scan alone. Additionally, we present an approach to quantify the uncertainty associated with the estimated parameters. In the following two sections we describe the approach used to estimate micro-structural parameters from both micro-CT scans and SEM images.

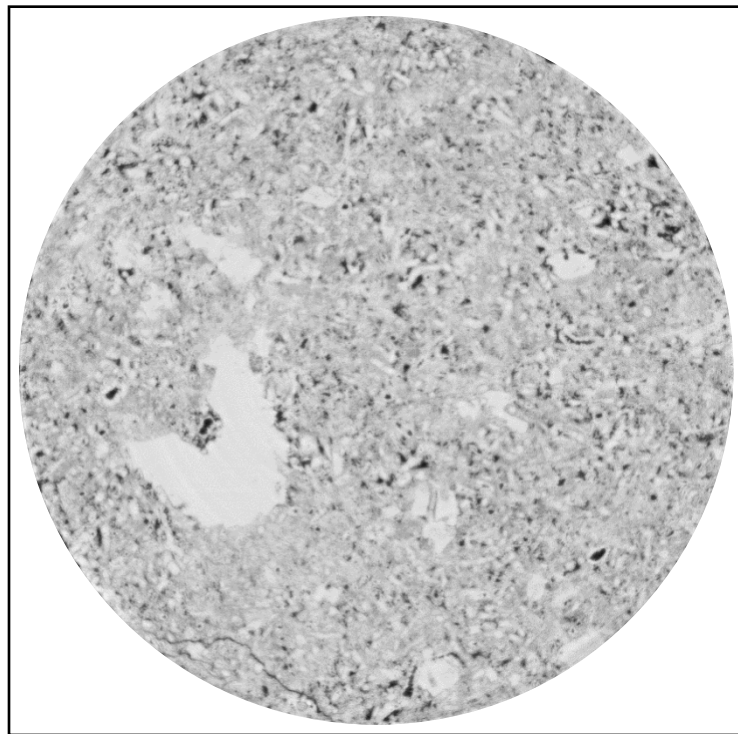


Figure 5.3: 2D slice image extracted from the micro-CT scan of a selected sample showing the intensity response of solid grains (white/light grey), macro-pores (black) and micro-porous micrite (gray). The diameter of the sample is 8 mm, while the micro-CT scan belongs to sample Tg1.

5.3.3.1 Estimation of Parameters from CT Scans

All samples used for transport and elastic property measurements were 1.0 inch in diameter and they were cored out of 1.5 inch diameter plugs. The remnant material was used to extract 8-millimeter-sized plugs for micro-CT scanning, which was provided by Chevron. Micro-CT scans were obtained for 11 samples producing a 3D digital volume of the rock with spatial resolution of 3.5 $\mu\text{m}/\text{pixel}$. The extraction of millimeter-sized plugs from the other four samples was not possible because there was not enough material available to have both 1.0 inch diameter and 8 mm diameter cores from the original 1.5 inch core. Figure 5.3 shows a 2D slice of a scanned sample, in which the micrite exhibits an intensity response (gray) that is in between that of macro-porosity (black) and solid grains (white). This variation in the intensity response allowed us to segment the images and retrieve three different distinct phases. It is important to mention here that the macro-porosity in this case includes all pores that are large enough to be recovered from the micro-CT scan images. We used a code implemented in MATLAB to segment the CT scans and calculate the percentage of macro-porosity, solid grains, and micro-porous micrite. The input is a set of approximately 2000 images (2D slices) on average reconstructing the 3D volume of each micro-sample. A smoothing filter was first applied to reduce the noise level by subdividing the image into squares 3x3 pixels in size. In each square, the code calculates the average gray-scale intensity value. We then manually selected a threshold (based on grey-scale intensity) to segment the image, allowing the code to calculate the fraction associated with the intensities below the threshold. We followed a two-step segmentation scheme (i.e., with two threshold values) to obtain three micro-structural parameters as follows: (1) the first threshold separates the macro-pores (i.e., black regions in CT scans) from the rest of the image, thus allowing the calculation of the macro-porosity (ϕ_{macro}) as shown in Figure 5.4b, and (2) the second threshold has higher value than the first one and separates the solid grains from the rest of the image as shown in Figure 5.4c. The code calculates the percentage associated with intensities below the second threshold (f_2), which correspond to the content of ϕ_{macro} and micrite aggregates (highlighted in black in Figure 5.4c). The percentage of the grains (f_{grains}) can then be calculated simply by $100 - f_2$ while the fraction of the micrite aggregates is equal to $f_2 - \phi_{macro}$. The percentage of the micrite aggregates consists of two quantities, namely the percentage of solid micrite crystals

($f_{micrite}$) and micro-porosity (ϕ_{micro}). Since the micro-porosity could not be directly estimated from the CT-scans, we subtracted ϕ_{macro} from the measured helium porosities (ϕ) to obtain ϕ_{micro} . Finally, the micrite content ($f_{micrite}$) is thus given by $f_{micrite} = f_2 - (\phi_{macro} + \phi_{micro}) = f_2 - \phi$. The micrite-to-grain indicator (i.e., the percentage of solid micrite out of the total solid volume) is then given by $[f_{micrite} / (f_{micrite} + f_{grains})]$. The percentages of macro-pores, grains, and micrite were estimated on all 2D slices and then averaged through the 3D volume. The standard deviation of the estimated parameters was also calculated based on the values obtained from all 2D slices. This is a measure of uncertainty since it indicates how the values of a certain parameter vary around the reported average.

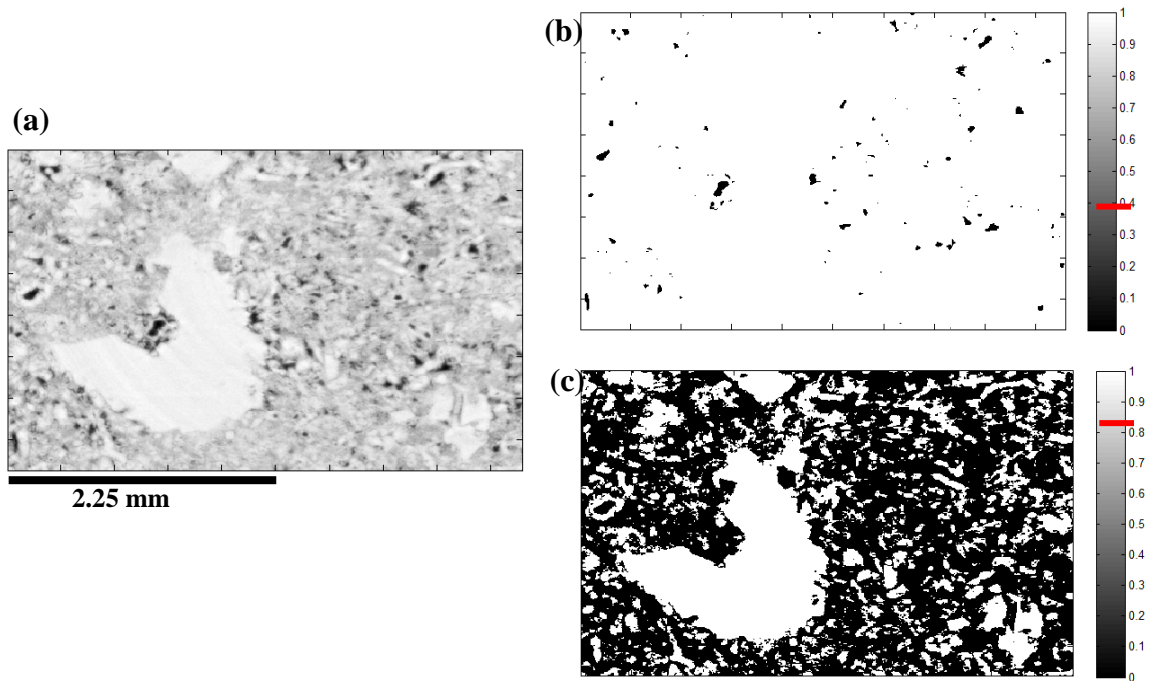


Figure 5.4: Demonstration of the segmentation scheme, (a) zoomed section (before segmentation) from the CT scan image shown in Figure 5.3, (b) the output of segmentation after the selection of the first threshold (marked by red line in the grey scale bar) which recovers the fraction of macro-pores (shown in black), while everything with intensities above the threshold is shown in white, (c) the output of the segmentation after selecting the second threshold (has higher value than the first one); the code calculates the fraction of intensities below the threshold (micrite and macro-pores) as highlighted in black while the white color corresponds to the solid grains.

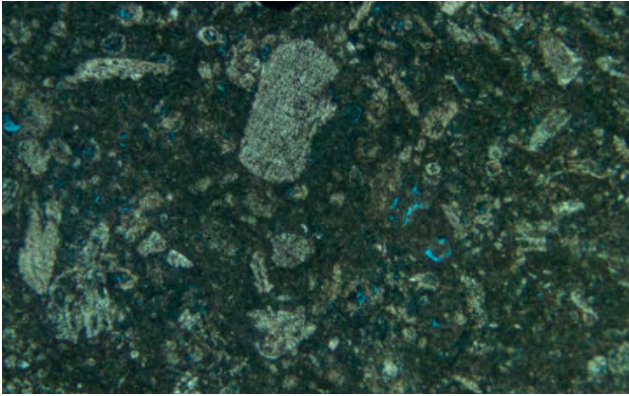
5.3.3.2 Estimation of Parameters from SEM Images

We extracted one thin section per sample from 14 samples, and then imaged the thin sections under the SEM. The extraction of thin section was not possible in one sample since it was contaminated with oil which leaked into the sample upon the recovery from the pressure vessel. We used the SEM images to achieve three main objectives. First, for the four samples where micro-CT scans were not available, the micro-structural parameters were estimated based on SEM images obtained from thin sections of the samples. Second, when both micro-CT scans and SEM images are available, we compare the parameters estimated using each technique in order to evaluate how well they match and comment on possible reasons for any discrepancies. Micro-CT scans represent a 3D volume from the rock while SEM images correspond to a single 2D slice from the surface of the samples. Thus, by comparing the results obtained from each approach, we aim to examine how well the parameters estimated from SEM images represent the actual 3D volume. Based on this comparison, we also quantify the uncertainty associated with estimating parameters from SEM images alone. Finally, we utilized the higher resolution and magnification of the SEM images to directly estimate the micro-porosity within the micrite aggregate of the samples and compared the results with the indirect approach (i.e., subtracting macro-porosity from the measured total helium porosity). This allowed us to examine some limitations of the current approach for estimating the parameters of interest from both micro-CT scans and SEM images.

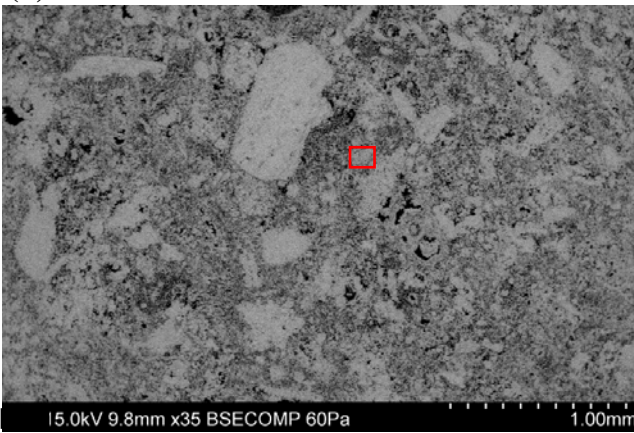
We imaged thin sections under the SEM instead of imaging the actual plug surface because thin sections can produce a flat 2D cross-section of the sample surface. This can eliminate changes of grey-scale intensity that are caused by variations in the surface topography as frequently observed in the SEM images of actual plugs. An example of thin section and the corresponding SEM image is given in Figure 5.5. In order to segment the SEM images and estimate the micro-structural parameters, we followed the same approach used for micro-CT scans. We obtained eight different SEM images from various locations within the thin section of each sample, and then estimated the micro-structural parameters by averaging the values obtained from all images. The SEM images were taken at the lowest magnification (x 25) to cover the largest area possible and with spatial resolution of 2 $\mu\text{m}/\text{pixel}$. Figure 5.6 shows an example of the segmentation output separating solid gains

from the porous phases (micro-porous micrite and macro-pores). SEM images have higher resolution and magnifications compared to micro-CT scans and, consequently, a higher noise level. We note that the gray-intensity within a single grain can vary because of the presence of speckles, conferring some parts of the solid grains with grey-intensity that are similar to the micro-porous micrite (Figure 5.6a). This resulted in classifying some parts of solid grains as micro-porous micrite (red arrows in Figure 5.6b). Similarly, some parts of the micrite were misclassified as solid grains based on their grey-intensity (green arrows in Figure 5.6b) which corresponds, instead, to solid micrite particles that could be recovered from the SEM. We attempted to reduce the effect of this noise by applying a larger smoothing filter (5x5 pixels in size, compared to 3x3 filter used for CT scans) prior to segmentation (Figure 5.6a), but the segmented image still showed a considerable level of noise and misclassification. Therefore, we developed a code in MATLAB that processes the segmented image and removes the noise in each segmented phase. First, the code locates all the bodies (solid and porous) that are equal to or smaller than 5x5 pixels in size (equivalent to 10x10 μm), and are isolated (i.e., solid phase dispersed in porous phase and vice versa). The code then re-classifies these tiny isolated bodies according to the surrounding phase (i.e., dispersed solid phase in micrite will be turned into micrite, and vice versa) as shown in Figure 5.6c. The fraction of each micro-structural parameter was then recalculated. In some cases, this correction resulted in changing the grain or micrite percentage by up to 5%, which suggests the importance of applying such a post segmentation process.

(a)



(b)



(c)

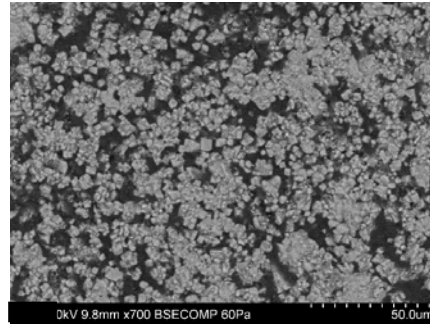


Figure 5.5: Thin section optical image (from sample Tg13) under the microscope (a) and the SEM image (b) obtained from the same location. The SEM image in (c) corresponds to a highly magnified image of the micrite aggregate highlighted by red box in (b).

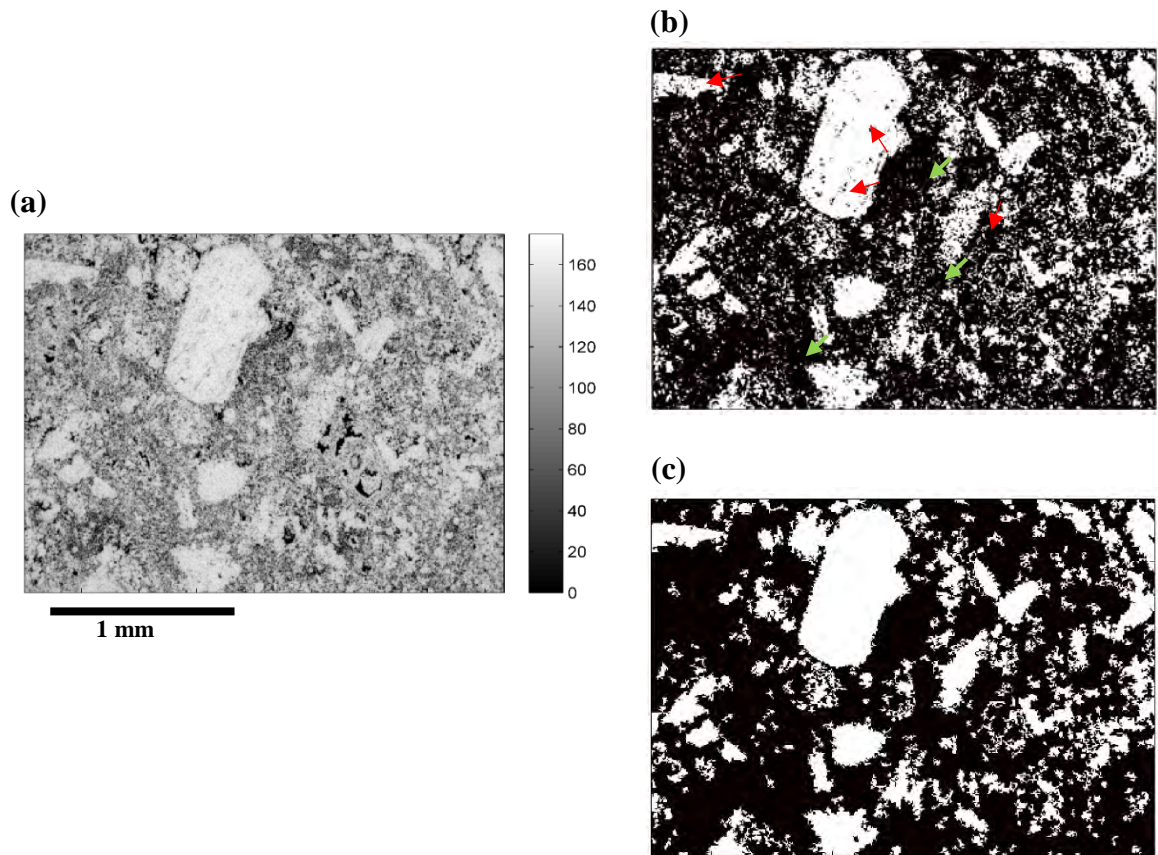


Figure 5.6: Demonstration of the segmentation of SEM image (from sample Tg13); (a) original SEM image after applying smoothing filter, (b) segmentation output where solid grains are highlighted in white, and the porous phase (macro-pores and micro-porous micrite) is highlighted in black. Note the presence of very small porous phase dispersed within a solid grain (highlighted by red arrows) and presence of solid grain within the porous phase (highlighted by green arrows), (c) the final segmented image after applying the post segmentation correction process.

The SEM images were also used to characterize the micrite particles (shape and size) and directly estimate the micro-porosity within the micrite aggregates. For each sample, we obtained SEM images of the micrite aggregate from four different locations, and used them to estimate the average porosity within the micrite aggregate. We first obtained highly magnified SEM images ($\sim x700$) of the micrite aggregate (Figure 5.7a), segmented the images (Figure 5.7b), and finally calculated the average percentage of porosity within the micrite aggregate of each sample.

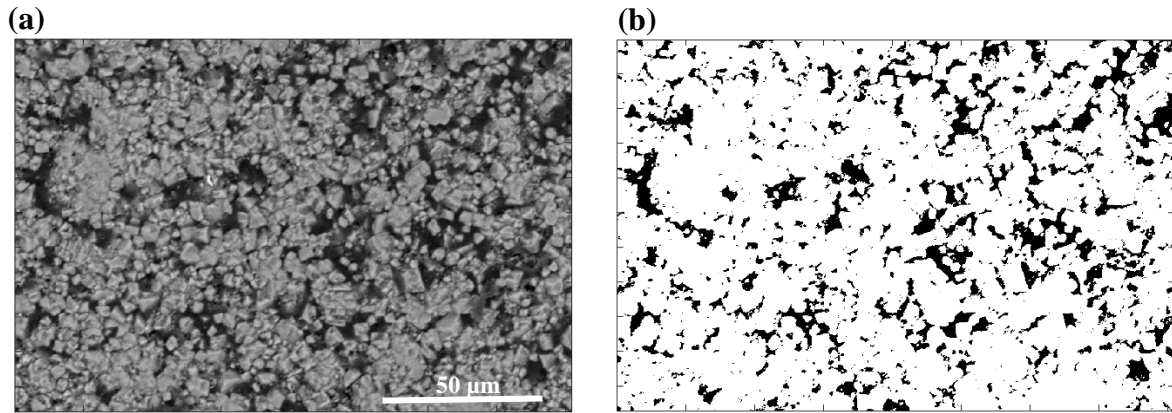


Figure 5.7: Demonstration of the segmentation of SEM images of micrite aggregates (from sample Tg3); (a) original SEM image obtained from the micrite aggregate of a sample, (b) segmentation output where the pores within the micrite aggregate are highlighted in black. Micrite particles show a micro-rhombic morphology as shown in (a).

5.4 Results

Figure 5.8 shows SEM images for several samples exhibiting a varying content of micrite. Table J.1 (Appendix J) summarizes the measured transport and elastic properties of the selected samples from the Tengiz field. It also shows the volume percentage of micro-structural parameters such as macro-porosity (ϕ_{macro}), micro-porosity (ϕ_{micro}), content of solid grains (f_{grains}), and micrite ($f_{micrite}$) estimated from both micro-CT scans and SEM images. The micro-structural parameters estimated from the micro-CT scans were considered to be the reference values (except for samples where micro-CT scans are not available) since micro-CT scans represent a larger 3D volume compared to the SEM images. That is, we will use the micro-structural parameters estimated from micro-CT scans for the first 11 samples shown in Table J.1 while the parameters estimated from SEM images will be used for the last four samples (no micro-CT scans available) in Table J.1. The last column in Table J.1 shows the porosity within the micrite aggregates estimated utilizing highly magnified SEM images of the micrite aggregates as shown previously in Figure 5.7.

Figure 5.9 shows a porosity-permeability cross plot for the Tengiz samples. Although permeability increases in general with porosity, the relationship exhibits a noticeable scatter (Figure 5.9) as permeability varies by up to more than one order of magnitude for a

given porosity. This observation suggests two points: 1) porosity alone does not fully control permeability in carbonate samples, and 2) additional micro-structural parameters need to be extracted to explore higher-order relationships that may be hidden within the observed scattered data. Figure 5.10 shows the same porosity-permeability cross plot as in Figure 5.9, except that data points are now color-coded by micrite content ($f_{micrite}$). We can see that for a given porosity, samples with lower micrite content have higher permeability (Figure 5.10). This agrees with the trends observed for the analog samples (Chapter 3). Figure 5.11 shows the same porosity-permeability plot, color-coded by micrite content but with the size of data points proportional to the amount of macro-porosity. Samples with higher percentages of macro-porosity tend to have higher permeability at a given porosity as suggested by Figure 5.11.

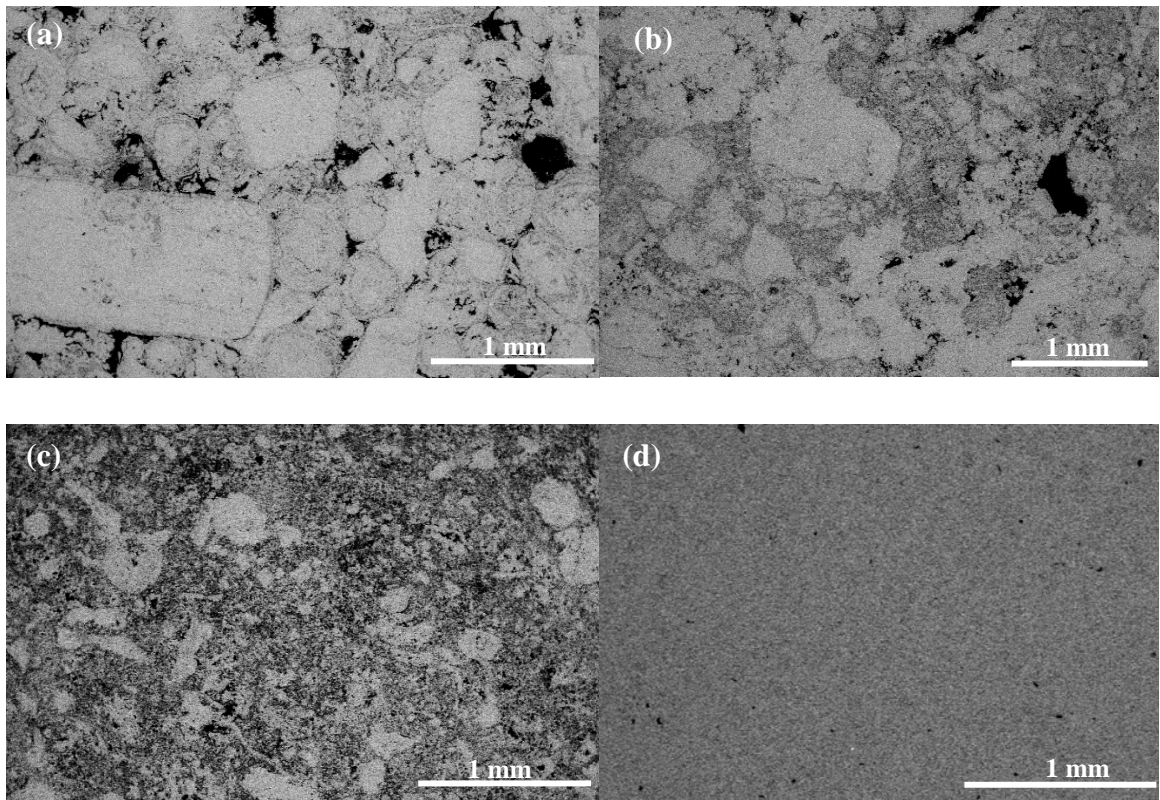


Figure 5.8: Samples with varying texture: (a) sample Tg12, (b) sample Tg4, (c) sample Tg13, and (d) sample Tg7. The micrite content increases from (a) to (d).

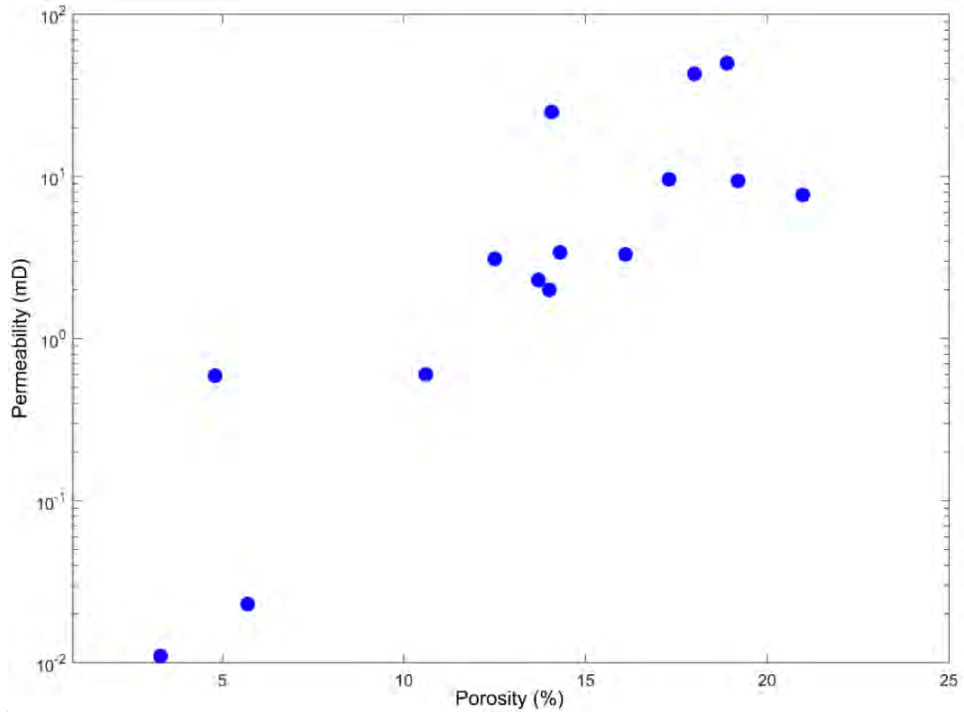


Figure 5.9: Plot of permeability as function of porosity for the selected samples. It can be noticed that permeability varies by up to one order of magnitude for a given porosity.

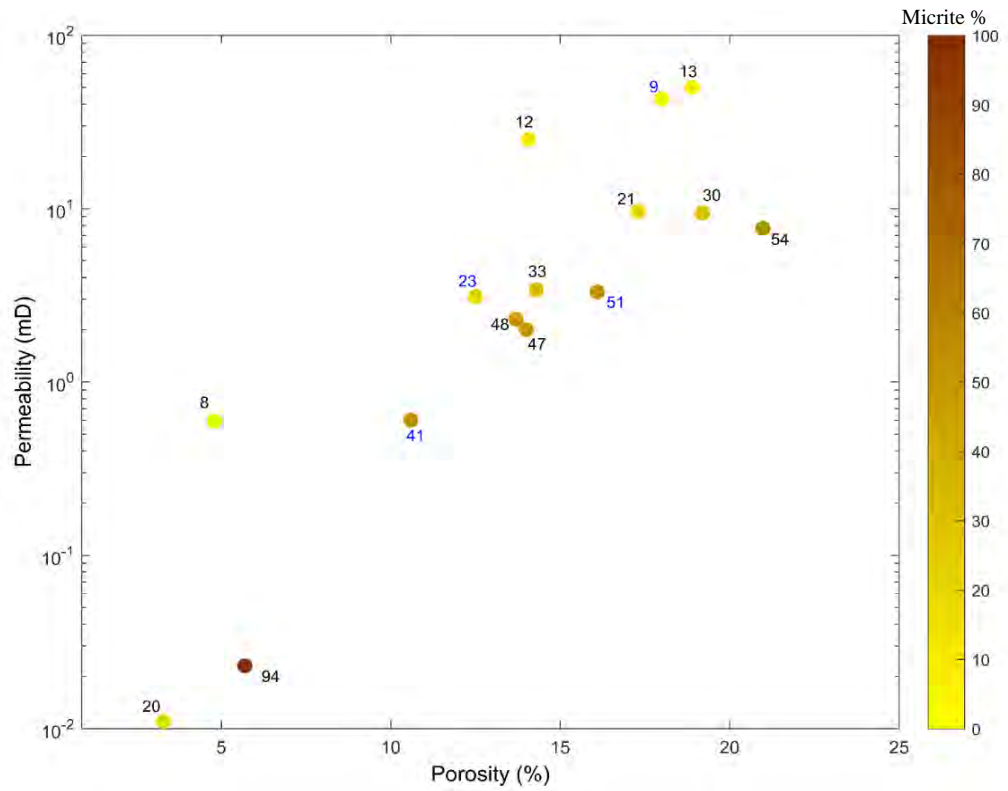


Figure 5.10: Plot of permeability as function of porosity for the selected samples. The plot has the same data as in Figure 5.9 but data is color-coded by micrite content (shown in numbers beside the data point as well). The micrite content shown in blue numbers refers to samples where the micrite content was estimated from SEM images (no micro-CT scans available).

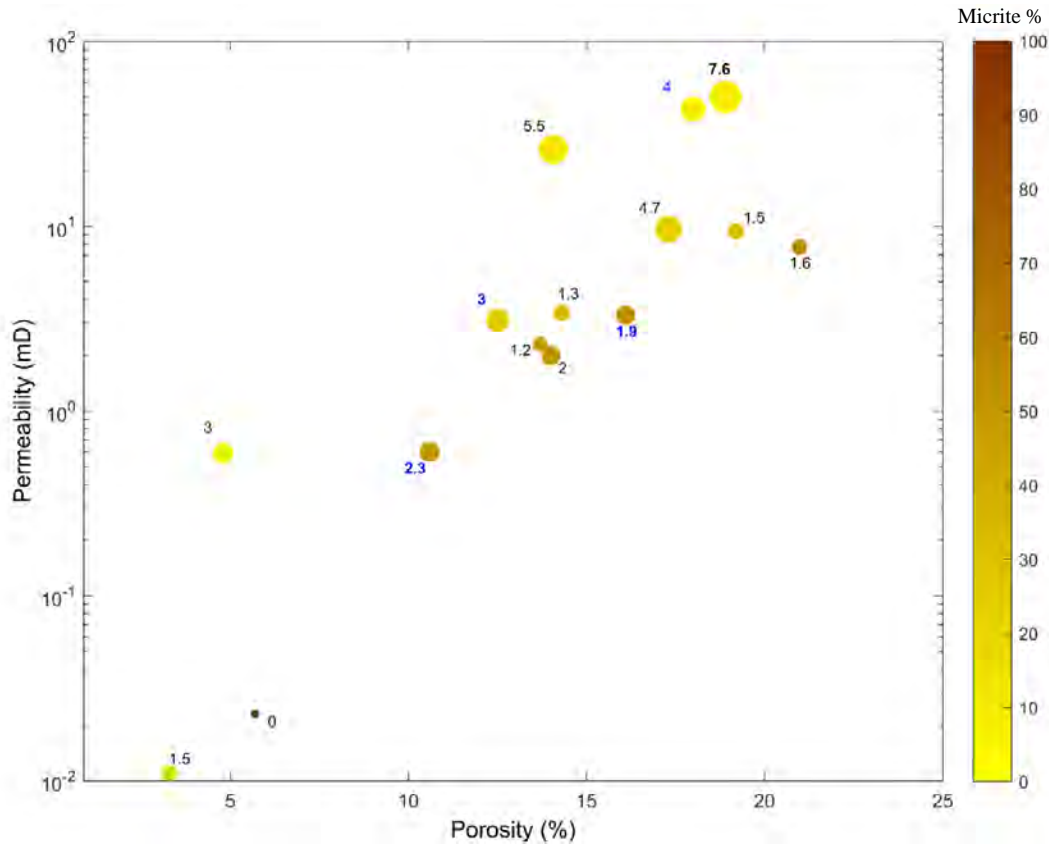


Figure 5.11: Plot of permeability as function of porosity for the selected samples. Data is color coded by micrite content while the size of the circles is proportional to the percentage of macro-porosity (shown in numbers beside the data point as well).

Figure 5.12 shows the relationship between porosity and benchtop acoustic velocities of the samples where data is color-coded by micrite content. The size of data points is proportional to the amount of macro-porosity. Samples characterized by higher micrite content and lower macro-porosity tend to have higher acoustic velocity at a given porosity although a scatter remains in the data. Figure 5.13 reports the variation of acoustic velocities (normalized to velocity measured at 1 MPa) as a function of confining pressure. The values of acoustic velocities at the different pressures are reported in Table J.2 (Appendix J). The data in Figure 5.13 indicates that the velocity of the samples characterized by a larger grain content (less micrite) appears to be much more sensitive to pressure compared to the micrite-supported samples. Such trends agree with what we observed for the analog samples (Chapter 4) regarding the effect of micrite on the velocity sensitivity to pressure. Figure 5.14 shows the relation between the maximum normalized

P-wave velocity (represented by the ratio between the velocity measured at highest and lowest pressure), and major transport properties and micro-structural parameters including: micrite content (Figure 5.14a), porosity (Figure 5.14a b), permeability (Figure 5.14c), and macro-to-micro-porosity ratio (Figure 5.14d). Figure 5.15 shows the same relations as Figure 5.14 but for S-wave velocity. The relations shown in Figures 5.14 and 5.15 suggest that the sensitivity of velocity to pressure is best correlated with micrite content among other physical properties and micro-structural parameters. Although the velocity of samples characterized by larger macro-porosity tend to be more sensitive to pressure, the scatter in Figures 5.14d and 5.15d suggest no strong correlation between the two variables. The change in length, normalized by sample length, is shown in Figure 5.16, which indicates that grain-supported samples experienced larger length changes, in general, compared to micrite-supported samples.

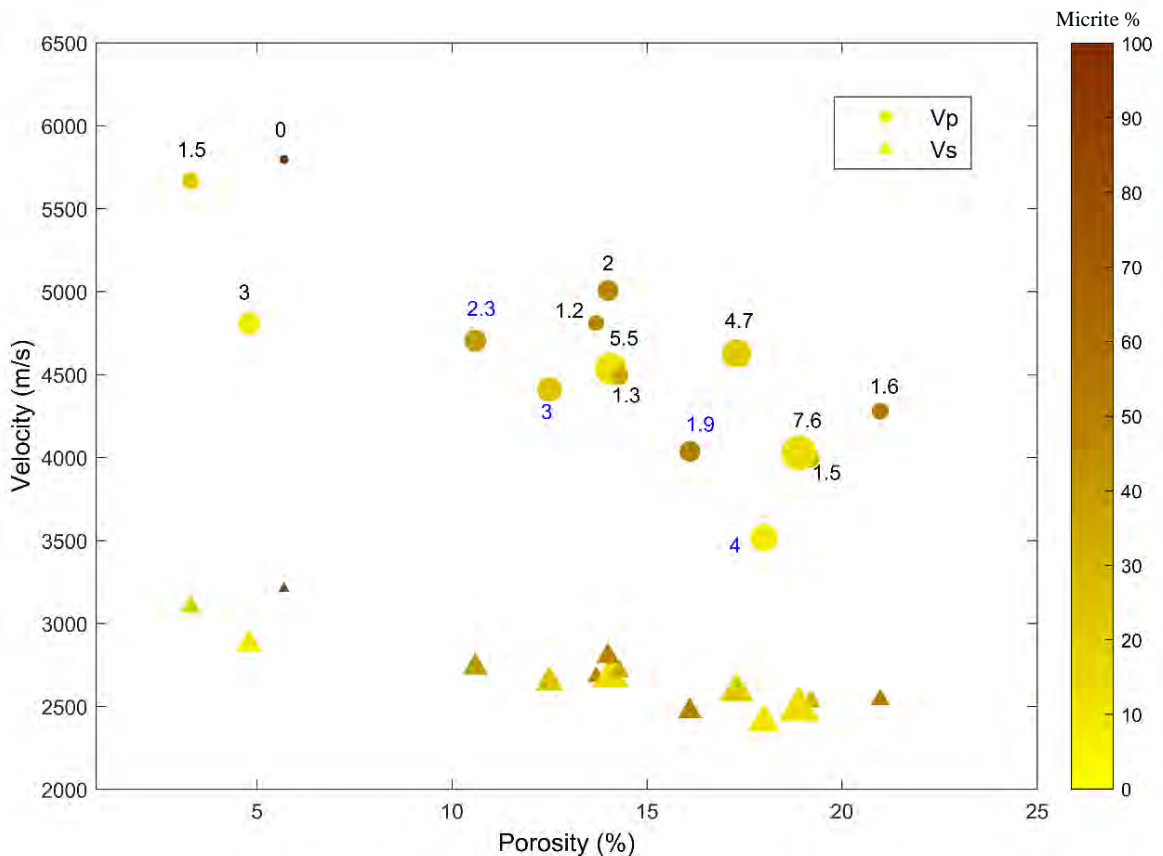


Figure 5.12: Plot of P- and S-wave benchtop velocities as function of porosity; data is color coded by micrite content while the size of the data point is proportional to the macro-porosity (shown in numbers beside the data points for V_p). Measurements were done under dry conditions.

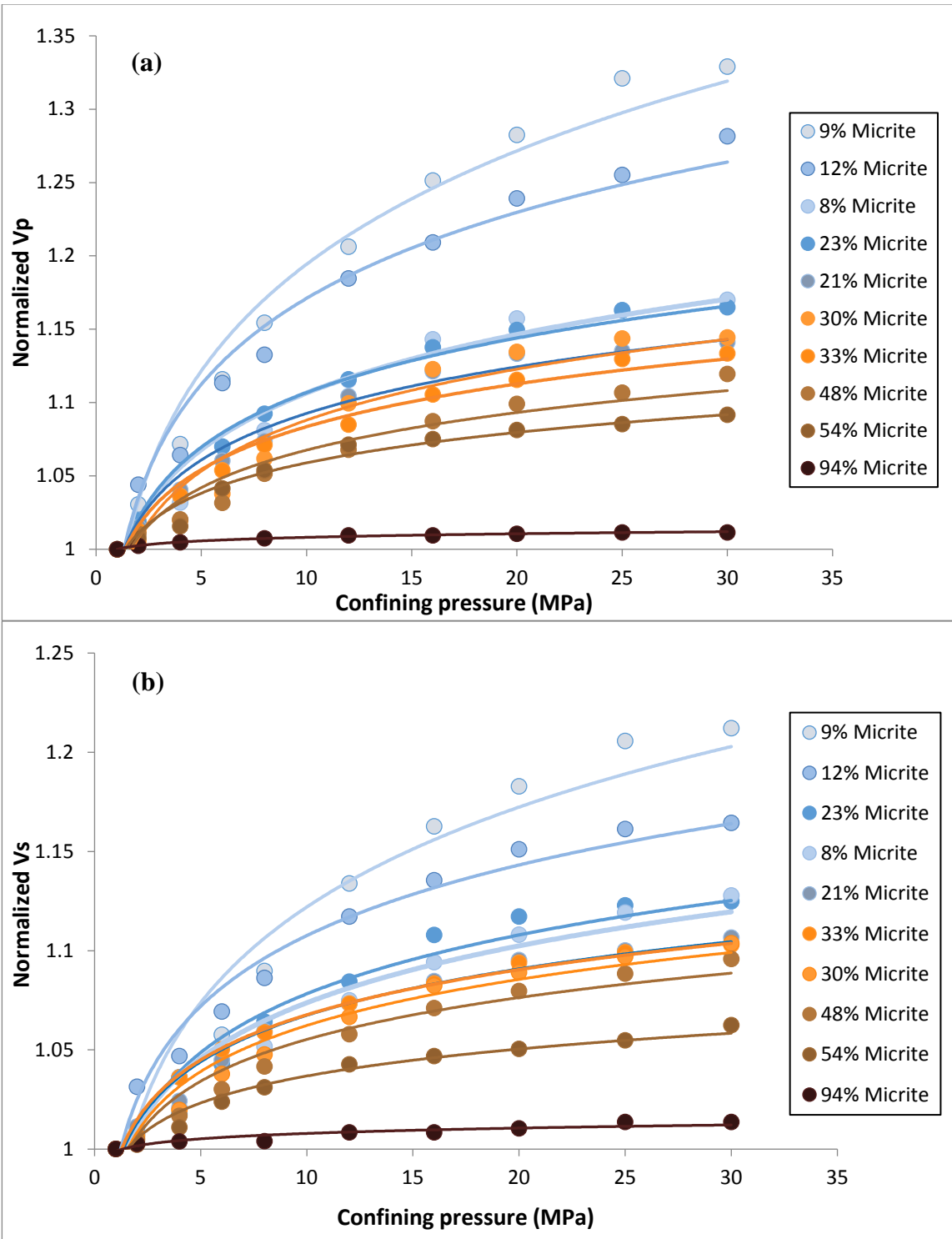


Figure 5.13: Plot of P-wave velocity (a) and S-wave velocity (b), both normalized by velocity at 1 MPa, as a function of confining pressure. Data is color coded by micrite content. The data points for each micrite content were fitted by a best fit power function.

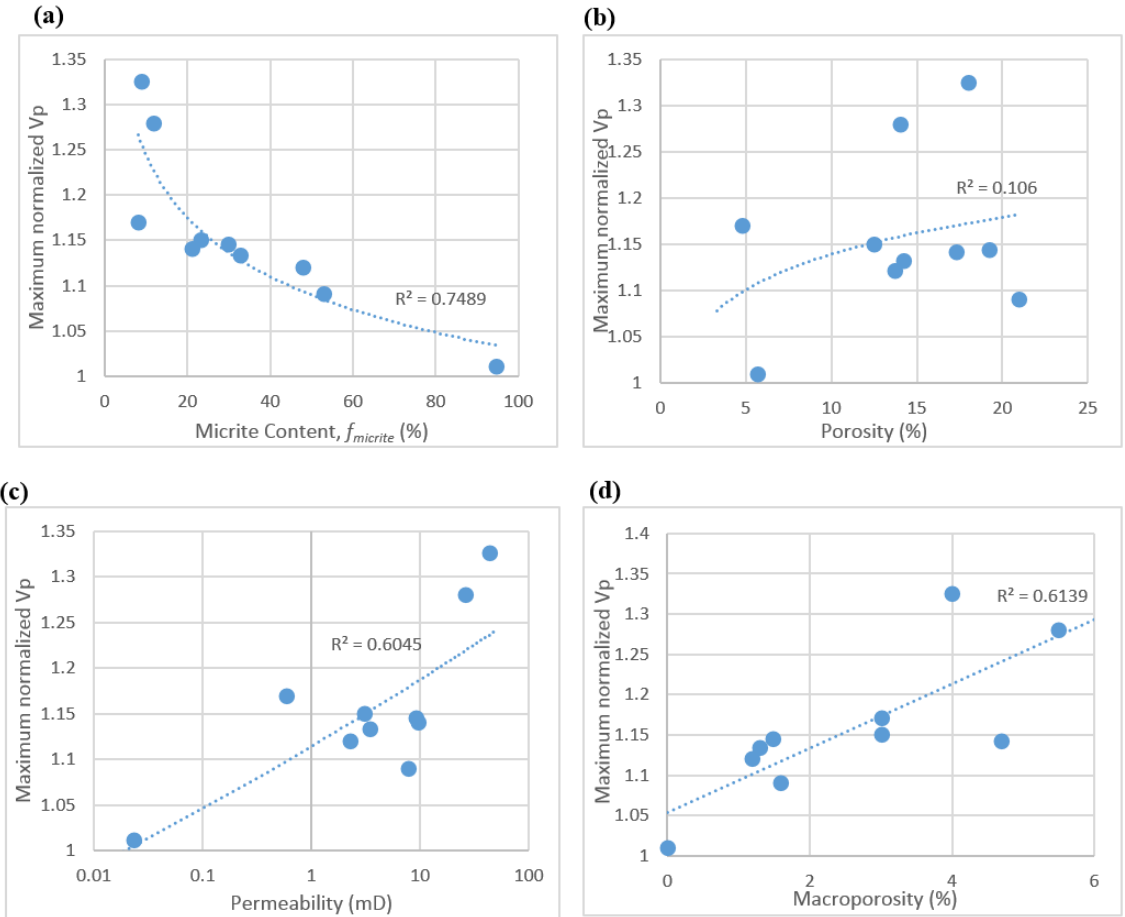


Figure 5.14: Plot of maximum normalized P-wave velocity (V_p measured at 30 MPa divided by V_p measured at 1 MPa) as function of several properties and micro-structural parameters including: (a) micrite content, (b) porosity, (c) permeability, and (d) macro-porosity. The dashed curves correspond to the best fit functions while R^2 refers to the coefficient of determination.

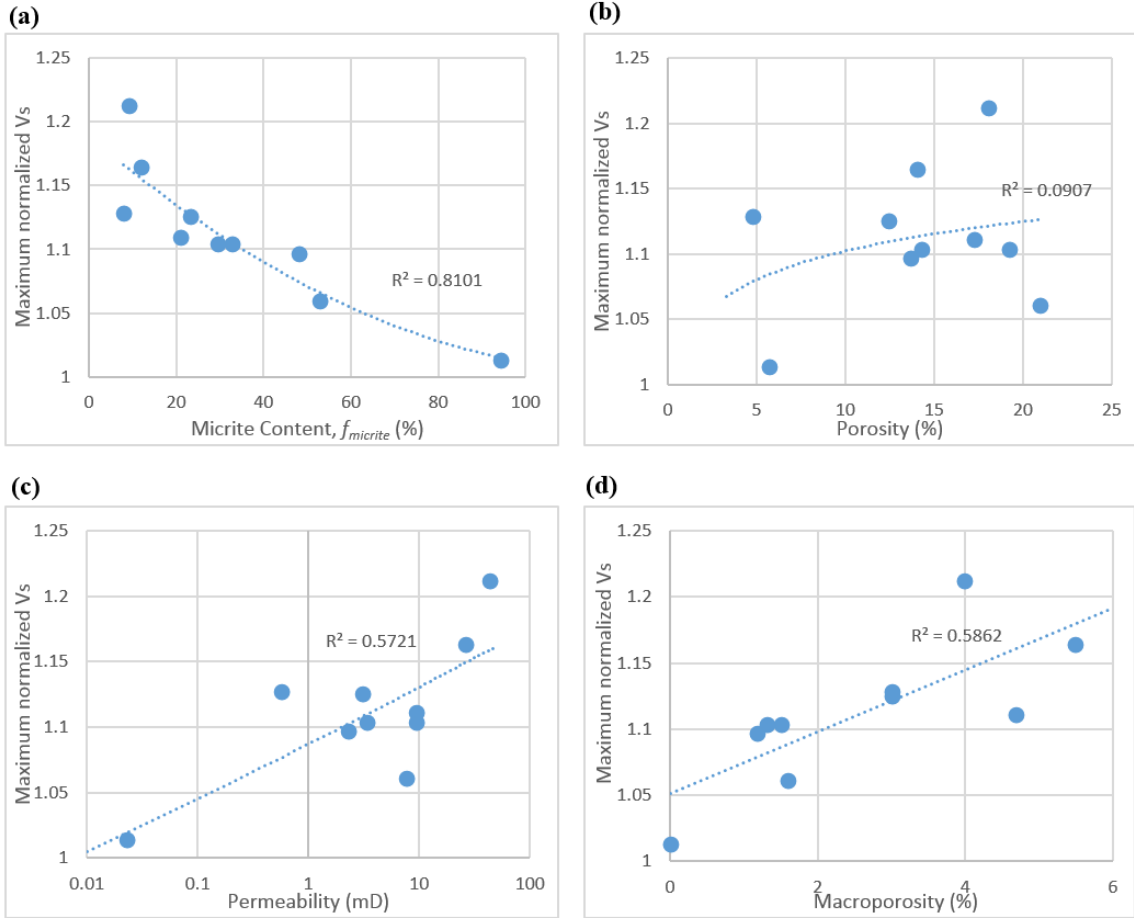


Figure 5.15: Plot of maximum normalized S-wave velocity (V_s measured at 30 MPa divided by V_s measured at 1 MPa) as function of several properties and micro-structural parameters including: (a) micrite content, (b) porosity, (c) permeability, and (d) macro-porosity. The dashed curves correspond to the best fit functions while R^2 refers to the coefficient of determination.

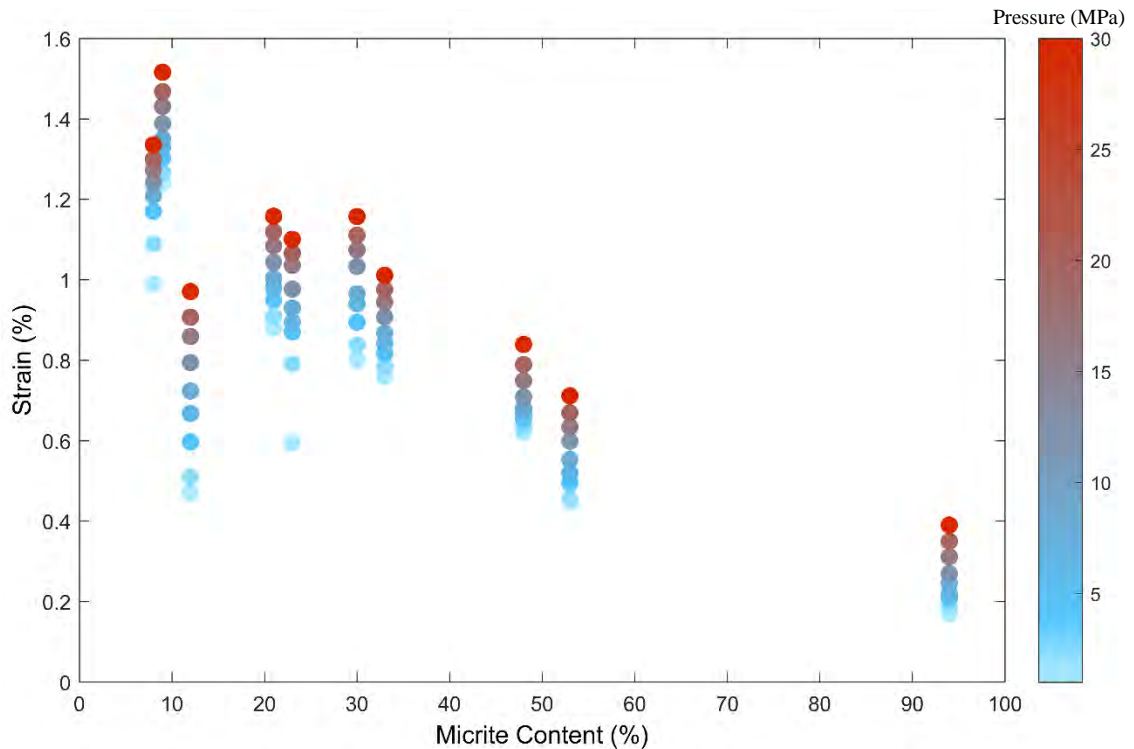


Figure 5.16: Normalized percentage change in length ($100 \times \text{change in length} / \text{sample length}$) as a function of micrite content measured at different pressures (highlighted by different colors).

5.5 Discussion

5.5.1 Parameter Estimation Based on Image Analysis

5.5.1.1 Uncertainty Associated with Parameter Estimation

In this section, we discuss the uncertainty associated with estimation of micro-structural parameters using both micro-CT scans and SEM images. Quantifying the uncertainty is important to determine the appropriate size of the interval used when grouping samples based on a certain parameter. For example, an average error of 7% in estimating micrite content would suggest the use of about 10%-sized intervals when grouping or classifying samples based on their micrite content. The size of the interval must always be larger than the size of error or uncertainty.

One major source of uncertainty is how well the micro-CT scans or SEM images represent the actual core plug sample. The micro-structural parameters in this study were estimated mainly using micro-CT scans except for four samples where no micro-CT scans

were available. When using the micro-CT scans, the standard deviation can be used as a measure of uncertainty indicating how an estimated parameter varies around the mean value (see Table J.1). The standard deviation can be a measure of the heterogeneity in the sample, i.e., how much a certain micro-structural parameter varies throughout the 3D volume obtained from micro-CT scans. The smaller the standard deviation, the higher the chance that the reported average value represents the rock overall. Nevertheless, the proportion of the sample analyzed by the micro-CT scan is much larger than that analyzed by the SEM and hence, the standard deviation obtained when using one technique should not be compared with the other. For the four samples where SEM images were used to estimate the parameters, a lower standard deviation may not necessarily mean relatively lower uncertainty compared to samples where micro-CT scans were used. This suggests the need for an alternative approach to quantify the uncertainty associated with estimating parameters from the SEM images alone in those four samples.

Micro-CT scans can represent the actual micro-structure better than SEM images which are obtained from a single horizontal 2D slice. The question is then: how well do such SEM images represent the actual 3D volume? In order to address this question, we compare the major parameters estimated using micro-CT scans with those obtained from SEM images where both imaging techniques were available (i.e., first 10 samples in Table J.1). Based on this comparison, we can evaluate how well using SEM images reproduces the results of the micro-CT scans, and thereby quantify the uncertainty associated with estimating parameters from SEM instead of CT scans (i.e., for the last four samples in Table J.1, where micro-CT scans were not available). Figure 5.17 demonstrates a comparison between the micrite content ($f_{micrite}$) estimated using micro-CT scans and that estimated based on SEM images. The two techniques are comparable for samples characterized by very low or high micrite content, while there is a non-negligible mismatch for samples with intermediate micrite content (20-60%). We can also notice that the mismatch is more significant for samples where the standard deviation is higher in general (Figure 5.17). That is, the more heterogeneous a sample is, clearly the less likely that a 2D slice from thin section can represent the overall 3D volume. The coefficient of determination between $f_{micrite}$ estimated from micro-CT scans and those obtained from SEM ($R^2=0.88$) can be used as a measure of the overall uncertainty associated with estimating $f_{micrite}$ from SEM instead

of micro-CT. Another measure of uncertainty could be the use of root mean square error (RMSE), which was found to be 8.3%. The magnitude of the error is however much higher at intermediate values (i.e., $20 < f_{micrite} < 60$ as shown in Figure 5.17), thus the RMSE could be expressed as a function of the estimated $f_{micrite}$. We grouped samples based on their estimated micrite content using a 10% increment and then recalculated the RMSE for each group as shown in Figure 5.18. This can provide a measure of uncertainty as a function of the estimated micrite content so that samples with intermediate micrite content would have larger associated RMSE (Figure 5.18). The values of RMSE shown here can be a better measure of uncertainty than standard deviation reported in Table J.1 when micro-CT scans are not available.

The analysis shown in Figures 5.17 and 5.18 can be applied for macro-porosity as shown in Figures 5.19 and 5.20. The results shown in Figure 5.19 indicate that SEM images can reproduce the macro-porosity estimated from micro-CT scans with an overall uncertainty quantified by R^2 of 0.81 and RMSE of 0.98%. The error seems however to be higher for samples characterized by higher macro-porosity as shown in Figure 5.20 where the RMSE is plotted as a function of macro-porosity.

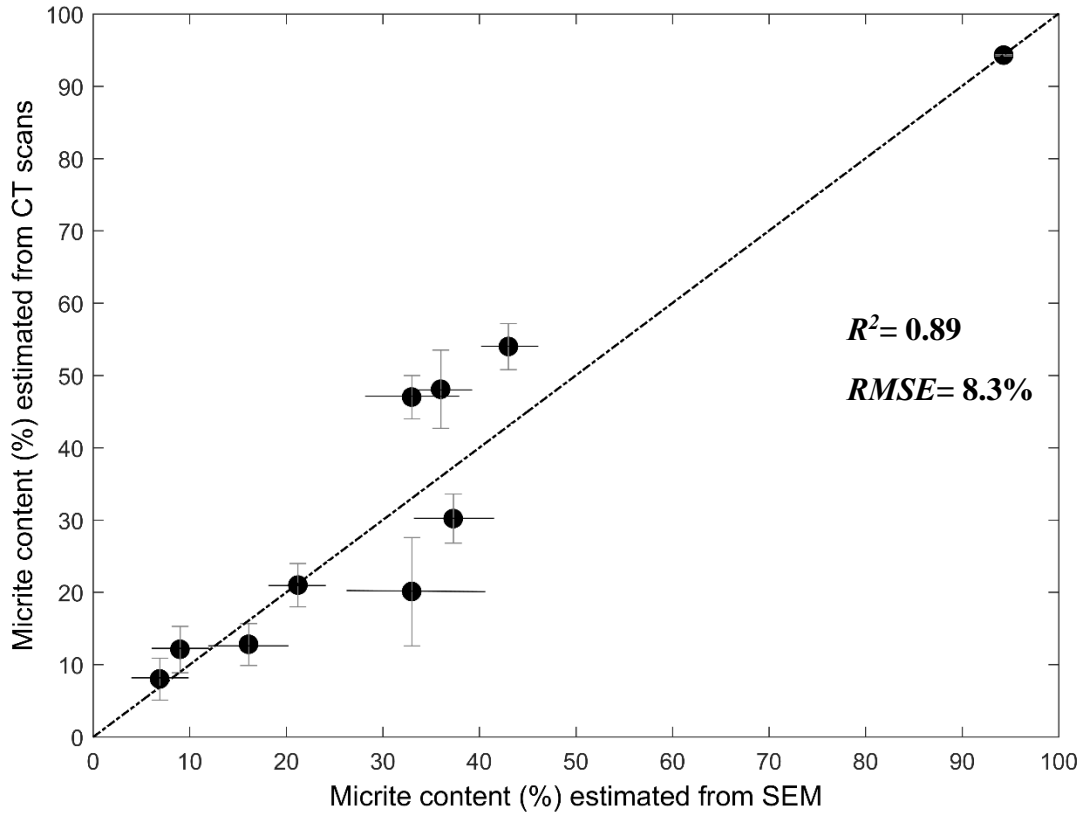


Figure 5.17: Plot of micrite content estimated from SEM versus that obtained from CT scans. The vertical and horizontal bars correspond to the standard deviation associated with average reported micrite content from each technique. The dashed line refers to the one-to-one line. R^2 and RMSE are also reported to the right.

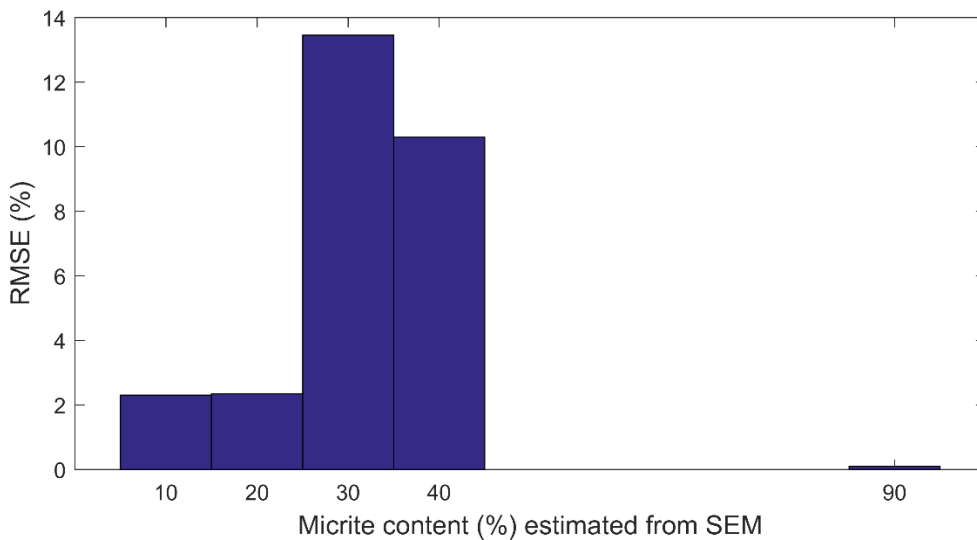


Figure 5.18: RMSE as function of micrite content estimated from SEM for the samples shown in Figure 5.17 but grouped using 10% intervals of micrite content. Each column represents a group of samples based on which the RMSE was calculated.

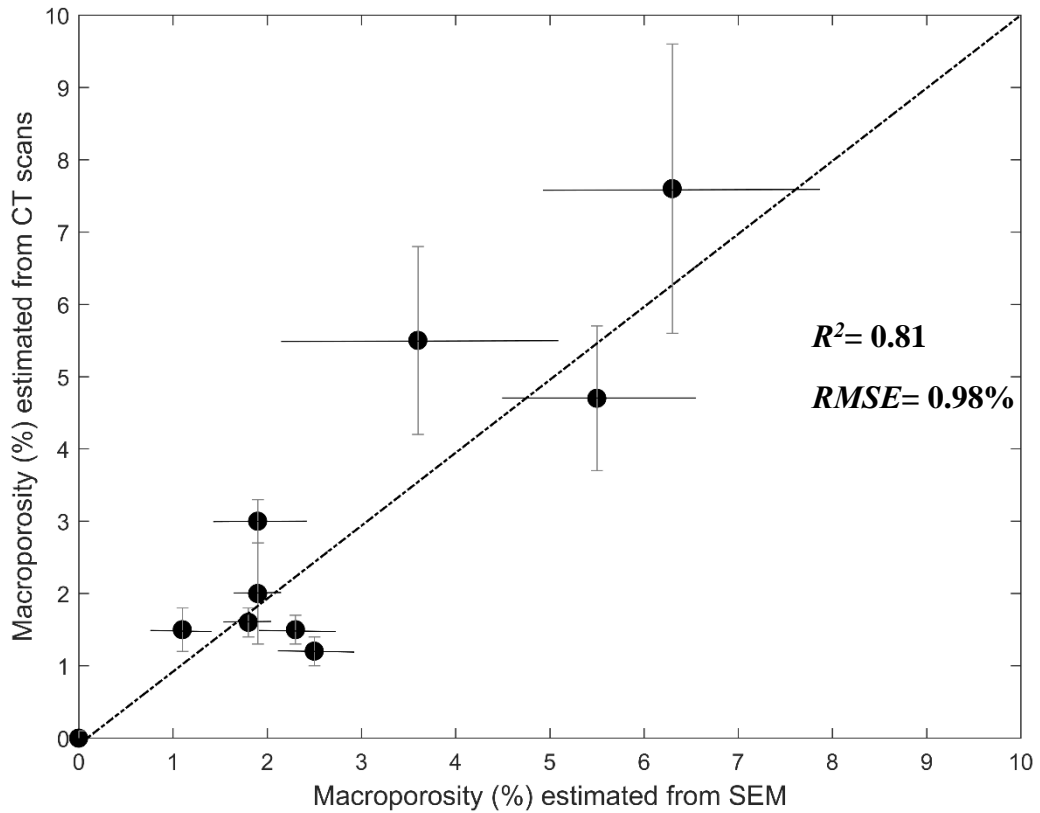


Figure 5.19: Plot of the macro-porosity estimated from SEM versus that obtained from CT scans. The vertical and horizontal bars correspond to the standard deviation associated with average reported macro-porosity estimated using each technique. The dashed line refers to the one-to-one line. R^2 and RMSE are also reported to the right.

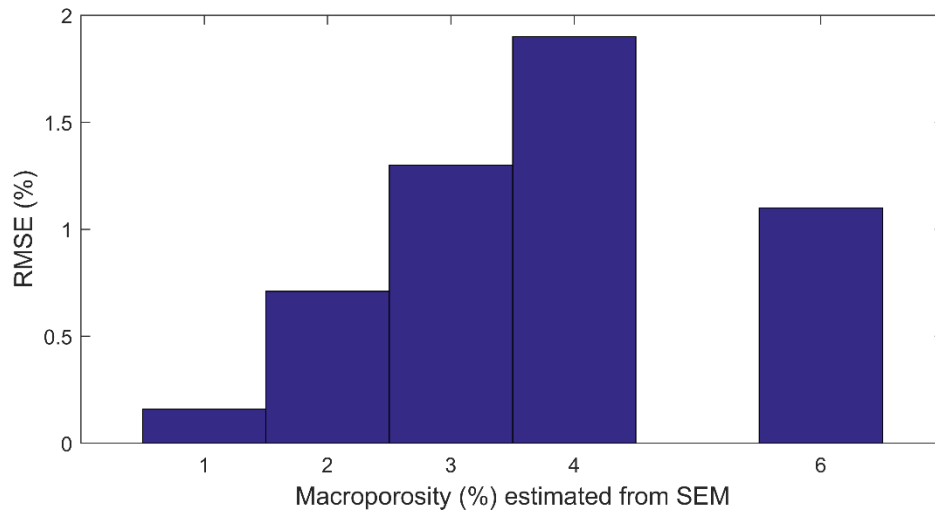


Figure 5.20: RMSE as function of macro-porosity estimated from SEM for the samples shown in Figure 5.19 but grouped using 1% intervals of macro-porosity. Each column represents a group of samples based on which the RMSE was calculated.

5.5.1.2 Limitations in Characterizing Micro-porosity Indirectly

As mentioned earlier, the micro-porosity of the samples was estimated indirectly by subtracting macro-porosity (estimated from micro-CT scans or SEM images) from the total helium porosity. Assuming that all micro-porosity exists within the micrite aggregates, we can indirectly obtain the porosity within the micrite aggregates ($\phi_{micrite_indirect}$) using the estimated parameters from Table J.1 as follows:

$$\phi_{micrite_indirect} = (\phi_{micro}) / (\phi_{micro} + f_{micrite}) \quad (5.1)$$

We then compare the values of the estimated $\phi_{micrite_indirect}$ with the values obtained directly ($\phi_{micrite_direct}$) from the highly magnified SEM images (see Figure 5.7) of micrite aggregates as shown in Figure 5.21. The values obtained from the direct approach are considered the reference values in this case since they better represent the actual micrite aggregates. Through this comparison, we aim to evaluate how well our indirect approach in estimating micro-porosity was successful in reproducing the porosity within the actual micrite aggregates. Based on Figure 5.21, we can notice that $\phi_{micrite_indirect}$ agrees with $\phi_{micrite_direct}$, with slight over-prediction within the uncertainty in general, except for five samples as highlighted in Figure 5.21. The indirect approach significantly over-estimated the porosity within the micrite aggregates for these five samples. Although the porosity within micrite can vary from one location to another within the fabric, such variation, as indicated by the standard deviation in Figure 5.21, is not expected to explain the significant and consistent over-estimation observed.

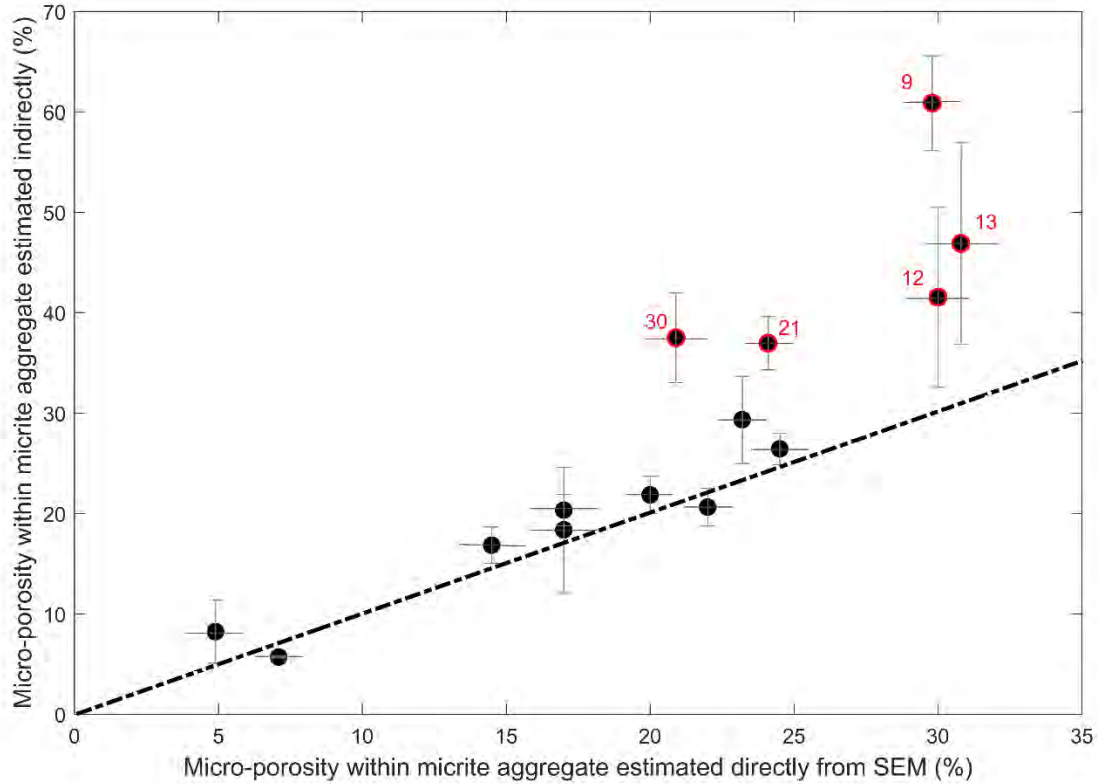


Figure 5.21: Plot of the micro-porosity within micrite aggregate estimated directly from SEM ($\phi_{micrite_direct}$), versus the micro-porosity within micrite estimated indirectly ($\phi_{micrite_indirect}$). The dashed black line refers to the one-to-one line. The five samples showing the most significant discrepancies between ($\phi_{micrite_direct}$) and ($\phi_{micrite_indirect}$) are highlighted in red with their micrite content shown in red numbers beside the data point.

One possible explanation for this observed discrepancy is that our assumption about micro-pores, being exclusively present within the micrite aggregates, may not be valid. The five samples have mainly grain-supported textures, which showed higher sensitivity of acoustic velocities to pressure (Figure 5.13). Therefore, it is expected that those rocks have more micro-cracks compared to micrite-supported samples. The presence of micro-cracks between or within the grains is supported by the SEM observation from those rocks as shown in Figure 5.22, for example. Micro-cracks can add to the volume of micro-pores in those grain-supported samples. Thus, assuming that the whole volume of micro-pores is within the micrite aggregate can lead to an overestimation of porosity within micrite aggregate. However, it is worth noting that the volume of micro-cracks has to be significant (about one-third of total pore volume) in some samples in order to account for the total discrepancies observed in Figure 5.21. This is unlikely given that the volume of micro-

cracks is significantly smaller than the volume of micrite in general, leading the micrite to be the dominant source of micro-porosity in micritic carbonates (Cantrell and Hagerty, 1999; Lucia, 1999; Mallon et al., 2005). We therefore propose an additional explanation for the mismatch observed in those five samples: the macro-porosity is under-represented (and hence, the micro-porosity is over represented) in the millimeter-sized plugs and thin sections compared to the one-inch core plug. Examining the core plugs physically, we can clearly notice the presence of very large vugs (Figure 5.23a) in the samples where there is a large error in estimating the porosity within the micrite aggregates, compared to other samples where the error is small (Figure 5.23b). Such large vugs are avoided when extracting thin sections or millimeters-sized plugs for micro-CT scans in order to obtain an intact sample and avoid breaking the rock. As a result, the macro-porosity in the extracted thin sections or millimeter-sized plug can be significantly lower than the macro-porosity of the original one inch core. This leads to an over-estimation of the micro-porosity which is indirectly estimated by subtracting ϕ_{macro} from the total helium porosity. Consequently, using this over-estimated micro-porosity to obtain $\phi_{micrite_indirect}$ according to equation 5.1 would lead to significant over-estimation compared to the direct approach. In practice, the under-representation of macro-porosity in the extracted millimeter-plugs can be confirmed and corrected if ϕ_{macro} is determined for the one-inch core plug. This can be done using multi-scale CT scans including low resolution scans of the whole one-inch plug in addition to the micro-CT scans. This is however outside the scope of this study since such data was not available.

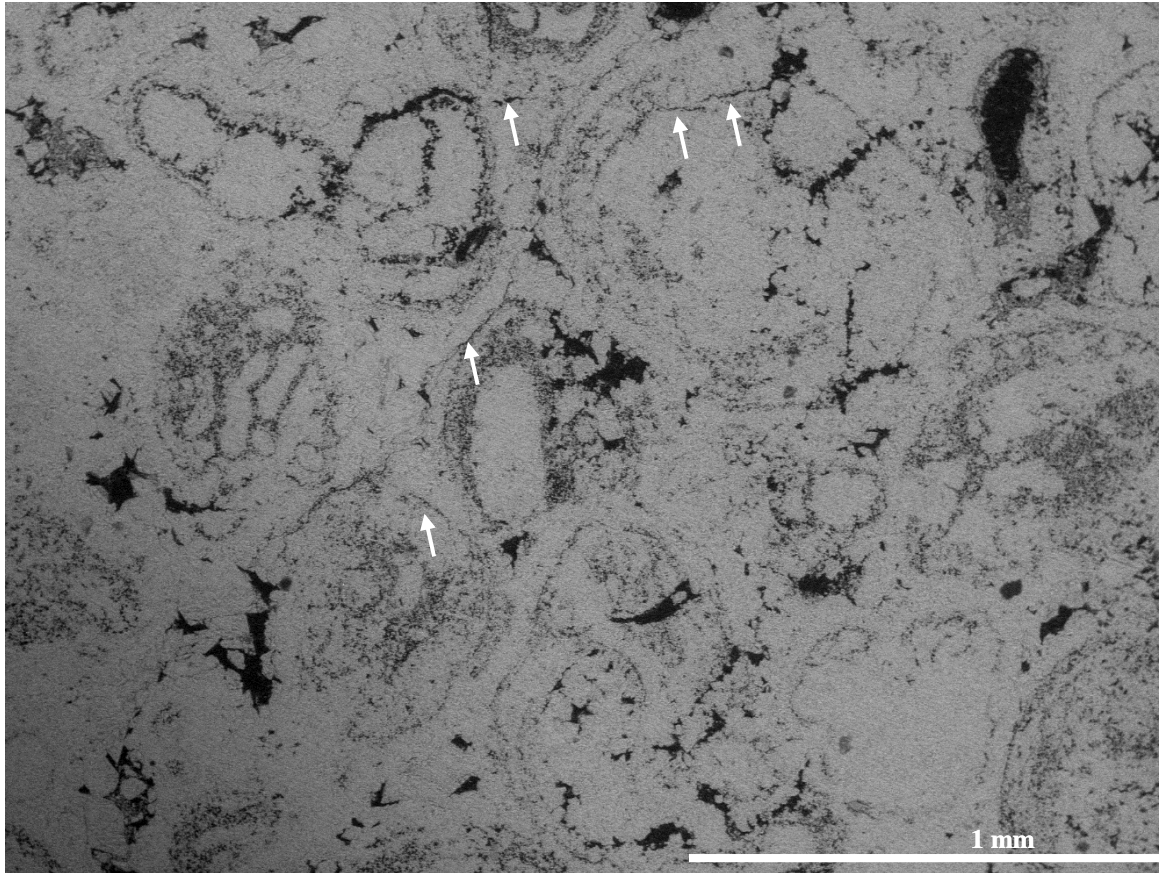


Figure 5.22: SEM image for Tg5 sample; note the presence of micro-cracks as highlighted by white arrows.

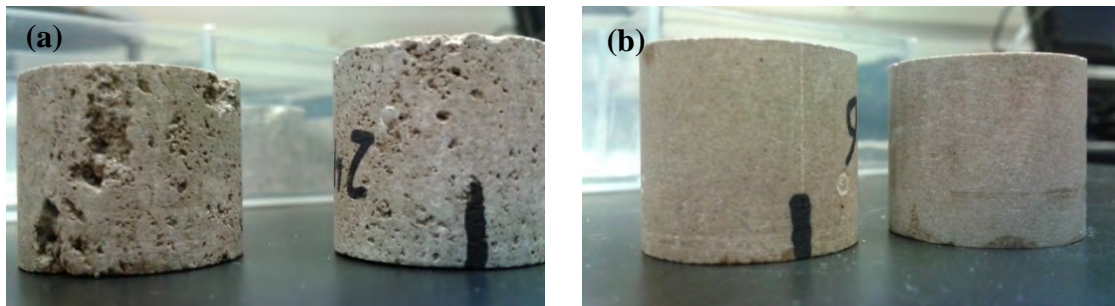


Figure 5.23: Pictures for one-inch core plug samples showing (a) the presence of large vugs for samples where $\phi_{micrite_indirect}$ significantly over-estimated $\phi_{micrite_direct}$, and (b) the absence of large vugs in samples where $\phi_{micrite_indirect}$ and $\phi_{micrite_direct}$ showed good agreement.

5.5.2 Porosity-Permeability Relationships

The results shown in this study (Figures 5.10 and 5.11) suggest that the correlation between porosity and permeability could be improved by incorporating information about key micro-structural parameters including micrite content and macro-porosity. In order to quantify this improvement, we calculate R^2 between porosity and permeability, before and after incorporating the values of each micro-structural parameter. Figure 5.24 shows that R^2 increased from 0.75 to 0.93 when expressing permeability as a function of both porosity and micrite content. The equation relating permeability (k) in mD, to porosity (ϕ) and micrite content ($f_{micrite}$) in percentages, is given by:

$$\log(k) = -5.143 + 0.7933 (\phi) - 0.02004 (f_{micrite}) - 0.01541 (\phi^2) - 0.001835 (\phi)(f_{micrite}) \quad (5.2)$$

Similarly, R^2 increased from 0.75 to 0.94 when expressing the permeability as a function of both porosity and macro-porosity (ϕ_{macro}) as shown in Figure 5.24c. This relation is given by the following equation:

$$\log(k) = -8.139 + 0.7657 (\phi) + 1.291 (\phi_{macro}) - 0.01381 (\phi^2) - 0.05045 (\phi)(\phi_{macro}) \quad (5.3)$$

The effect of increasing micrite content on the porosity-permeability relation can be explained utilizing the approximation of the Kozeny-Carman equation for a pack of spheres, following the same approach shown in Chapter 3 (Section 3.5.2.2). The summary of the modeling approach and the obtained results are shown in Appendix K. Such analysis showed that micrite can exert a major influence on the porosity-permeability relationship of carbonates by: a) reducing the effective particle size (i.e., reducing the sorting of particles) which in turn reduces the pore throat sizes, and b) increasing the percolation porosity below which the porosity is totally disconnected with no contribution to fluid flow. Consequently, the permeability decreases as micrite content increases for a given porosity (Figure 5.24b).

On the other hand, permeability increases as macro-porosity increases for a given porosity (Figure 5.22c). This can be explained by the significant contribution of macro-pores to fluid flow since they have much larger pore sizes compared to micro-pores (Lucia, 1999; Vanorio and Mavko, 2011). Interparticle macro-porosity is generally formed by the deposition of well-sorted calcareous sand-sized particles while such porosity decreases as

the micrite content increases due to decrease in the energy of the depositional environment. Additionally, micrite has fine-grained texture with high surface area and hence, it is prone to diagenesis processes such as dissolution and leaching. This can lead to the introduction of macro-pores at the expense of micrite. As a result, macro-porosity is expected to increase with the decrease of micrite content which is suggested by the general trend shown in Figure 5.25. The scatter in Figure 5.25 might however be explained by the effect of some processes that can create or destroy macro-porosity without significantly affecting micrite content such as dissolution of solid calcareous grains (as shown in Figure 5.26a) or cementation (Figure 5.26b). The content of micrite and macro-pores can then carry information about both the depositional environment and diagenesis whose combined effect determines the porosity-permeability relationship in carbonates.

In order to combine the effect of both micrite content and macro-porosity on permeability, we can utilize linear regression to find the least squares fit of the form:

$$\log(k) = a + b (\phi) + c (f_{micrite}) + d (\phi_{macro}) \quad (5.4)$$

where a, b, c, and d are coefficients. Since the relation between permeability, porosity, micrite content, and macro-porosity is not linear, we need first to linearize the relation so that we can apply the linear regression. Linearization was done by trying different operations (e.g., taking square root or logarithm of ϕ and $f_{micrite}$...etc.), applying the linear regression, and finally examining R^2 between the measured and predicted permeability. We found that the relation in equation 5.4 can be linearized by taking the logarithm of both ϕ and $f_{micrite}$ where it is possible to predict permeability as a function of ϕ , $f_{micrite}$, and ϕ_{macro} using the following equation (obtained by linear regression):

$$\begin{aligned} \log(k) = & -4.4699 + 3.9026 \log(\phi) - 1.3820 \log(f_{micrite}) \\ & + 0.0564 (\phi_{macro}) \end{aligned} \quad (5.5)$$

Figure 5.27 shows the comparison between the measured permeability and the predicted values obtained using equation 5.5. The results shown in Figure 5.27 indicate that equation 5.5 can accurately predict the permeability values ($R^2=0.98$) incorporating the values of both micrite content and macro-porosity. It is important to mention that using three parameters (equation 5.5) improved the prediction of permeability ($R^2=0.98$) but not significantly compared to the use of two parameters only (equation 5.2 or 5.3 where $R^2=0.94$). This could be due to the general inverse relation between micrite content and

macro-porosity (Figure 5.25), and that most macro-pores exist between grains (Figure 5.26). We nonetheless present the approach of linear regression in equation 5.5 since it might be of significant importance in reducing the scatter in other studies and data sets where micrite content and macro-porosity are totally uncorrelated. Incorporating either micrite content or macro-porosity alone may not be sufficient in this case to model and interpret the porosity-permeability relationship. This could correspond for example to isolated moldic or vuggy porosity dispersed in micrite matrix and hence, such macro-porosity will not contribute significantly to the flow. In such case, using equation 5.3 to predict permeability may result in poor predictions, thus suggesting the need to account for the content of micrite as well.

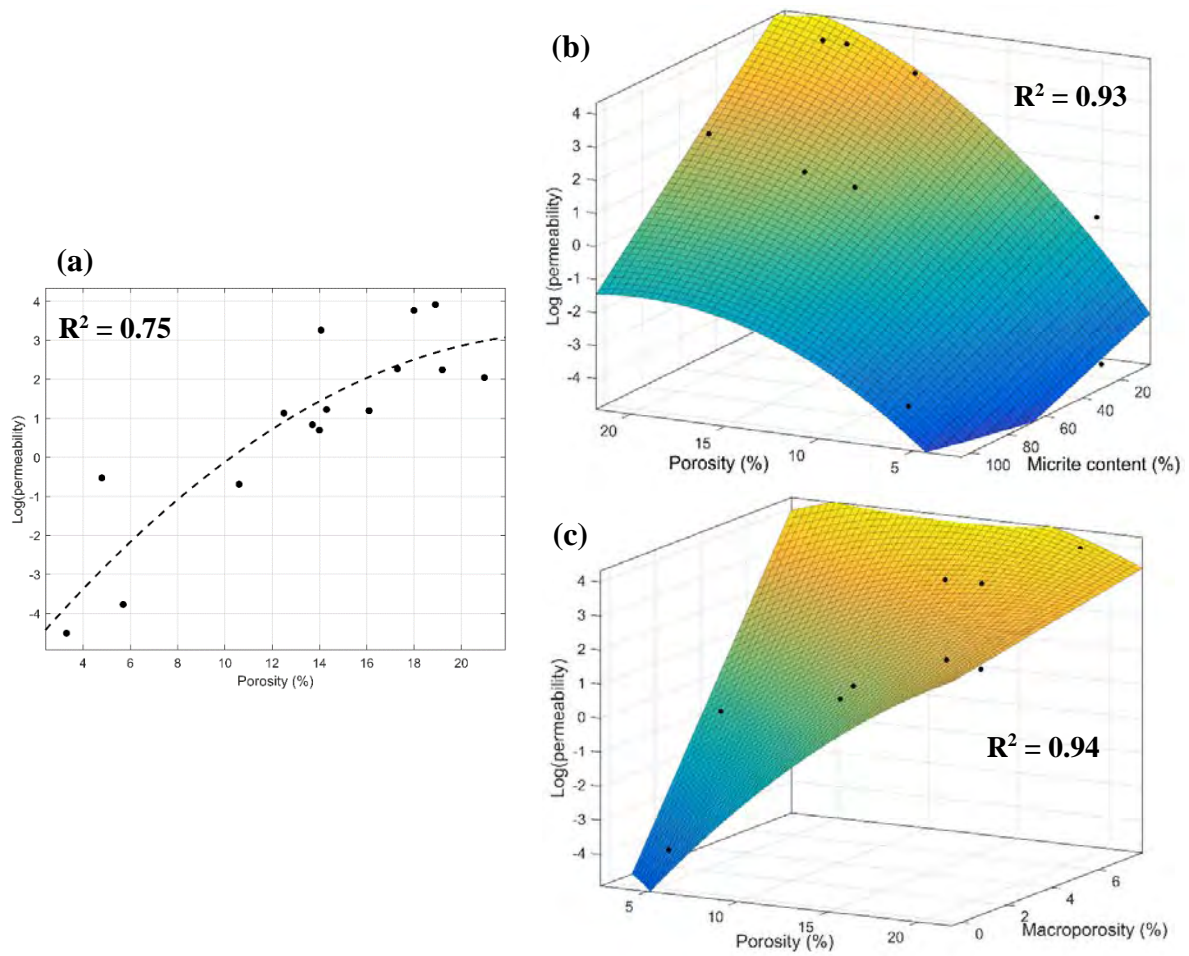


Figure 5.24: Plots of permeability: (a) as function of porosity, (b) as function of both micrite content and porosity, and (c) as function of both porosity and macro-porosity (c). The dashed curve in (a) corresponds to the best fit polynomial (second degree) where R^2 is equal to 0.75. The surface in (b) corresponds to the function (2x1 polynomial) that relates permeability to both porosity and micrite content as shown in equation 5.2. The surface in (c) corresponds to the function (2x1 polynomial) that relates permeability to both porosity and macro-porosity according to equation 5.3. The largest values of permeability (surface is colored in yellow) correspond to samples with largest macro-porosity and smallest micrite content.

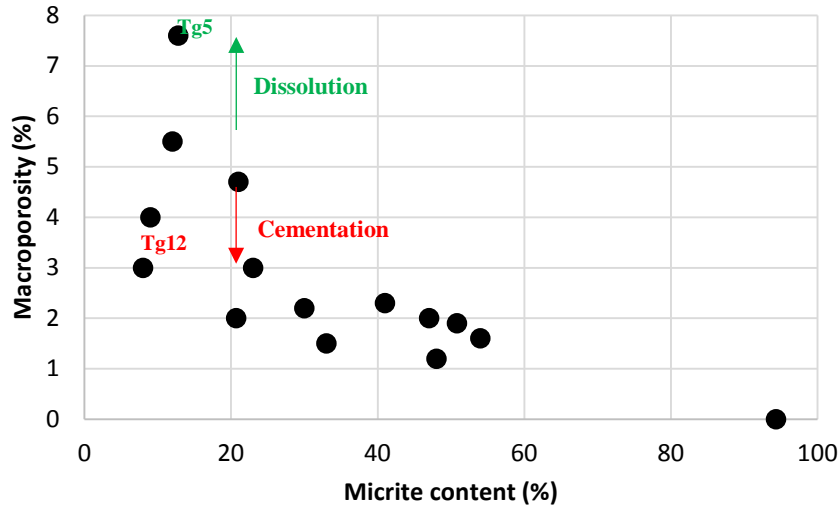


Figure 5.25: Plot of macro-porosity versus micrite content estimated from the selected Tengiz samples. Micrite-supported samples tend to have less macro-porosity compared to samples with low micrite content. For a given micrite content (i.e., given depositional environment), macro-porosity can increase due to dissolution within grains (as shown in Figure 5.26a for sample Tg5) or decrease due to cementation (sample Tg12 in Figure 5.26b).

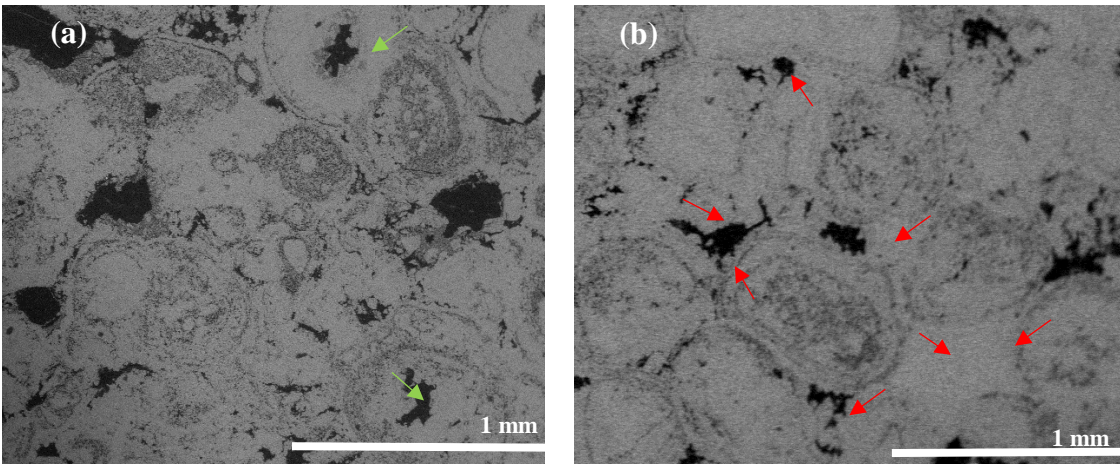


Figure 5.26: SEM images demonstrating: (a) the presence of macro-pores within the grains (highlighted by green arrows) due to dissolution in sample Tg5, and (b) the reduction of macro-porosity in sample Tg12 due to cementation (highlighted by red arrows).

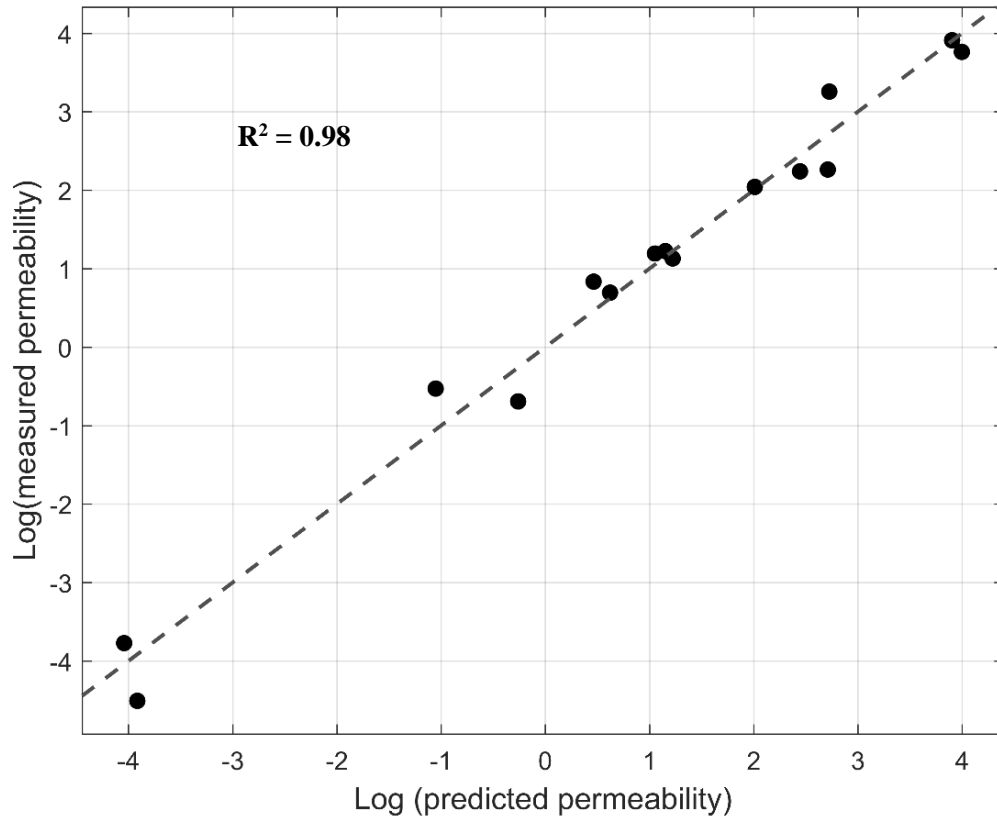


Figure 5.27: Plot of logarithm of measured permeability versus the predicted permeability (using equation 5.5). The dashed black line refers to the one-to-one line.

5.5.3 Effect of Micrite Content and Macro-porosity on Elastic Properties

Figure 5.12 suggested that samples characterized by higher micrite content and lower macro-porosity tend to have higher acoustic velocities. In order to better quantify the effect of micrite content and macro-porosity on the acoustic velocities, we plot the benchtop acoustic velocities as a function of porosity before and after incorporating micrite content and macro-porosity (Figure 5.28). Our analysis showed that R^2 for the V_p -porosity relationship increased from 0.64 to 0.68 and then to 0.8 when adding information about macro-porosity and micrite content, respectively (Figure 5.28 and Table 5.1). A similar trend was also observed for the V_s -porosity relationship where R^2 increased from 0.76 to 0.81 and 0.9 (Figure 5.29 and Table 5.2). Samples with higher micrite content tend to have higher acoustic velocity at a given porosity as suggested by Figures 5.28c and 5.29c. The velocity sensitivity to pressure data may explain why samples with more micrite content

are characterized by larger acoustic velocities. The sensitivity of velocity to pressure increases as the micrite content decreases (Figures 5.13, 5.14a, and 5.15a). The trend of V_p and V_s versus confining pressure in the micrite-supported samples indicates that the samples are tight, with very few compliant pores. Conversely, as the micrite content decreases, the sensitivity of velocity to pressure increases suggesting that grain-supported samples have a more compliant pore structure. This agrees with the change of length for the samples with pressure, as the grain-supported samples suffered from larger decrease in length (Figure 5.16), i.e., larger closure of compliant pores. Therefore, the softer pore structure in grain-supported samples made them less stiff compared to micrite-supported samples. The observations documented here match the ones obtained from the analog samples as shown earlier in Chapter 4.

Since micrite consists of microcrystalline calcite crystals, the stiffer pore structure in micrite might be explained by the interlocking of crystals which form a stiff framework. The process of interlocking crystals and the formations of intercrystalline porosity were suggested by Anselmetti et al. (1997) to increase the stiffness of sucrosic dolomite. Additionally, samples characterized by dominant intercrystalline pores were found to have higher elastic stiffness at a given porosity (Weger et al., 2016). Another factor that might explain the higher elastic stiffness of micrite-supported samples, is the presence of more crack-like pores in grain-supported samples. A close examination of the SEM of grain-supported samples shows the presence of crack-like pores at the grain contacts and within the grains, which are sometimes also crushed (Figure 5.30). The presence of such compliant pores is very rare in samples characterized by higher micrite content (Figures 5.5b, 5.8c and d). Supporting the same argument, an experimental study done by Bhattacharyya and Friedman, 1979 showed that a linear relationship exists between increasing the micrite content and the proportion of the un-deformed and un-cracked grains. Comparable results were also found in geological situations where ooids and shells remain unbroken in micrite-rich carbonates as reported by Shinn et al., 1997, although the rock has undergone significant compaction. The presence of more micro-cracks and crushed grains in the grain-supported samples could be explained by the higher likelihood to break and crack grains during compaction and lithification where cracks radiate from points of contact between grains (Fruth et al., 1966). A high proportion of micrite can keep

the grains in a floating dispersed state and apparently cushions the effect of compaction, where micrite accommodates compaction through ductile deformations (Fruth et al., 1966). Another possibility to explain the presence of micro-cracks in grain-supported samples is that such fabrics are more permeable and likely to become cemented very early, thus are prone to brittle deformation (i.e., fracturing) during shallow burial. Moreover, the pore-lining cement could be preferentially dissolved resulting in crack-like pores along grains boundary. On the other hand, fabrics with higher micrite content (i.e., low permeability) are less likely to be subjected to early cementation and can thus deform in a more ductile manner.

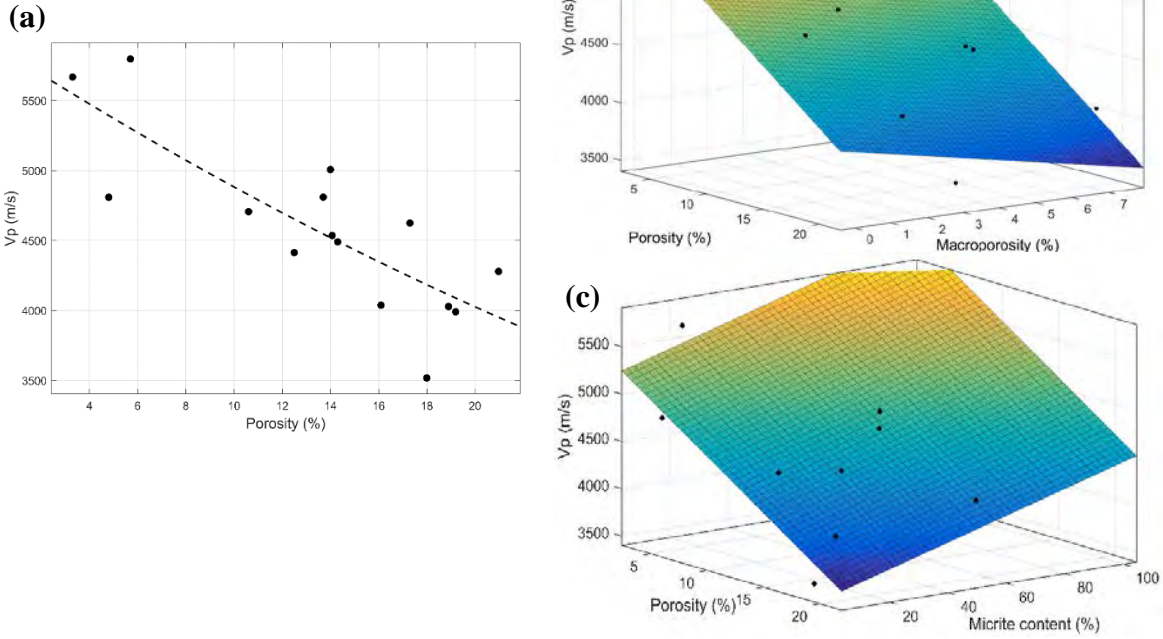


Figure 5.28: P-wave velocity: (a) as function of porosity, (b) as function of both macro-porosity and porosity, and (c) as function of both porosity and micrite content. The dashed curve in (a) corresponds to the best fit polynomial (second degree) while the surface corresponds to the best fit function that relates V_p to both porosity and macro-porosity in (b) and to both porosity and micrite content in (c). The equations of the best fit curves and surfaces are shown in Table 5.1. The change in the color of the surface from blue to yellow corresponds to changing V_p from low to high values, respectively.

Table 5.1: Relations for predicting V_p as function of several parameters

(a) $V_p = 5904 + 0.828 (\phi^2) - 110.5 (\phi)$	$R^2 = 0.64$
(b) $V_p = 5881 - 82.52 (\phi) - 63.85 (\phi_{macro})$	$R^2 = 0.68$
(c) $V_p = 5419 - 84.57 (\phi) + 9.1 (f_{micrite})$	$R^2 = 0.80$

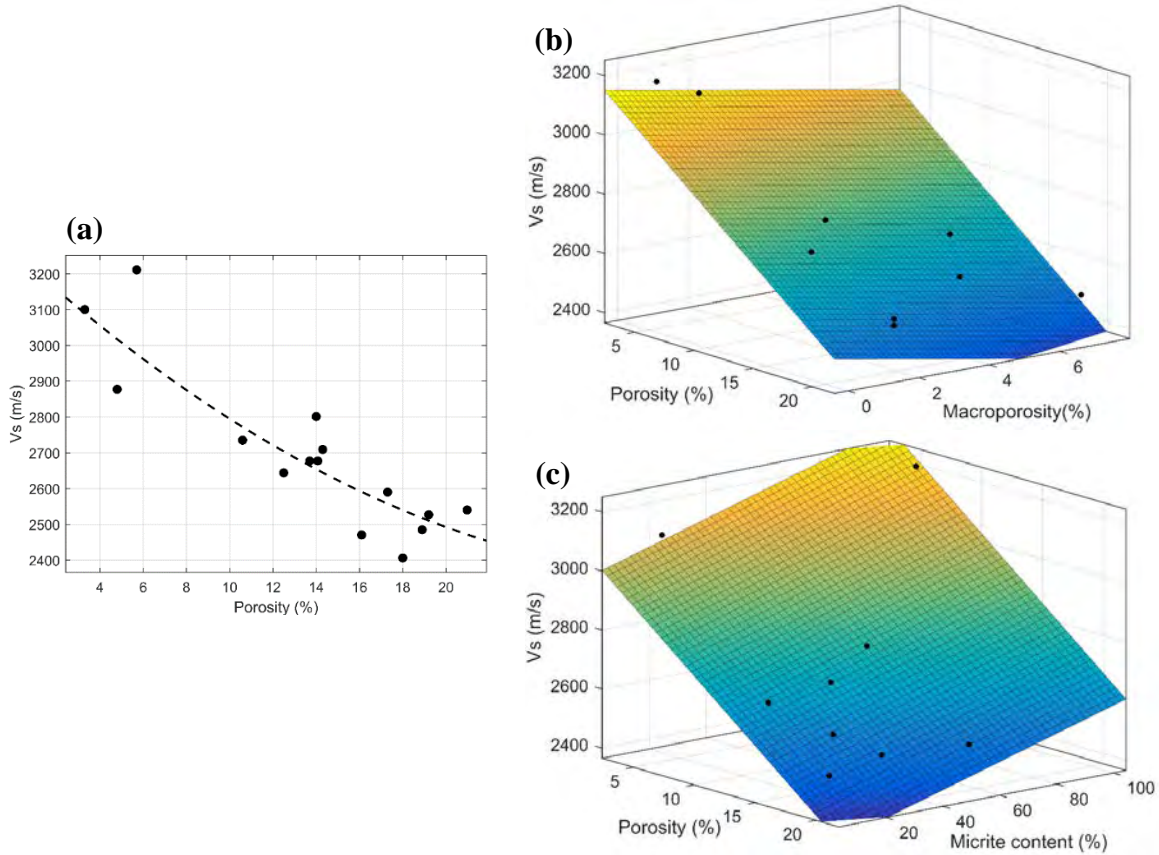


Figure 5.29: S-wave velocity: (a) as function of porosity, (b) as function of both macro-porosity and porosity, and (c) as function of both porosity and micrite content. The dashed curve in (a) corresponds to the best fit polynomial (second degree) while the surface corresponds to the best fit function that relates V_s to both porosity and macro-porosity in (b) and to both porosity and micrite content in (c). The equations of the best fit curves and surfaces are shown in Table 5.2. The change in the color of the surface from blue to yellow corresponds to changing V_p from low to high values, respectively.

Table 5.2: Relations for predicting V_s as function of several parameters

(a) $V_s = 3262 + 0.8245 (\phi^2) - 54.98 (\phi)$	$R^2 = 0.76$
(b) $V_s = 3226 - 34.46 (\phi) - 21.72 (\phi_{macro})$	$R^2 = 0.81$
(c) $V_s = 3078 - 35.31 (\phi) + 2.878 (f_{micrite})$	$R^2 = 0.90$

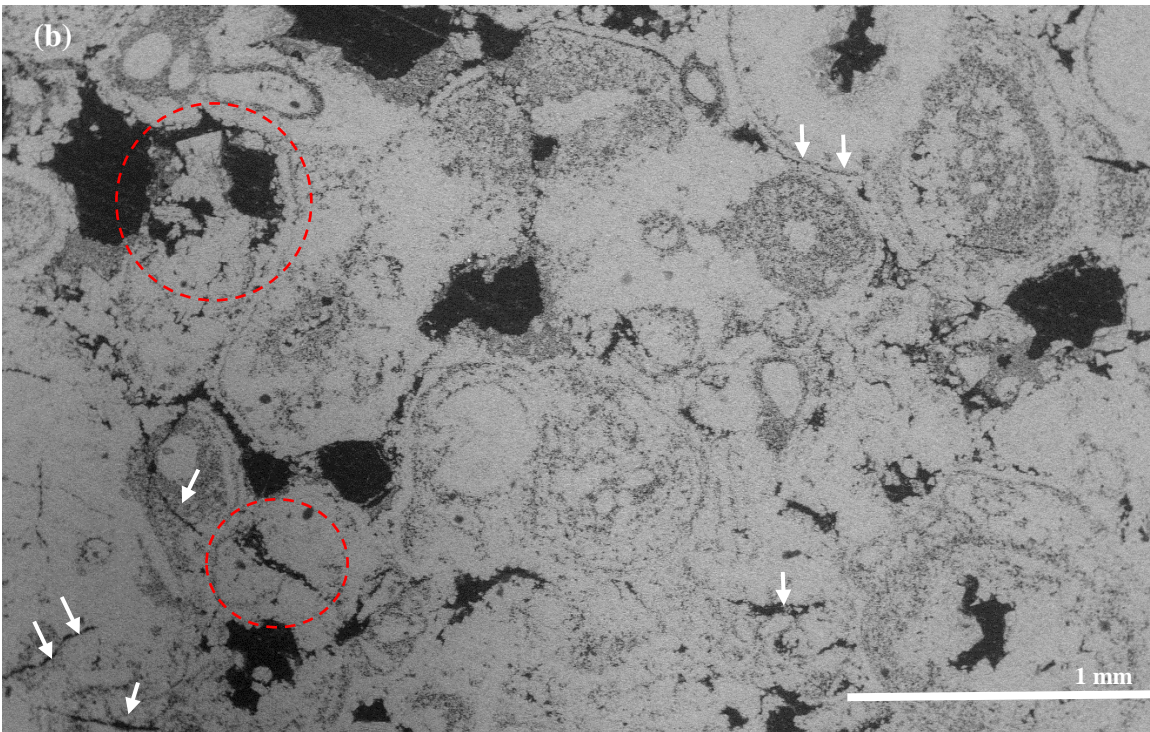
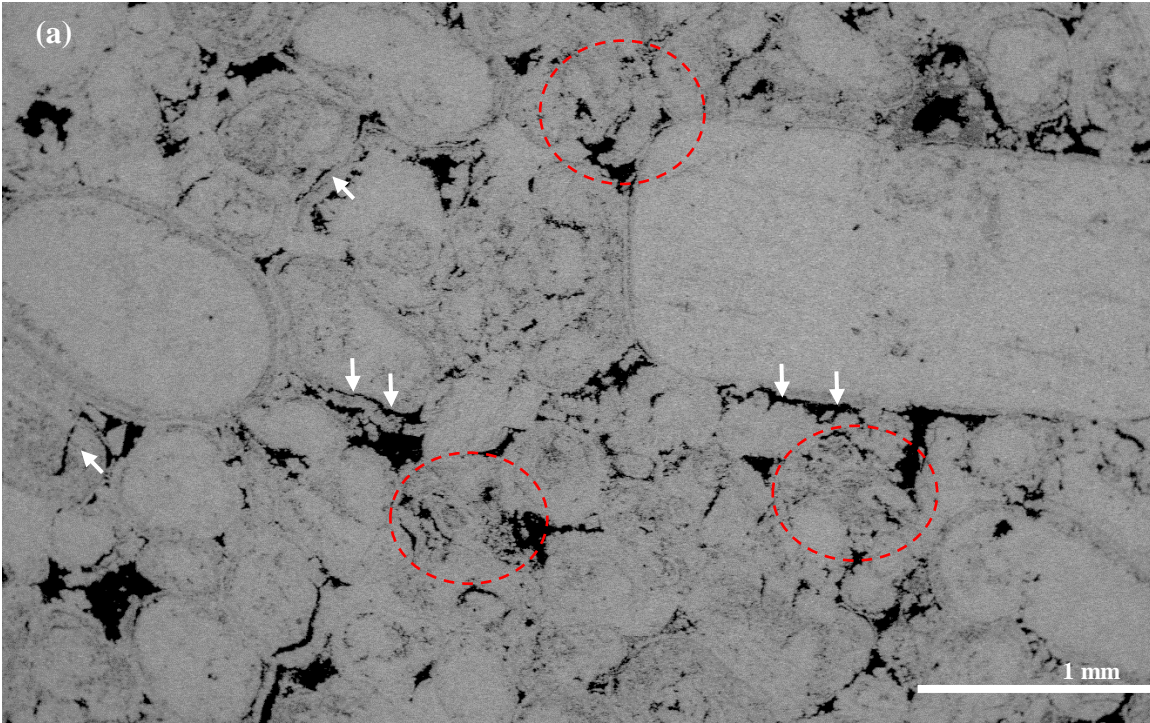


Figure 5.30: SEM images for grain supported samples (a) Tg12 and (b) Tg5 highlighting the presence of crack-like pores (shown by white arrows) between and within the grains. Micro-cracks in this case could be result of brittle deformation or preferential dissolution along grains boundaries. We can also notice the presence of crushed and deformed grains (highlighted by red circles)

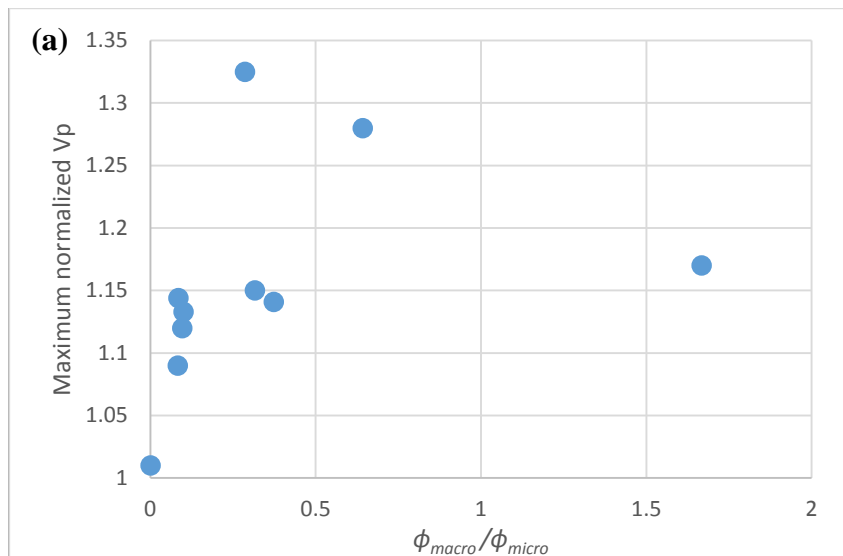
Regarding the effect of macro-porosity on acoustic velocities, samples with larger macro-porosity tend to have lower velocity (Figure 5.28b and 5.29b) and higher sensitivity of velocity to pressure (Figures 5.14d and 5.15d), but a significant scatter remained in the data as suggested by the relatively low R^2 . The R^2 for the velocity-porosity relationship increased very slightly when incorporating macro-porosity into the analysis (Tables 5.1 and 5.2). This result suggests that the amount of macro-pores does not have a major impact on the elastic properties. In order to better examine the effect of relative pore sizes on the elastic properties, we plot the macro-to-micro-porosity ratio versus the velocity sensitivity to pressure as shown in Figure 5.31. The absence of correlation in Figure 5.31 confirms that the size of the dominant pores carries no major information about pore shape and compliance, which agrees with the conclusion we reach in Chapter 4.

5.5.4 Limitations and Possible Further Work

The results of this chapter reported variations of the transport and elastic properties for samples characterized by varying micrite content. Among the selected 15 samples, only one sample has a micrite content larger than 60%. The trends and analysis shown in Figures 5.14 through 5.17 could be consolidated further by adding more samples characterized by very high micrite content. Our results also showed the limitation of estimating micro-porosity indirectly based on the micro-CT scans (Section 5.5.1.2). In order to overcome such limitations, future work on image analysis could consider the use of SEM images along with multi-scale CT scans including low resolution scans of the whole one-inch plug in addition to the micro-CT scans. This can allow for the estimation of macro- and micro-porosity which better represent the actual values of the one-inch core plug used to measure the transport and elastic properties. It is worth mentioning that the texture of core plugs may not represent the large scale depositional environment from which the core was extracted. For example, an extracted plug may capture a fragment with microcrystalline fabric within an overall grain-dominated facies. It is also important to note that the methodology and conclusions of this study may not be applicable for carbonates characterized by dense fractures, which were not the focus of this study. The dominant presence of fractures may control and determine the transport and elastic properties of the rock regardless of its texture. Careful attention should be given to such cases including

challenges related to the characterization of fractures using image analysis and the extraction of representative samples. This can be an important direction for future research which can contribute to better characterization of specific types of carbonates not addressed by this work.

Future work can also consider the incorporation of more rigorous carbonate sedimentology and diagenetic characterization into the analysis shown in this work. This can include classifying the different types of micrite based on their origins (i.e., depositional and variable diagenetic overprints), and analyze the data accordingly. The dominant type of macro-porosity can also be incorporated into the analysis by breaking down macro-porosity into different types including: inter-granular, intra-granular and moldic/vuggy pores.



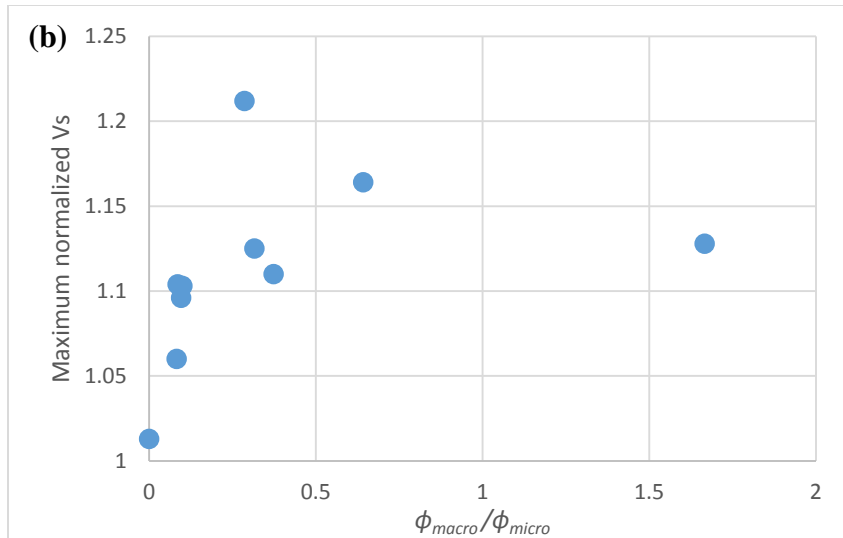


Figure 5.31: Plot of maximum normalized P-wave (a) and S-wave (b) velocity (velocity measured at 30 MPa divided by that measured at 1 MPa) as function of macro-to-micro-porosity ratio.

5.6 Conclusions

The main goal of this study has been to build upon our previous work on carbonate analogs and apply the work flow to carbonate reservoir rocks from the Tengiz Field. We showed how the approach of quantifying micro-structural parameters (such as micrite content and macro-porosity) can be utilized to better interpret and model the rock properties for natural carbonates. We first presented an approach to estimate major micro-structural parameters including micrite content, micro-, and macro-porosity based on micro-CT scans and thin sections of the selected samples. We also developed a method to quantify the uncertainty associated with the estimated parameters and how well they represent the 3D volume of the rock. Our analysis showed that estimating micro-structural parameters from thin sections instead of micro-CT scans can result in larger errors when samples are characterized by intermediate micrite content (20-60%) or large macro-porosity (>3%). The estimated micro-structural parameters were then correlated with the measured transport and elastic properties of the samples. The results of this study show that the trends observed in analog samples hold for the natural carbonates from Tengiz regarding the effect of micrite and macro-porosity on porosity-permeability relation as well as sensitivity of acoustic velocity to pressure. While micrite content in analog samples corresponds to

variations in depositional carbonate mud (i.e., variations in texture from grainstone to mudstone), micrite in the selected samples of this study corresponds to multiple origins of microcrystalline calcite that results from variable diagenetic overprints. This could suggest that the work shown in this thesis may not only hold for analyzing depositional trends, but also for diagenetic characterization in carbonates.

Regarding the effect of micrite content and macro-porosity on the transport properties, samples with higher micrite content and lower macro-porosity were found to have lower permeability at any given porosity. Decreasing micrite content correlates well with increasing permeability because: a) micro-porosity within micrite does not contribute to fluid flow, and b) the fraction of inter-granular macro-pores increases as micrite content decreases in the studied samples. This study suggests that estimating both micrite content and macro-porosity, could play a significant role in the modeling of porosity-permeability relations in dual-grain size, dual-porosity carbonates. Predicting permeability from porosity was improved by 32% when incorporating the micrite content and macro-porosity into the modeling.

Our results regarding the effect of micrite content on elastic properties, showed that micrite aggregates make the rock stiffer — that is, the sensitivity of acoustic velocity to pressure decreases as the micrite content increases. This suggests a stiffer pore structure in micrite aggregates (i.e., intercrystalline porosity between interlocking crystals) compared to that in grain aggregates. Supporting the same argument, samples with higher micrite content experienced less change in length under pressure (i.e., less closure of pores and hence, stiffer pores) compared to grain-supported samples. Moreover, our observation from SEM images showed the presence of more micro-cracks between and within grains in grain-supported samples. Such compliant pores might have formed in this particular data set due to: 1) brittle deformation of early-cemented grains, 2) preferential dissolution of cement along grains boundaries, or 3) concentrated stress in the grain-to-grain contacts in the absence of micrite cushioning the effect of compaction. Unlike micrite content, the amount of macro-pores and the relative pore sizes showed no clear correlation with acoustic velocities and their sensitivity to pressure.

Chapter 6

FINAL REMARKS

In this thesis, we addressed the need for better characterization and, in turn, modeling of the transport (porosity and permeability) and elastic (P- and S-wave velocities) properties of carbonates. In particular, a missing piece of information in the literature is understanding how sedimentology-related parameters such as micrite-to-grain ratio and macro-to-microporosity ratio affect the variability of transport and elastic properties of carbonates.

Towards this goal, I started with studying those relationships on controlled analogs serving as a proof of concept for the analysis of microstructural parameters and then extended the investigation to reservoir carbonates. The primary accomplishment of this thesis is to establish functional relationships between quantifiable sedimentology-related parameters (such as the content of micrite, microporosity, and macropores) and the transport and elastic properties of carbonates. The outcomes of this thesis indicated that

estimates of micrite content, microporosity, and macroporosity are of paramount importance to interpret and model porosity-permeability relationships in carbonates. Another important outcome of this dissertation is to show that increasing micrite content is correlated with an increase in acoustic velocity and a decrease in the sensitivity of velocity to pressure.

While the outcomes of this work can improve the interpretation and modeling of elastic and transport properties in carbonates, it is important to consider potential caveats of the current work, which can point the way to future work. This research reported variations of the transport and elastic properties as a function of varying micrite content. In the preparation of our analog samples, we used micrite particles that have the same shape (sub-rounded) and size (4 μm), since the focus was on the role of micrite content. However, variations in micrite morphology (i.e., shape of particles and their contacts as highlighted in Figure 1.4, Chapter 1) may occur in nature due to dissolution/recrystallization, frequently through fresh-water related diagenesis or subaerial exposure (Lambert et al., 2006; Brigaud et al., 2010; Deville de Periere et al., 2011). Such variations in the shape of micrite particles alter the nature of the contacts at the scale of the grain (i.e., point-contact vs. face-contact), which in turn can affect the transport and elastic properties of the micrite aggregate (Regnet et al., 2015). For instance, the rounded and sub-rounded micrite morphologies are a direct consequence of dissolution of micrite crystal edges, which can result in an overall increase in porosity of the micrite aggregate (Lambert et al., 2006; Fournier et al., 2011). According to Regnet et al. (2015), the porosity of the micrite aggregate increases while the acoustic velocity decreases as the micrite morphology changes from anhedral compact/fused to rounded/sub-rounded. This raises the question of how variations in the morphology of micrite affect elastic and transport properties. We expect that variations in micrite morphology would change the magnitude rather than the nature of the functional relationships observed in this thesis. The presence of compact, anhedral micrite with respect to that of sub-rounded micrite may slightly shift the porosity and/or pore size toward lower values. As a consequence, we may expect a shift of permeability to lower values. This is mainly due to the fact that the permeability of the micrite aggregates will still remain much lower than the grain aggregates regardless of the micrite morphology being mainly influenced by the intergranular porosity.

The second contribution of this thesis is the presentation of an approach to estimate the micrite content, macro-, and microporosity based on the image analysis of micro-CT scans. Due to the documented heterogeneity of carbonates, the results presented in Chapter 5 show that the limited representation of the micro-CT scans compared to the one-inch plug may result in considerable errors, especially when microporosity is estimated indirectly (i.e., as a difference between Helium porosity and macroporosity). This effect is particularly significant for samples characterized by large vugs, whose sampling is missed when extracting millimeter-sized plugs needed for micro-CT scans. Consequently, the macroporosity in the extracted millimeter-sized plug can be significantly lower than the macroporosity of the original one-inch plug. This leads to an over-estimation of the microporosity. In order to overcome this limitation, future work on image analysis could consider the use of multi-scale CT scans including CT scans of the whole one-inch plug for the purpose of macroporosity estimation in addition to the high resolution micro-CT scans, which could instead still be used for the estimation of the micrite content.

An additional caveat that is important to highlight is that the presented approach is not appropriate to distinguish micrite matrix from micritized grains since both can exhibit the same grey scale intensity in CT scans. Micritization is a diagenetic process that occurs due to the action of non-skeletal algae boring into the grains which results in complete or partial transformation of grains from their original internal structure into micrite (Flügel, 2010) as shown in Figure 6.1. Figure 6.2 shows a schematic for cubic packing of coarse spherical grains before (Figure 6.2a) and after (Figure 6.2b) micritization. Estimating micrite content, based on image analysis, would lead to very high values of micrite in samples characterized by the presence of micritized grains (Figure 6.2b) compared to non-micritized grains (Figure 6.2a). This can create a significant scatter in the plot of permeability versus porosity or micrite content. The micrite content of the non-micritized sample in Figure 6.2b should be assigned a value of zero since micrite does not occupy the matrix but rather exists within micritized grains. In addition, the total porosity of the micritized sample will also be higher than the non-micritized sample due to the replacement of solid grains by microporous micrite aggregates. Nevertheless, the permeability of both

samples can be very similar since microporosity within micritized grains does not contribute to flow thus leaving the estimation of macro interparticle porosity unaffected.

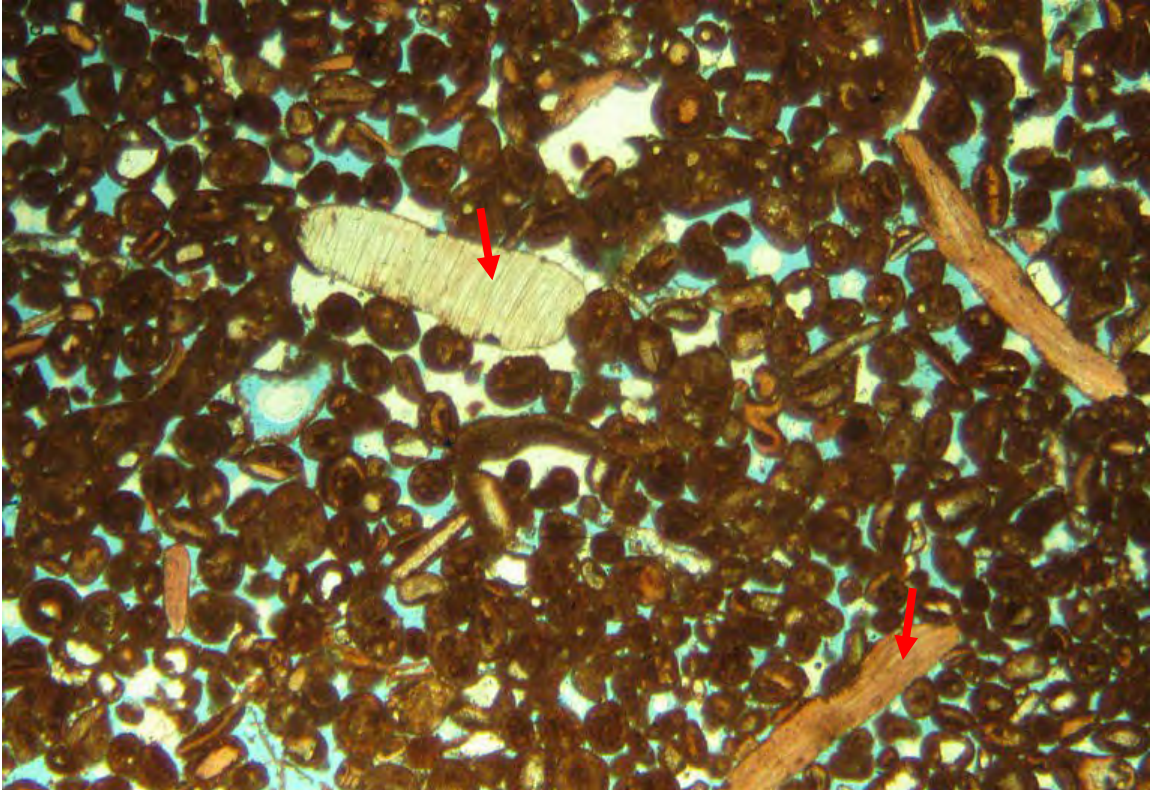


Figure 6.1: Thin section imaged under the optical microscope showing abundant micritized oolites (spherical particles). Porosity is shown by the blue resin. The red arrows refer to examples of non-micritized particles and their internal structure. The field of view is 10 mm. Image is obtained and modified from Imperial College Rock Library.

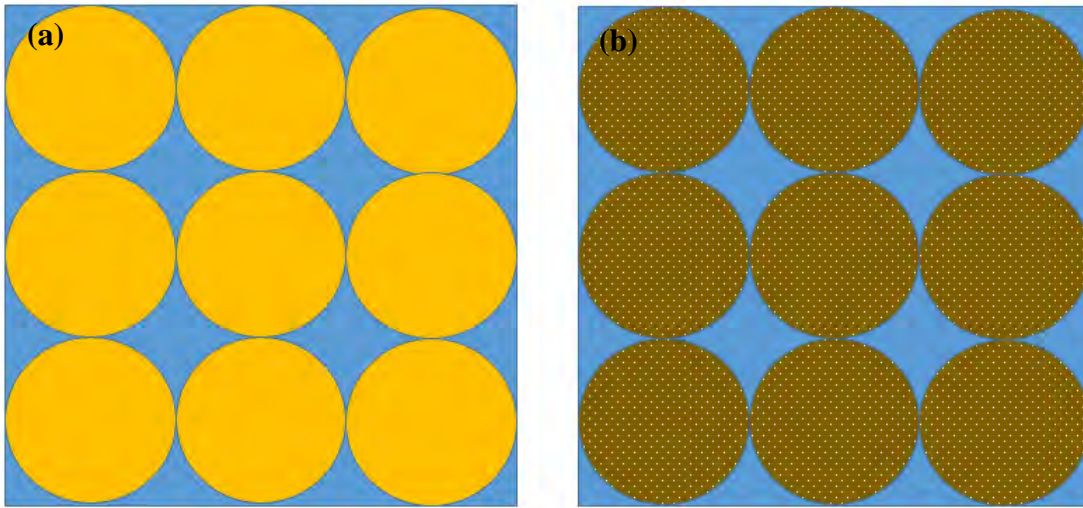


Figure 6.2: Schematic showing cubic packing of non-micritized grains (a) and completely micritized grains (b). The micrite-to-grain indicator (i.e., micrite solid percentage out of total solid volume) is 0% for sample (a) while it is 100% for sample (b). The permeability of both samples would however be similar since both have the same fraction of large interparticle pores (shown in blue) controlling the flow.

It is finally important to note that the findings of this study may not apply to fractured carbonates. The presence of fractures may control and determine the transport and elastic properties of the rock regardless of its micrite content. An example for the role of fractures is demonstrated in Figures 6.3 through 6.5. Figure 6.3 shows the SEM images for four carbonate samples, provided by the OMV Company, that are characterized by variable content of fractures (based on qualitative examination of thin sections). Figures 6.4 and 6.5 demonstrate the porosity-permeability and porosity-velocity relationships respectively for the four samples where data is color coded by micrite content (estimated based on thin sections imaged under SEM). Samples characterized by high micrite content (samples a and b from Figure 6.3) were found to have higher permeability (Figure 6.4) and lower acoustic velocity (Figure 6.5), at a given porosity compared to samples characterized by less micrite content (samples c and d from Figure 6.3). This can be explained by the presence of dominant fractures in these samples (Figure 6.3a and 6.3b) resulting in higher permeability and lower velocity compared to other samples at a given porosity. Fractures can enhance permeability by creating preferential pathways to flow even within the tight matrix while the low aspect ratio of the fractures (i.e., compliant porosity) results in reducing the elastic stiffness. Careful attention should be given to the role of fractures in

controlling the transport and elastic properties as well as to the characterization (size and density) of fractures using image analysis. This can be an important direction for future research, which can contribute to better characterization of a specific type of carbonates that was not addressed by this work.

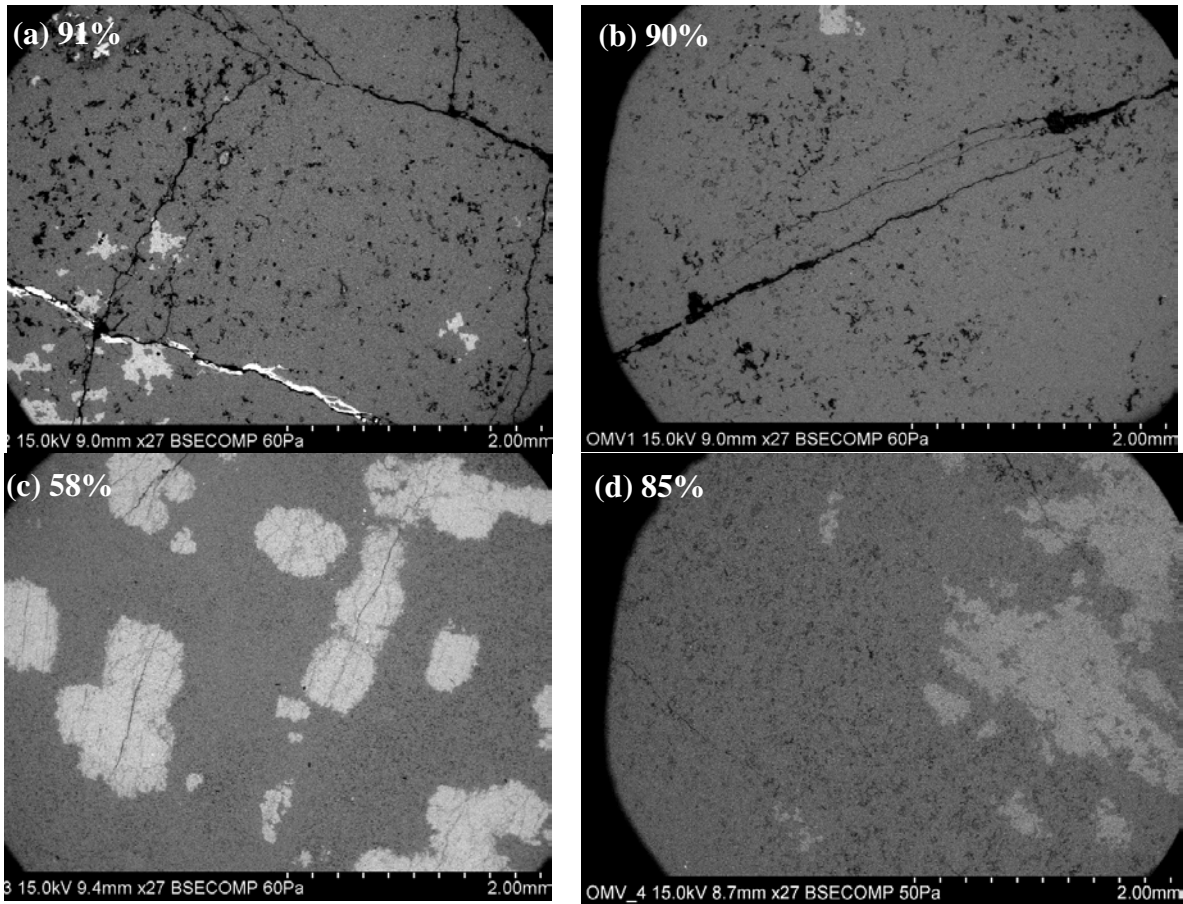


Figure 6.3: SEM images of four different samples characterized by varying content of fractures. The presence of fractures decreases from sample (a) to sample (d). The micrite content of each sample is shown in the upper left corner of each SEM image.

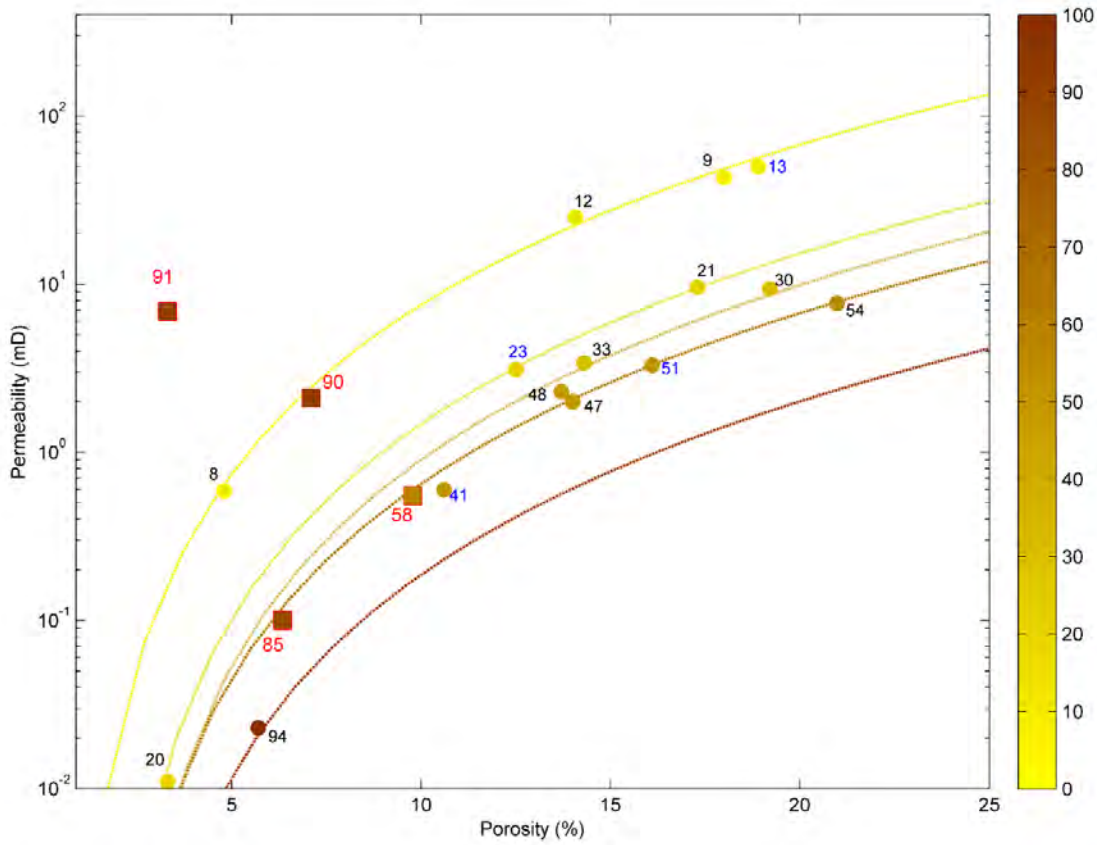


Figure 6.4: Permeability as a function of porosity for all Tengiz samples shown in circles (same data as in Figure K.1; Appendix K), and the four fractured samples (shown in squares). The superimposed dashed curves (yellow to brown color) correspond to the porosity-permeability relationship estimated using Kozeny-Carman relation (Appendix K). All data is color-coded by micrite content which is also specified by the number beside each data point. We notice that the data of the fractured samples does not match the porosity-permeability trends of the Tengiz (un-fractured) samples. Samples with dense fractures (micrite content of 91% and 90%) were found to have higher permeability at a given porosity compared to other samples.

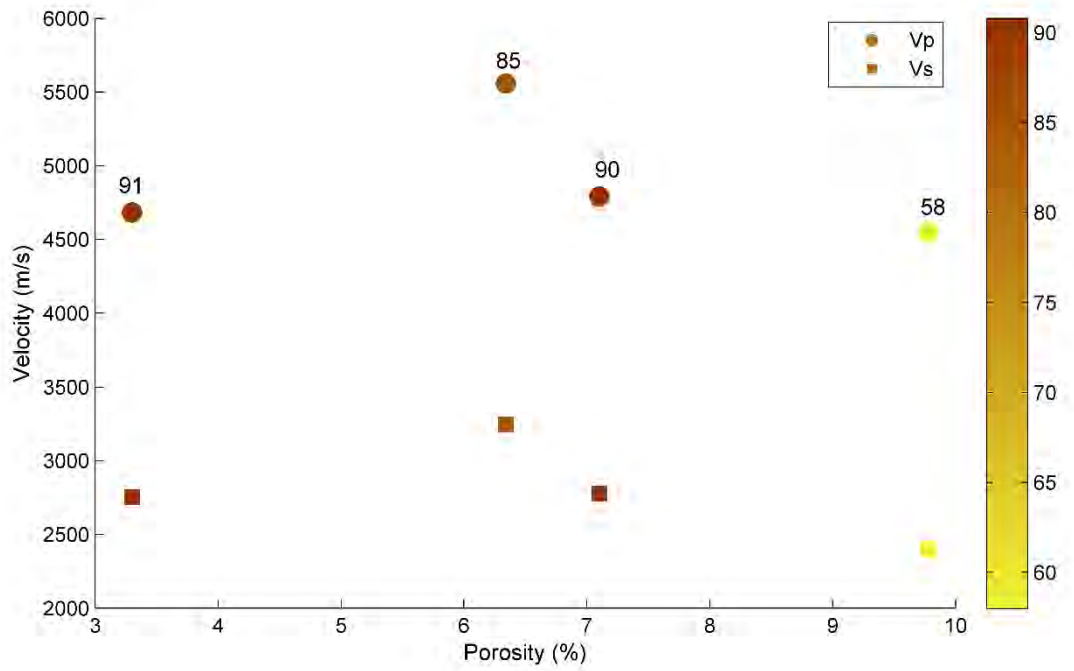


Figure 6.5: P- and S-wave velocity as a function of porosity for the four samples characterized by fractures. Data is color coded by micrite content, which is also shown by the numbers beside the data points for P-wave velocity. The presence of dominant fractures in some samples (Figures 6.3a and 6.3b) resulted in lower acoustic velocity despite the low porosity and high micrite content of the samples.

REFERENCES

- Adam, L., M. Batzle, and I. Brevik, 2006, Gassmann's fluid substitution and shear modulus variability in carbonates at laboratory seismic and ultrasonic frequencies: *Geophysics*, 71, no. 6, F173–F183, doi: 10.1190/1.2358494.
- Allan, A., 2015, Thermal maturation-induced evolution of the elastic and transport properties of organic-rich shales: PhD Dissertation, Stanford University.
- Anselmetti, F. S., and G. P. Eberli, 1993, Controls on sonic velocity in carbonates: *Pure and Applied Geophysics*, 141, 287–323, doi: 10.1007/BF00998333
- Argo IV, T. F., M. D. Guild, P. S. Wilson, M. Schroter, C. Radin, and H. L. Swinney, 2011, Sound speed in water-saturated glass beads as a function of frequency and porosity: *Journal of Acoustical Society of America*, 129, no. 4, EL101-EL107, doi: 10.1121/1.3544678.
- Assefa, S., C. McCann, and J. Sothcott, 2003, Velocities of compressional and shear waves in limestones: *Geophysical Prospecting*, 51, 1–13, doi:10.1046/j.1365-2478.2003.00349.x.
- Baechle, G. T., R. J. Weger, G. P. Eberli, J. L. Massaferrro, and Y. F. Sun, 2005, Changes of shear moduli in carbonate rocks: Implications for Gassmann applicability: *The Leading Edge*, 24, no. 5, 507-510, doi: 10.1190/1.1926808.
- Radiozamani, K., F.T. Mackenzie, and D. C. Thorstenson, 1977, Experimental carbonate cementation: salinity, temperature and vadose-phreatic effects: *Journal of sedimentary petrology*, 47, no. 2, 529-542, doi: 10.1306/212F71CB-2B24-11D7-8648000102C1865D.
- Bentz, D.P., E.J. Garboczi, C. J. Haecker, and O.M. Jensen, 1999, Effects of cement particle size distribution on performance properties of Portland cement-based materials: *Cement and Concrete Research*, 29, 1663-1671
- Berge, P. A., B. P. Bonner, and J. G. Berryman, 1995, Ultrasonic velocity-porosity relationships for sandstone analogs made from fused glass beads: *Geophysics*, 60, no. 1, 108-119, doi: 10.1190/1.1443738.
- Berryman, J. G., 1995, Mixture theories for rock properties, in T. J. Ahrens, ed., *Handbook of physical constants*: AGU, 205–228.
- Berryman, J. G., 1992, Single-scattering approximations for coefficients in Biot's equations of poroelasticity: *Journal of the Acoustical Society of America*, 91, 551–571, doi: 10.1121/1.402518
- Bhattacharyya, A., and G. M. Friedman, 1979, Experimental compaction of ooids and lime mud and its implication for lithification during burial: *Journal of sedimentary petrology*, 49, 1279-1286.
- Boumiz, A., D. Sorrentino, C. Vernet, and F. Tenoudji, 1997, Modelling the development of the elastic moduli as a function of the hydration degree of cement pastes and mortars: *Proceedings 13, 2nd International RILEM Symposium on Hydration and Setting*, ISBN: 2-912143-16-0
- Brigaud, B., B. Vincent, C. Durlet, J. F. Deconinck, P. Blanc, and A. Trouller, 2010, Acoustic properties of ancient shallow marine carbonates: effect of depositional environments and diagenetic processes (Middle Jurassic, Paris Basin, France): *Journal of Sedimentary Research*, 80, 791-807, doi:10.2110/jsr.2010.071.

- Brown, G. G. *Unit Operations*; John Wiley & Sons: New York, 1950.
- Brunauer, S., P. H. Emmett, and E. Teller, 1938, Adsorption of gases in multimolecular layers: *J. Am. Chem. Soc.*, 60, no. 2, 309-319.
- Budd, D. A., 1989, Micro-rhombic calcite and microporosity in limestones: A geochemical study of the lower cretaceous thamama group, U.A.E.: *Sedimentary Geology*, 63, no. 3-4, 293-311, doi: 10.1016/0037-0738 (89)90137-1.
- Cantrell, D. L., and R. M. Hagerty, 1999, Micro-porosity in Arab formation carbonates, Saudi Arabia: *GeoArabia*, 4, no. 2, 129-154.
- Chilingar, V., H. J. Bissell and R. W. Fairbridge, 1967, *Carbonate rocks*, Elsevier Pub. Co.
- Collins, J. F., J. A. M. Kenter, P. M. Harris, G. Kuanysheva, D. J. Fischer, and K. L. Steffen, 2006, Facies and reservoir-quality variations in the late Viséan to Bashkirian outer platform, rim, and flank of the Tengiz buildup, Precaspian Basin, Kazakhstan, in P. M. Harris and L. J. Weber, eds., *Giant hydrocarbon reservoirs of the world: From rocks to reservoir characterization and modeling: AAPG Memoir 88/SEPM Special Publication*, p. 55- 95.
- Craze, R.C., 1950, Performance of limestone reservoirs, *Trans AIME*, 189, 287-94.
- Cumberland, D. J., and R. J. Crawford, 1987, *The packing of particles*, Elsevier Science: Amsterdam, The Netherlands, 1987.
- De Larrard, F., 1999, *Concrete mixture proportioning: A scientific approach*. London: E & FN Spon.
- Deville de Periere, M., C. Durllet, E. Vennin, L. Lambert, R. Bourillot, B. Caline, and E. Poli, 2011, Morphometry of micrite particles in cretaceous microporous limestones of the Middle East: Influence on reservoir properties: *Mar. Pet. Geol.*, 28, 1727-1750, doi:10.1016/j.marpetgeo.2011.05.002.
- Dias, R.P., C. S. Fernandes, J. A. Teixeira, M. Mota, and A. Yelshin, 2008, Permeability analysis in bisized porous media: Wall effect between particles of different size: *Journal of Hydrology*, 349, 470-474.
- Dias, R., J. A. Teixeira, M. Mota, and A. Yelshin, 2006, Tortuosity variation in a low density binary particulate bed: *Separation and Purification Technology* 51, 180-184, doi:10.1016/j.seppur.2006.01.010
- Dou, Q., Y. Sun and C. Sullivan, 2011, Rock-physics-based carbonate pore type characterization and reservoir permeability heterogeneity evaluation, Upper San Andres reservoir, Permian Basin, west Texas: *Journal of Applied Geophysics*, 74, 8-18.
- Dullien, F. A. L., 1992, *Porous Media: Fluid Transport and Pore Structure*: San Diego, CA: Academic Press.
- Dunham, R.J., 1962, Classification of carbonate rocks according to depositional texture, In Ham, W.E. *Classification of carbonate rocks: American Association of Petroleum Geologists Memoir*, 1, 108-121.
- Eberli, G. P., G. T. Baechle, F. S. Anselmetti, and M. L. Incze, 2003, Factors controlling elastic properties in carbonates sediments and rocks: *The Leading Edge*, 22, 654-660, doi:10.1190/1.1599691.
- Egerton, R. F., 2005, *Physical principles of electron microscopy: an introduction to TEM, SEM, and AEM*: Springer.

- El Husseiny, A., and T. Vanorio, 2015, The effect of micrite content on the acoustic velocity of carbonate rocks: *Geophysics*, 80, no. 4, L45-L55, doi: 10.1190/geo2014-0599.1
- Flügel, E., 2010, *Microfacies of carbonate rocks: analysis, interpretation and application*, Springer, New York
- Folk, R. L., 1962, Spectral subdivision of limestone types, in W. E. Ham, ed., *Classification of carbonate rocks—A Symposium: AAPG Memoir*, 62–84.
- Fournier, F., and J. Borgomano, 2009, Critical porosity and elastic properties of microporous mixed carbonate-siliciclastic rocks: *Geophysics*, 74, no. 2, E93–E109, doi:10.1190/1.3043727.
- Fournier, F., P. Leonide, K. Biscarrat, A. Gallois, J. Borgomano, and A. Foubert, 2011, Elastic properties of microporous cemented grainstones: *Geophysics*, 76, no. 6, E211–E226, doi: 10.1190/gpysa7.76.e175_1.
- Fruth, L. S., G. R. Orme, and F. A. Donath, 1966, Experimental compaction effects in carbonate sediments: *J. Sed. Petrology*, v. 36, p. 747-754.
- Furnas, C. C., 1928, The relationship between specific volume, voids, and size composition in
- Gassmann, F., 1951, Ueber die Elastizitaet poroeser Medien: *Vierteljahrsschrift der Naturforschenden Gesellschaft Zuerich*, 96, 1–23.
- German, R. M., 1989, *Particle Packing Characteristics*, Metal Powder Industries Federation, Princeton, NJ, 1989.
- Goddard, J. D. _1990_. “Nonlinear elasticity and pressure-dependent wave speeds in granular media.” *Proc. R. Soc. London, Ser. A* 430, 105–131.
- Grasby S. E. and R. N. Betcher, 2002, Regional hydrogeochemistry of the carbonate rock aquifer, southern Manitoba: *Canadian Journal of Earth Sciences*, 39, no. 7, 1053–1063, doi:10.1139/e02-021.
- Han, D. H., 1986, *Effects of Porosity and Clay Content on Acoustic Properties of Sandstones and Unconsolidated Sediments: Ph.D. Dissertation*, Stanford University
- Han, D. H., A. Nur, and D. Morgan, 1986, Effects of porosity and clay content on wave velocities in sandstone: *Geophysics*, 51, 2093–2107, doi:10.1190/1.1442062.
- Hawkins, P., P. Tennis, and R. Detwiler, 2003, *The Use of Limestone in Portland Cement: A State-of-the-Art Review*, EB227, Portland Cement Association, Skokie, Illinois.
- Iannella, M., 1985, *The effect of particle shape on porosity*, B. Engineering Thesis, The Univeristy of Wollongong, Australia.
- Ismail, M. A., H. A. Joer, M. F. Randolph, and A. Meritt, 2002, Cementation of porous materials using calcite: *Geotechnique*, 52, no. 5, 313–324, doi:10.1680/geot.2002.52.5.313.
- Kamann, P.J., R.W. Ritzi, D.F. Dominic, and C.M. Conrad, 2007, Porosity and permeability in sediment mixtures: *Ground Water*, 45, 429–438.
- Kenter, J. A. M., H. Braaksma, K. Vewer, and X. M. T. Lanen, 2007, Acoustic behavior of sedimentary rocks: Geological properties versus Poisson’s ratio: *The Leading Edge*, 26, 436–444, doi: 10.1190/1.2723206.
- Klinkenberg, L. J., 1941, *The Permeability Of Porous Media To Liquids And Gases: SPE* 41-200.

- Knoll, M. D., 1996, A petrophysical basis for ground penetrating radar and very early time electromagnetics: electrical properties of sand-clay mixtures, PhD thesis, The University of British Columbia.
- Kowallis, B. J., L. E. A. Jones, and H. F. Wang, 1984, Velocity–porosity–clay content systematics of poorly consolidated sandstones: *Journal of Geophysical Research*, 89, B12, 10355–10364, doi:10.1029/JB089iB12p10355.
- Kozeny, J., 1927, Überkapillareleitung des Wassers im Boden: *Sitzungsberichte der Wiener Akademie des Wissenschaften*, 136, p. 271–306.
- Kwan, A. K. H., V. Wong, and W. W. S. Fung, 2015, A 3-parameter packing density model for angular rock aggregate particles: *Powder Technology*, 274, 154–162.
- Lambert, L., C. Durllet, J. P. Loreau, and G. Marnier, 2006, Burial dissolution of micrite in Middle East carbonate reservoirs (Jurassic-Cretaceous): Keys for recognition and timing: *Marine and Petroleum Geology*, 23, no. 1, 79–92.
- Ling, H., Z. Lun, L. Jianxin, M. Ji, L. Ruilin, W. Shuqin and Z. Wenqi, 2014, Complex relationship between porosity and permeability of carbonate reservoirs and its controlling factors: A case study of platform facies in Pre-Caspian Basin: *PETROL. EXPLOR. DEVELOP.*, 41, no. 2, 225–234.
- Lucia, F.J., 1995, Rock-Fabric/Petrophysical Classification of Carbonate Pore Space for Reservoir Characterization, *American Association of Petroleum Geologists Bull.*, 79 (9): 1275-1300.
- Lucia, F. J., 1999, *Carbonate reservoir characterization*. Springer.
- Mallon, J. A., R. E. Swarbrick and T. J. Katsube, 2005, Permeability of fine-grained rocks: New evidence from chalks: *Geology*, 33, no.1, 21-24, doi: 10.1130/G20951.
- Marion, D., A. Nur, H. Yin, and D. Han, 1992, Compressional velocity and porosity in sand-clay mixtures: *Geophysics*, 57, 554–563, doi:10.1190/1.1443269.
- Marion, D. P., 1990, Acoustical, mechanical and transport properties of sediments and granular materials: Ph.D. dissertation, Stanford University.
- Mavko, G., and D. Jizba, 1991, Estimating grain-scale fluid effects on velocity dispersion in rocks: *Geophysics*, 56, 1940–1949.
- Mavko, G., T. Mukerji, and J. Dvorkin, 2009, *The rock physics handbook: Tools for seismic analysis in porous media*: Cambridge University Press.
- Mavko, G. and A. Nur, 1997, The effect of a percolation threshold in the Kozeny–Carman relation: *Geophysics*, 62, 1480–1482.
- Mazzullo, S.J., 2004, Overview of porosity evolution in carbonate reservoirs, *Kansas Geol. Surv. Bull.*, 79, pp. 22–28.
- McGeary, R. K., 1961, Mechanical packing of spherical particles: *J. Am. Ceram. Soc.*, 44, 513-522.
- Milewski, J. V., 1978, The Combined packing of rods and spheres in reinforcing plastics: *Ind. Eng. Chem. Prod. Res. Dev.*, 17, 363-366
- Milewski, J. V., 1973, A study of the packing of fibers and spheres, Ph.D thesis, Rutgers University, New Brunswick, NJ.
- Mota, M., J. A. Teixeira, W. R., Bowen, and A. Yelshin, 2001, Binary spherical particle mixed beds: porosity and permeability relationship measurements: *Trans. Filt. Soc.*, vol 1 (4), 101.

- Mota, M., J. A. Teixeira, W. R. Bowen, and A. Yelshin, 2003, Interference of coarse and fine particles of different shape in mixed porous beds and filter cakes: *Minerals Engineering*, 16, 135-144.
- Mota, M., J. A. Teixeira, W. R. Bowen, and A. Yelshin, 2001, Binary spherical particle mixed beds : porosity and permeability relationship measurement: *Transactions of the Filtration Society*, 1, no. 4, 101-106.
- Moshier, S. O., 1989, Micro-porosity in micritic limestones: A review: *Sedimentary Geology*, 63, no. 3-4, 191-213, doi:10.1016/0037-0738(89)90132-2.
- Norris, A. N., 1985, A differential scheme for the effective moduli of composites: *Mechanics of Materials*, 4, 1-16, doi: 10.1016/0167-6636(85) 90002-X.
- Osuji, S. O., and I. Inerhunwa, 2015, Determination of optimum characteristics of binary aggregate mixtures: *Civil and Environmental Research*, 7, no. 6, ISSN 2224-5790.
- Petty, D.M., 1988, Depositional Facies, Textural Characteristics, and Reservoir Properties of Dolomites in Frobisher-Alida Interval in Southwest North Dakota, *American Association of Petroleum Geologists Bull*, 72, 1229-1253.
- Pingitore, N. E., S. B. Fretzdorff, B. P. Seitz, L.Y. Estrada, P. M. Borrego, G. M. Crawford, and K. M. Love, 1993, Dissolution kinetics of CaCO₃ in common laboratory solvents: *Journal of Sedimentary Petrology*, 63, no. 4, 641-645.
- Phillips, P. M., 2007, Porosity and permeability of bimodal sediment mixtures using natural sediment, Master thesis, Wright State University.
- Podczec, F. and M. Sharma, 1995, The influence of particle size and shape of components of binary powder mixtures on the maximum volume reduction due to packing: *International journal of pharmaceutics*, 137, 41-47
- Rathore, J. S., E. Fjaer, R. M. Holt, and L. Renlie, 1994, P- and S-wave anisotropy of a synthetic sandstone with controlled crack geometry: *Geophysical Prospecting*, 43, 711-728, doi: 10.1111/j.1365-2478.1995.tb00276.x.
- Regnet, J. B., P. Robion, C. David, J. Fortin, B. Brigaud, and B. Yven, 2015 Acoustic and reservoir properties of microporous carbonate rocks: Implication of micrite particle size and morphology: *J. Geophys. Res. Solid Earth*, 120, 790-811, doi:10.1002/2014JB011313.
- Reuss, A., 1929, Berechnung der fliessgrenze von mischkristallen auf grund der plastizitätsbedingung für einkristalle: *Zeitschrift für Angewandte Mathematik and Mechanik*, 9, 49-58.
- Revil, A., and L. M. Cathles, 1999, Permeability of shaly sands: *Water Resources Research*, 35, 651-662.
- Ridgway, K., and K. J. Tarbuck, 1968, Particulate mixture bulk densities: *Chem. Proc. Eng.*, 49, 103-105.
- Rogen, B., I. L. Fabricious, P. Japsen, C. Hoier, G. Mavko, and J. M. Pedersen, 2005, Ultrasonic velocities of North Sea chalk samples: Influence of porosity, fluid content, and texture: *Geophysical Prospecting*, 53, 481- 496, doi: 10.1111/j.1365-2478.2005.00485.x.
- Rumpf, H. and A.R., Gupte, 1971, Einflüsse der Porosität und Korngrößenverteilung im Widerstandsgesetz der Porenströmung: *Chem-Ing.-Tech.*, 43, 367-375.
- Santamarina, J. C., K. A., Klein, and M. A. Fam, 2001, Soils and waves—Particulate materials behavior, characterization and process monitoring, Wiley, New York.

- Santomaso, A., Lazzaro, P., Canu, P., 2003. Powder flowability and density ratios: the impact of granules packing. *Chem. Eng. Sci.* 58, 2857–2874.
- Scotellaro, C., T. Vanorio, and G. Mavko, 2008, The effect of mineral composition and pressure on carbonate rocks: 77th Annual International Meeting, SEG, Expanded Abstracts, 26, 1684–1689.
- Skalinski, M., Y. Se, T. Playton, P. Theologou, W. Narr, M. Sullivan, and R. Mallan, 2015, Petrophysical challenges in giant carbonate Tengiz Field, Republic of Kazakhstan: *Petrophysics*, vol. 56, no. 6, p 615-647.
- Shinn, E. A., R. B. Halley, J. H. Hudson, and B. H. Lidz, 1977, Limestone compaction: An enigma: *Geology*, v. 5, p 21-24.
- Stovall, T., de Larrard, F., and M. Buil, 1986, Linear packing density model of grain mixtures: *Powder Technology*, 48(1), 1–12.
- Sun, Y.F., 2004. Effects of pore structure on elastic wave propagation in rocks, AVO modeling. *Journal of Geophysics and Engineering* 1, 268–276.
- Suzuki, M., T. Oshima, 1985, Verification of a Model for Estimating the Void Fraction in a Three Component Randomly Packed Bed. *Powder Technol.*, 43, 147-153.
- Teh, W. J., G. P., Willhite, J. H. Doveton, and J. S. Tsau, 2011, Improved Predictions of Porosity from Microresistivity Logs in a Mature Field through Incorporation of Pore Typing, paper SPE 149506 presented at the SPE Eastern Regional Meeting, Columbus, OH, August, 17-19.
- Tiab, D. and E. C. Donaldson, 1996, *Petrophysics: Theory and Practice of Measuring Reservoir Rock and Fluid Transport Properties*, Gulf Publishing Company.
- Tillotson, P., J. Sothcott, A. I. Best, M. Chapman, and X. Y. Li, 2012, Experimental verification of the fracture density and shear-wave splitting relationship using synthetic silica cemented sandstones with a controlled fracture geometry: *Geophysical Prospecting*, 60, 516–525, doi: 0.1111/j.1365-2478.2011.01021.x.
- Tucker, M. E., and R. G. C. Bathurst, 1990, *Carbonate diagenesis*, Reprint Series 1 of the IAS: Blackwell Scientific Publications.
- Tucker, M. E., and V. P. Wright, 1990, *Carbonate Sedimentology*: Blackwell Scientific Publications
- Vanorio, T., C. Scotellaro, and G. Mavko, 2007, To fluid-substitute or not to fluid-substitute; How pore shape and chemical processes affect Gassmann's predictability: 77th Annual Meeting, SEG Expanded Abstracts, 1584.
- Vanorio, T., 2008, The effect of chemical and physical processes on the acoustic properties of carbonate rocks: *The Leading Edge*, 27, 1040–1048, doi:10.1190/1.2967558.
- Vanorio, T., and G. Mavko, 2011, Laboratory measurements of the acoustic and transport properties of carbonate rocks and their link with the amount of microcrystalline matrix: *Geophysics*, 76, no. 4, E105–E115, doi:10.1190/1.3580632.
- Vanorio, T., A. Nur, and Y. Ebert, 2011, Rock physics analysis and time-lapse rock imaging of geochemical effects due to the injection of CO₂ into reservoir rocks: *Geophysics*, 76, no. 5, 1-11.
- Vanorio, T., M. Prasad, and A. Nur, 2003, Elastic properties of dry clay mineral aggregates, suspensions and sandstones: *Geophys J. Int.*, 155, 319-326.
- Vanorio T., Y. Elbert, and D. Grombacher, 2015, What laboratory-induced dissolution trends tell us about natural diagenetic trends of carbonate rocks, Geological Society, London, Special Publications, 406, <http://dx.doi.org/10.1144/SP406.4>

- Vega, S., J. V. Prajapat, A. A. Al Mazrooei, 2010, Preliminary experiments to evaluate the Gassmann equation in carbonate rocks: calcite and dolomite: *The Leading Edge*, **29**, no. 8, 906-911, doi: 10.1190/1.3480002.
- Verwer, K., H. Braaksma, and J. A. Kenter, 2008, Acoustic properties of carbonates: Effects of rock texture and implications for fluid substitution: *Geophysics*, **73**, no. 2, B51–B65, doi: 10.1190/1.2831935.
- Vialle, S., and T. Vanorio, 2011, Laboratory measurements of elastic properties of carbonate rocks during injection of reactive CO₂-saturated water: *Geophysical Research Letters*, **38**, L01302, doi:10.1029/2010GL045606.
- Vidal, D., C. Ridgway, G. Pianet, J. Schoelkopt, R. Roy, and F. Bertrand, 2009, Effect of particle size distribution and packing compression on fluid permeability as predicted by lattice-Boltzmann simulations: *Computers and Chemical Engineering*, **3**, 256-266
- Visser, J., 1989, Van der Waals and other cohesive forces affecting powder fluidization. *Powder Technol.* **58**, 1–10.
- Wang, Z. Z., R. H. Wang, R. J. Weger, T. Y. Li, and F. F. Wang, 2015, Porescale modeling of elastic wave propagation in carbonate rocks: *Geophysics*, **80**, no. 1, D51–D63., doi: 10.1190/geo2014-0050.1.
- Weber, L. J., B. P. Francis, P. M. Harris, and M. Clark, 2003, Stratigraphy, lithofacies, and reservoir distribution, Tengiz field, Kazakhstan, in W. M. Ahr, P. M. Harris, W. A. Morgan, and I. D. Somerville, eds., *PermoCarboniferous carbonate platforms and reefs: SEPM Special Publication 78 and AAPG Memoir 83*, p. 351–394.
- Weger, R. J., 2006, Quantitative pore/rock type parameters in carbonates and their relationship to velocity deviation: Ph.D. dissertation, University of Miami.
- Weger, R. J., G. P. Eberli, G. T. Baechle, J. L. Massafferro, and Y. F. Sun, 2009, Quantification of pore structure and its effect on sonic velocity and permeability in carbonates: *AAPG Bulletin*, **93**, 1297–1317, doi: 10.1306/05270909001.
- Westman, A. E. R., and H. R. Hugill, 1930, The Packing of Particles: *J. Am. Ceram. Soc.*, **13**, 767-779.
- Wilson, J. L., 1975, *Carbonate facies in geologic history*: Springer-Verlag.
- Wilson, M. L., and S. H. Kosmatka, 2002, Design and control of concrete mixtures: *PCA Engineering Bulletin EB 001*, Portland Cement Association, Skokie, IL 2002
- Winkler, K. W., 1983, Frequency Dependent Ultrasonic Properties of High-Porosity Sandstones: *Journal of Geophysical Research*, **88**, B1, 9493-9499, doi: 10.1029/JB088iB11p09493.
- Winkler, K. W., 1983, Frequency Dependent Ultrasonic Properties of High-Porosity Sandstones: *Journal of Geophysical Research*, **88**, B1, 9493-9499, doi: 10.1029/JB088iB11p09493.
- Witt, W., and H. Gokdag, 1994, Orbitolinid biostratigraphy of the Shuaiba Formation (Aptian), Oman. Implications for reservoir development, in M. D. Simmons, ed., *Micropalaeontology and hydrocarbon exploration in the Middle East*: Chapman & Hall, 221–234.
- Wyllie, M. R. J., A. R. Gregory, and L. W. Gardner, 1956, Elastic wave velocities in heterogeneous and porous media: *Geophysics*, **21**, 41–70, doi: 10.1190/1.1438217.

- Wynn, T. C., and F. J. Read, 2006, Sequence-stratigraphic analysis using well cuttings, Mississippian Greenbrier Group, West Virginia, AAPG Bulletin, V. 90, 1869-1882, DOI:10.1306/06140605099
- Yilmaz, Y., 2009. A study on the limit void ratio characteristics of medium to fine mixed graded sands: Eng. Geol. 104, 290–294.
- Yu, A. B., N. Standish, 1987, Porosity Calculation of Multi-Component Mixtures of Particles: Powder Technol, 7, 52, 233-241.
- Yu, A. B., N. Standish, 1988, An Analytical-Parametric Theory of the Random Packing of Particles: Powder Technol, 55, 171-186.
- Yu, A. B., and N. Standish, 1991, Estimation of the porosity of particle mixtures by a linear-mixture packing model: Industrial and Engineering Chemistry Research, 30(6), 1372–1385.
- Yu, A. B., R. P. Zou, and N., Standish, 1992, the packing of ternary mixtures of non-spherical particles: J. Am. Ceram. Soc., 75, 2765-2772.
- Yu, A. B., and N. Standish, 1993, Characterization of Non-Spherical Particles from Their Packing Behavior: Powder Technol, 74, 205-213.
- Yu, A. B., N. Standish, and A. Mclean, 1993, Porosity calculation of binary mixture of non-spherical particles: J. Am. Ceram. Soc., 76 (11), 2813-2816
- Yu, A.B., R. P. Zou, and N. Standish, 1996, Modifying the linear packing model for predicting the porosity of non-spherical particle mixtures: Ind. Eng. Chem. Res., 35, 3730–3741
- Yu, A.B., J. Bridgwater, and A. Burbidge, 1997, On the modelling of the packing of fine particles: Powder Technol., 92, 185–194
- Zhang, S., M. S. Paterson, and S. F. Cox, 1994, Porosity and permeability evolution during hot isostatic pressing of calcite aggregates, J. Geophys Res., 99, 15,741-15,760.
- Zhang, X., and C.J. Spiers, 2005, Compaction of granular calcite by pressure solution at room temperature and effects of pore fluid chemistry: International Journal of Rock Mechanics & Mining Sciences, 42, 950–960.
- Zhang, Z. F., A. L. Ward, and J. M. Keller, 2010, Determining the porosity and saturated hydraulic conductivity of binary mixtures: Vadose Zone Journal, 10, 313-321.
- Zhu, W., B. Evans and Y. Bernabe, 1999, Densification and permeability reduction in hot-pressed calcite: A kinetic model, J. Geophysical research, 104, no. B11, 501-511
- Zou, R. P., and A. B. Yu, 1996, Evaluation of the packing characteristics of mono-sized non-spherical particles: Powder Technol, 88, 71-79.
- Zou, R. P., C. L. Feng, J. Q. Xu, and A. B. Yu, 2005, Prediction of the porosity of multicomponent mixtures of wet coarse spheres: Ind. Eng. Chem. Res., 44, 8401-8408
- Zou, R. P., M. L. Gan, and A. B. Yu, 2011, Prediction of porosity of multi-component mixtures of cohesive and non-cohesive particles: Chemical Engineering Science, 66, 4711-4721.

APPENDICES

APPENDIX A

Composition and transport properties of the analog samples.

Table A.1: The volume percentages of the four components in the created analogs including: solid micrite, solid grains, primary porosity (predominantly microporosity) and newly created macropores. The last column correspond to the volume percentage of solid micrite out of total solid volume.

Set Name	Micrite (%)	Grains (%)	Primary porosity (%)	Newly created macroporosity (%)	Permeability (mD)	Micrite-to-Grain Indicator (%)
Set MCR	0	73.2	26.8	-	100	0
	7.6	68.0	24.4	-	20	10
	15.2	60.6	24.2	-	7	20
	22.8	53.1	24.1	-	3	30
	29.9	44.8	25.3	-	2.6	40
	43.9	29.3	26.8	-	2	60
	57.6	14.4	28.0	-	1.7	80
	70.4	0.0	29.6	-	1.6	100
Additional set MCR (made using 5 MPa)	82.2	0.0	17.8	-	0.1	100
	26.1	60.8	13.1	-	0.18	30
	0	83.9	16.1	-	22	0
Set MACRO	0.0	64.0	20.7	15.3	250	0
	3.9	62.3	22.3	11.5	90	6
	7.8	62.1	22.6	7.5	30	11
	8.1	56.8	19.9	15.2	46	13
	11.4	61.0	24.0	3.6	14	16
	15.5	54.3	22.8	7.4	12	22
	23.1	46.3	23.1	7.5	5	33
	46.7	15.6	22.6	15.1	4.4	75
	51.8	14.8	25.9	7.5	3	78
	64.5	0.0	28.0	7.5	2.8	100

Appendix B:

Ideal packing model for grains-micrite mixture.

Let us first define the input parameters:

- m : micrite volume fraction which is defined as the ratio of the volume of micrite (micrite solid material and associated microporosity between the particles) to the bulk volume of the mixture.
- ϕ_m : porosity of pure micrite
- ϕ_{sg} : porosity of pure skeletal grains
- ρ_m and ρ_{sg} : particle density of the micrite and skeletal grains respectively.
- f_m : micrite weight fraction defined as the ratio of micrite mass to mass of the mixture.

Then, the porosity of the mixture (ϕ) can be estimated using the following set of equations (redefined after Marion et al., 1992):

$$\phi = \phi_{sg} - m(1 - \phi_m) \quad \text{for } m < \phi_{sg} \quad (\text{B.1})$$

$$\phi = \phi_{sg} \phi_m \quad \text{for } m = \phi_{sg} \quad (\text{B.2})$$

$$\phi = m \phi_m \quad \text{for } m > \phi_{sg} \quad (\text{B.3})$$

Equations B.1 and B.3 corresponds to the porosity of the grain supported and micrite supported regime respectively. In order to plot the results as function of micrite weight fraction, the micrite volume fraction m can be related to the micrite weight fraction (f_m) using the following equations:

$$f_m = \frac{m(1 - \phi_m)\rho_m}{m(1 - \phi_m)\rho_m + (1 - \phi_{sg})\rho_{sg}} \quad \text{for } m < \phi_{sg} \quad (\text{B.4})$$

$$f_m = \frac{m(1 - \phi_m)\rho_m}{m(1 - \phi_m)\rho_m + (1 - m)\rho_{sg}} \quad \text{for } m > \phi_{sg} \quad (\text{B.5})$$

Since the particle density for both skeletal grains and micrite is the same, the ρ_m and ρ_{sg} terms will cancel out in equations B.4 and B.5

Appendix C

Summary of non-ideal packing model for binary mixture of spheres (more details can be found in Yu and Standish, 1988 & Yu et al., 1996)

- The system considered is composed of 2 components/end-members of equal density, non-deformable spheres, each with a certain uniform diameter d (where d_f and d_c correspond to the diameter of the fine and coarse spheres respectively). The subscript f and c would refer to fine and coarse particles respectively, throughout this study.
- Each packing system for the two end-members has initial specific volume, V , defined as the volume occupied by unit solid volume of the particles. V can be related to porosity by: $V = 1/(1-\phi)$.
- Furnas (1928) suggested that this system of particulate mixtures can be considered in general analogous to a system of solutions of thermodynamics. Then, the total specific volume of the mixture can be estimated using:

$$V_{total} = \sum_{i=1}^n v_i f_i \quad (C.1)$$

- where $n=2$, f is the fraction of each component i , and v_i is the partial specific volume which is the specific volume of component i in the mixture. Note that in case of ideal packing, both the initial specific volume of pure component and its partial specific volume are equal ($V_i = v_i$).
- In the case of non-ideal packing ($d_f/d_c \gg 0$), we have $V_i \neq v_i$ and hence, correction functions have to be introduced to estimate v_i . Correction functions account for the loosening effect $L(R)$ and wall effect $W(R)$ as explained in section 3.4.2.2b depending on the ratio of diameters R :

- When coarse particles are dominant, the specific volume of the mixture, V_a , can be estimated using the following equations (Yu et al., 1996):

$$V_a = V_c f_c + V_f f_f - [1-L(R)] * V_f f_f \quad (C.2)$$

$$L(R) = 1 - (1 - R)^{3.3} - 2.8 * R * (1 - R)^{2.7} \quad (C.3)$$

- When fine particles are dominant, the specific volume of the mixture V_b can be estimated using the following equations:

$$V_b = V_c X_c + V_f X_f - [1-W(R)] * V_c X_c * (1 - 1/V_c) \quad (C.4)$$

$$W(R) = 1 - (1 - R)^2 - 0.4 * R * (1 - R)^{3.7} \quad (C.5)$$

- Since the volume of particles occupied by a unit solid volume of particles should not be less than the volume that can accommodate all the particles, the overall specific volume of the mixture at any given f_f can then be determined by:

$$V_{total} = maximum \{V_a, V_b\} \quad (C.6)$$

- Note that the same set of equations were re-written in terms of porosity as shown in section 3.4.2.2b.

Appendix D

Determination of equivalent packing diameter, d_p (more details can be found in Yu and Standish, 1993)

For binary mixtures of spheres, it is known that the specific volume variation (or porosity variation) is equal to zero when the two end-members have the same diameter ($R=1$). This corresponds to the maximum porosity at a given fraction of an end-member as shown in Figure D.1 (Yu and Standish, 1993). The Figure shows how the porosity of the binary mixture of spheres changes at constant fractional solid volume (0.5), as the diameter of one of the end members increases. The horizontal axis corresponds to the diameter ratio between the two spheres where the diameter of one of them is kept constant while increasing the other sphere diameter. The maximum porosity is obtained when the two spheres have the same diameter or when the difference between the two diameters is very small (Figure D.1). For any spherical particle, the equivalent packing diameter d_p is equal to the diameter of the sphere itself and hence, d_p can be defined as the diameter of the sphere which, when combined with a particle at a given fractional solid, gives maximum porosity (Yu and Standish, 1993).

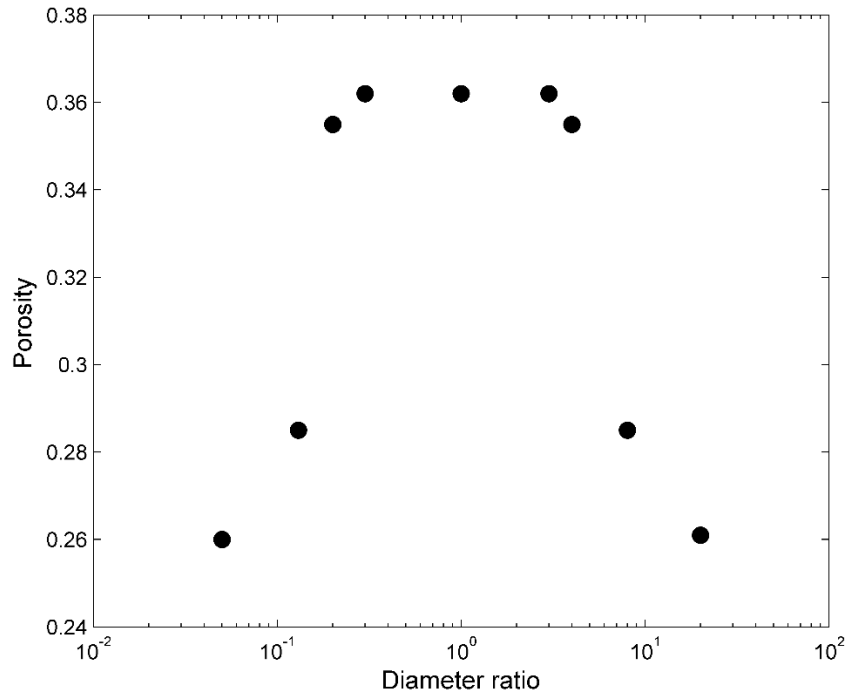


Figure D.1: Porosity of binary mixtures of spherical particle and spheres of different diameters, at constant fractional solid volume ($f_f=f_c=0.5$). Figure is modified after Yu and Standish, 1993.

Experimentally, d_p for a non-spherical particle, can be determined by: (a) mixing the non-spherical particles with spheres that have different diameters, at a constant fractional volume of spheres, (b) measuring the porosity of each mixture, and (c) d_p of the non-spherical particle is then equal to the diameter of sphere that resulted in the maximum porosity. An example of such approach is shown in Figure D.2 (Yu and Standish, 1993).

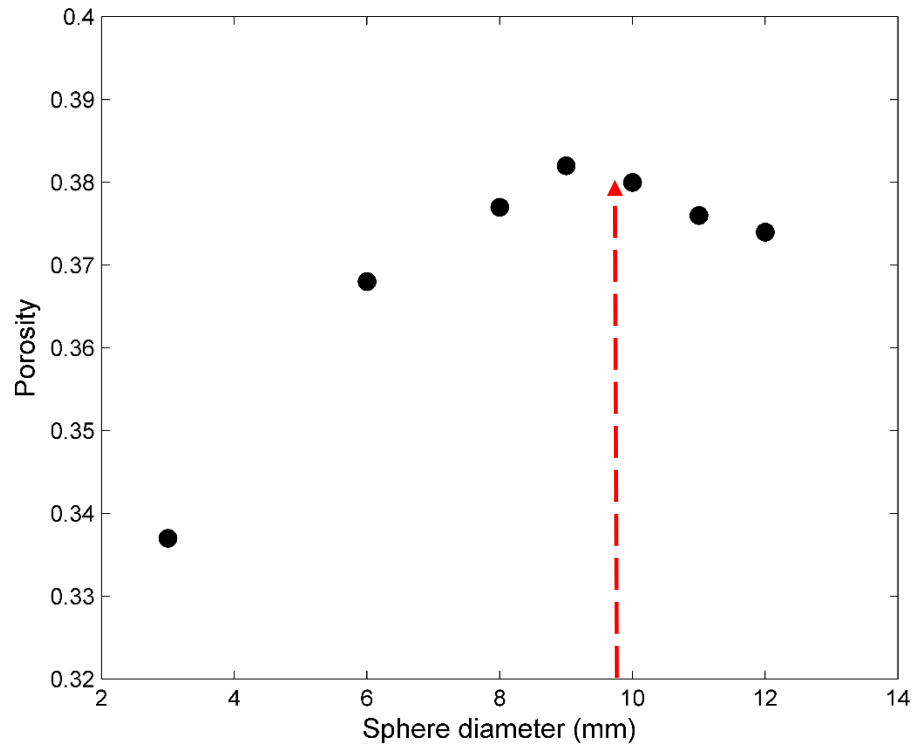


Figure D.2: Porosity of binary mixtures of cylinder (length, $L=12$ mm, diameter, $D=6$ mm) and spheres of different diameters, at constant fraction of spheres (0.5). Figure is modified after Yu and Standish, 1993. Maximum porosity for the cylinders-spheres mixture was obtained when using spheres of 9 mm in diameter (highlighted by red arrow). Therefore, d_p for this cylinder is 9 mm.

Appendix E

Relating d_p to d_v and ψ (more details can be found in Zou and Yu, 1996)

Zou and Yu, 1996 used experimentally determined d_p for cylinders, disks and cubes of different dimensions reported by Milewski, 1973 and Yu et al., 1992, and established an empirical relation between d_p , d_v and ψ . Both d_v and ψ can be calculated for uniform shapes like cylinders as shown in equations E.1 and E.2:

For the calculation of d_v :

$$\begin{aligned} \text{Volume}_{\text{sphere}} &= \text{Volume}_{\text{cylinder}} \\ \frac{4}{3}\pi \left(\frac{d_v}{2}\right)^3 &= \pi \left(\frac{D}{2}\right)^2 L \\ d_v &= 1.145 \left(\frac{L}{D}\right)^{1/3} D \end{aligned} \quad (\text{E.1})$$

(where D is the diameter of the cylinder base and L is the length of the cylinder).

For the calculation of ψ :

$$\begin{aligned} \psi &= \frac{\text{Surface Area}_{\text{sphere}}}{\text{Surface Area}_{\text{cylinder}}} \\ \psi &= \frac{4\pi \left(\frac{d_v}{2}\right)^2}{2\pi \left(\frac{D}{2}\right) \left[L + \left(\frac{D}{2}\right)\right]} = 2.621 \frac{\left(\frac{L}{D}\right)^{2/3}}{1 + 2\left(\frac{L}{D}\right)} \end{aligned} \quad (\text{E.2})$$

Similarly, the d_v and ψ for all uniform non-spherical particles were obtained and then plotted against the measured d_p values as shown in Figure E.1. The following empirical equation was obtained:

$$d_p = \frac{d_v}{\psi^{2.785} \exp[2.946(1 - \psi)]} \quad (\text{E.3})$$

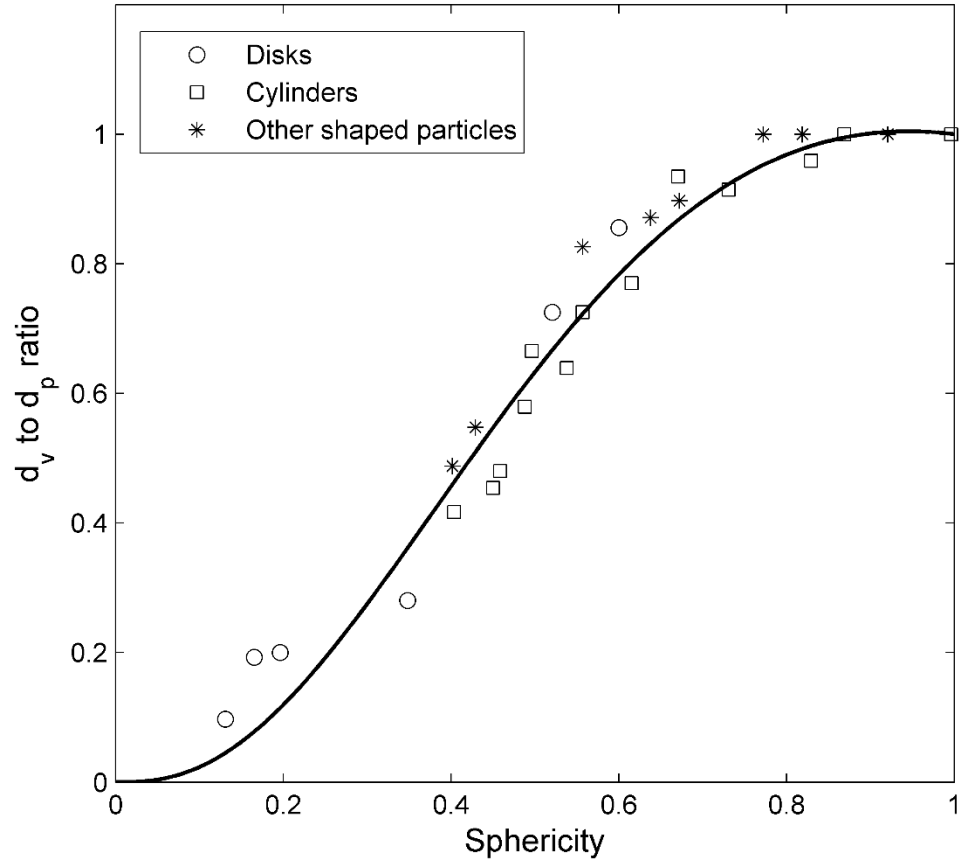


Figure E.1: Dependence of d_v/d_p on sphericity ψ ; Figure modified after Zou and Yu, 1996. The solid curve corresponds to trend obtained from equation E.3

Yu et al. 1996 proposed to use equation E.3 to find d_p for both the coarse and fine non-spherical particles, obtain $R = d_{pf} / d_{pc}$, and finally use equations 3.1 through 3.5 to predict the porosity of the non-spherical binary mixture. The authors were able to successfully apply this approach to binary mixtures of cylinders of different length-to-diameter ratios (Yu et al., 1996).

Appendix F

Defining d_v and ψ in terms of specific surface area

- For any particle:

$$\frac{\text{Surface Area}}{1 \text{ gram}} = A = \frac{S_{\text{particle}}(N)}{1 \text{ gram}} = \frac{(S_{\text{particle}})(N)}{\rho(\mathcal{V}_{\text{particle}})(N)} \quad (\text{F.1})$$

$$\text{so we have: } \mathcal{V}_{\text{particle}} = \frac{S_{\text{particle}}}{A \rho} \quad (\text{F.2})$$

where A is specific surface area, S is surface area, \mathcal{V} is volume, N is number of particles in one gram, and ρ is particle density.

- By definition, d_v is the diameter of the sphere having the same volume as the particle, so:

$$\begin{aligned} \mathcal{V}_{\text{particle}} &= \mathcal{V}_{\text{sphere}} \\ \frac{S_{\text{particle}}}{A \rho} &= \frac{4}{3} \pi \left(\frac{d_v}{2}\right)^3 \\ \left(\frac{d_v}{2}\right)^3 &= \frac{3 S_{\text{particle}}}{4 \pi A \rho} \end{aligned} \quad (\text{F.3})$$

which suggest that d_v can be fully defined by the specific surface area (note that ρ is a property of the particle and that the surface area of the particle is related to the specific surface area through N as shown in equation F.1).

- Similarly, sphericity ψ is defined as:

$$\psi = \frac{S_{\text{sphere with same volume}}}{S_{\text{particle}}} = \frac{4 \pi \left(\frac{d_v}{2}\right)^2}{S_{\text{particle}}} \quad (\text{F.4})$$

$$\psi = \frac{4 \pi \left(\frac{3 S_{\text{particle}}}{4 \pi A \rho}\right)^{2/3}}{S_{\text{particle}}} = \left(\frac{4 \pi}{S_{\text{particle}}}\right)^{1/3} \left(\frac{3}{A \rho}\right)^{2/3} \quad (\text{F.5})$$

which also indicates that ψ can be fully defined by the specific surface area.

Appendix G

Defining the specific surface area (A) for different uniform shaped particles. The notations used below are as follow: A is specific surface area, S is surface area, V is volume, N is number of particle in one gram, and ρ is particle density

- Cylinders or disks, (L is length, D is diameter of the base):

$$\begin{aligned} A_{cylinder} &= \frac{S_{cylinder}(N)}{1 \text{ gram}} = \frac{(S_{cylinder})(N)}{\rho(\mathcal{V}_{cylinder})(N)} \\ &= \frac{2\pi \left(\frac{D}{2}\right)\left(L + \frac{D}{2}\right)}{\rho \pi \left(\frac{D}{2}\right)^2 L} = \frac{2 \left(L + \frac{D}{2}\right)}{\rho \left(\frac{D}{2}\right)L} \end{aligned} \quad (\text{G.1})$$

- Cubes, (L is length):

$$\begin{aligned} A_{cylinder} &= \frac{S_{cube}(N)}{1 \text{ gram}} = \frac{(S_{cube})(N)}{\rho(\mathcal{V}_{cube})(N)} \\ &= \frac{6 L^2}{\rho L^3} = \frac{6}{\rho L} \end{aligned} \quad (\text{G.2})$$

Appendix H

Transport and elastic properties of analog samples

Table H.1: Summary of transport and elastic properties of set MCR samples

Micrite (wt%)	Porosity (%)	Permeability (mD)	Bulk density (g/cc)	Ambient conditions																							
				1 MPa		2 MPa		4 MPa		6 MPa		8 MPa		12 MPa		20 MPa		25 MPa									
				V_p (m/s)	V_s (m/s)	V_p (m/s)	V_s (m/s)	V_p (m/s)	V_s (m/s)	V_p (m/s)	V_s (m/s)	V_p (m/s)	V_s (m/s)	V_p (m/s)	V_s (m/s)	V_p (m/s)	V_s (m/s)	V_p (m/s)	V_s (m/s)	V_p (m/s)	V_s (m/s)	V_p (m/s)	V_s (m/s)				
0	26.7	110	1.97	2040	1180	2175	1380	2446	1490	2672	1599	2807	1645	2889	1675	2994	1725	3125	1793	3146	1810						
10	24.5	20	2.04	2140	1245	2208	1373	2530	1490	2720	1580	2843	1629	2930	1657	3032	1702	3174	1766	3234	1800						
20	24.2	7.2	2.04	2152	1373	2187	1429	2320	1520	2487	1590	2630	1655	2780	1715	2920	1780	3123	1842	3184	1843						
30	24.3	3.1	2.04	2116	1354	2280	1438	2470	1513	2643	1587	2798	1621	2899	1655	3016	1709	3163	1797	3214	1834						
40	25.3	2.6	2.01	2106	1349	2300	1498	2437	1558	2660	1645	2840	1709	2940	1750	3099	1822	3211	1888	3252	1906						
60	26.8	2.0	1.97	2304	1430	2339	1544	2426	1590	2565	1585	2634	1618	2707	1640	2834	1693	2980	1759	3042	1780						
80	28.0	1.7	1.94	2471	1490	2735	1588	2812	1616	2865	1649	2919	1673	2954	1687	—	—	3025	1728	3025	1728						
100	29.6	1.7	1.90	2590	1540	2750	1607	2800	1628	2835	1643	2890	1647	2903	1654	2932	1670	2987	1699	3016	1714						

Table H.2: Summary of transport and elastic properties of set MACR samples

Micrite (wt %)	Induced macro-porosity (%)	Total porosity (%)	Bulk density (g/cc)	V_p (m/s)	V_s (m/s)
78	7.5	33.4	1.796	1850	1180
11	7.5	30.1	1.886	1425	900
100	7.4	35.5	1.739	1960	1263
32	7.5	30.6	1.87	1400	890
6	11.5	33.8	1.806	1165	717
11	15.2	35.1	1.759	1265	715

Appendix I

Summary of the DEM theory (more details can be found in Mavko et al., 2009)

DEM theory models the effective elastic moduli of two-phase composite by adding infinitesimal volume fraction of inclusions to the host phase. The effective bulk (K) and shear (G) moduli of the composite vary as function of the volume fraction of inclusion (f), according to the following system of equations:

$$(1 - f) \frac{d}{df} [K(f)] = P(K_i - K) (f) \quad (\text{I.1})$$

$$(1 - f) \frac{d}{df} [G(f)] = Q(G_i - G) (f) \quad (\text{I.2})$$

with initial conditions $K(0) = K_l$ and $G(0) = G_l$ where the subscript 1 refers the initial host material. The bulk and shear moduli of the inclusion material are represented by K_i and G_i respectively. In the micrite-grains mixtures, f is the volume fraction of micrite. The coefficients P and Q are geometric factors that are dependent on the shape of the inclusion as well as on the elastic moduli of the host and inclusion materials. For spherical inclusions, P and Q are given by the following relations (Berryman, 1995):

$$P = \frac{K_h + (\frac{4G_h}{3})}{K_i + (\frac{4G_h}{3})} \quad (\text{I.3})$$

$$P = \frac{G_h + \Sigma_h}{G_i + \Sigma_h} \quad \text{where: } \Sigma_h = \frac{G_h(9K_h + 8G_h)}{6(K_h + 2G_h)} \quad (\text{I.4})$$

In the above relations, the transcript i and h refer to the inclusion and host materials respectively.

Appendix J

Properties of Tengiz samples

Table H Table J.1: Summary of the measured transport and elastic properties of the selected Tengiz samples; as well as the microstructural parameters estimated using both micro-CT scans and SEM images: total He-porosity ϕ , permeability k , ultrasonic P-wave velocity V_p , ultrasonic S-wave velocity V_s , macroporosity ϕ_{macro} , microporosity ϕ_{micro} , content of solid coarse grains f_{grains} , and content of micrite particles $f_{micrite}$. The last column refers to the porosity within the micrite matrix ($\phi_{micrite_direct}$) estimated directly from SEM images as shown in Figure 5.7. The number after the \pm sign refers to the standard deviation of the estimated average parameter.

Samp le ID	Measured physical properties				Microstructural parameters estimated from micro-CT scans				Micro-structural parameters estimated from SEM images				$\phi_{micrite_dir}$ $_{ect}$ (%)
	ϕ (%)	k (mD)	V_p (m/s)	V_s (m/s)	ϕ_{macro} (%)	ϕ_{micro} (%)	f_{grains} (%)	$f_{micrite}$ (%)	ϕ_{macro} (%)	ϕ_{micro} (%)	f_{grains} (%)	$f_{micrite}$ (%)	
Tg1	21.0	7.7	4279	2540	1.6±0.2	19.4±0.2	26.0±3.2	54.0±3.2	1.8±0.4	19.2±0.4	36±2.5	43±2.5	24.5±2.9
Tg2	17.3	9.6	4625	2590	4.7±1	12.6±1	61.7±3	21.0±3	5.5±2	11.8±3	61.5±3.1	21.2±3.1	20.9±3.1
Tg3	13.7	2.3	4810	2677	1.2±0.2	12.5±0.2	38.2±5.4	48.1±5.4	2.5±0.8	11.2±0.8	50.3±3.2	36±3.2	22.0±2
Tg4	19.2	9.4	3990	2527	2.2±0.2	17.0±0.2	50.6±3.4	30.2±3.4	2.3±0.8	16.9±0.8	43.5±4.5	37.3±4.5	24.1±2.7
Tg5	18.9	50.0	4028	2485	7.6±2	11.3±2	68.3±2.9	12.8±2.9	6.3±2.9	12.6±2.9	65.0±4.3	16.1±4.3	30.8±3.4
Tg6	14.1	26.0	4535	2677	5.5±1.3	8.6±1.3	73.8±3.2	12.1±3.2	3.6±3	10.5±3	76.9±3.4	9±3.4	30.0±3
Tg7	5.7	0.02	5797	3211	0±0.1	5.7±0.1	0.0±0.1	94.3±0.1	0±0.1	5.7±0.1	0±0.1	94.3±0.1	7.1±1.9
Tg8	4.8	0.6	4809	2877	3.0±0.3	1.8±0.3	87.2±2.9	8.0±2.9	1.9±1	2.9±1	88.3±3	6.9±3	17.0±2.8
Tg9	14.0	2.0	5006	2801	2.0±0.7	12.0±0.7	39.0±3	47.0±3	1.9±0.5	12.1±0.5	53±4	33±4	17.0±3.1
Tg10	3.3	0.01	5668	3100	2.0±0.3	1.3±0.3	76.6±7.5	20.1±7.5	1.1±0.7	2.2±0.7	67.7±10	33±10	4.9±2.2
Tg11	14.3	3.4	4490	2709	1.5±0.3	12.8±0.3	52.7±2.8	33.0±2.8	Thin section not available				-
Tg12	18.0	43.0	3517	2406	Micro-CT scans not available				4.0±0.9	14.0±0.9	73.0±1	9.0±1	29.8±3.2
Tg13	16.1	3.3	4037	2470	Micro-CT scans not available				1.9±0.7	14.2±0.7	33.1±4.5	50.8±4.5	20.0±2
Tg14	10.6	0.5	4706	2735	Micro-CT scans not available				2.3±0.5	8.3±0.5	48.4±4.4	41.0±4.4	14.5±3
Tg15	12.5	3.1	4413	2644	Micro-CT scans not available				3.0±1.1	9.5±1.1	64.6±3	22.9±3	23.2±2.4

Table J.2: Acoustic velocities as function of confining pressure for 10 selected samples from Tengiz field.

Sample	94% Micrite (Tg7)		9% Micrite (Tg12)		54% Micrite (Tg1)		48% Micrite (Tg3)		12% Micrite (Tg6)	
Pressure (MPa)	V_p (m/s)	V_s (m/s)	V_p (m/s)	V_s (m/s)	V_p (m/s)	V_s (m/s)	V_p (m/s)	V_s (m/s)	V_p (m/s)	V_s (m/s)
1	5695	3368	3516	2405	4287	2692	4888	2831	4717	2811
2	5709	3376	3623	2427	4319	2698	4939	2844	4924	2906
4	5722	3380	3768	2481	4354	2721	4988	2879	5020	2952
6	-	-	3923	2526	4465	2756	5043	2917	5251	3020
8	5738	3380	4058	2594	4518	2776	5140	2949	5342	3071
12	5750	3394	4241	2686	4593	2807	5219	2995	5587	3164
16	5750	3394	4399	2747	4609	2818	5315	3033	5703	3219
20	5755	3400	4508	2790	4636	2828	5372	3057	5845	3266
25	5761	3410	4644	2838	4653	2839	5410	3082	5920	3297
30	5761	3410	4672	2851	4680	2860	5472	3102	6045	3306

Sample	30% Micrite (Tg4)		21% Micrite (Tg2)		23% Micrite (Tg15)		33% Micrite (Tg11)		8% Micrite (Tg8)	
Pressure (MPa)	V_p (m/s)	V_s (m/s)	V_p (m/s)	V_s (m/s)	V_p (m/s)	V_s (m/s)	V_p (m/s)	V_s (m/s)	V_p (m/s)	V_s (m/s)
1	4275	2530	4574	2753	4520	2614	4610	2672	5630	2928
2	4298	2543	4644	2782	4607	2632	4667	2690	5731	2950
4	4359	2579	4760	2815	4687	2660	4777	2768	5809	2989
6	4437	2625	4850	2868	4837	2725	4858	2806	-	-
8	4540	2650	4911	2905	4938	2782	4937	2829	6087	3079
12	4700	2698	5052	2940	5044	2834	5001	2868	6279	3147
16	4800	2738	5129	2969	5142	2896	5096	2895	6436	3204
20	4850	2755	5184	2996	5196	2920	5142	2923	6516	3244
25	4889	2775	5192	3008	5257	2935	5207	2937	6548	3277
30	4892	2792	5220	3025	5266	2940	5225	2947	6587	3302

Appendix K

Modeling the effect of micrite content on permeability utilizing the approximation of Kozeny-Carman equation for a pack of spheres.

The porosity-permeability relationships for the natural rocks from Tengiz (Figure 5.10) showed similar trends to those observed from the analog samples (Figure 3.4, Chapter 3). That is, micrite rich samples have lower permeability at a given porosity compared to grain-supported samples. In order to model the data, we followed the same approach shown in Chapter 3 (Section 3.5.2.2) utilizing the approximation of Kozeny-Carman equation for a pack of spheres:

$$k = \frac{(\phi - \phi_c)^3 d^2}{36 B (1 - \phi - \phi_c)^2}, \quad (\text{K.1})$$

where B is geometric factor (corresponding to the complexity of pore geometry), and ϕ_c is percolation porosity, below which the remaining porosity is disconnected and does not contribute to the flow (Mavko and Nur, 1997; Bentz et al., 1999; Mavko et al., 2009). For granular media with mixed grain sizes (poor sorting), Rumpf and Gupta (1971), and Dullien (1992) suggested that the effective grain diameter d , is given by:

$$\frac{1}{d} = \sum_i \frac{f_i}{d_i}, \quad (\text{K.2})$$

where f_i is the volume fraction of the particle i with average diameter d_i .

We used a simplified sphere packing system, where the micrite particles have a diameter of 4 μm while the grains were assigned a diameter of 500 μm . Both diameter values were based on observations from SEM images (see Figures 5.5a, c, 5.7a, and 5.8), and were kept constant for all samples for simplicity. The relative fraction of micrite and grains is known based on the micrite-to-grain indicator (i.e., the percentage of solid micrite out of the total solid volume). Samples with similar micrite-to-grain indicators were grouped together, where the average value was used to model the porosity-permeability relationships for the samples. The porosity-permeability relationship for samples with a certain micrite-to-grain

indicator, can then be represented by the Kozeny-Carman relation utilizing equation K.1, for a given d (i.e., given micrite %) determined by equation K.2, as explained previously in Chapter 3. We finally examined all possible values of geometric factor B and percolation porosity ϕ_c in an effort to fit the data for each trend (i.e., each average micrite content). Figure K.1 shows that the porosity-permeability data points for samples with similar micrite content were found to follow a single Kozeny-Carman curve (Figure K.1), which agrees with the observation from the analog samples. The curves were constructed following the approach detailed above and by choosing a pair value for ϕ_c and B from the possible ranges shown in Figure K.2 for each micrite-to-grain indicator. The data show that micrite-supported samples have relatively larger percolation porosities, ϕ_c , but lower geometric factor, B , compared to grain-supported samples (Figure K.2). The increase of percolation porosity with micrite content is consistent with the observations from analog samples (see Figure 3.21a). This could be explained by the micrite likely reducing and blocking more pore throats and adding more microporosity that does not contribute to the flow. The relatively higher B in grain-supported samples suggests a slightly more complicated pore geometry compared to micrite-supported samples although the change in B is not significant, unlike what was observed for the analog samples (Figure 3.21 in Chapter 3). In the analog samples, skeletal grains have very complex and irregular shape compared to micrite and hence, they had more complex pore geometry (i.e., higher B). On the other hand, the grains found in the Tengiz samples (Figure 5.8 a-c) appear to have more regular shape (sub-rounded to rounded), thus their pore geometry may not be very different from that of micrite.

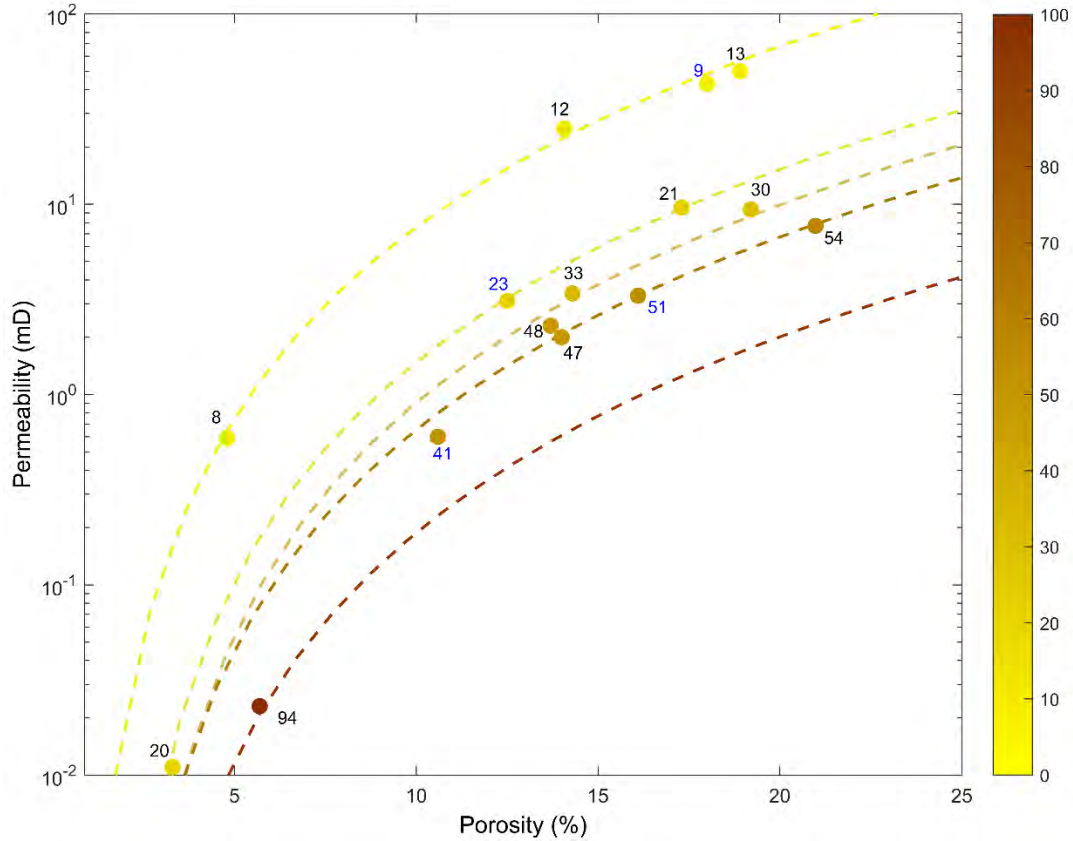


Figure K.1: Permeability as function of porosity for all selected Tengiz samples (same data as in Figure 5.10). The superimposed dashed curves (yellow to brown color) correspond to the porosity-permeability relationship estimated using equation K.1 by selecting one value of B and ϕ_c (from their ranges shown in Figure K.2) for each curve.

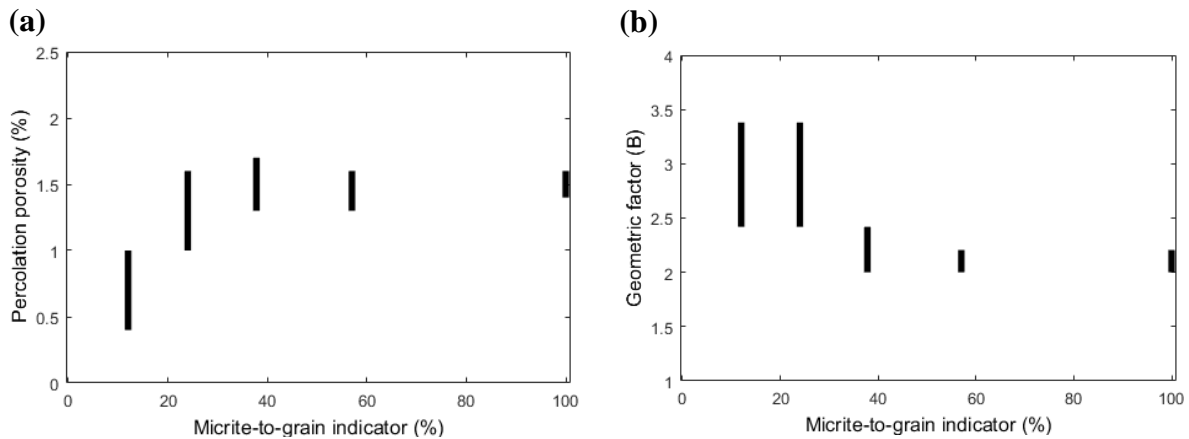


Figure K.2: Percolation porosity (a) and geometric factor (b) as function of micrite-to-grain indicator. Each percentage corresponds to one curve in Figure K.1. The ranges of the percolation porosities and geometric factors cover all possible values that can fit data for samples with similar micrite content using equation K.1.